Development of New Cr-based Hardmetals by Liquid Phase Sintering and Spark Plasma Sintering

by

Xiangxing Deng

in partial fulfillment of the requirements for the degree of Doctor in

Department of Materials Science and Engineering and Chemical Engineering

Universidad Carlos III de Madrid

Advisor:

Andrea García-Junceda Ameigenda

Tutor:

Paula Alvaredo Olmos

Defense Date: March 25th, 2019

ACKNOWLEDGEMENTS

I would like to acknowledgement many friendly people who have helped me and inspired me during my PhD study in IMDEA Materials Institute (IMDEA) and Universidad Carlos III de Madrid (UC3M).

Firstly, I am extremely grateful to my supervisor Andrea García-Junceda (IMDEA) for her patient and professional guidance on my project. Without her dedicated mentorship and continuous guidance, I would have never finished this thesis and grown up as a scientist in hardmetal field. She taught me how to design and implement new experiments, and how to combine them with published references, to advance the development of Cr-based WC hardmetals. She contributed to grow my confidence and to give me a sense of achievement and inspiration after many hard-working days and nights. Specially, I am very gratitude for her edition with my thesis for N times (N>8). I can imagine what her facial expression will be when she begins to read my thesis.

Meanwhile, I must thank the technical staffs or other members in IMDEA for their help: Marcos Angulo for the Gleeble experiments, Jingya Wang for thermodynamic modelling, Dr. Miguel Castillo for FIB operation and TEM characterisation, Vanesa Martínez and José Luis Jiménez for compressive testing, Dr. Soundes Djaziri and Antón Jormescu for XRD measurements, Dr. Juan Pedro Fernández for TGA testing, and Dr. Miguel Monclús for Nanoindentation testing. Their warm-hearted help always made my research at IMDEA much easier.

In addition, I also grateful to Dr. José Manuel Torralba for helping me finish the Ph.D project from his busy schedule. I want to thank him for giving many precious advises during my whole Ph.D career. I like to thank Dr. Paula Alvaredo Olmos and Dr. Sophia Alexandra Tsipas (UC3M) for helping me learning Thermo-Calc and DICTRA software from the beginning. At the same time I want to thank all my dear collogues and friends in UC3M. I need to thank Marta Cartón for giving me tips in mechanical milling and compressing testing. I must thank my friends for their help in Laser diffraction testing, liquid phase sintering, pycnometer using, LECO testing and wear resistance measurement, such as Eduardo Tabares, Eric Macía Rodríguez, Juan Alberto Meza, Dr. Amaya García Casas, Andrea Galán, Andrea Alcántara, Sara Lopez de Armentia and Julia María Ureñ.

I need specially thank Dariusz Garbiec from Instytut Obrobki Plastycznej for SPS supporting and Dr. Nuria Cinca from Hyperion Materials & Technologies for wear resistance testing.

I also want to thank IMDEA Materials Institute for providing me with competitive research infrastructures and creating a friendly environment. I will remember all the activities and parties I attended, like Christmas dinner, IMDEA day, and multi-culture festival. I want to thank Rosa María Bazán, Mariana Huerta, Mar García, Vanessa Hernán-Gómez, and Ainhoa Zapatero for helping me deal with many things in working and living in Spain. I want to thank many friends in IMDEA, Angel Alvaredo, Jaime Castro, Gustavo Esteban, and Andrea Fernández.

I am also very lucky to meet many Chinese friends at IMDEA and in Getafe in my daily life: Dr. De-Yi Wang, Dr. Xiaomin Zhao, Dr. Yetang, Chuanyun Wang, Dr. Zhi Li, Jingya Wang, Jing Zhang, Na Li, Jifeng Li, Lu Zhang, Shidong Fen, Wenliang Fen, Peikan Xia, Dr. Lingwei Yang, Jing Zhang and Yunfu Ou. I specially want to think Fu Can for bring me good memories. I need to thank Dr. Jie Hu for attending different sports together. I would like to think Sai Jiang for giving me inspiration in writing thesis.

I would like to acknowledge to China Scholarship Council (CSC) for supporting me pursuing Ph.D degree in IMDEA and UC3M.

Finally, thanks for my family unselfish supports: Zhongping Deng (father), Qingjian Yun (mother), Xiangqun Deng and Xiangjun Deng (sisters). They are the source of power of my hard-working forever.

Xiangxing Deng

January 3th, 2019

PUBLISHED AND SUBMITTED CONTENT

1. A. García-Junceda, I. Sáez, X.X. Deng, J.M. Torralba, "Development of a Cr-Based Hard Composite Processed by Spark Plasma Sintering". **Metallurgical and Materials Transactions A**, 49(4), 1363-1371. 2018. DOI: 10.1007/s11661-018-4477-7. (I performed partly characterisation of the milled powder. This item is partly related to Chapters 1, 2 and 4. The material from this source included in this thesis is not singled out with typographic means and references)

2. Xiangxing Deng, Jingya. Wang, José Manuel Torralba, Dariusz Garbiec, Andrea García-Junceda1. "Development of Cr-based Hardmetals by Spark Plasma Sintering: Thermodynamic Modelling and Hardness/Toughness Assessment". **Euro PM 2018 Conference.** (I performed all the experimental work and the analysis of results. This item is wholly related to the Chapters 4 and 7. The material from this source included in this thesis is not singled out with typographic means and references)
3. Xiangxing Deng, José Manuel Torralba, Andrea García-Junceda. ¨Field-Assisted Sintering of WC Hardmetals with Cr-Based Binder¨. **Euro PM 2017 Conference**. (I performed all the experimental work and the analysis of results. This item is partly relation to the Chapter 5. The material from this source included in this thesis is not singled out with typographic means and references)

Index

ABSTRACT

Traditional hardmetals based on a cobalt-based tungsten carbide (WC) system are currently the most commonly used hard materials in a wide range of applications, in particular rock drilling tools and cutting tools for metals, plastics, wood and composite materials, due to their outstanding properties in terms of hardness, fracture toughness and wear resistance. The interest in finding alternative binders has been driven by the need for the protection of human health and the environment, since binder alloys including cobalt (Co) and nickel (Ni) are reported as being carcinogenic to human health and toxic chemicals for the environment. In addition, Co binder has another important drawback: the fluctuation in its high price due to its poor availability. Thus, this investigation aims to develop novel hardmetals with outstanding properties avoiding the use of Co and Ni. Within this framework, a chromium-based (Cr-based) alloy is proposed as an alternative binder, as a consequence of its easy availability, reduced price, lower toxicity compared to Co and/or Ni alloy, and the possibility of providing an improvement in the oxidation and wear resistance of the hardmetals.

In the present investigation, the development of Cr-based WC hardmetals is based on a combination of thermodynamic modelling (Thermo-Calc with database TCFE7) and experimental studies. Firstly, Thermo-Calc is used to optimise the compositional design by studying the effect of adding extra iron (Fe) or extra iron and carbon (Fe/C) contents on the phase formation. Then, the hardmetals are processed by a powder metallurgy (PM) route including mechanical milling of the powders and two different sintering techniques: liquid phase sintering (LPS) and spark plasma sintering (SPS). Commercial powders are used as raw materials to prepare Cr-based WC hardmetal powders with 70 vol.% of reinforcement (hard WC) by mechanical milling at 350 rpm during 20 h of milling time. The average size of the WC particles embedded in the Cr-based WC hardmetal powders is close to 80 nm, which demonstrates that high-energy milling is an efficient way to produce nanoscale WC particles in these Cr-based hardmetal powders. Then, Cr-based WC hardmetals with the designed compositions (a 3 wt.% of extra iron content and extra carbon contents varying from 0 to 2 wt.%) are processed by liquid phase sintering at 1450 °C for 30 min. The LPSed Cr-based WC hardmetal with extra 3 wt.% Fe and 1 wt.% C contents has achieved the best hardness and facture toughness values (1647 HV30 and 6.0 MPam1/2). However, the fracture toughness achieved is still not sufficiently high due to the existence of large brittle carbides within the microstructure, together with a porosity

greater than 3%. Thus, the viablity of using an alternative processing route by field assisted solid-state sintering is also studied, in order to limit or prevent the formation of undesirable brittle carbides and further improve the hardness/fracture toughness relationship in these materials. Consequently, the parameters for the consolidation by spark plasma sintering are optimised based on their effect on shrinkage, phase formation, microstructure and mechanical properties. Thus, a sintering temperature of 1350 ºC, a heaing rate of 400 °C, and an applied pressure of 80 MPa during a holding time equal to 10 min, are benificial experimental conditions to improve the relative densification of the bulk sample while maintaining a nanosized WC grain. The SPSed Cr-based WC hardmetal with an extra 3 wt.% Fe content and extra 0.5 wt.% C content reaches the best combination of hardness and toughness fracture values (2219 HV30 and 8.2 MPam1/2). This extremely high hardness comes from the uniform distribution of nanosized prismatic WC grains (around 100 nm), whereas the good toughness is due to the achievement of a near full densification (> 99%), the existence of a thin (W,Cr)2C interphase between WC and Cr2O3 acting as a bonding phase, and to the inhibition of the formation or growth of undesirable brittle carbides. In addition, this hardmetal achieves the highest compressive strength in a temperature range between 25-600ºC, which is also related to its high hardness and toughness values. All the SPSed Cr-based WC hardmetals evaluated in this study have reached a higher oxidation resistance than Fe-based and Co-based WC hardmetals under the same oxidation conditions, mainly due to their high values of activation energy for oxidation. Another important property required for hardmetals, as is the case of wear resistance, is found to be outstanding for these SPSed Cr-based WC hardmetals, even under aggressive wear conditions, in comparison to other commercial Co-based WC hardmetals.

In conclusion, the newly developed SPSed Cr-based WC hardmetals presented in this work exhibit an excellent combination of hardness, toughness, oxidation resistance and wear resistance. Furthermore, these Cr-based WC hardmetals have a lower price and are less toxic than Co-based or Ni-based WC hardmetals. Therefore, Cr-based hardmetals seem to be promising materials for their introduction in industrial applications, in particular for those in which high oxidation and wear resistances are demanded.

Chapter 1

Introduction: State-of-the-art for hardmetals

Contents

1.1 Nature of hardmetals

The terms “hardmetal” and “cemented carbide” are equivalent. “Hardmetal” is commonly accepted in Europe and “cemented carbide” is preferably used in North America. In this work, the designation of hardmetal will be used. The usual constituents of hardmetals comprise two phases: the embedded hard and brittle carbide (usually WC, TaC or NbC) and the relatively soft and ductile metallic binder (commonly Co, Ni or Fe) or their compounds [1]. Figure 1.1 shows the microstructure of the most widely used WC-6 wt.% Co hardmetal. The hard phase WC with the shape of triangular prisms (bright color) is embedded in the soft Co phase (dark color).

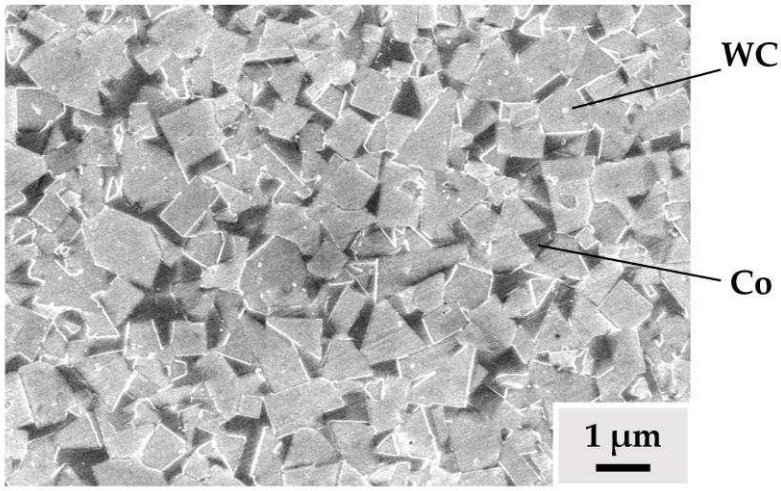

Figure 1.1. Typical microstructure of a WC-Co hardmetal (SEM image) [1] .

The traditional process of hardmetal production is based on a powder metallurgy route, including the following steps: milling of powders, pressing, pre-sintering, liquid phase sintering (LPS) or solid phase sintering by hot isostatic pressing (HIP) [2]. During a liquid sintering process the binder phase transforms into the liquid state, while the hard phase, having a higher melting point than the sintering temperature, remains in solid state. Thus, the hard carbide grains are embedded into the soft binder phase after cooling, creating a composite material with excellent properties. The high hardness and high wear resistance usually found in hardmetals come from the hard phase, whereas the soft bonding metallic alloy enhances the toughness, what finally makes hardmetals to exhibit a good combination of properties, including high hardness, high strength with acceptable fracture toughness, high wear resistance, high corrosion resistance, low coefficient of thermal expansion, high chemical stability, etc. [3]. Recently, solid-state sintering is also adapted to obtain fine-grained hardmetals, where the heating temperature is lower than the melting

point and fast heating rates are applied to reduce the growth of grain size and the total processing time [4]. By adjusting different parameters, including grain size, binder content, refractory carbide addition and carbon content, a manufacturer of hardmetals can design the performance according to the specific applications or requirements from clients or customers [5]. A wide range of properties of commercial WC-Co hardmetals is listed as followed: density (9.0-15.0 g/cm^3), Vickers hardness (1100-2200 HV), toughness (8-25 MPam$^{1/2}$), transverse rupture strength (1000-3000 N/mm^2), hot transverse rupture strength (900-1000 N/mm^2), and compressive strength (4000-7000 MPa) [5]. Therefore, hardmetals are extensively used in industrial and daily applications such as cutting tools (turning and milling of metallic and nonmetallic materials), mining tools (oil well drill bits and rock drill bits), snow plows, road work, nozzles (sand blasting and painting), abrasive waterjet, etc. (Figure 1.2) [6].

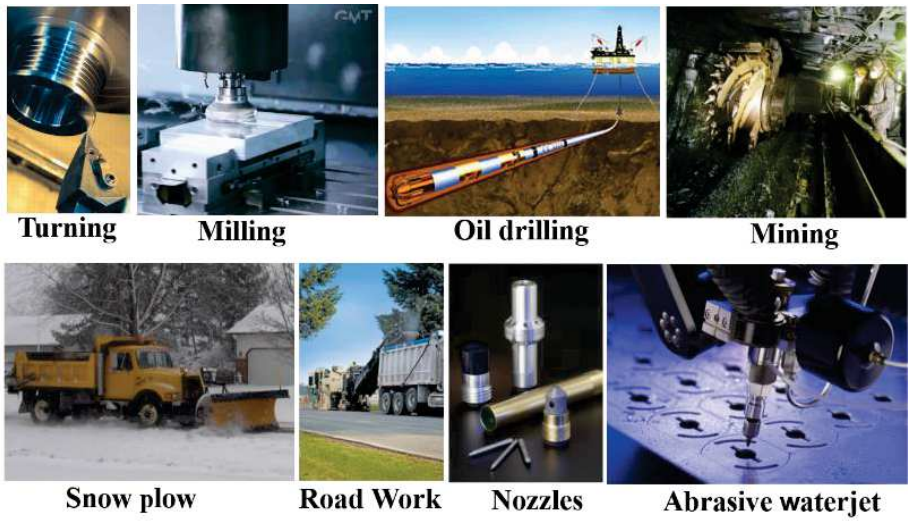

Figure 1.2. Applications of hardmetals [6].

There are also other types of hard materials utilised as cutting tools, but hardmetals are the most commonly and widely used. Figure 1.3 shows the classification of the hard materials and their corresponding use in the global metal cutting market [7]. These hard materials are divided into different categories based on their different combinations of hardness and toughness values. The hardest material is the diamond, followed by cubic boron nitride (CBN) and ceramics, and therefore their applications are focused on abrasion resistant materials where a high level of hardness is needed. Cermets are based on titanium carbonitrides with varied amounts of other alloying elements (Mo, W, and Ta) and metallic binders. Cermets have a typical core-rim structure: core composed of Ti(C,N) and rim of (Ti, N, Mo, W, Ta)C, which generally leads to a higher level of hardness than that achieved by hardmetals, since Ti(C,N) is harder than WC [8-9]. The

inferior fracture toughness and bending strength of cermets than hardmetals indicates why hardmetals are preferred when impacts or vibrations are applied. On the other hand, high-speed steels (HSS) can withstand relatively high temperatures without losing their hardness. However, in the metal cutting market, hardmetals have gradually taken over high-speed steels in many of the tool applications since the usable cutting speed range of high-speed steels is lower compared to hardmetals.

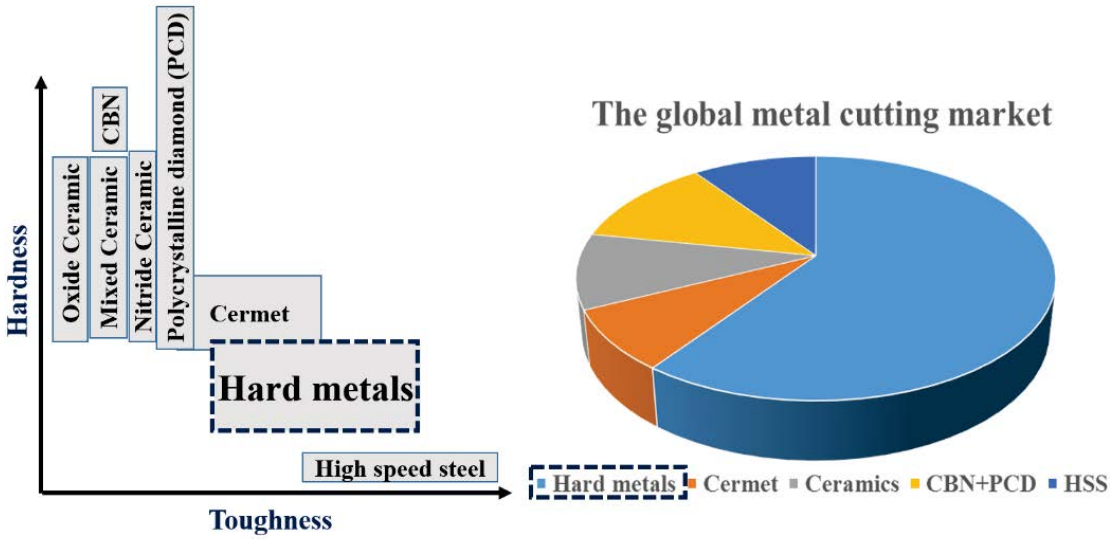

Figure 1.3. Materials and market shares used in the manufacturing of cutting tools [7].

Hardmetals are currently the most important technical hard materials covering a wide range of hardness and toughness combinations. As it is shown in Figure 1.3, hardmetals always take the largest share of the global metal cutting market. From the economic point of view, a small but productivity-enhancing improvement in cutting tools may result in a vastly great saving in the operational outlay. The invention, development and application of hardmetals have greatly saved the cost of products and improved their efficiency, which have led to a great economic value. More specifically, the cost of manufacturing (such as turning, milling, cutting and drilling) has been significantly reduced [10]. Nowadays, Kennametal (USA) and Sandvik (Sweden) are the two largest hard materials producers in the world. The development of hardmetals has led to an increasing rise of production in the past 90 years, as shown in Figure 1.4. The main increasing consumption of hardmetals comes from the rising tendency to manufacture metal parts of complex geometries under the influence of computation numerical control [8]. Nowadays, hardmetals is playing a key part in the growth of the world economy.

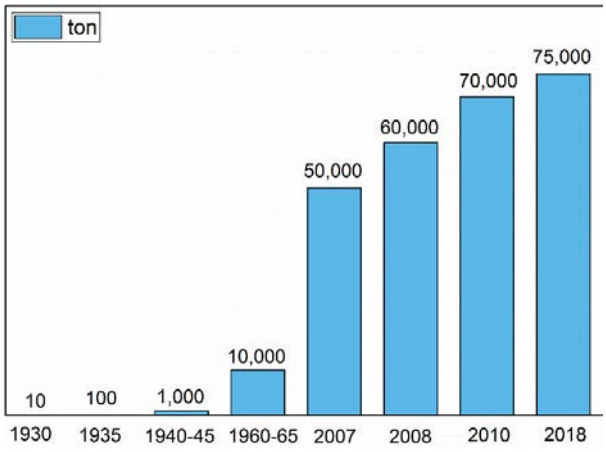

Figure 1.4. Worldwide production of hardmetals in the period of years between 1930-2018 [8].

1.2 History of hardmetals

The origin of hardmetals comes from the light bulbs industry and the need to produce tungsten filaments. The main purpose of Fried Krupp's group (Germany) was to develop a material to replace diamond in the dies for production of tungsten filament. Thus, they invented a WC-Co material that would bring a revolutionary improvement of metal cutting in 1923 [11]. The development of hardmetals has evolved from a temporary solution in industry to a very successful and almost irreplaceable material for the manufacturing industry after a period of more than 90 years. Table 1.1 shows some important developments in the hardmetals chronology from the very beginning (the optimal combination of WC and Co was chosen) to some new trends in hardmetals [12]. WC-Co consisting of 6 wt.% cobalt binder was firstly introduced to the market by Fried Krupp in 1925 under the name *Widia* ("like diamond" in German) which survived today [5]. In many industrial environments, the name "widia" is used as a generic name for hardmetals. Klaus Dreyer and Hans Kolaska published an invention related to hardmetal body and the process for its production in 1926 [13]. Then, one major discovery promoted the development of hardmetals in the 1940s and provided economic advantages in the cutting industry: a small addition of refractory carbides would improve the performance of WC-Co hardmetals [14]. Therefore, TiC, TaC, VC, Cr_3C_2, NbC, and HfC were added in the WC-Co based hardmetals to obtain a higher cutting performance [5]. Hot isostatic pressing (HIP) technique was applied to decrease the porosity of hardmetals, thus further improving the mechanical properties and workability [15]. Another important advance happened in the late 1960s and early 1970s with the application of coatings like TiC, TiN, TiCN and Al_2O_3 on hardmetal tools, which were extremely hard and with high abrasion resistance [16]. More than 80% of all turning inserts and about 70% of all milling inserts

were coated to extend the whole lifetime in industrial applications [17]. In the late of 1970s, the multilayer coatings including carbide/carbonitride/nitride layer sequences were developed with exactly tailored properties for each respective application [18]. Ni, Fe, and other binders were used in 1997 to fully or partially replace Co binder due to its limited availability and its toxicity [19]. According to the Hall-Petch relationship [20], the mechanical behavior of the material may improve significantly when the grain size is reduced to a nanometer scale. Fine grained WC-Co (WC grain size < 1 μm) hardmetals were introduced as early in 1946 [21]. These hardmetals tended to replace quickly high-speed steels for applications requiring high levels of hardness, wear resistance, and cutting speed. However, nanosized hardmetals were not developed until 1995, since the growth of grain size was quickly fast and uncontrolled under the traditional liquid phase sintering. After the 20th century, new sintering processes were widely used to obtain nanostructured WC-Co hardmetals with outstanding properties by varied field-assisted sintering techniques (FAST), such as microwave sintering [22], high-frequency induction heated sintering (HFIHS) [12-13], pulse plasma sintering (PPS) [25], field-assisted hot pressing (FAHP) [26] and spark plasma sintering (SPS) [27]. Meanwhile, there has been a trend to use calculation of phase diagrams as a tool to promote fundamental understanding and to speed up the development of hardmetals [28]. The recent development of hardmetals over 1990-2018 includes changes from submicron to nanocrystalline hardmetals, use of alternative binders, and application of integrated computed material engineering for developing new hardmetals.

Table 1.1. Important developments of hardmetals [12]

1923-25	WC-Co
1926	The patent of hardmetals
1929-31	WC-TiC-Co
1930-31	WC-TaC(VC,NbC)-Co
1938	WC-Cr_3C_2-Co
1946	Sub-micron WC-Co
1956	Hot isostatic pressing
1965-78	WC-TiC-Ta(Nb)C-Cr_3C_2-Co
1965-75	TiC, TiN, Ti(C,N), HfC, HfN and AI_2O_3 coatings
1968-69	WC-TiC-Ta(Nb)C-HfC-Co
1968-69	WC-TiC-Nb(Ta)C-HfC-Co
1974-77	Multi-carbide, carbonitride/nitride and multiple carbide/carbonitride/nitride coating
1994	Fine-grain WC/Co agglomerates in tougher WC/Co matrix
1995	Nanosized hardmetals
1997	Ni, Fe substitute Co partial or fully
After 20th century	Modern sintering technologies such as microwave sintering, HFIHS, PPS, FAHP, SPS, Integrated computed material engineering

1.3 Nanosized hardmetals

The microstructural design of hardmetals consisting of a hard phase and a soft phase determines the balance between hardness and toughness values. It was difficult to obtain traditional hardmetals with high hardness and high toughness simultaneously, which restricted their further application. Therefore, over the past three decades, substantial research works have been focused on the synthesis of hardmetals with nanocrystalline-grain structure, which could improve their hardness dramatically, and maintain the good level of toughness. Jia *et al.* [29] reported that the hardness of nanostructured hardmetals could achieve extremely high levels of hardness values, higher than 2000 HV, with a slight decrease of toughness, as shown in Figure 1.5. The authors demonstrated that the deformation mechanism depended on grain boundary sliding. The high strength in nanosized hardmetals was due to the large volume fraction of grain boundaries, which impeded the motion of dislocations and improved the fracture toughness. In order to synthesise WC-Co hardmetals with nanoscale grain size, numerous studies have been attempted to prepare nanosized WC-Co powders and then different field-assisted sintering techniques have been subsequently introduced to consolidate the final products.

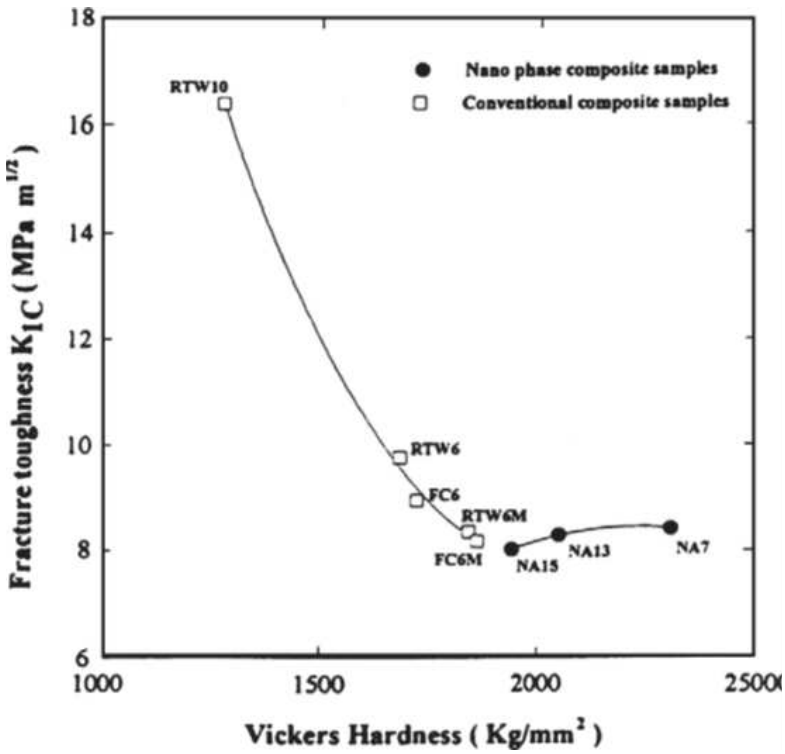

Figure 1.5. Fracture toughness versus hardness of WC-Co hardmetals comparing nanocrystalline composite samples to conventional composite samples [29].

Table 1.2 lists the average grain size and mechanical properties of some nanocrystalline WC-Co hardmetals consolidated by different sintering techniques.

Table 1.2. Hardness and fracture toughness of consolidated WC-Co hardmetals with nanosized WC.

Composition	Consolidation process	Sintered average grain size (nm)	Hardness (HV30)[a]	Fracture toughness ($MPam^{1/2}$)[b]	WC phase (wt.%)
WC-0.6VC-10Co [30]	HP	169	2084	8.8	89.4
WC-14Co [31]	HP	100	1100	14.0	86.0
WC-10Co [32]	SPS	200	2030	13.5	90.0
WC-12Co-1.5VC [33]	SPS	470	1587	11.4	86.5
WC-12Co [33]	SPS	800	1450	10.9	88.0
WC-12Co [34]	SPS	280	1569	9.5	88.0
WC-12Co-0.9VC [34]	SPS	180	1726	9.1	87.1
WC-12Co-0.9NbC [34]	SPS	260	1620	8.6	87.1
WC-12Co-0.9Cr_3C_2 [34]	SPS	220	1685	10.0	87.1
WC-10Co [35]	SPS	350	1800	12.0	90.0
WC-10Co-0.8VC [36]	SPS	100	1887	11.5	89.2
WC-10Co [37]	HFIHS	270	1886	13.5	90.0
WC-12Co [38]	PPS	60	2250	15.5	88.0
WC-6Co [39]	Rapid omnidirectional compaction+HIP	350	2025	8.5	94.0

[a] For uniforming the unit of hardness, the hardness values from the original paper were converted to Vickers hardness.
[b] Fracture toughness values were obtained based on the palmqvist indentation method.

Lin *et al*. [30] produced WC-0.6VC-10Co hardmetals with nanosized WC powders by monoaxial vacuum hot pressing (HP). The microstructure observation revealed the restriction on the grain growth of WC from starting powders due to the VC addition. The average grain size of WC, hardness and toughness values of the sintered hardmetals were 169 nm, 2084 HV30 and 8.8 $MPam^{1/2}$, respectively. However, the inhomogeneous distribution of the Co binder reduced the improvement of the toughness of the ultrafine hardmetals. Sherif *et al*. [31] obtained the nanocrystalline WC powders by high-energy ball milling of W and C powders. The X-ray diffraction results revealed the only existence of a single hcp-WC phase with a size of 70-90 nm. The consolidated WC-Co hardmetals still maintained the nanocrystalline structure with an average grain size of 100 nm. However, the hardness decreased dramatically to 1100 HV30 due to the high content of Co binder. Zhao *et al*. [32] analysed the properties of WC-10Co hardmetals sintered by SPS using different conditions of raw powders: sub-micron WC/nano-Co mixed powders and sub-micron WC/micron Co. The samples prepared with the nano-Co mixed powders had low hardness (<1800 HV30) and low fracture toughness (<8 $MPam^{1/2}$), since the smaller Co particles could not cover the WC particle with a thin film and the difference between the conductivity of the powders and the die tools led to inhomogeneous

distribution of temperature. In the case of sub-micron WC/micron Co, the milled WC-Co powders showed nanocrystalline WC particles with a thin film of Co coat, which was very favourable for the electric current distribution during the SPS process, leading to a good combination of hardness (2030 HV30) and toughness (13.5 $MPam^{1/2}$). Sivaprahasam *et al*. [33] studied and determined the microstructure, grain size, hardness and fracture toughness values of WC-12Co nanocrystalline hardmetals with powders (40-250 nm) consolidated by SPS. Addition of VC, as grain growth inhibitor, improved the hardness and toughness simultaneously. The improvement of hardness in this hardmetal could be directly correlated with the finer WC grain size and homogenous cobalt distribution, whereas the toughness was enhanced by the addition of VC which probably reduced the crack propagation in the cobalt layer and at the interface. Huang *et al*. [34] systematically investigated the effect of three different VC, NbC, and Cr_3C_2 grain growth inhibitors on the microstructure and the mechanical properties of WC-12Co hardmetals sintered by SPS and LPS. The microstructural results revealed that the solid state sintering by SPS was very effective to limit the growth of WC grain size when compared to the traditional LPS. The addition of inhibitors was also efficient in the solid state sintering. What is more, the effect of VC carbide as grain growth inhibitors was more significant than those obtained for NbC and Cr_3C_2, resulting in a higher hardness and lower toughness. On the other hand, the addition of Cr_3C_2 enhanced the hardness and toughness simultaneously. Cha *et al*. [35] and Zhu *et al*. [36] also reported similar mechanical properties of nanocrystalline WC-10Co hardmetals consolidated by SPS. Kim *et al*. [37] used high-frequency induction heated sintering (HFIHS) with a rapid consolidation system (less than 2 min) of WC-Co hardmetals. The average WC grain size, the fracture toughness and hardness values were 270 nm, 1886 HV30 and 13.5 $MPam^{1/2}$, respectively. Michalski and Siemiaszko [38] reported an exceptional combination of hardness and toughness (2250 HV30 and 15.3 $MPam^{1/2}$) when WC-12Co hardmetals with an average WC grain size of about 60 nm were sintered by pulsed plasma sintering (PPS). A patent regarding “dense fine grained monotungsten carbide-transition metal cemented carbide body and preparation” was approved in 1998 [39]. These ultra-fine hardmetals consisted of a transition metal binder phase selected from the group VIII (Fe, Ni and Co) and WC grains (< 500 nm in diameter). Hardmetals were formed by mechanical mixing of WC with the binder metal powder, shaping of the mixture by rapid omnidirectional compaction (ROC) and sintering by hot isostatic pressing, uniaxial hot pressing, or pressureless vacuum sintering. The authors revealed a good combination of hardness and

toughness values (2025 HV30 and 8.5 $MPam^{1/2}$). Nowadays, commercial processes are available for producing nanosized WC particles. However, the control of the grain growth during sintering and the achievement of nano-scale grain size in bulk hardmetals at the sintering state are still critical technology challenges [40].

1.4 Alternative binders

Cobalt has been the optimal binder for more than 90 years due to its excellent solubility in WC, leading to an outstanding combination of hardness and toughness [41]. However, the high price and unstable cost of cobalt are the two direct reasons for industry to look for alternative binders to cobalt [28]. Some Fe-based binders were developed to be used in some wear parts and wood working where the price was more critical than the production rate [7] [19]. Currently, the research of alternative binders in hardmetals industry is also driven by the new European Community Regulation on chemicals and their safe use, known as the REACH regulation [42]. Both Co powder and Co-based hardmetals have been included as ‘‘reasonably anticipated to be human carcinogens’’ in the 14th report on carcinogens of November 2016 [43]. The Horizon 2020 program continued to support innovators to bring green solutions to the market aiming at seeking to reduce or replace the use of cobalt as binder alloy [44], since the traditional Co-based binder is a threat to the human health. Some investigations have proven the toxicity factors of cobalt application. An industry-wide mortality study on the association between lung cancer and exposure to cobalt and tungsten carbide, showed that those workers exposed to Co-based hardmetals had an increased mortality from lung cancer [45]. The potential health risk of inhalation of WC-Co hardmetal raw powders and dust in the industry production lines was also reported by Wild *et al.* [46]. Bastian *et al*. [47] published a paper about an acute inhalation toxicity of Co even in a short time and the possible carcinogenic effect. So a number of researchers have been searching alternatives for the full or partial substitution of cobalt as binder alloy [28]. On one side, cobalt is partially or fully substituted by nickel for the improvement of the corrosion and erosion resistance [48]. On the other side, due to its availability and low price, iron has been considered to suppress the cobalt and reduce the toxicity [49]. We recently firstly reported that chromium-based alloy may be another alternative binder to Co [50]. Thus, some alternative binder systems have emerged during last decades, as is the case of nickel-based, iron-based and chromium-based alloys.

1.4.1 Ni-based binder systems

Ni as an interesting alternative binder displays its advantage in corrosion resistance. Mingard *et al*. [51] observed that additions of nickel could stabilize the face centered cubic structure to give an austenitic ductile binder, which may improve the corrosion resistance of hardmetals. Ekemar *et al*. [52] also reported that WC-Ni hardmetals showed more corrosion resistance than WC-Co hardmetals, especially when Cr and Mo were added into Ni-based binders. Another advantage is the similar coefficient of thermal expansion between Ni and Fe. Kennametal Inc. applied a patent for welding Ni-based hardmetals directly to iron-base substrate in 1981 [53]. This hardmetal comprised a tungsten carbide and a binder consisting of 15 to 30 wt.% Ni/Co. Co-based hardmetals have a coefficient of thermal expansion which is half that of iron-base metal, so that cracks are developed in hardmetal due to the thermal stresses during the welding. When a Ni-based binder is used, the thermal cracking would be avoided due to the suppression of thermal stresses.

Barlow [54] investigated the possibility of consolidating WC-Ni hardmetals with characteristics comparable to WC-Co hardmetals, in terms of hardness, transverse rupture strength and wear resistance. Barlow pointed out that the substitution of Co by Ni in fine-grained hardmetals was unsuitable due to carbide grain growth and the resulting severe strength decrease. A main drawback of Ni-based hardmetals was their reduced mechanical strength. So refractory carbides were added into the matrix to improve the performance of WC-Ni hardmetals. With VC and TaC as inhibitors, ultrafine WC-Ni hardmetals with high hardness were fabricated by utilising high energy milling together with SPS [55]. Tracey [56] discussed the status of Ni in industrial WC-Ni hardmetals. It was necessary to use increased sintering time and temperature to obtain satisfactory densification, which led to a tendency to pick-up carbon from the graphite vacuum furnaces leading to graphite precipitation. More importantly, the higher vapor pressure of Ni (ten times that of Co) at sintering temperature caused a considerable loss of the nickel binder, which needed a more accurate control of the working pressure. An investigation of high temperature oxidation of WC-16%Co, WC-16%Ni and WC-8%Co-8%Ni hardmetals was performed to study the effect of metallic binders on oxidation resistance in the temperature range 500-1200 °C [57]. Oxidation of pure WC was also carried out as the reference. Thus, Voitovich *et al.* [57] found that all metallic binders (Co, Ni and Ni-Co) decreased the oxidation rate of WC- hardmetals compared to pure WC. The author

further demonstrated that oxidation of binders and features of oxide formation determined oxidation resistance of WC-hardmetals. WC-Co hardmetal was the most resistant to oxidation, whereas WC-Ni hardmetal was the least resistant to oxidation due to the lowest content ratio of MWO_4 to $MWO_4 + WO_3$ since MWO_4 (M=Co, Ni) is the oxide conferring more oxidation resistance to the hardmetal. Considering the REACH program, the toxicity of Ni is at the same level as that of Co, which could limit further development of Ni-based hardmetals.

1.4.2 Fe-based binder systems

As mentioned before, the hardmetal industry is very sensitive to the fluctuations and high price of Co. Many companies and researchers investigated the possibility of Fe as an alternative binder to cobalt due to its low price, easy availability, and no toxicity. Alvaredo *et al.* [58] [59] reported that Fe could be a possible alternative binder for bonding TiCN-based cermets. The authors studied the effect of C content on Fe matrix cermets using a combination of experimental and thermodynamic methods. The obtained results showed a significant influence of the C content on the solidus temperature, which influenced the sintering behavior, leading to changes in the microstructure and hardness. Many companies and researchers also reported properties and uses of different Fe-binder hardmetals as listed in Table 1.3.

Table 1.3. Properties and applications of some Fe-binder hardmetals.

Company/ Researcher	binder	Hardness (HV30)	Density (g/cm^3)	TRS (MPa)	Toughness ($MPam^{1/2}$)	Applications
Ceratizit [60]	FeNiCo	1250	13.1	3500	12.1	Wood cutting
Tigra [61]	FeNiCo	1400	13.1	3800	12.0	Knives for machining wood
Gille *et al.* [62]	FeNiCo	1817	14.5	3289	12.5	Partial substitution of WC-Co in special application
Marques *et al.* [63]	FeCrNi	1408	13.2	1521	10.9	Special oxidation an wear resistance
Furushima *et al*. [64]	FeAl	1530	13.1	1180	7.9	Special oxidation resistance

Ceratizit Inc. reported the application of hardmetals with Fe-Ni-Co as the binder alloy in woodcutting [60]. The inserts fabricated with these hardmetals had smaller cutting angles, sharper edges, and good wear resistance. Tigra Inc. also developed a similar hardmetal with good toughness and high abrasion resistance [61]. Gille *et al*. [62] reported that WC-9 wt.%(75Fe-15Ni-10Co) had higher hardness than that of traditional WC-9 wt.% Co hardmetals. However, one main drawback in Fe-Ni-Co binder hardmetals was the more

difficult control of the carbon balance, in order to achieve microstructures without undesirable phases. The nature of the binder formed by Fe-Ni-Co determined the growth behavior of WC by influencing the metal-to-carbon bond relationship [65]. The phase diagrams of the WC-Co and WC-Fe systems were compared by thermodynamic simulations [12]. In general, the addition of Fe narrowed the preferable "carbon window" of the WC + FCC (face-centered cubic) region due to its poorer solubility in WC compared to Co, which will be explained in more detail in 1.5.3 section "Effect of carbon on phase diagrams". Marques *et al.* [63] used an Fe-based binder containing Cr and Ni elements to densify WC-AISI304 hardmetals obtained by vacuum liquid phase sintering, followed by hot isostatic pressing to reduce residual porosity. Furishima *et al*. [64] studied the WC grain size and mechanical properties of WC-FeAl hardmetals fabricated by a vacuum sintering technique. They pointed that oxygen suppressed the WC grain growth, and improved the hardness and the strength due to the formation of α-Al_2O_3 at the WC/WC interface. They further confirmed the existence of α-Al_2O_3 by selected area diffraction analysis, demonstrating that the composition of FeAl binder varied by the generation of an α-Al_2O_3 phase.

A comprehensive characterisation of WC-AISI304 hardmetals was followed including: mechanical properties, oxidation resistance [66], wear resistance [67], and corrosion resistance [68]. This tungsten carbide-stainless steel hardmetal achieved a good balance between hardness (1461 HV30) and toughness (10 $MPam^{1/2}$). The oxidation resistance of WC-AISI304 hardmetals was superior to that of WC-Co hardmetals due to the high Cr content of the binder. However, a ŋ-phase (M_6C) was detected, especially for hardmetals with a higher Fe content, which would reduce the toughness significantly. Then, Fernandes *et al*. [66] reported that the transverse rupture strength of stainless steel hardmetals was improved with small C additions due to the inhibition of M_6C phase formation. Further characterisation of their abrasive wear and corrosion resistances showed that Fe-based WC hardmetals were comparable to the commercial WC-Co hardmetals, indicating that stainless steel could be a promising substitute to Co. The effect of NbC on densification, grain growth, and properties of WC-10AISI304 hardmetals was further investigated by Bao *et.al* [69]. A smaller amount addition of NbC (2 wt.%) inhibited the growth of WC grains and reduced the formation of ŋ-phase during sintering. This Fe-based hardmetal exhibited the highest Vickers hardness (1820 HV) with moderate fracture toughness (7.7 $MPam^{1/2}$).

On the other hand, Fe has the highest affinity to carbon, followed by cobalt and nickel. This affinity could influence the ability to form stable and undesirable metal-carbon bonds leading to brittle phases. For example, the η-phase formation lowered the performance of hardmetals and should be avoided [70]. Schubert *et al*. [71] studied three Fe-based binder systems: Fe-Ni, Fe-Ni-Co and Fe-Mn, in which comprehensive mechanical properties of these three Fe-based hardmetals were compared to that of conventional cobalt alloys. Fe-based hardmetals exhibited a large amount of ŋ-phase for binder contents less than 10 wt.%, which decreased their toughness significantly. Moreover, their high temperature properties (hardness at high temperature, creep resistance) were inferior to those of cobalt-based materials.

Compared to Co and Ni-based binders, alternative Fe-based binders provide the advantages of having lower price, lower toxicity, higher oxidation and/or corrosion resistance, and the possibility of improving hardness and/or toughness with addition of refractory carbides and/or graphite, based on the above mentioned results from laboratory research and products from industry. Then a question arises: why these alternative binders are not widely used? There are two main reasons from the aspect of producers and customers. For the hardmetal producers, changing the composition or any other parameters during process means requalification for customers and the potential risk of losing important users. For the customers, Co-based WC hardmetals still have the best comprehensive properties, although the properties of Fe-based hardmetals could be improved by addition of refractory carbides. A series of commercial Co-based WC hardmetals can meet the different needs of customers. Hardmetals without or with less Co are generally used at some wear parts, woodworking and unimportant cutting tools, where the user pays more attention to price than to stability and productivity [7]. For all these investigations in laboratory with a small scale of production, it should be noted the possible difficulty of a large scale production. Moreover, the lack of knowledge concerning the interaction between alternative binders and hard phases represents a drawback, especially compared to the WC-Co system with a fully studied database.

1.4.3 Cr-based binder systems

Addition of chromium or chromium carbide to WC-Co hardmetals is known as a way to inhibit the growth of WC particle during sintering [72]. Stecher *et al*. [73] and Rudy *et al*. [74] showed the ternary phase diagram of W-C-Cr at 1350 and 1300 °C, respectively, which displayed the possible existence of two tungsten carbides: WC and W_2C, and three

chromium carbides: Cr_3C_2, Cr_7C_3, and $Cr_{23}C_6$, as shown in Figure 1.6. Both authors pointed out that there was a phase equilibrium between tungsten carbide (WC) and chromium carbide (Cr_3C_2). Tükör *et al.* [75] experimentally studied the phase formation in the W-C-Cr system, which was determined by reaction kinetics of phase transformation. A $(W,Cr)_2C$ phase was formed as a collector for Cr within the tungsten matrix, where the main part of chromium was dissolved into the hexagonal W_2C lattice. In addition, experimental and thermodynamic evaluation of Cr-Co-C [76], Cr-Fe-C [77], Cr-Fe-W [78], and Cr-Fe-W-C [70] systems were reported. All these works provide useful information to explore the phase formation of hardmetals with Cr addition, commonly $M_{23}C_6$, M_3C_2 and M_7C_3 (M represents Cr, Fe, and/or W).

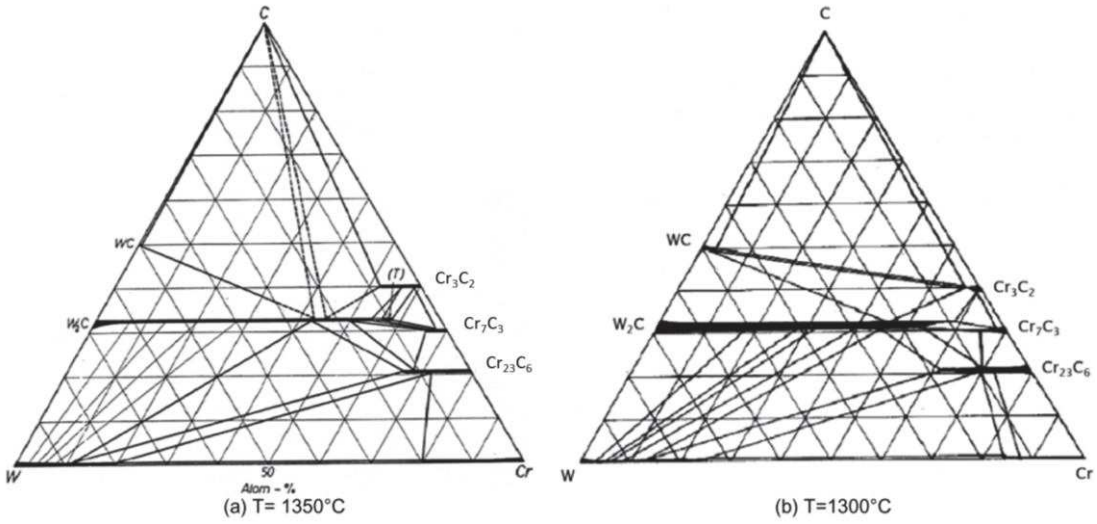

Figure 1.6. Phase diagram of W-C-Cr system (a) at T =1350 °C [73] and (b) at T =1300 °C [74].

Hardmetals with Cr-based binders have not been extensively studied. Cr was only used within limited amounts in some hardmetal compositions to control the grain growth and to improve oxidation and corrosion resistance [51]. Cr possesses a strong affinity to carbon, leading to the formation of chromium carbide phases, normally presenting a brittle behavior and reducing the mechanical resistance of hardmetals. Kaplan studied the WC-Co-Cr system in his doctoral thesis motivated by the widespread addition of Cr as a WC grain growth inhibitor and to improve the oxidation and corrosion resistance [79]. Thus, an expected smaller WC grain increased the hardness of the material with Cr addition. Then, Kaplan investigated the effect of Cr on the phase equilibrium diagram by thermodynamic modelling (Figure 1.7). Adding Cr to WC-Co system led to a decrease in the melting interval temperature of the Co-based binder and to the formation of two Cr-carbides: Cr_7C_3 and Cr_3C_2 [80]. Frisk and Markström [81] also reported the effect of Cr

on phase equilibria in WC-Co hardmetals. Cr addition could decrease the melting temperature over 100 °C. Brieseck *et al*. [82] discussed the diffusion and solubility of Cr in WC. They found that Cr could be dissolved in WC and subsequently a carbide phase, $(Cr,W)_2C$, was found at the interface of the diffusion couple WC and Cr_3C_2. The addition of the inhibitor Cr_3C_2 was an efficient method for controlling the grain growth in the solid state, even in the case of in which rapid sintering processes were performed [83]. Cr-segregation to interfaces with cubic structure was observed in hardmetals using Cr as inhibitor [84]. Addition of Cr to Fe-based [66] and Ni-based [85] hardmetals also confirmed that Cr improved the performance of oxidation and corrosion resistance. Fernandes *et al*. [12] found the formation of M_7C_3 carbides with a Cr content around 12.26 wt.% in the W-C-Cr-Fe phase diagram. The thermodynamic calculations for Fe-based and Ni-based hardmetals confirmed that a M_7C_3 would be formed at a high C content. The melting temperature of the binder was decreased with a lower Cr content. Pirso *et al*. [86] added different chromium carbides (Cr_3C_2 and Cr_7C_3) to Ni-based cermets since they are extremely hard and corrosion resistant. Cr_3C_2 has an orthorhombic crystal structure with a microhardness of 2280 kg/mm^2 and Cr_7C_3 has a hexagonal crystal structure and a microhardness of 1336 kg/mm^2 [87]. The hardness, transverse rupture strength, abrasive wear, and erosion resistance of Ni-based cermets were improved.

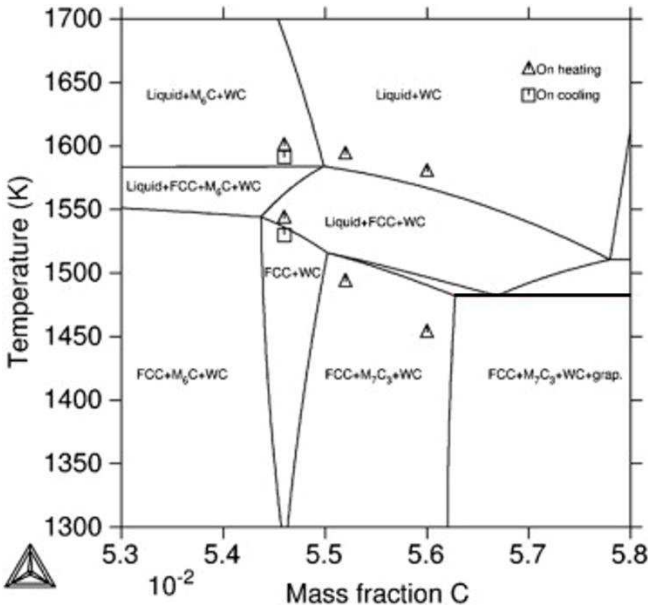

Figure 1.7. Vertical section of the W-C-Co-Cr phase diagram, calculated at 9 wt.% Co and 10 wt.% Cr [80].

Moreover, hard materials containing Cr have been deposited as coatings of pure metals and alloys due to their high hardness, good wear resistance and corrosion resistance.

Rezaei-Sameti *et al.* [88] studied the effect of pulsed electrodepositions on the morphology, hardness and wear behavior of nano-structured WC-Cr composite coatings. They found good wear resistance of the coating with an extremely fine average size of WC (70 nm). In addition, the hardness and tribological behavior of the coating increased with the increase of the current density. Bolelli *et al.* [89] compared the microstructure and abrasive wear behavior of WC-FeCrAl and WC-CoCr hard coatings deposited by high velocity oxygen-fuel spraying onto steels and aluminum alloy substrates. The deposition of WC-FeCrAl layer showed more decarburisation and oxidation compared to WC-CoCr layer due to the stronger affinity of Fe and Cr to oxygen. However, the wear performance of an optimised WC-FeCrAl coating was comparable to that of the WC-CoCr coating.

As far as this author knows, there are no published studies in literature with regard to the processing of hardmetals using Cr-based alloys as a binder. We firstly reported the possibility of processing a new Cr-based WC hard composite by a powder metallurgy route including mechanical milling of commercial WC and Cr-based powders, followed by spark plasma sintering in 2018 [50]. The hardness and toughness values achieved by this Cr-based WC hard composite were 1479 HV30 and 3.4 $MPam^{1/2}$, respectively, which were low values compared to that reached by commercial WC-Co hardmetals. The relative low hardness was attributed to the low volume fraction of WC reinforcement (30 vol.%) compared to that of commercial WC-Co hardmetals (generally, 80 vol.% of WC). The low fracture toughness was caused by the presence of porosity and brittle ternary carbides such as M_4C, $M_{23}C_6$ and M_6C. Despite the achievement of inferior mechanical properties, we confirmed the possibility of using a new binder with less toxicity and less price than Co or Ni binders. So Cr-based alloys could become potential binders to be used in hardmetals, using conventional liquid phase sintering techniques or FAST sintering techniques, as it will be shown in this work.

1.5 Thermodynamic and kinetic studies in hardmetals

Computational materials study has been frequently used in a wide range of fields and, definitely has been crucial in the development of new hardmetals. Integrated computational materials engineering (ICME) is an approach to design materials, products, and their associated materials processing methods by linking materials models at multiple length scales from the atomistic to macro level. The key link is composition-structure-

property i.e. understanding how processes produce material structures, how those structures give rise to material properties, as shown in Figure 1.8 [90]. Ab initio calculations based on density functional theory (DFT) determine the electronic structure at the atomic scale with basic physical principles and models of electron orbitals. CALculation of PHAse Diagram (CALPHAD) is a modelling technique to calculate and map thermo-kinetic properties of materials for materials study and design [91]. Thermo-Calc simulates the thermodynamics for prediction of equilibrium phase diagrams and even non-equilibrium phases, which is an important tool to predict the obtained phases of hardmetals after the sintering step. DIfusion Controlled TRAnsformation (DICTRA) is currently the most commonly used software package to simulate diffusion-controlled phase transformations in multiple systems. After the establishment of thermodynamic database for hardmetal systems, the DICTRA can simulate the atomic mobility and related diffusion behavior, which correlate with the structure in micro level. Macro properties depending on their microstructure are characterised by different mechanical tests. Therefore, ICME builds up a scientific network from atomistic, micro to macro, allowing materials scientists from different communities to share knowledge and best practice.

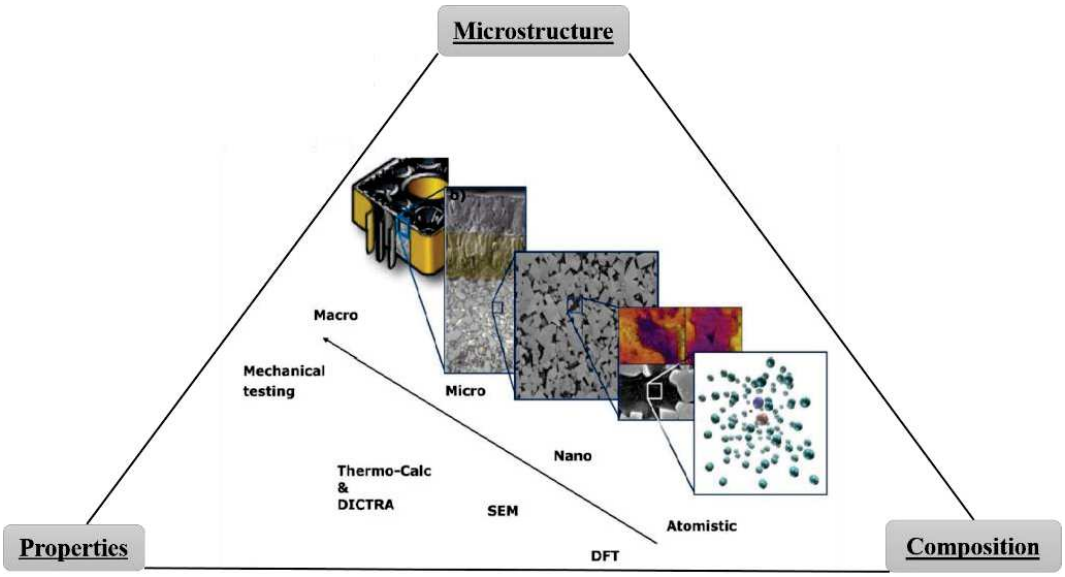

Figure 1.8. New hardmetals development: the composition-structure-property relationship chart by ICME [90].

Walbrühl [92] proposed in his doctoral thesis the development of hardmetals with alternative binder systems guided by ICME. Walbrühl mentioned the design of a Ni-Fe binder phase based on a general materials design method and a multiscale approach to model the surface gradient formation. The author focused on the room temperature

composite hardness and the surface gradient formation for Co-based and Ni-Fe binder systems by simulation and experimental investigations. The compositional design of binder phases plays a significant role in the microstructure and properties of hardmetals. Furthermore, the content of carbon also has an important effect on the calculation. The effect of binder and carbon on the processing of hardmetals would be discussed in more detail below.

1.5.1 Databases for hardmetals

The industrial production of hardmetals involves complex thermodynamic and kinetic processes. Sandvik and KIT Royal Institute of Technology have made a great research work on thermodynamic calculations and kinetic simulations, which is essential to establish sintering process parameters in the production of hardmetals [93-94]. The thermodynamic and kinetic databases are the keys to simulate the phase formation and diffusion behavior in hardmetals. In order to describe the thermodynamic behavior of all phases in the system, sublattice model was used in thermodynamic databases. For example, the liquid phase in hardmetals was generally described by a substitutional solution model. For pure elements and stoichiometric compounds, the Gibbs energy could be expressed as [91]:

$$G_m = a + b \times T + c \times T \times ln(T) + \sum d_i \times T_i \quad (1\text{-}1)$$

Where G_m is the Gibbs energy relative to a standard element reference state (at the temperature of 298.15 K and the pressure of 105 Pa), T means the temperature, and a, b, c, and d are the model parameters. The establishment of kinetic database is based on that of thermodynamic database, using CALPHAD to establish in each component the relationship between atomic mobility parameters and variables such as temperature and composition system. A high-quality database provides a deeper understanding of the materials and processes. Ekroth *et al*. [95] created a thermodynamic database for hardmetals containing Co-W-Ti-Ta-Nb-C-N with experimental and theoretical basis. Frisk *et al.* [96] assessed the thermodynamic database of Co-W-Ti-Ta-Nb-C-N system, including tests of the influence of model parameters on miscibility gaps in higher order systems, and measurements of the solubility of Ti, Ta, and Nb in liquid in multicomponent alloys. Peng *et al.* and Zhang *et al*. developed a new thermodynamic and kinetic data for the Co-Cr-W-Ta-Ti-Nb-C-N system, respectively: CSUTDCC1 (Central South University Thermodynamic Database for Cemented Carbides version-1) [97] and

CSUDDCC1 (Central South University Diffusion Database for Cemented Carbides version-1) [98]. The database contained the atomic mobility parameters for different diffusing elements in liquid and FCC phase [99]. The phase transformation temperatures of four-phase equilibria (L+ FCC + WC + M_6C, L + FCC + WC + C) of WC-20 wt.% (Co,Fe,Ni) hardmetals showed that the experimental data were well agreed with the simulation results. Fernandes and Senos [12] published a review of hardmetals phase diagrams, including the basic W-C-Co, W-C-Fe, W-C-Ni, and W-C-Cr systems. Sandvik has made great contributions to create the database for C-Co-N-Nb-Ta-Ti-W system [100]. Due to its technological monopoly, the system is a trade secret. Up to now, a high-quality database for hardmetals is not published and highly trustworthy.

1.5.2 Effect of binders on phase diagrams

Figure 1.9 shows the two-phase region (gray area) of a general equilibrium phase diagram of hardmetals with the typical binder alloys (Fe, Co, Ni) [101]. The best properties in hardmetals system have been obtained within the carbide phase and the binder metallic phase in the gray area. Hardmetals with different binders composition would have drawn different sizes of this region, which is determined by two points (circles in Figure 1.9). Point 1 represents the stoichiometry limit of the carbide for carbide-binder metal composites without reaction, and point 2 means carburisation or decarburisation tendency for carbides by binder-metals.

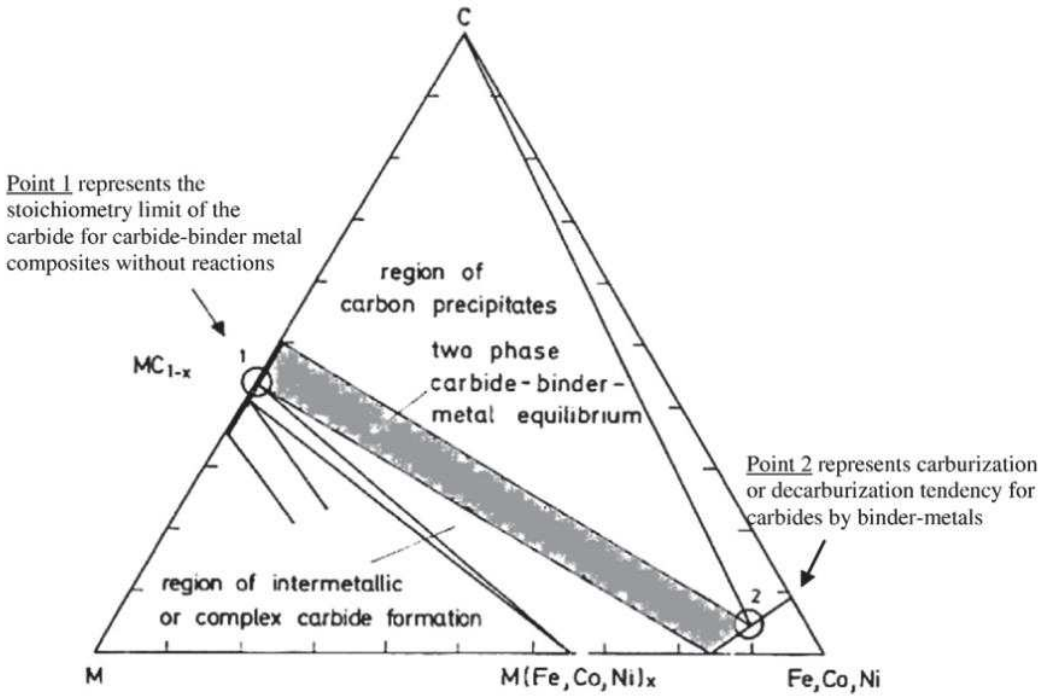

Figure 1.9. Schematical phase equilibrium of hardmetals [101].

The ternary phase diagrams for (Fe, Co and Ni)-WC in the binder-rich corner were further reported in detail by Holleck [29], [39] (Figure 1.10). The dotted lines represent the theoretical WC-binder metal compositions. The width of the two-phase zone limited by the blue lines was smaller for iron (Figure 1.10a) and similar for cobalt (Figure 1.10b) and nickel (Figure 1.10c) since iron would dissolve a much lower quantity of WC at eutectic temperature.

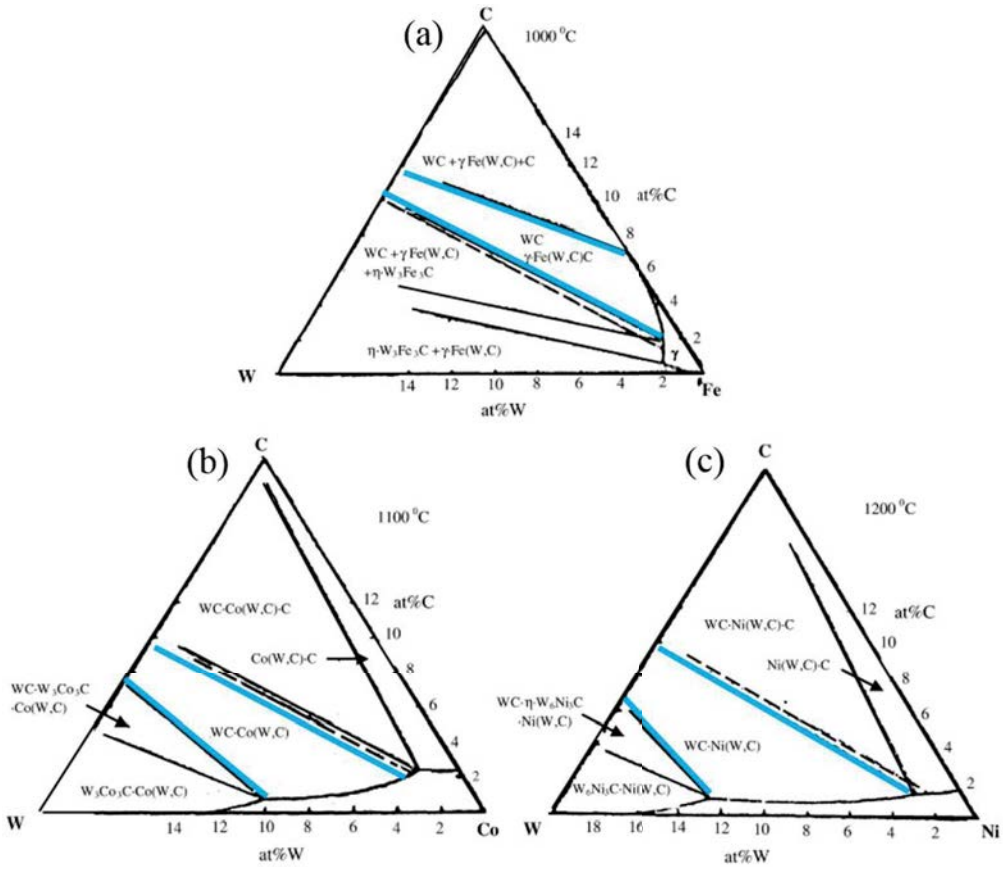

Figure 1.10. The two-phase region in ternary phase diagrams: a) W-Fe-C, b) W-Co-C and c) W-Ni-C [102].

1.5.3 Effect of carbon on phase diagrams

The C content has a significant effect on the phase formation since the brittle □-phase will be formed when the hardmetal has deficient C content, whereas graphite will be formed with an excess of carbon. Guillermet [103] published a phase diagram of WC-Co (Figure 1.11a) and a vertical section of the W-C-Co phase diagram calculated at 10 wt.% Co (Figure 1.11b). The "WC" symbol on the diagram shown in Figure 1.11a represents the content of W and C in the stoichiometric proportion for WC. The WC-Co phase diagram allowed to easily follow what occurred at each temperature during cooling. The content of carbon determines the phase compositions after the sintering process. The points "a" and "b" in Figure 1.11b defined the minimum and maximum carbon contents of the alloy,

respectively, which were in a two-phase state of FCC + WC after equilibrium solidification. The satisfactory combination of hardness and toughness strength of hardmetals will be achieved, when the optimised content of carbon is in the two-phase region, FCC +WC, and the precipitation of other phases (e.g. graphite, M_6C and $M_{12}C$ carbide) is avoided during cooling.

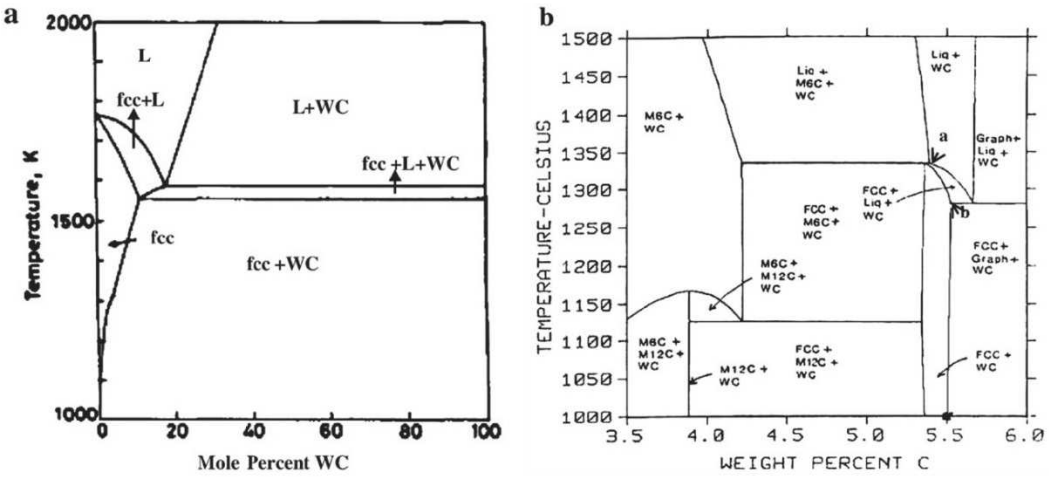

Figure 1.11. (a) WC-Co phase diagram and (b) W-C-Co vertical section calculated at 10 wt.% Co [103].

Fernandes *et al*. [104] reported the influence of introducing Cr and C within the binder Fe-Ni-Cr on the phase formation. M-WC3 and C-WC3 were hardmetals with 3 wt.% and 1 wt.% of Cr, respectively. C-WC3 + C was C-WC3 with extra addition of carbon. X-Ray diffraction (XRD) results indicated that a higher content of Cr in the binder induced the formation of Cr_2C carbide in the M-WC3 hardmetals (Figure 1.12). No Cr_2C phase was detected in the C-WC3 hardmetal with a lower content of Cr. However, another type of carbide phase, M_6C (□-phase), was formed. Both Cr_2C and M_6C are brittle phases, which would reduce the mechanical properties of hardmetals. When an excess of carbon was added to the C-WC3, the x-ray diffraction patterns of C-WC3 + C only showed the WC hard phase and the austenite (γ-Fe) binder phase.

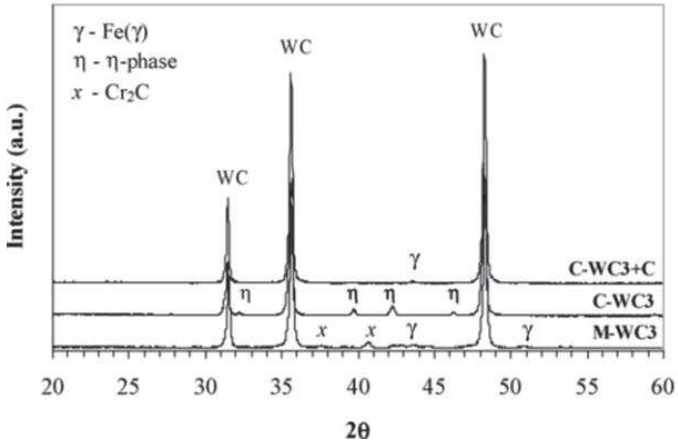

Figure 1.12. X-ray diffraction pattern of M-WC3, C-WC3 and C-WC3 + C hardmetals [104].

A hardmetal of this type was beneficial to obtain a combination of attractive mechanical properties such as high hardness (coming from the WC phase), reasonable toughness (coming from the austenitic phase) and good oxidation and corrosion resistance (coming from the Cr content and the austenitic metallic structure). Therefore, the amount of carbon should be carefully controlled to obtain the desired hard and binder phases. .

Fernandes *et al*. [66] investigated the effect of C on mechanical properties, wear resistance and corrosion resistance of WC-AISI304 hardmetals. The temperature projection of Fe-Ni-W-C system (Figure 1.13) showed that the investigated composition with a Ni/(Fe+Ni) ratio of 0.12 (red dotted line) and a stoichiometric carbon content (5.5 wt.%, as indicated by the solid circle on the carbon composition axis) induced the formation of a M_6C phase [105]. In this case, the addition of carbon could move the composition to a suitable composition range, with the presence of the "FCC+ WC" two phase region. The M_6C carbide was formed during heating by local reactions between WC and the main elements of the stainless steel (Fe, Cr and Ni). The subsequent XRD analysis and SEM microstructure images confirmed the existence of M_6C phase and the reduction of its formation by adding extra C contents. More importantly, transverse rupture strength of hardmetals was significantly improved from 551 MPa to 1086 MPa with the addition of carbon.

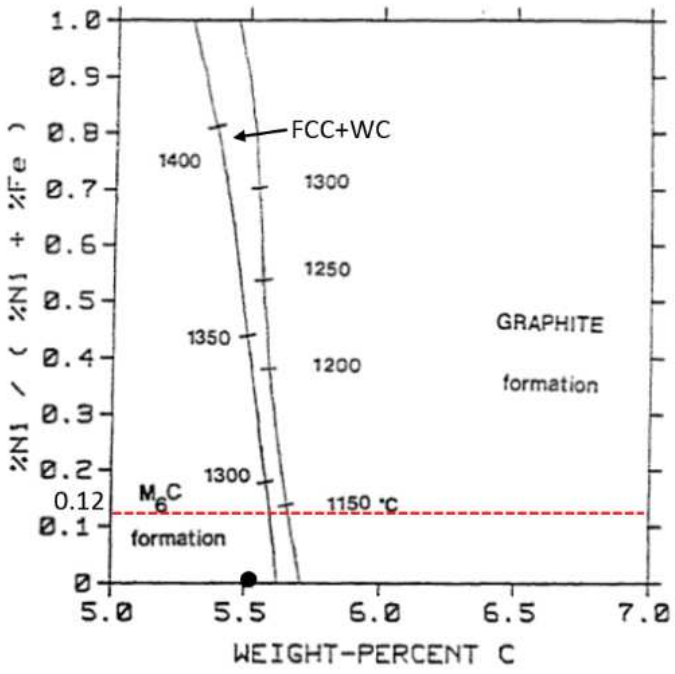

Figure 1.13. Temperature projection of the Fe-Ni-W-C phase diagram, calculated at Fe + Ni =10 wt.%. The solid lines describe the compositions of a mixture of WC + liquid in equilibrium with FCC + M_6C (left) or FCC + graphite (right). The solid symbol on the composition axis indicates the stoichiometric WC composition [12] [105].

In order to access the tribological properties of conventional WC-Co and WC-SS (stainless steel AISI304) hardmetals with and without carbon additions, a ball cratering method was performed by Vilhena *et al*. [67]. The abrasive wear resistance of WC-AISI 304 was higher than that of WC-Co specimen. The presence of η-phase in WC-AISI 304 promoted a strong interphase strength and a higher hardness, which was beneficial for the wear resistance. Figure 1.14 plots the corrosion behaviour of WC-Co and WC-SS hardmetals with and without carbon addition. The similar impedance of WC-SS and WC-SS-C was significantly higher than that of WC-Co. Thus, AISI 304 binder improved the corrosion resistance of hardmetals [68]. Li *et al*. [106] studied the effect of different C contents on the properties of ultrafine WC-10Co-0.5Ta hardmetals consolidated by vacuum liquid phase sintering. With increasing carbon content, the (Ta,W)C phase segregation was gradually eliminated, and both transverse rupture strength and hardness were increased.

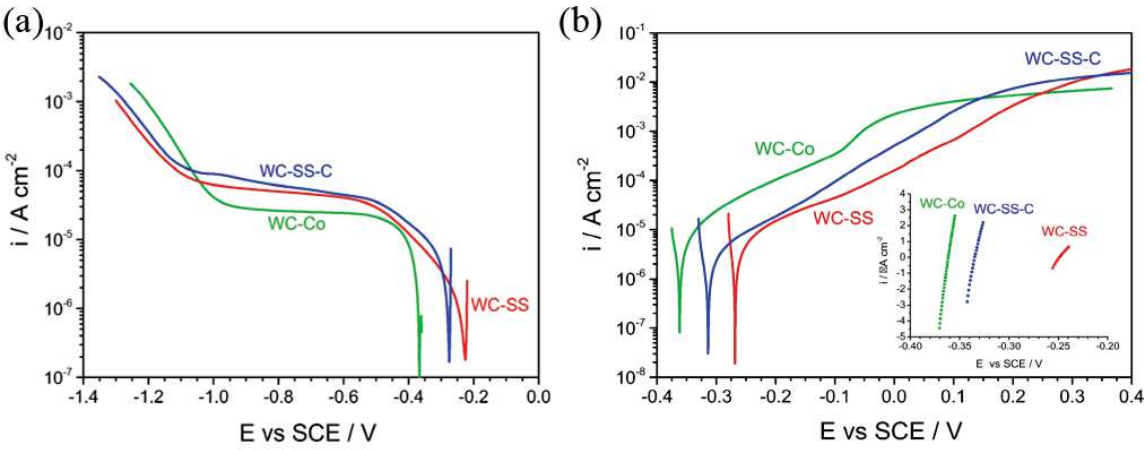

Figure 1.14. Cathodic (a) and anodic (b) current-potential curves of WC-Co, WC-SS and WC-SS-C. (inserted: polarisation resistance curves of the three composites) [68].

In the current work, the effect of the binder phase composition and of the addition of an excess C content on the final microstructure and properties will be studied by a combination of thermodynamic calculations and experimental observations, to design optimised hardmetals, avoiding some of the costly trial-and-error procedures.

1.6 Technical trends in hardmetals

The market of hardmetals is continuously growing. New technologies and new applications appear in the trend of hardmetals to improve their performance in cutting, wear and corrosion behavior. As mentioned previously, one trend is based on the production of nanosized WC-hardmetals, which have a great cutting and wear

performance due to the extremely high hardness and good toughness achieved. Consideration of alternative binders to cobalt have also been mentioned before. Furthermore, there are other emerging trends that will be addressed in the following sections: using of coating technologies, fast sintering techniques, and high resolution and 3D characterisation techniques.

1.6.1 Coating technologies: chemical vapor deposition (CVD) and physical vapor deposition (PVD)

The cutting performance of hardmetals is greatly improved by the introduction of the CVD method, where some hard coatings (such as TiAlN [107], TiCN [108] and Al_2O_3 [109]) are deposited on hardmetals at high temperature to produce high-performance thin films. PVD process produces vapor from a solid source by physical methods at relative lower temperature than CVD. Thus, PVD is a more flexible process that can generate a broad variety of coatings. Czettl *et al*. [110] reported a comparison of lifetime performance between PVD and CVD TiB_2 on WC-Co hardmetals with commercial CVD $TiCN/Al_2O_3$ and PVD TiAlN coatings on the same substrates, as shown in Figure 1.15. WC-Co hardmetals with PVD TiB_2 coating displayed a bit reduction in lifetime compared to hardmetals with commercial PVD TiAlN and CVD $TiCN/Al_2O_3$ coatings. However, the lifetime of hardmetals with CVD TiB_2 coating was extended more than a half compared to these commercial coatings. The combination of coatings in hardmetals has led to an improvement in cutting performance, such as increasing cutting speed and feed rate, for instance, allowing cutting the difficult-to-machine titanium alloys and superalloys. Therefore, coatings could obviously improve the performance in wear resistance, oxidation and corrosion resistance of hardmetals [111].

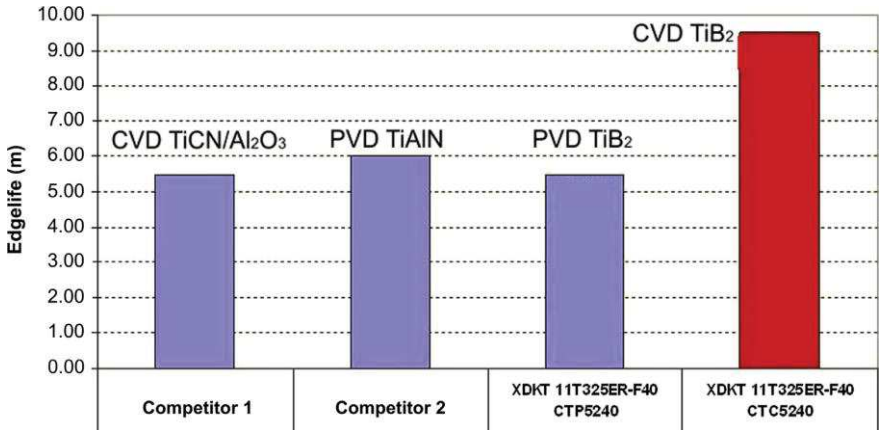

Figure 1.15. Cutting lifetime of WC-Co hardmetals with PVD/CVD TiB_2 coatings and commercial coatings [110].

1.6.2 Field-assisted sintering techniques (FAST)

Traditional WC-Co hardmetals are produced through high-energy milling of WC and Co powders, pressing of hardmetals powders into near shape products and followed by liquid phase sintering (LPS) or hot isotropic pressing (HIP). During LPS the microstructure coarsening appears quickly due to grain growth of carbides [112]. Nevertheless, the mechanical properties such as hardness and toughness relationship values, as well as wear resistance, will be improved by retaining a finer microstructure. In this sense, novel FAST techniques in solid-state have been acceptably used during last years, replacing LPS and HIP to produce hardmetals due to the great advantage that they introduce reducing the growth of WC grain size. Olivier Guillon *et al*. [4] described systematically the mechanisms, materials, and technology developments in FAST. They are based on a low voltage, a direct or an alternating current, and a pressure-assisted sintering. Figure 1.16 shows the working scheme of a general FAST apparatus, consisting of a mechanical loading system, and a high-power electrical circuit, placed in a controlled atmosphere. Regardless of conductive or non-conductive sintered powders, heat is quickly and efficiently transferred from the tools (good electrical conductivity) to the sample, since low voltages (typically below 10 V) produce high currents (typically from 1 to 10 kA), leading to an efficient Joule heating. The heating rate, pulse and pause durations, or more specialised pulse patterns, could be controlled exactly with the software and hardware. The heating rate, cooling rate and sintering temperature can reach 1000 °C/min, 150 °C/min, and 2400 °C, respectively. The simultaneous application of a uniaxial maximal load varied from 50 to 250 kN.

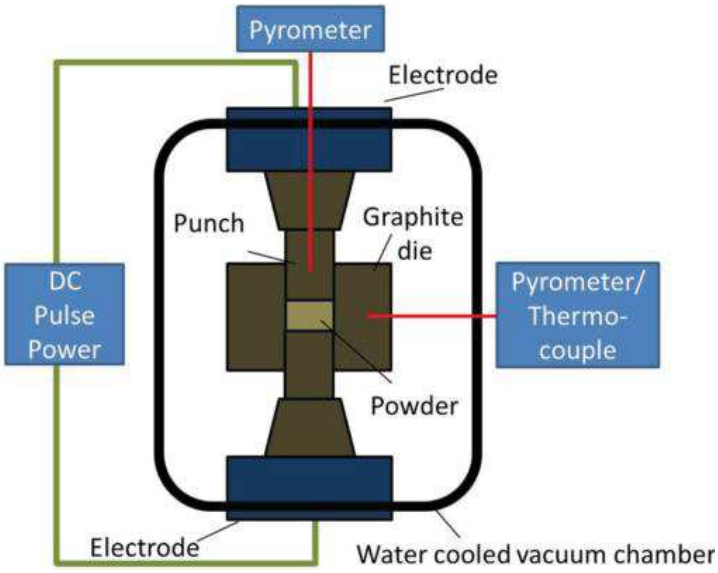

Figure 1.16. Working scheme of a FAST apparatus [4].

Spark plasma sintering (SPS) is one of most frequently used techniques among the FAST techniques used in the laboratory and industry [113]. The world's largest hybrid SPS sintering system was set up in Spain in 2012 to dense large ceramic blanks of 400 mm in diameter [114]. SPS process will be explained in more detail in the experimental process (Chapter 3) since it will be one of the applied sintering techniques in this work.

1.6.3 High resolution characterisation techniques

The use of high resolution techniques such as high resolution transmission electron microscopy (HRTEM) and scanning transmission electron microscopy (STEM) have been commonly performed to study the interface layers existing in hardmetals. Delanoë *et al.* [115] discovered by TEM a thin face centered cubic layer (Cr,W)C at the interface between WC and Co in Cr-doped WC-Co hardmetals. This layer was grown on the surface of the WC grains with two orientation relationships: mismatch of 0.2% for the basal plane of WC and 3% for the prismatic plane. To get more information about the structure and composition of the interface layers, a microstructural study using the combination of STEM and energy dispersive X-ray spectroscopy (EDX) was carried out. Jaroenworaluck *et al*. [116] demonstrated segregation of nanosized VC inhibitors in WC/Co phase boundary. HRTEM observations revealed that a small addition of VC in WC-Co was effective to suppress the grain growth of carbide grains, whereas EDX analyses clearly showed segregation of doped V along the interfaces. Meingast *et al*. [117] studied by TEM-EDX the interface layer formed between the WC grain and Co binder confirming the existence of two visible monolayers, one rich in Ti and one rich in W, as shown in Figure 1.17. Delanoë and Lay [118] investigated the evolution of the WC grain shape in Cr doped WC-Co alloys at several stages of the sintering treatment by TEM. The common shape of WC was a prism based on a truncated triangle. The Cr addition increased the anisotropy between prismatic facets in the W rich alloy. The inhibitors segregation between WC/Co phase boundaries could be explored by a method combining STEM and EDX. Thus, this method helps to explain the mechanisms of interfacial bonding strength and the limitations of WC grain growth. Furthermore, there exist 3D techniques that reconstruct the real 3D structure of hardmetals by the combination of focused ion Beam (FIB) and electron backscatter diffraction (EBSD) techniques. Borgh *et al.* [119] evaluated the microstructure and crystallographic orientations of WC and Co grains with 3D constructed images. Therefore, characterisation techniques with high resolution will allow the development of deep microstructural and compositional studies

aiming to acquire a strong knowledge related to the phase formation taking place during field-assisted sintering of new hardmetals.

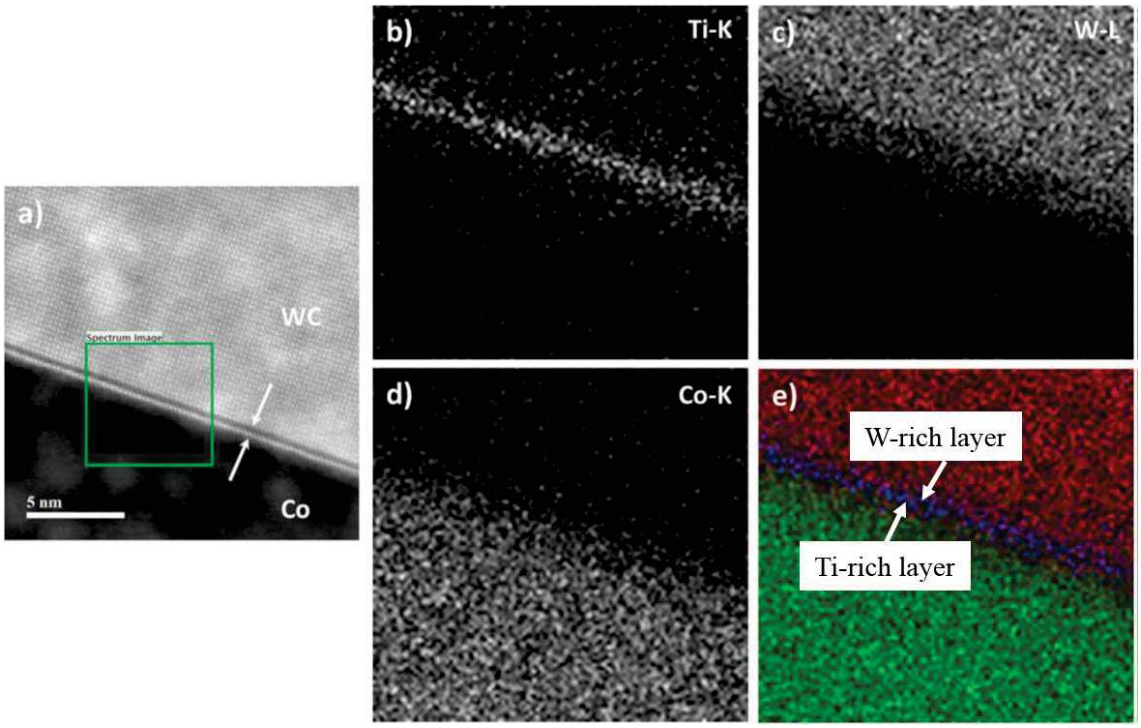

Figure 1.17. (a) STEM image of the interface between WC and Co with a thin interface layer indicated by two arrows. (b-d) EDX elemental distribution maps of Ti, W and Co. (e) Color coded RGB image revealing the position of the Ti-rich and W-rich layers and showing Co (green), Ti (blue), and W (red) [117].

1.7 Summary

After a development of more than 90 years, hardmetals have made great achievements and provide a cost-effective option in the manufacturing industry. On one hand, thermodynamic and kinetic simulations play an important role in the development of hardmetals from compositional design, process optimisation, expected properties, and final application and performance of products. On the other hand, with the increased research in field-assisted sintering techniques, for example SPS, the consolidation of nanosized hardmetals with an extreme high wear resistance is possible, even at industrial scale. Although Co has served as the best binder until today, there has been a quite high research activity on searching for alternative binders due to the high price, limited resource, and toxicity of Co. Fe-based alternative binders have been used in applications such as woodworking cutting tools and some wear parts. However, their reduced mechanical properties and the greater difficulty of controlling quality in the production

process restrict their applications in high-demanding manufacturing operations, such as in the case of the automotive and aerospace industries. There is still a need for further development of alternative binders to meet hardmetals with the current requirements needed in the tool industry.

1.8 References

[1] H. Mikado, S. Ishihara, N. Oguma, and S. Kawamura, "On the short surface fatigue crack growth behavior in a fine-grained WC-Co cemented carbide," *Metals (Basel).*, vol. 7, no. 254, pp. 1–17, 2017.

[2] W. Dawihl, *Handbuch der Hartmetalle*, no. 195. London: Her Majesty's Stationery Office, 1995.

[3] H.E. Exner, "Physical and chemica nature of cemented carbides," *Int. Met. Rev.*, vol. 1, no. 24, pp. 149–173, 1979.

[4] G. Olivier, G.J. Jesus, D. Benjamin, K. Tobias, S. Gabi, and M. Herrmann, "Field-assisted sintering technology/spark plasma sintering: Mechanisms, materials, and technology developments," *Adv. Eng. Mater.*, vol. 16, no. 7, pp. 830–849, 2014.

[5] G.S. Upadhyaya, *Cemented tungsten carbides: production, properties and testing*. William Andrew, 1998.

[6] K. Brookes, "Hardmetal statistics," *Met. Powder Rep.*, vol. 69, no. 1, pp. 23–25, 2014.

[7] K. Brookes, "There's more to hard materials than tungsten carbide alone," *Met. Powder Rep.*, vol. 66, no. 2, pp. 36–45, 2011.

[8] P. Ettmayer, H. Kolaska, and H.M. Ortner, *History of Hardmetals*, vol. 1. Elsevier Ltd, 2014.

[9] P. Ettmayer and W. Lengauer, *Nitrides*. Ullmann's Encyclopedia of Industrial Chemistry, 2000.

[10] B. Aronsson, "The origins and growth of cemented carbide," *Ord Form AB, Uppsala*, 2005.

[11] K. Schröter, "DRP 420.689: Sintered hardmetal alloy and procedure for its fabrication," Berlin issue of letters patent, 1923.

[12] C.M. Fernandes and A.M.R. Senos, "Cemented carbide phase diagrams: A review," *Int. J. Refract. Met. Hard Mater.*, vol. 29, no. 4, pp. 405–418, 2011.

[13] K. Dreyer and H. Kolaska, "Composite hard metal body and process for its production." Google Patents, 1992.

[14] P. Schwarzkopf, *Powder Metallurgy: Its Physics and Production*. Macmillan Company, 1947.

[15] I. Azcona, A. Ordonez, J.M. Sanchez, and F. Castro, "Hot isostatic pressing of ultrafine tungsten carbide-cobalt hardmetals," *J. Mater. Sci.*, vol. 37, no. 19, pp. 4189–4195, 2002.

[16] Z. Yao, J. Stiglich, and T.S. Sudarshan, "WC-Co enjoys proud history and bright future," *Met. Powder Rep.*, vol. 53, no. 2, pp. 32–36, 1998.

[17] R. Haubner, "The history of hard CVD coatings for tool applications at the University of Technology Vienna," *Int. J. Refract. Met. Hard Mater.*, vol. 41, pp. 22–34, 2013.

[18] C. Ducros, V. Benevent, and F. Sanchette, "Deposition, characterization and machining performance of multilayer PVD coatings on cemented carbide cutting tools," *Surf. Coatings Technol.*, vol. 163, pp. 681–688, 2003.

[19] T.W. Penrice, "Alternative binders for hard metals," *J. Mater. Shap. Technol.*, vol. 5, no. 1, pp. 35–39, 1997.

[20] A.H. Chokshi, A. Rosen, J. Karch, and H. Gleiter, "On the validity of the Hall-Petch relationship in nanocrystalline materials," *Scr. Metall.*, vol. 23, no. 10, pp. 1679–1683, 1989.

[21] G.E. Spriggs, "A history of fine grained hardmetal," *Int. J. Refract. Met. Hard Mater.*, vol. 13, no. 5, pp. 241–255, 1995.

[22] R. Bao, J. H. Yi, J.M. Zhang, Y.C. Liu, F.X. Li, and Y. Xin, "Double Inhibitory Actions on WC Grains of Microwave Sintered WC-12wt% Co-VC Alloy," in *Materials Science Forum*, 2015, vol. 816, pp. 715–721.

[23] I.J. Shon, I.K. Jeong, I.Y. Ko, J.M. Doh, and K.D. Woo, "Sintering behavior and mechanical properties of WC-10Co, WC-10Ni and WC-10Fe hard materials produced by high-frequency induction heated sintering," *Ceram. Int.*, vol. 35, no. 1, pp. 339–344, 2009.

[24] W. Kim, C.Y. Suh, K.M. Roh, S.W. Cho, K.I. Na, and I.J. Shon, "Mechanical properties of (W,Ti)C and (W,Ti)C-$NiAl_3$ cermet consolidated by the high-frequency induction-heating method," *J. Alloys Compd.*, vol. 568, pp. 73–77, 2013.

[25] R.M. Raihanuzzaman, M. Rosinski, Z. Xie, and R. Ghomashchi, "Microstructure and mechanical properties and of pulse plasma compacted WC-Co," *Int. J. Refract. Met. Hard Mater.*, vol. 60, pp. 58–67, 2016.

[26] X.X. Deng, J.M. Torralba, and A. García-Junceda, "Field-assisted sintering of WC hardmetals with Cr-based binder," in *Euro PM 2017*, pp. 3–8, 2017.

[27] S. Chanthapan, A. Kulkarni, J. Singh, C. Haines, and D. Kapoor, "Sintering of tungsten powder with and without tungsten carbide additive by field assisted sintering technology," *Int. J. Refract. Met. Hard Mater.*, vol. 31, pp. 114–120, 2012.

[28] S. Norgren, J. García, A. Blomqvist, and L. Yin, "Trends in the P/M hard metal industry," *Int. J. Refract. Met. Hard Mater.*, vol. 48, pp. 31–45, 2015.

[29] K. Jia, T.E. Fischer, and B. Gallois, "Microstructure, hardness and toughness of nanostructured and conventional WC-Co composites," *Nanostructured Mater.*, vol. 10, no. 5, pp. 875–891, 1998.

[30] C. Lin, E. Kny, G. Yuan, and B. Djuricic, "Microstructure and properties of ultrafine WC-0.6VC-10Co hardmetals densified by pressure-assisted critical liquid phase sintering," *J. Alloys Compd.*, vol. 383, pp. 98–102, 2004.

[31] M. Sherif, A.A. Mahday, H.A. Ahmed, and A.H. Amer, "Synthesis and characterizations of ball-milled nanocrystalline WC and nanocomposite WC-Co powders and subsequent consolidations," *J. Alloys Compd.*, vol. 312, pp. 315–325, 2000.

[32] S. Zhao, X. Song, J. Zhang, and X. Liu, "Effects of scale combination and contact condition of raw powders on SPS sintered near-nanocrystalline WC-Co alloy," *Mater. Sci. Eng. A*, vol. 473, pp. 323–329, 2008.

[33] D. Sivaprahasam, S.B. Chandrasekar, and R. Sundaresan, "Microstructure and mechanical properties of nanocrystalline WC-12Co consolidated by spark plasma sintering," *Int. J. Refract. Met. Hard Mater.*, vol. 25, pp. 144–152, 2007.

[34] S.G. Huang, L.Li, K. Vanmeensel, O. Van Der Biest, and J. Vleugels, "VC, Cr_3C_2 and NbC doped WC Co cemented carbides prepared by pulsed electric current sintering," *Int. J. Refract. Met. Hard Mater.*, vol. 25, pp. 417–422, 2007.

[35] S.I. Cha, S.H. Hong, and B.K. Kim, "Spark plasma sintering behavior of nanocrystalline WC-10Co cemented carbide powders," *Mater. Sci. Eng. A*, vol. 351, pp. 31–38, 2003.

[36] L.H. Zhu, Q. W. Huang, and H.F. Zhao, "Preparation of nanocrystalline WC-10Co-0.8 VC by spark plasma sintering," *J. Mater. Sci. Lett.*, vol. 22, no. 22, pp. 1631–1633, 2003.

[37] H. Kim, I. Shon, I. Jeong, I. Ko, J. Yoon, and J. Doh, "Rapid sintering of ultra fine wc and wc-co hard materials by high-frequency induction heated sintering and their mechanical properties," *Met. Mater. Int.*, vol. 13, no. 1, pp. 39–45, 2007.

[38] D. Michalski, A., Siemiaszko, "Nanocrystalline cemented carbides aintered by the pulse plasma method," *Int. J. Refract. Met. Hard Mater.*, vol. 25, no. 2, pp. 153–158, 2007.

[39] T. Robert, H. Metals, H. Materi, P. Examiner, and N. Mai, "United States Patent: Dense fine grained monotungsten carbide-transition metal cemented carbide body and preparation thereof. Patent No 5,773,735," 1996.

[40] Z.Z. Fang, X. Wang, T. Ryu, K.S. Hwang, and H.Y. Sohn, "Synthesis, sintering, and mechanical properties of nanocrystalline cemented tungsten carbide-A review," *Int. J. Refract. Met. Hard Mater.*, vol. 27, no. 2, pp. 288–299, 2009.

[41] S. Haglund and J. Ågren, "W content in Co binder during sintering of WC–Co," *Acta Mater.*, vol. 46, no. 8, pp. 2801–2807, 1998.

[42] "'REACH Program, European adoption process for the new chemicals legislation' http://ec.europa.eu/environment/chemicals/reach/background/index_en.htm. Accessed 28.09.2018." .

[43] A. Valavanidis, "Environmental Carcinogenic Substances, Exposure and Risk Assessment for Carcinogenci Potential. Classifications and Regulations by International and National Institutions," *NTP (National Toxicol. Program), 2016 Rep. Carcino- gens, 14th ed., Res. Triangle Park.*

[44] "2020, Horizon. Environment & Climate Action. Https://ec.europa.eu/programmes/horizon2020/en/area/environment-climate-action. Acessed 28.09.2018." .

[45] J.J. Moulin, P. Wild, S. Romazini, G. Lasfargues, and A. Peltier, "Lung cancer risk in hard-metal workers," *Am. J. Epidemiol.*, vol. 148, no. 3, pp. 241–248, 1998.

[46] P. Wild, A. Perdrix, S. Romazini, J.J. Moulin, and F. Pellet, "Lung cancer mortality in a site producing hard metals," *Occup. Environ. Med.*, vol. 57, no. 8, pp. 568–573, 2000.

[47] S. Bastian, W. Busch, D. Kühnel, A. Springer, and T. Meißner, "Toxicity of tungsten carbide and cobalt-doped tungsten carbide nanoparticles in mammalian cells in vitro," *Enrion Heal. Perspect*, vol. 117, no. 4, pp. 530–536, 2009.

[48] E. Kny and L. Schmid, "New hardmetal alloys with improved erosion and corrosion resistance," *Int. J. Refract. Met. Hard Mater.*, vol. 6, no. 3, pp. 145–148, 1987.

[49] L. Prakash, "Properties of tungsten carbide hard metals with Fe-Co-Ni binder in sintered and thermally treated state," *KFK Nachrichten*, pp. 35–42, 1979.

[50] A. García-Junceda, I. Sáez, X. X. Deng, and J. M. Torralba, "Development of a Cr-based hard composite processed by spark plasma sintering," *Metall. Mater. Trans. A*, vol. 49, no. 4, pp. 1363–1371, 2018.

[51] K.P. Mingard, B. Roebuck, J. Marshall, and G. Sweetman, "Some aspects of the structure of cobalt and nickel binder phases in hardmetals," *Acta Mater.*, vol. 59, no. 6, pp. 2277–2290, 2011.

[52] S. Ekemar, L. Lindholm, and T. Hartzell, "Nickel as a binder in WC-based cemented carbides," *Int. J. Refract. Hard Met.*, vol. 1, no. 1, pp. 37–40, 1982.

[53] K. Naruse, T. Harada, A. Fukawa, and K. Kaisha, "United States Patent (19) Method for welding hard metal," No. 4306139. Washington, DC. Patent and Trademark Office., 1981.

[54] G. Barlow, "Tungsten carbide bonded with nickel," in *Preprints of Fourth Europe Symp. for Powder Metallurgy, Crenoble, France*, 1975, pp. 13–15.

[55] H. Rong, Z. Peng, X. Ren, Y. Peng, C. Wang, and Z. Fu, "Ultrafine WC-Ni cemented carbides fabricated by spark plasma sintering," *Mater. Sci. Eng. A*, vol. 532, pp. 543–547, 2012.

[56] V.A. Tracey, "Nickel in hardmetals," *Int. J. Refract. Met. Hard Mater.*, vol. 11, no. 3, pp. 137–149, 1992.

[57] V.B. Voitovich, V.V Sverdel, R.F. Voitovich, E.I. Golovko, and I.N. Frantsevich, "Oxidation of WC-Co, WC-Ni and WC-Co-Ni hard metals in the temperature range 500 ~ 800 °C," *Int. J. Refract. Met. Hard Mater.*, vol. 14, no. 4, pp. 289–295, 1996.

[58] P. Alvaredo, E. Gordo, O. Van der Biest, and K. Vanmeensel, "Microstructural development and mechanical properties of iron based cermets processed by pressureless and spark plasma sintering," *Mater. Sci. Eng. A*, vol. 538, pp. 28–34, 2012.

[59] P. Alvaredo, S.A. Tsipas, and E. Gordo, "Influence of carbon content on the sinterability of an FeCr matrix cermet reinforced with TiCN," *Int. J. Refract. Met. Hard Mater.*, vol. 36, pp. 283–288, 2013.

[60] "Ceratizit: wood working main catalogue," *https://www.ceratizit.com/uploads/tx_extproduct/files/GD_KT_PRO-0425-0515_SEN_ABS_V1.pdf. Acessed 30.09.2018*.

[61] "Tigra: Tools cut in woodworking," *http://www.tigra.de/fileadmin/user_upload/PDF/Holzkatalog_2014.pdf. Acesssed 30.09.2018*.

[62] G. Gille, J. Bredthauer, B. Gries, B. Mende, and W. Heinrich, "Advanced and new grades of WC and binder powder - their properties and application," *Int. J. Refract. Met. Hard Mater.*, vol. 18, no. 2, pp. 87–102, 2000.

[63] B.J. Marques, C.M. Fernandes, and A.M.R. Senos, "Sintering, microstructure and properties of WC-AISI304 powder composites," *J. Alloys Compd.*, vol. 562, pp. 164–170, 2013.

[64] R. Furushima, K. Katou, K. Shimojima, H. Hosokawa, and A. Matsumoto, "Control of WC grain sizes and mechanical properties in WC-FeAl composite fabricated from vacuum sintering technique," *Int. J. Refract. Met. Hard Mater.*, vol. 50, pp. 16–22, 2015.

[65] B. Wittmann, W.D. Schubert, and B. Lux, "WC grain growth and grain growth inhibition in nickel and iron binder hardmetals," *Int. J. Refract. Met. Hard Mater.*, vol. 20, no. 1, pp. 51–60, 2002.

[66] C.M. Fernandes, L.M. Vilhena, L, C.M.S. Pinho, F.J. Oliveira, E. Soares, J. Sacramento, and A.M.R. Senos, "Mechanical characterization of WC-10wt% AISI 304 cemented carbides," *Mater. Sci. Eng. A*, vol. 618, pp. 629–636, 2014.

[67] L.M. Vilhena, C.M. Fernandes, E. Soares, J. Sacramento, A. M. R. Senos, and A. Ramalho, "Abrasive wear resistance of WC- Co and WC-AISI 304 composites by ball-cratering method," *Wear*, vol. 346–347, pp. 99–107, 2016.

[68] C.M. Oliveira, A.B. Bastos, A.C. Fernandes, C.M.S. Pinho, A.M.R. Senos, E. Soares, and J. Sacramento, "Corrosion behaviour of WC-10 % AISI 304 cemented carbides," *Corros. Sci.*, vol. 100, pp. 322–331, 2015.

[69] T. Bao, H. Zuhailawati, Z. Arifin, and K. N. Ishihara, "Grain growth , phase evolution and properties of NbC carbide-doped WC-10AISI304 hardmetals produced by pseudo hot isostatic pressing," *J. Alloys Compd.*, vol. 552, pp. 20–25, 2013.

[70] P. Gustafson, "A thermodynamic evaluation of the C-Cr-Fe-W System," *Metall. Trans. A*, vol. 19, pp. 2547–2554, 1988.

[71] W.D. Schubert, M. Fugger, B. Wittmann, and R. Useldinger, "Aspects of sintering of cemented carbides with Fe-based binders," *Int. J. Refract. Met. Hard Mater.*, vol. 49, no. 1, pp. 110–123, 2015.

[72] V. Bounhoure, S. Lay, S. Coindeau, S. Norgren, E. Pauty, and J. M. Missiaen, "Effect of Cr addition on solid state sintering of WC-Co alloys," *J. Refract. Hard Mater.*, vol. 52, pp. 21–28, 2015.

[73] P. Stecher, F. Benesovsky, and H. Nowotny, "Untersuchungen im System Chrom–Wolfram–Kohlenstoff.," *Planseeber Pulvermetall*, vol. 12, pp. 89–95, 1964.

[74] E. Rudy and Y.A. Chang, "F. Benesovsky, Reute/Tirol," in *5th Plansee Seminar,* 1964, pp. 786–822.

[75] Z. Tükör, W. D. Schubert, A. Bicherl, A. Bock, and B. Zeiler, "Formation of W-Cr- Phases d uring the production of Cr-doped WC powders," vol. 4, pp. 1–10.

[76] A. Markström, S. Norgren, K. Frisk, B. Jansson, and T. Sterneland, "Experimental and thermodynamic evaluation of the Co-Cr-C system," *Int. J. Mater. Res.*, vol. 97, no. 9, pp. 1243–1250, 2006.

[77] A.V. Khvan, B. Hallstedt, and C. Broeckmann, "A thermodynamic evaluation of the Fe-Cr-C system," *Calphad Comput. Coupling Phase Diagrams Thermochem.*, vol. 46, pp. 24–33, 2014.

[78] P. Gustafson, "An experimental study and a thermodynamic evaluation of the Cr-Fe-W-C system," *Metall. Trans. A*, vol. 19A, pp. 2531–3546, 1988.

[79] B. Kaplan, "Equilibrium aspects of Cr-alloyed cemented carbides (Doctoral dissertation, KTH Royal Institute of Technology)," 2015.

[80] B. Kaplan, S. Norgren, M. Schwind, and M. Selleby, "Thermodynamic calculations and experimental verification in the WC-Co-Cr cemented carbide system"," *Int. J. Refract. Met. Hard Mater.*, vol. 49, no. 1, pp. 400–405, 2015.

[81] K. Frisk and A. Markström, "Effect of Cr and v on phase equilibria in Co-WC based hardmetals," *Int. J. Mater. Res.*, vol. 99, no. 3, pp. 287–293, 2008.

[82] M. Brieseck, M. Bohn, and W. Lengauer, "Diffusion and solubility of Cr in WC," *J. Alloys Compd.*, vol. 489, no. 2, pp. 408–414, 2010.

[83] J. Zackrisson, B. Jansson, G.S. Uphadyaya, and H. Andrn, "WC-Co based cemented carbides with large Cr_3C_2 additions," *Int. J. Refract. Metals Hard Mater.*, vol. 16, pp. 417–422, 1998.

[84] K. H. Shi, K. C. Zhou, Z. Y. Li, X. Q. Zan, S. Z. Xu, and Z. Y. Min, "Effect of adding method of Cr on microstructure and properties of WC-9Ni-2Cr cemented carbides," *Int. J. Refract. Met. Hard Mater.*, vol. 38, pp. 1–6, 2013.

[85] K.H. Shi, K.C. Zhou, Z.Y. Li, and X.Q. Zan, "Effect of adding method of Cr on microstructure and properties of WC-9Ni-2Cr cemented carbides," *Int. J. Refract. Hard Mater.*, vol. 38, pp. 1–6, 2013.

[86] J. Pirso, M. Viljus, S. Letunovits, and K. Juhani, "Reactive carburizing sintering - A novel production method for high quality chromium carbide-nickel cermets," *Refract. Met. Hard Mater.*, vol. 24, pp. 263–270, 2006.

[87] O.M. Cintho, E.A.P. Favilla, and J.D.T. Capocchi, "Mechanical–thermal synthesis of chromium carbides," *J. Alloys Compd.*, vol. 439, no. 1–2, pp. 189–195, 2007.

[88] M. Rezaei-Sameti, S. Nadali, J. Rajabi, and M. Rakhshi, "The effects of pulse electrodeposition parameters on morphology, hardness and wear behavior of nano-structure Cr-WC composite coatings," *J. Mol. Struct.*, vol. 1020, pp. 23–27, 2012.

[89] G. Bolelli, T. Börner, F. Bozza, V. Cannillo, G. Cirillo, and L. Lusvarghi, "Cermet coatings with Fe-based matrix as alternative to WC-CoCr: Mechanical and tribological behaviours," *Surf. Coat. Technol.*, vol. 206, no. 19–20, pp. 4079–4094, 2012.

[90] W.D. Callister Jr and D.G. Rethwisch, *Fundamentals of materials science and engineering: an integrated approach*. John Wiley & Sons, 2012.

[91] J.O. Andersson, T. Helander, L. Hoglund, P. Shi, and B. Sundman, "Thermo-Calc & DICTRA, computational tools for materials science," *Calphad Comput. Coupling Phase Diagrams Thermochem.*, vol. 26, no. 2, pp. 273–312, 2002.

[92] M. Walbrühl, "ICME guided development of cemented carbides with alternative binder systems (Doctoral dissertation, KTH Royal Institute of Technology)," 2017.

[93] M. Ekroth, R. Frykholm, and M. Lindholm, "Gradient zones in WC-Ti(C,N)-Co-Baed cemented carbides: exprimental study and computer simulations," *Acta Mater.*, vol. 48, pp. 2177–2185, 2000.

[94] R. Frykholm, M. Ekroth, B. Jansson, J. Agren, and H.O. Andren, "A new labyrinth factor for modelling the effect of binder volume fraction on gradient sintering of cemented carbides," *Acta Mater.*, vol. 51, pp. 1115–1121, 2003.

[95] M. Ekroth, L.F. S. Dumitrescu, K. Frisk, and B. Jansson, "Development of a thermodynamic database for cemented carbides for design and processing simulations," *Metall. Mater. Trans. B*, vol. 31, no. 4, pp. 615–619, 2000.

[96] K. Frisk, L. Dumitrescu, M. Ekroth, B. Jansson, O. Kruse, and B. Sundman, "Development of a database for cemented carbides: thermodynamic modeling and experiments," *J. Phase Equilibria*, vol. 22, no. 6, pp. 645–655, 2001.

[97] Y. Peng, Y. Du, P. Zhou, W. Zhang, W. Chen, and L. Chen, "CSUTDCC1-A thermodynamic database for multicomponent cemented carbides," *Int. J. Refract. Met. Hard Mater.*, vol. 42, pp. 57–70, 2014.

[98] W. Zhang, Y. Du, W. Chen, Y. Peng, P. Zhou, and S. Wang, "SUDDCC1-A diffusion database for multicomponent cemented carbides," *J. Refract. HardMaterials*, vol. 43, pp. 164–180, 2014.

[99] P. Zhou, Y. Peng, C. Buchegger, Y. Du, and W. Lengauer, "Experimental investigation and thermodynamic assessment of the C-Co-Fe-Ni-W system," *Surf. Coatings Technol.*, vol. 306, pp. 370–377, 2016.

[100] K. Frisk, L. Dumitrescu, M. Ekroth, B. Sunduman, B. Jansson, and O. Kruse, "Development of a database for cemented carbides: thermodynamic modeling and experiments," *J. phase equilibria*, vol. 22, no. 6, pp. 645–655, 2001.

[101] L. Prakash, "A review of the properties of tungsten carbide hardmetals with alternative binder systems," *13 th Int. Plansee Semin.*, vol. 2, pp. 80–109, 1993.

[102] Y. He, L. Li, S. Huang, J. Vleugels, and O. Van der Biest, "Computer simulating the diffusion behavior of V and W in Co binder layer of WC-Co cemented carbide," *J. Alloys Compd.*, vol. 436, no. 1–2, pp. 146–149, 2007.

[103] A. F. Guillermet, "The Co-Fe-Ni-W-C phase diagram: a thermodynamic description and calculated sections for (Co-Fe-Ni) bonded cemented WC tools," *Z. Met.*, vol. 80, no. 2, pp. 83–94, 1989.

[104] C.M. Fernandes, V. Popovich, M. Matos, A. M. R. Senos, and M. T. Vieira, "Carbide phases formed in WC-M (M = Fe/Ni/Cr) systems," *Ceram. Int.*, vol. 35, no. 1, pp. 369–372, 2009.

[105] A.F. Guillermet, "An Assessment of the Fe-Ni-W-C Phase Diagram," *Z. Met.*, vol. 78, no. 3, pp. 165–171, 1987.

[106] N. Li, W. Zhang, Y. Du, W. Xie, and S. Wang, "A new approach to control the segregation of (Ta,W)C cubic phase in ultrafine WC-10Co-0.5Ta cemented carbides," *Scr. Mater.*, vol. 100, pp. 48–50, 2015.

[107] P.H. Mayrhofer, A. Hörling, L. Karlsson, J. Sjölén, T. Larsson, and C. Mitterer, "Self-organized nanostructures in the Ti-Al-N system," *Appl. Phys. Lett.*, vol. 2049, no. 2003, pp. 8–11, 2011.

[108] A. Larsson and S. Ruppi, "Microstructure and properties of Ti(C,N) coatings produced by moderate temperature chemical vapour deposition," *Thin Solid Films*, vol. 402, pp. 203–210, 2002.

[109] S. Ruppi, "Advances in chemically vapour deposited wear resistant coatings," *Le J. Phys. IV*, vol. 11, no. PR3, pp. 847–89, 2001.

[110] C. Czettl, J. Thurner, and U. Schleinkofer, "Knowledge based coating design of CVD TiN-TiBN-TiB2 architecture," *Int. J. Refract. Met. Hard Mater.*, vol. 71, pp. 330–334, 2018.

[111] U. Schleinkofer and C. Czettl, *Coating Applications for Cutting Tools*, vol. 1. Elsevier Ltd, 2014.

[112] W.D. Kingery, J.M. Woulbroun, and F.R. Charvat, "Effects of applied pressure on densification during sintering in the presence of a liquid phase," *J. Am. Ceram. Soc.*, vol. 46, no. 8, pp. 391–395, 1963.

[113] M. Eriksson, M. Radwan, and Z. Shen, "Spark plasma sintering of WC, cemented carbide and functional graded materials," *Refract. Met. Hard Mater.*, vol. 36, pp. 31–37, 2013.

[114] "Fabrication of large components by spark plasma sintering. http://www.cinn.es/industry-and-commercialisation/spark-plasma-sintering/. Accessed 30.09.2018." .

[115] A. Delanoë, M. Bacia, E. Pauty, S. Lay, and C. H. Allibert, "Cr-rich layer at the WC/Co interface in Cr-doped WC-Co cermets: Segregation or metastable carbide," *J. Cryst. Growth*, vol. 270, no. 1–2, pp. 219–227, 2004.

[116] A. Jaroenworaluck, T. Yamamoto, Y. Ikuhara, and T. Sakuma, "Segregation of vanadium at the WC/Co interface in VC-doped WC-Co," *J. Mater. Res.*, vol. 13, no. 3, pp. 2450–2452, 1998.

[117] A. Meingast, E. Coronel, A. Blomqvist, S. Norgren, M. Lattemann, and G. Wahnström, "High resolution STEM investigation of interface layers in cemented carbides," *Int. J. Refract. Metals Hard Mater.*, vol. 72, pp. 135–140, 2018.

[118] A. Delanoë and S. Lay, "Evolution of the WC grain shape in WC-Co alloys during sintering: Cumulated effect of the Cr addition and of the C content," *J. Refract. Met. Hard Mater.*, vol. 27, no. 2, pp. 189–197, 2009.

[119] I. Borgh, P. Hedstro, J. Odqvist, A. Borgenstam, A. John, and A. Gholinia, "On the three-dimensional structure of WC grains in cemented carbides," *Acta Mater.*, vol. 61, pp. 4726–4733, 2013.

Chapter 2

Motivation and objectives

Contents

2.1 Motivation

Hardmetals are composite materials consisting of one hard phase (generally WC) and a soft phase from the group VIII (usually Co) [1]. Hardmetals cover a wide range of applications: mining tools and cutting tools, engineered components and industrial wear parts [2]. There has been a continuous rise in the worldwide demand of hardmetals, from an annual total consumption of 10 tons in 1930 to estimated 75.000 tons in 2018 [3]. Hardmetals have taken a vital part in process of world's economic growth. Actually, few products have made such contribution in the global industrial economic growth compared to hardmetals, which have significantly decreased the price of making products in the industry and our daily life [4].

WC-Co hardmetals have many applications due to their good properties, such as their excellent combination of hardness and toughness values, their high wear resistance together with a good chemical stability at room temperature and at high temperature. Co has been used as the optimal binder for its good wettability in WC for more than 90 years. However, there is a great interest in the search for alternatives to Co-based binder driven by its high and fluctuating price due to its shortage of resources (0.003 % of the earth's crust) [5]. And now more motivation is triggered by its toxicity, since both Co and Ni have been listed in the report of potential substances carcinogenic to human health in the REACH program [6]. Thus, developing new alternative binders for hardmetals without Co or Ni is of great importance for the industry and has a substantial economic profit.

Iron also exists in the group VIII with atomic number 26, which is nearby Co. The use of iron-based binder as an alternative to Co has been extensively studied [7]. Fe (one of the most common elements on earth) has obvious advantages compared to Co and Ni alloys: cheaper price, easier availability, and no toxicity. However, a major disadvantage of Fe is the poor wettability in WC compared to Co. The good properties of Fe-based WC hardmetals require an accurate control of the composition, in order to guarantee the absence of η-phase (M_6C) and graphite after cooling, since these two phases will deteriorate the mechanical properties. Different types of Fe-based binders have been developed, such as FeNi alloy binder with a ratio of 3:1 [7] and FeCoNi with a ratio of 7:2:1 [8]. However, the addition of Ni and Co would increase the toxicity and cost of the Fe-based binders. Another problem of Fe-based binders is the existence of a narrow carbon window, representing the desirable two-phase region FCC+WC, even in the cases in which Co and/or Ni are added, which increases the difficulty of avoiding either M_6C

or graphite during sintering, leading to a more complex process for industrial manufacturing.

Chromium also belongs to group VIII and has an atomic number equal to 24 [9]. Cr metal is of high value for its good corrosion resistance, high hardness, and high melting point (1907 °C). A well-known application of Cr is focused on the production of stainless steels with 10 to 30 wt.% Cr, which are highly resistant to corrosion and oxidation [10]. Chromium or chromium carbides have been frequently added to hardmetals as grain growth inhibitors to improve the hardness and also to maintain the good level of toughness [11]. Meanwhile, coating with Cr is also used in metallic alloys and hardmetals for improving the corrosion and oxidation resistance [12]. Even more importantly, Cr (0.014 % of the earth's crust) has lower toxicity, lower price, and easier availability compared to Co [13]. The Cr-C-W phase diagram suggests a certain solubility of Cr in WC lattice [14]. Cr-based hardmetals without any Co or Ni have not been studied before, as far as this author knows. Our preliminary results obtained in Cr-based composites have shown that Cr-based hard materials could exhibit promising hardness values in comparison to Co-based hardmetals with the same level of WC volume fraction [15]. One disadvantage of using a Cr alloy as metallic matrix in WC-hardmetals could be the low solubility existing between Cr binder phase and WC hard phase, which may influence the final properties of the developed new materials.

In the present work, a combination of thermodynamic modelling and experimental studies will be used to optimise the compositional design and to reduce the trial-error process and speed up the cycle. Thus, the viability of using a Cr alloy as a binder without Co, for processing novel Cr-based WC hardmetals by a traditional liquid sintering technique and by a fast sintering technique, is assessed in the present investigation. The knowledge of the phase equilibrium diagram of these hardmetals is used to predict the possible phases obtained after the sintering step. The effect of adding extra Fe or Fe/C contents on the microstructure and mechanical properties of Cr-based hardmetals is investigated by addition of carbonyl iron powders (CIP) or carbonyl iron+graphite powders, respectively. The processing parameters during liquid and solid phase sintering techniques are also optimised to achieve near full density and to limit the existence of brittle phases. This comprehensive study approaching the analysis of the relationship between composition, microstructure, processing and properties aims to introduce a deep knowledge into the possibility of using these new hardmetals in industrial tool applications.

2.2 Objectives

The main objective of this investigation is to develop innovative Cr-based WC hardmetals, without Co or Ni, with good performance, low cost and healthy. These developed new materials must combine all the requirements needed in the tool industry, including high hardness, good toughness, high wear resistance, good compressive strength and high oxidation resistance. This study aims to know the viability of processing Cr-based WC hardmetals to partially replace commercial WC-Co hardmetals in some applications, such as in cutting tools and structured parts in which a good behaviour against wear, corrosion, and oxidation is needed. In order to achieve this goal, this research covers the following more specific secondary aims:

1) Comprehensive knowledge of the effect of high-energy mechanical milling process on the composition, microstructure, phase formation, crystalline parameters and size distribution of milled Cr-based WC powders.
2) Investigation of the viability of sintering Cr-based WC hardmetals by two different sintering techniques: liquid phase sintering (LSP) and spark plasma sintering (SPS).
3) Assessment of the effect of different SPS parameters, including heating rate, sintering temperature, and holding time, on the densification of Cr-based WC hardmetals.
4) Analysis of the influence of different extra Fe or Fe/C contents on the phase formation, microstructure, and properties of the sintered Cr-based WC hardmetals by a combination of simulation and experimental approaches. More specifically, the effect of Fe or Fe/C on phase diagrams is calculated by Thermo-Calc software with the TCFE7 database. Then, Cr-based WC hardmetals with different Fe or Fe/C additions are consolidated by LPS and SPS, respectively. The mechanical properties of the obtained Cr-based WC hardmetals are fully characterised to select the most optimal hardmetals.
5) Understanding of the sintering mechanisms experienced by Cr-based WC hardmetals from the particle-state to the sintered-state, in terms of phase formation, microstructural evolution, and final properties.
6) Characterisation of the density, hardness, toughness, Young's modulus, compressive strength, oxidation behaviour and wear resistance of the optimised Cr-based WC hardmetals. Exploration of the relationship between composition-microstructure-properties of Cr-based WC hardmetals. Then, comparison of the developed Cr-based WC hardmetals with some commercial WC-Co hardmetals used in the cutting tool industry.

2.3 References

[1] H.E. Exner, "Physical and chemica nature of cemented carbides," *Int. Met. Rev.*, vol. 1, no. 24, pp. 149–173, 1979.

[2] H.M. Ortner, P. Ettmayer, H. Kolaska, and I. Smid, "The history of the technological progress of hardmetals," *Int. J. Refract. Met. Hard Mater.*, vol. 49, no. 1, pp. 3–8, 2015.

[3] P. Ettmayer, H. Kolaska, and H.M. Ortner, *History of Hardmetals*, vol. 1. Elsevier Ltd, 2014.

[4] K. Brookes, "Hardmetal statistics," *Met. Powder Rep.*, vol. 69, no. 1, pp. 23–25, 2014.

[5] S. Norgren, J. García, A. Blomqvist, and L. Yin, "Trends in the P/M hard metal industry," *Int. J. Refract. Met. Hard Mater.*, vol. 48, pp. 31–45, 2015.

[6] "REACH Program, European adoption process for the new chemicals legislation, " http://ec.europa.eu/environment/chemicals/reach/background/index_en.htm. Accessed 28.09.2018.

[7] W.D. Schubert, M. Fugger, B. Wittmann, and R. Useldinger, "Aspects of sintering of cemented carbides with Fe-based binders," *Int. J. Refract. Met. Hard Mater.*, vol. 49, no. 1, pp. 110–123, 2015.

[8] L.J. Prakash, "Development of tungsten carbide hardmetals using iron-based binder alloys (Doctoral dissertation, Kernforschungszentrum Karlsruhe G.m.b.H)," 1980.

[9] E.A. Brandes, H.T. Greenaway, and H.E.N. Stone, "Ductility in chromium," *Nature*, vol. 178, no. 4533, pp. 587–591, 1956.

[10] B.F. Weiss and R. Stickler, "Phase instabilities during high temperature exposure of 316 austenitic stainless steel," *Metall. Trans.*, vol. 3, no. 4, pp. 851–866, 1972.

[11] K.H. Shi, K.C. Zhou, Z.Y. Li, X.Q. Zan, S.Z. Xu, and Z.Y. Min, "Effect of adding method of Cr on microstructure and properties of WC-9Ni-2Cr cemented carbides," *Int. J. Refract. Hard Mater.*, vol. 38, pp. 1–6, 2013.

[12] G. Bolelli, T. Börner, F. Bozza, V. Cannillo, G. Cirillo, and L. Lusvarghi, "Cermet coatings with Fe-based matrix as alternative to WC-CoCr: Mechanical and tribological behaviours," *Surf. Coat. Technol.*, vol. 206, no. 19–20, pp. 4079–4094, 2012.

[13] J. Barnhart, "Occurrences, uses, and properties of chromium," *Regul. Toxicol. Pharmacol.*, vol. 26, no. 1, pp. S3–S7, 1997.

[14] M. Brieseck, M. Bohn, and W. Lengauer, "Diffusion and solubility of Cr in WC," *J. Alloys Compd.*, vol. 489, n. 2, pp. 408–414, 2010.

[15] A. García-Junceda, I. Sáez, X.X. Deng, and J.M. Torralba, "Development of a Cr-based hard composite processed by spark plasma sintering," *Metall. Mater. Trans. A*, vol. 49, no. 4, pp. 1363–1371, 2018.

Chapter 3

Materials, experimental procedure and techniques

Contents

3.1 Raw materials

All the powders used as raw materials are commercial powders. WC powder provided by Alfa Aesar (USA) acts as the reinforcement, whereas CrFe powder supplied by Höganäs (Sweden) represents the metallic binder. The densities of WC (99.5 % purity) and CrFe powders are 16.53 and 7.55 g/cm^3, respectively. Table 3.1 shows the specified composition of the CrFe powder. The content of Cr in the CrFe powder is 71.4 wt.% and the Fe content is fixed to 28.1 wt.%, with a small amount of other alloying elements (Si, C, N, P and S). Consequently, the metallic binder in this work is designated as Cr-based binder due to its main Cr content.

Table 3.1. Composition of CrFe powder.

Element	Cr	Fe	Si	C	N	P	S
Weight percent (wt.%)	71.4	balance	0.4	0.042	0.03	0.021	0.004

The carbonyl iron powder (CIP) added as extra Fe (99.9 % purity) is provided by William Rowland Limited (United Kingdom) with a density of 7.85 g/cm^3. Graphite powder (99.0 % purity) added as extra carbon is supplied by ISMAF (Spain) with a density of 2.10 g/cm^3.

3.2 Experimental procedure

Developing a new type of hardmetal involves a lot of important steps, all of them with a critical weight. A small change in the process from the compositional design to the sintering process may affect the final properties. So a combination of experiments and simulation is a good approach to design the material, products, and final properties by the link of process-structure-properties. The scheme of the experimental process carried out in this investigation is reflected in Figure 3.1. The processing of the novel Cr-based WC hardmetal follows a powder metallurgy (PM) route to process the mechanically milled powders and the sintered samples. The milling parameters are optimised after the study of the evolution of the milled Cr-based WC powders with different milling times. This optimisation of the milling process is based on the characterisation of Cr-based WC powders by SEM, particle size distribution measurements (laser diffraction technique), and XRD analyses. Subsequently, the selected Cr-based WC powders are sintered and consolidated by both LPS and SPS, respectively, to investigate the effect of traditional and fast sintering techniques on the densification, microstructure and properties of Cr-based WC hardmetals. The influence of the composition on the phase diagram in terms of Fe or Fe/C contents is calculated by Thermo-Calc with TCFE7 database. Accordingly, the composition and sintering parameters are optimised based on experimental and

thermodynamic studies of the W-C-Cr-Fe system. The microstructural characterisation of milled powders and sintered materials takes an important part of this work, so a combination of different microscopic techniques including optical microcopy (OM), scanning electron microcopy (SEM) and transmission electron microcopy (TEM) are used. The phase formation of Cr-based WC samples after cooling is characterised by X-ray diffraction technique (XRD) together with energy dispersive X-ray spectroscopy (EDX). Finally, the properties of Cr-based WC hardmetals are fully characterised to compare their performance with commercial WC-Co hardmetals, including hardness, fracture toughness, Young's modulus, compressive strength, oxidation resistance and wear resistance.

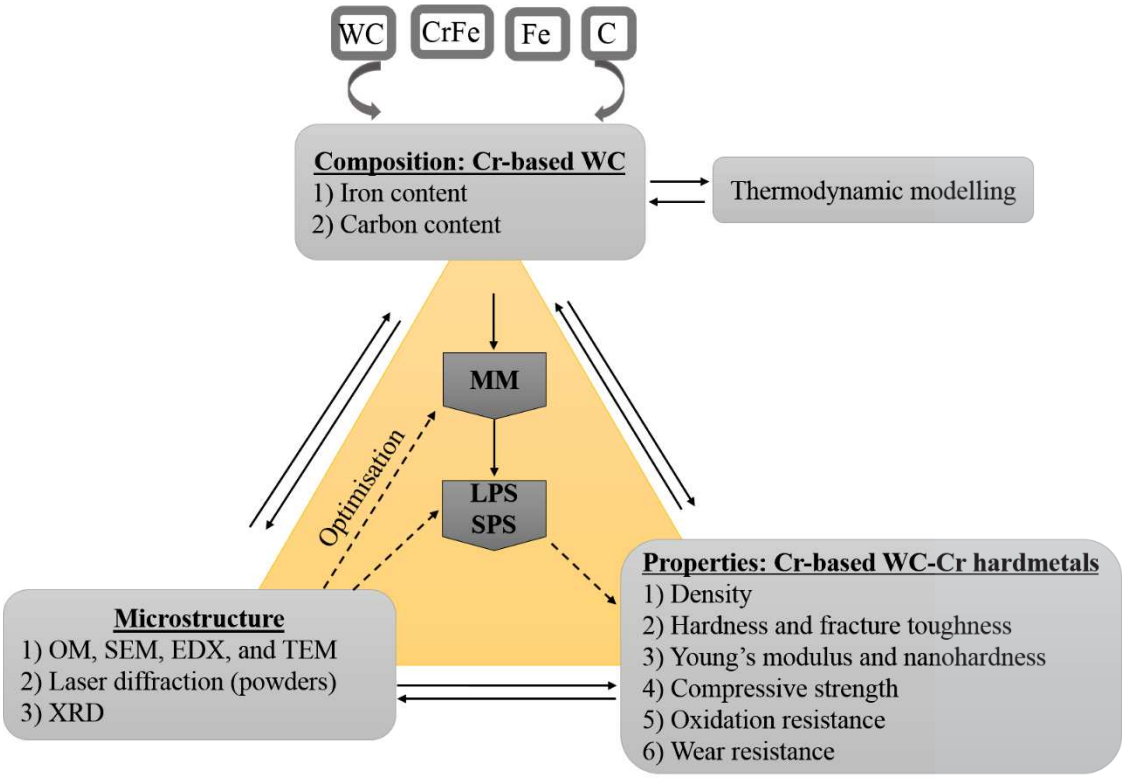

Figure 3.1. Scheme of the experimental procedure followed in this work.

3.2.1 Mechanical milling (MM)

The experimental parameters used during MM are shown in Table 3.2. The hard WC particles and the binder CrFe alloy are mechanically milled in a planetary ball mill (Pulverisette 6) at 350 rpm using a WC-6Co hardmetal vessel and balls with the same composition. The protective argon is inserted into the milling vessel after every 2 h of milling to reduce the oxidation during the milling process. 2, 4, 6, 8, 10 and 20 h of milling time are selected in order to study the evolution of Cr-based WC powders with milling

time. The amount of powder (40 g) is calculated keeping the constant ball-to-powder ratio at 10:1. The mechanical properties of hardmetals are mainly related to the volume fraction of hard particles (usually from 70 % to 90 %). A higher volume fraction of WC hard phase will improve the hardness, but also deteriorate the toughness. Considering a good balance between hardness and toughness, the volume fraction of WC particles is fixed to 70 %. A process control agent (PCA) is added to the powder mixture to reduce the effect of cold welding. As PCA, 0.5 wt.% of stearic acid ($C_{18}H_{36}O_2$) is used with a purity of 95 %.

Table 3.2. Parameters of mechanical milling.

Speed (rpm)	350
Volume fraction of WC (%)	70
Mass of WC (g)	30.51
Mass of CrFe (g)	9.29
Mass of Stearic Acid (g)	0.2
Milling time (h)	2, 4, 6, 8, 10, 20
Protective gas	Argon
Cycle time (min)	30 minutes grinding plus 60 minutes rest
Ball-to-powders weight ratio	10:1
Number of balls	50
Ball composition	Hardmetal WC-6Co
Vessel composition	Hardmetal WC-6Co
Density of a ball (g/cm^3)	14.7
Mass of a ball (g)	7.8

The Fe and C contents in Cr-based WC powders are varied by extra addition of carbonyl iron powder and graphite powder, respectively. The effect of Fe content on the microstructure of Cr-based WC powders and hardmetals is studied first. Subsequently, the effect of the C content on the final microstructure is investigated on Cr-based WC hardmetals with the previously optimised Fe content.

3.2.1.1 Extra Fe addition

The Fe content in milled Cr-based WC powders is adjusted through extra different Fe additions (1 wt.%, 3 wt.% and 5 wt.%) as listed in Table 3.3, whereas the content of WC phase is fixed to 83.2 wt.%.

Table 3.3. Weight percent of Fe, Cr, W and C in Cr-based hardmetals with different extra Fe additions.

Fe (wt.%)		Total Fe (wt.%)	Cr (wt.%)	W (wt.%)	C (wt.%)
Extra Fe (addition)	Fe (CrFe powders)				
0	4.8	4.8	12.0	78.1	5.1
1	4.5	5.5	11.3	78.1	5.1
3	3.8	6.8	10.0	78.1	5.1
5	3.4	8.4	8.4	78.1	5.1

3.2.1.2 Extra C addition

After the investigation of the effect of Fe content on the microstructure and properties of Cr-based WC hardmetals, the extra 3 wt.% Fe addition is selected, based on the simulation results (more details in chapter 4.3). The C content in Cr-based WC powders with extra 3 wt.% Fe is adjusted through different extra C additions (0.5 wt.%, 1 wt.% and 2 wt.%). The corresponding compositions of Cr-based WC hardmetals with different C additions are shown in Table 3.4. The mass fraction of Cr-based binder is fixed to 16.8 wt.%.

Table 3.4. Weight percent of Fe, Cr, W and C in Cr-based hardmetals with different extra C additions

C (wt.%)		Fe (wt.%)	Cr (wt.%)	W (wt.%)	Total C (wt.%)
Extra C (addition)	C (WC powders)				
0	5.10	6.8	10.0	78.10	5.10
0.5	5.09	6.8	10.0	77.61	5.59
1	5.03	6.8	10.0	77.17	6.03
2	4.96	6.8	10.0	76.24	6.96

3.2.2 Sintering techniques

Different sintering processes will influence the microstructure and mechanical properties of the final product. This study explores the feasibility of sintering Cr-based WC powders through two different sintering routes: LPS and SPS.

3.2.2.1 Liquid phase sintering (LPS)

The milled Cr-based WC powders need green-forming into desired shapes so that they can be sintered to full density by LPS. There are different possible routes to produce the green compacts: uniaxial pressing, cold isostatic pressing, extrusion, and injection molding. Among others, uniaxial pressing is the most commonly used [1].

In the typical LPS process, the solid grains are soluble in the liquid at the sintering temperature. This solid solubility causes the liquid to spread and wet the solid grains, providing a capillary force that pulls the solid grains together. Geman *et al.* [2] reported four stages in LPS process: solid-state heating, rearrangement, solution-precipitation, and solid skeletal sintering. Sintering temperature is primarily determined by the composition of hardmetals. The practical sintering temperature of WC-Co hardmetals is selected slightly above their meting temperature, which depends on their components, for example, a range between 1320-1370 ºC for sintering WC-10wt.% Co hardmetals [3]. Additionally, sintering temperature is also effected by the size and shape of the milled particles. The sintering temperature generally decreases as the particle size decreases, since diffusion distances are shorter [4].

In this work, the selected Cr-based WC powders are pressed uniaxially at 300 MPa into cylindrical samples with diameter of 16 mm and height of around 2 mm. Then, the pressed green parts are put inside an Al_2O_3 crucible for sintering by using a Carolite TZF 16/450 Tube Furnace. The sintering temperature of Cr-based WC hardmetals is selected at 1450 °C, which is around 100 °C above the eutectic temperature of W-C-Cr-Fe system, as it will be shown in the following Chapter 4 entitled "Thermodynamic simulation". Figure 3.2 shows the sintering cycle applied: heating rate is 5 °C/min, with a holding time of 30 minutes at 1450 °C, followed by cooling in furnace under protective Ar atmosphere.

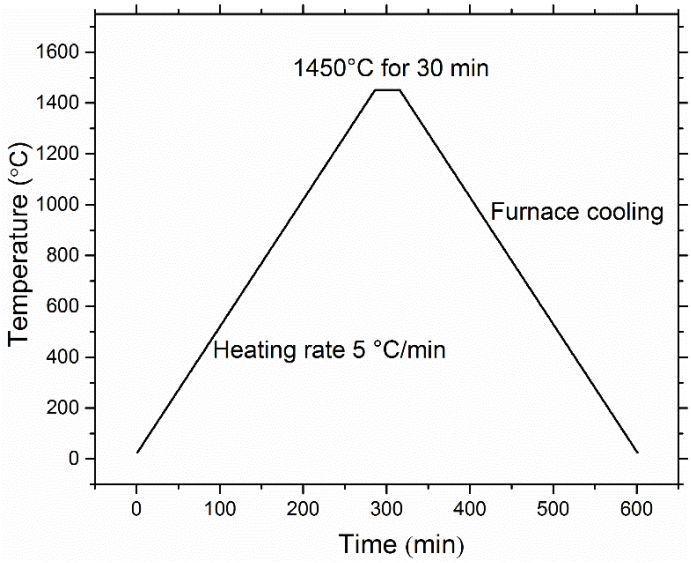

Figure 3.2. Temperature versus time cycle followed during liquid phase sintering.

3.2.2.2 Spark plasma sintering (SPS)

The consolidation of WC-hardmetals requires the sintering at relatively high temperatures, for achieving a good densification, and the use of a protective gas or vacuum to avoid oxidation phenomena. SPS technique can be used to consolidate hardmetals and enables a better control of the final microstructure, thanks to the application of pressure, high-heating rates and short dwell times, together with high vacuum or protector atmosphere [5]. The applied compressive stress leads to a better contact between particles, enhancing the grain boundary diffusion and lattice diffusion [6]. The high-heating rates and short dwell times can be beneficial to improve the densification rate, while maintaining the fine microstructure. Usually, the composition of the sintering atmosphere and its partial pressure have an influence on the structure and diffusivity of sintered materials. However, as the specimen is enclosed in the pressing tools, the pressure and the atmospheric composition inside the tool strongly differ from the atmosphere outside. Therefore, low vacuum (in the range of 10^{-4} to 10^{-5} bar) is given in most of the literature [7-8].

In this work, Cr-based WC powders are consolidated by SPS in a HPD 25-3 model developed by FCT System GmbH (Germany), located in the Metal Forming Institute (Poland) (Figure 3.3). As was discussed in the introduction chapter, SPS technique is based on a hydraulic loading system and a high-power electrical circuit. This technique uses a pulsed direct current (DC) to heat up the powder by Joule effect. The pressure is applied in the vertical direction. SPS can enhance the densification of Cr-based WC hardmetals in comparison with LPS technique by two primarily effects: (i) current flow through the specimen rather than the surrounding graphite tools, providing interaction between the electric current and the microstructure formation and (ii) local melting of the powders surface as well as elimination of the oxide surface layer due to higher local temperature at the sintering neck [9]. The pyrometer is located at the upper punch, about 5 mm from the center of the sample, to measure the sintering temperature. In this work, two different cylindrical samples (10 and 20 mm diameter) are employed, depending on the mechanical test performed.

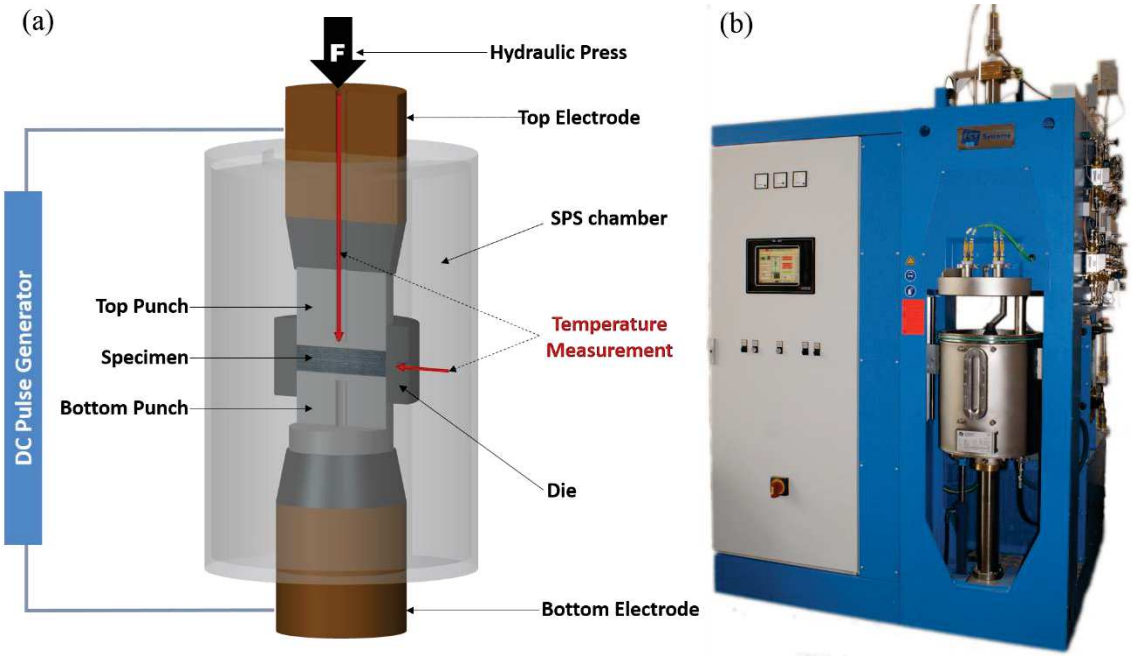

Figure 3.3. Scheme (a) and image (b) of HPD 25-3 SPS apparatus.

Table 3.5 lists the different SPS parameters applied to consolidate the corresponding Cr-based WC powders with different Fe or Fe/C additions. The powders are poured into the graphite die. The consolidation temperature selected is varied in a range of 1200-1350 °C. This selection of consolidation temperatures is based on the phase diagrams calculated in this work and in conditions reported in the literature [10], where the temperature in solid-state sintering is around 100 °C lower than the eutectic temperature. The maximum

pressure is maintained during the consolidation at the sintering temperature. Heating rate, holding time and applied pressure are set in a range of 200-400 °C/min, 5-10 min and 50-80 MPa, respectively, in order to study their effect on densification. The sintering is performed under low vacuum (10^{-2}-10^{-3} mbar). The cycle followed for the thermo-mechanical sintering process at 1350 °C/min for 10 min, with an applied pressure of 80 MPa, is presented in Figure 3.4. In some tests, a pure tungsten foil (thickness of 25 μm) is interposed between the graphite die/punches and the Cr-based WC powders, in order to avoid the carbon contamination coming from the graphite tools [11]. The real final C content in the consolidated Cr-based WC hardmetals is measured by a chemical analysis using a LECO CS230 analyser, located in the University Carlos III of Madrid (Spain).

Table 3.5. SPS parameters for Cr-based WC powders with different Fe/C additions.

Cr-based WC powders with different Fe additions	Consolidation temperature (°C)	Heating rate (°C/min)	Holding time (min)	Applied pressure (MPa)	Applied W foil
0 wt.% Fe	1200	200	5	50	No
1 wt.% Fe	1200	200	5	50	No
1 wt.% Fe	1200	400	5	50	No
3 wt.% Fe	1200	400	5	50	No
3 wt.% Fe	1200	400	10	50	No
3 wt.% Fe + 0.5 wt.% C	1350	400	10	80	No
3 wt.% Fe + 0.5 wt.% C	1350	400	10	80	Yes
3 wt.% Fe + 1 wt.% C	1350	400	10	80	Yes
3 wt.% Fe+ 2 wt.% C	1350	400	10	80	Yes

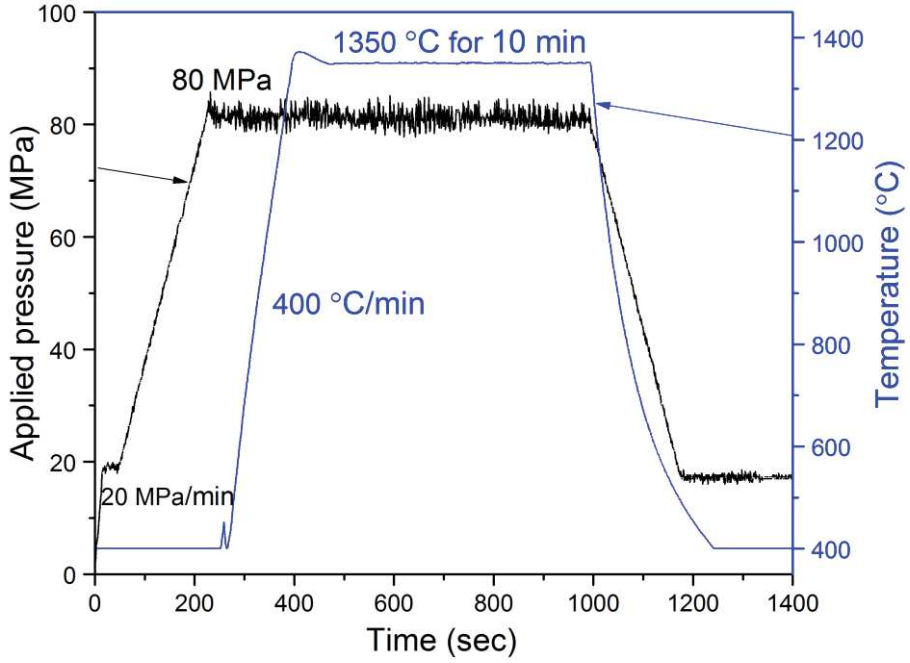

Figure 3.4. Schematic cycle followed during one of the designed SPS sintering processes (1350 °C-400 °C/min-10 min-80 MPa).

3.3 Particle size characterisation

A Malvern Mastersizer 2000 particle size analyser (based on laser diffraction) is used to measure the particle size distribution of the raw powders and the milled powders. The measurements are carried out by using a wet dispersion unit Hydro 2000, using water as dispersion medium. The software measures each sample three times. The average curve of particles size distribution is obtained automatically. Particle size D (D_{10}, D_{50}, *and* D_{90}) represents the undersize of cumulative distribution. For example, particle size D_{10} means that 10 vol.% of the particles are smaller than D_{10}.

3.4 Phase and composition characterisation

3.4.1 X-Ray diffraction (XRD)

In this work, on the one hand, the microstrain level and the crystalline size of MMed powders, and on the other hand, phases of powders and sintered samples, are studied by the XRD technique. The X-ray diffractometer (Empyrean, PANalytical) is equipped with a X-ray platform for the analysis of powders and bulk samples. The voltage applied is 45 kV and an intensity of 40 mA. Moreover, it is employed a Cu-$k\alpha$ tube (λ=1.5405 Å). The X-ray diffraction patterns are measured from 20° to 130° with a step size of 0.0263°. Then, the obtained patterns are analysed to identify the formed phases using the Highscore software and the database PDF-4 from the International Center for Diffraction Ddata (ICDD).

The MM process increases the distortions of the network and the microstrains, which is of importance for the sintering process. In order to identify the most suitable milling time for the subsequent powder consolidation, the crystalline size (D) and the microstrain ($\mu\mathcal{E}$) of MMed powders are calculated from the spectra by utilizing the Scherrer method and the X-Pert HighScore software [12-13], in which:

$$D = K\lambda / (B\cos\theta) \tag{3-1}$$

$$\mu\mathcal{E} = B / (4\tan\theta) \tag{3-2}$$

where K is a constant with a value equal to 0.9, λ is the wavelength of the beam incidence, B is the width at half maximum of the most intense peak of WC in the diffraction pattern (value of B must be in radians) and θ is the Bragg angle.

3.4.2 Elemental analyser

Elemental analysis is a process in which a material is analysed for knowing its elemental and sometimes isotopic composition. The determination of the exact C content in sintered hardmetals is crucial for controlling their properties. In this work, the C content of sintered Cr-based WC hardmetals is quantitatively calculated by a CS-230 LECO analyser. A sample of 300 mg is introduced into an alumina crucible where it is subsequently melted in an induction furnace. In order to ignite and correctly reach the combustion of the sample, it is necessary to add a small amount of an accelerator (called Lecocel II: tungsten/tin mixture) supplied by the manufacturer of the equipment. The carbon resulting from the combustion reacts with a stream of oxygen to form CO/CO_2, obtaining finally the C content. In order to get precise values of C content, each test is repeated for 6 times.

3.5 Density analysis

The densities of milled Cr-based WC powders and hardmetals are measured by two different methods. For the one hand, a gas pycnometer is used to measure the density of the milled powders. This measurement is repeated three times to obtain the average value. On the other hand, Archimedes´ method is used to calculate the density of the sintered bulk samples. The weight of samples is measured in three different conditions to calculate the density value: dry (m_1), wet (m_2) and after wetting and drying the surface (m_3).

$$\rho = \frac{m_1}{m_3 - m_2} \tag{3-3}$$

where m_1 is the dry mass, m_2 is the wet mass (submerged and without bubbles stuck on the surface of sample) and m_3 is the swamped mass (after immersion).

This is a common way to express relative density in PM products, since it gives an indication of the residual porosity. In this work, the relative density of each sample is determined using the ratio between the experimental Archimedes´ density and the calculated theoretical density. The theoretical density of each sample is calculated by the following equation [14]:

$$\rho_{theo} = W_W \times \rho_W + W_{Cr} \times \rho_{Cr} + W_{Fe} \times \rho_{Fe} + W_C \times \rho_C \tag{3-4}$$

where W and ρ are the corresponding weight percent and density of each element, respectively.

3.6 Microstructural Characterisation

3.6.1 Optical microscopy (OM)

OM is a type of microscopy that uses visible light and a system of lenses to magnify images of small subjects from 5X to 1000X. In the study of the microstructure of hardmetals, it plays an important role to observe porosities and grain size in a convenient way. In this work, all sintered Cr-based WC samples are rough with SiC papers from 600 to 2000, followed by polishing with diamond pastes from 6 to 1 μm. These polished samples are characterised by OM firstly to check the porosity before the characterisation with a higher resolution technique, such as SEM. Besides, the calculation of the fracture toughness is based on the measurement of the total length of the cracks produced by a hardness testes from optical images, which will be explained in section 3.7.1.

3.6.2 Scanning electron microscopy (SEM) and energy dispersive X-ray spectroscopy (EDX)

Scanning electron microscopy produces images of a sample with a higher resolution than optical microscopy. Energetic electron beams are generated by the electron gun, then focused to a spot size of about 0.4 nm to 5 nm in diameter by a series of magnetic condenser lens and rastered along the surface of the specimen with the aid of the scanning coils [15]. The interaction of the electron beam with the sample surface produces various emission signals that contain information on the size, shape, texture and composition of the sample. In particular, secondary electrons (SE) are emitted very close to the specimen surface, providing mainly topographical information, while back scattered electrons (BSE) and X-rays, generated deeper below the surface, provide crystallographic, atomic and compositional information.

In this work, a ZEISS EVO MA15 SEM microscope coupled to an EDX Oxford INCA 350 detector, and a Helios NanoLab 600i FEI FIB-FEGSEM microscope coupled to an EDX Oxford Instruments X Max EDX detector, are employed. SE images provide the morphology of Cr-based WC powders and sintered samples. BSE images offer the distribution of hard phase and binder phase, since hard phases with heavy elements (high atomic number) backscatter electrons more strongly than binder phases with light elements (low atomic number), and thus appear brighter in the images. The WC average grain sizes (d) in the milled powder and the sintered bulks are measured using the linear intercept method on representative BSE images, since the shape and size of WC are

distinguished from the other phases [16]. On the other hand, EDX technology provides qualitative or semi-quantitative information of the elemental content in the sintered bulks. In addition, the focused ion beam (FIB) technique is used to prepare the thin TEM samples. The basic concept of the FIB microscope is similar to that of the scanning electron microscope, but uses ions like Gallium (Ga+), instead of electrons for imaging or removal of material. The final size of the electron transparent cross-section should be around 100 square microns.

3.6.3 Transmission electron microcopy (TEM)

Transmission electron microscopy is another powerful imaging technique that uses high-energy electrons to provide microstructural information down to atomic resolution. Specimens for TEM characterisation must be electron transparent (generally <100 nm), enabling the transmission of the incident electrons. In the TEM, the incident electrons, also called primary electrons, emitted from the electron gun are accelerated towards the specimen at energies between 100 and 400 keV. Depending on the operation of the objective and projection lenses and the set of objective apertures selected, different types of images can be generated. Bright-field (BF) and dark-field (DF) imaging hold information about morphology, grain size and defect structure, while selected area electron diffraction (SAED) patterns provide crystallographic information such as crystal orientation, lattice parameters. An annular dark field image formed only by very high angle is highly sensitive to variations in the atomic number of atoms in the sample. This technique is known as high-angle annular dark-field imaging (HAADF). A combination of HAADF image and EDX mapping enables to obtain the elemental distribution in the corresponding microstructural image with a very high magnification. Finally, phase contrast analysis by combining the direct and diffracted beams allows the generation of high-resolution transmission electron microscopy (HRTEM) images that can be used to infer information about the crystalline lattice at atomic resolution. Therefore, in order to characterise in more detail the microstructure and composition of the sintered Cr-based WC hardmetals, transmission electron microcopy (TEM) in a FEI Talos F200X microscope, coupled to EDX for elemental mapping analysis, is performed on the previously prepared FIB samples at 200 kV. The diffraction patterns are obtained to identify some phase structures in selected areas. The interface between the WC hard phase and binder phase is characterised by HRTEM.

3.7 Mechanical properties characterisation

3.7.1 Vickers hardness and fracture toughness measurements

The hardness of Cr-based WC hardmetals is characterised using a Vickers hardness tester (NEXUS 4000 tester equipped with a Vickers diamond indenter) with a load of 30 kgf (F) applied during 10 s. These Cr-based WC samples are well polished with diamond paste down to 1 μm before testing. The diagonals produced by the indenter are measured to calculate the Vickers hardness with the equation 3-6. One sample is tested for each material and four indentations are made at least to obtain the average value of the Vickers hardness.

The fracture toughness (K_{IC}) is determined by measuring the total length of the cracks emanating from the four corners of the Vickers hardness indentation and using the Palmqvist crack equation 3-5, based on the international standard ISO 28079 [17] [18]. Figure 3.5 shows a schematic diagram with the measurement of the length of the cracks and an optical micrograph of an indentation performed in a Cr-based WC hardmetal sintered in this investigation.

The hardmetal Vickers hardness, HV, is given by the following equation:

$$HV = \frac{1.8544 \times F}{d^2} \tag{3-5}$$

where $d = (d_1+d_2)/2$. d_1 and d_2 are the lengths of indentation diagonals as shown in Figure 3.5.

The sum length (L) of cracks is measured from the indentation corner to the crack tip:

$$L = l_1 + l_2 + l_3 + l_4 \tag{3-6}$$

Equation for Palmqvist fracture toughness K_{IC}:

$$K_{IC} = A\sqrt{\frac{F \times HV}{L}} \tag{3-7}$$

where the constant A is equal to 0.2784, F is the applied load and HV is the Vickers hardness. All the quantities are expressed in SI units and the average value is calculated from six data.

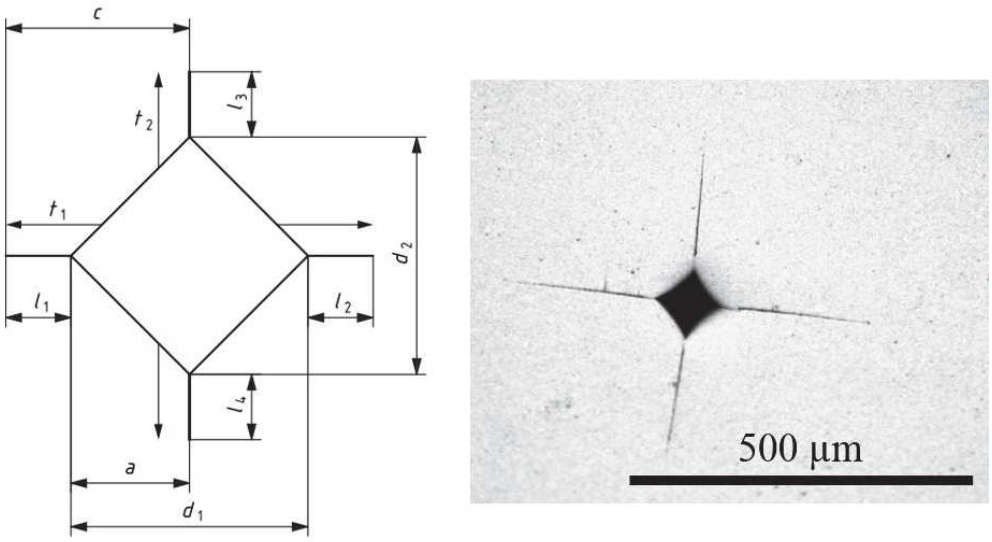

Figure 3.5. Schematic diagram with the measurement of the length of the cracks and diagonals of the indentation and optical micrograph of an indentation performed in a Cr-based WC hardmetal.

3.7.2 Nanoindentation tests

Nanoindentation method is widely used to study the mechanical properties of materials at very small length scales, ranging from nanometre to micrometre [19]. The hardness of WC-Co hardmetals have been reported in terms of macro, micro and nanoindentation length scale to understand the microstructure-hardness relationship [20]. The nanohardness (H) and Young's modulus (E) of a hardmetal can be obtained by analysing the load-displacement curve obtained by indenting small volumes of material with a diamond tip and recording both the load and the displacement with the Oliver-Pharr method [21]. Thus, Figure 6 shows an example of a load–displacement curve, in which P_{max} is the peak indentation load, h_{max} is the displacement at the peak load, and h_f is the final depth of the contact impression after unloading [21].

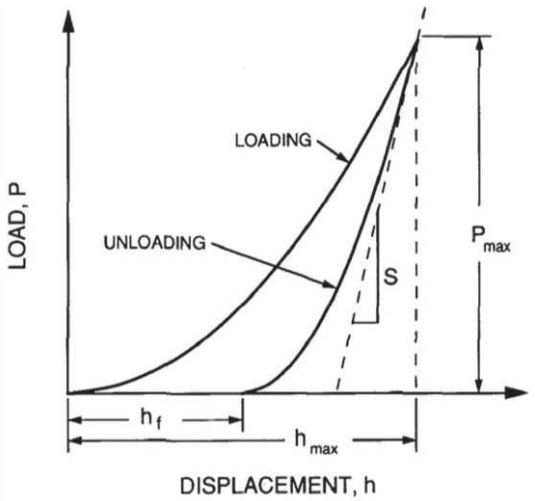

Figure 3.6. Schematic representation of the load –displacement curve [21].

The reduced modulus (E_r) can be calculated with the contact area (A_C) by the following equation:

$$E_r = \frac{S\sqrt{\pi}}{2\sqrt{A_C}} \tag{3-8}$$

where S is the initial unloading stiffness, which can be directly determined from the load-displacement curve. Then, the real elastic modulus (E) can be given by:

$$\frac{1}{E_r} = \frac{(1-v^2)}{E} + \frac{(1-v_i^2)}{E_i} \tag{3-9}$$

where E and v stand for the real elastic modulus and Poisson's ratio of the tested sample, respectively, and E_i and v_i are the elastic modulus (1139.2 GPa) and Poisson's ratio (0.07) of the diamond indenter, respectively. The nanohardness (H) is calculated by the equation:

$$H = \frac{P_{max}}{A_C} \tag{3-10}$$

where P_{max} is the maximum load applied.

In this work, the nanohardness and the elastic modulus are characterised by nanoindentation compressive work at room temperature, using a Hysitron TI950 Triboindenter equipped with a high-load transducer and a Berkovich diamond tip. The maximum load is determined at 400 mN by a cyclic loading method [22], where the hardness value becomes stable with the increase of the penetration depth. The load control mode is used with a loading rate of 80 mN/s up to the maximum load of 400 mN with a holding time of 2 seconds, followed by 5 second for unloading. A homogenous array of 25 indents (5 by 5) is carried out on the surface of Cr-based WC hardmetals. The spacing between indents is 40 μm along each row and 40 μm in the column direction in order to avoid any overlapped effect. The surfaces of all tested samples are carefully polished with diamond paste down to 1 μm.

3.7.3 Compressive tests

The compressive strength of Cr-based WC samples is determined by uniaxial pressing using an Instron 3384 equipment coupled to a furnace in air atmosphere, as shown in Figure 3.7. The maximum applied load and the strain rate are 15 kN and 4×10^{-3} s^{-1}, respectively. The tested samples have a cuboid shape with 2×2×4 mm size. With the aim of investigating the effect of the temperature on the compressive strength, room temperature (RT), 300 °C and 600 °C are programmed and reached using a temperature control panel. Due to the high hardness of the investigated materials, the sample is

mounted between two hardmetal disks to avoid the development of cracks within the punches made of nickel superalloy. The top and bottom surfaces of the sample being tested should be parallel between them and perpendicular to the direction of application of the compressive pressure, in order to avoid the twisting of the samples. Teflon sheets are inserted at room temperature between the tested sample and the hardmetal disks to lower the friction at the interface. Each experiment is repeated 3 times to ensure the consistency during the pressing process.

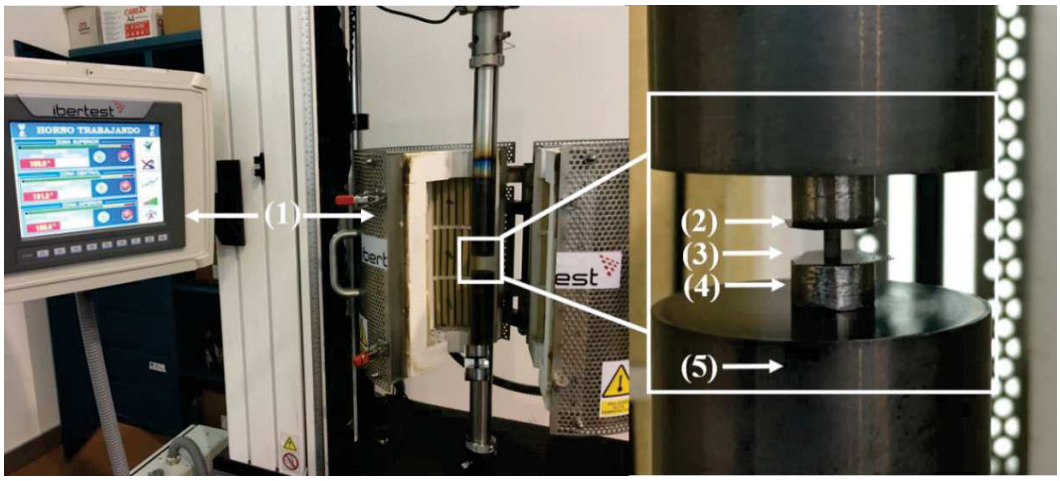

Figure 3.7. Instron 3384 equipment for compressive testing at high temperatures: (1) furnace and temperature control panel, (2) Teflon sheet, (3) sample, (4) hardmetal disk, and (5) superalloy punch.

3.8 Oxidation resistance

Hardmetals have a wide application in industry due to their good combination of fracture toughness and hardness. Hardmetals also need a good oxidation resistance for applications in which high stresses are applied together with high temperatures, as it is the case of hot rolling. In this work, the oxidation resistance of Cr-based WC hardmetals samples with a cuboid shape (2×2×3 mm) is evaluated by two methods: (1) samples exposed at 900 °C for 24 h in furnace with used air atmosphere; (2) samples following thermogravimetric analysis (TGA, Q50 instrument) for a dwelling time of 1 h at three different temperatures (750 °C, 800°C and 850 °C) with a flow of synthetic air of 10 ml/min. Two heating rates (5 and 20 °C/min) are used to calculate the activation energy. In order to ensure the consistence of the results, all these experiments are repeated 2 times. Prior to the oxidation tests, samples are well polished and cleaned in propanol for 10 min followed by drying in furnace at 110 °C for 30 min.

The analyses of the microstructure, the phase constitution and the kinetics of formation of the oxide scale are the main aspects collected in the investigation of oxidation in this

work. The microstructural images and phases of the oxide layers are characterised by SEM and XRD techniques. The kinetic analyses are performed in terms of plotting the curves of mass gain per area or the thickness of the oxide scales vs. oxidation temperature. The apparent activation energy (E_a) is calculated by an isoconversional method based on the following equation [23] [24]:

$$\frac{d_\alpha}{d_t} = A \exp\left(\frac{-E_\alpha}{RT}\right) f(\alpha) \tag{3-11}$$

where α is the relative mass gain per unit area, A is the Arrhenius factor, E_α is the activation energy, R the gas constant (8.31 J/mol·K) and T the absolute temperature. Figure 3.8 shows the isoconversional method for determining E_α from the curve of α vs time calculated from two different heating rates and at two temperatures, T_1 and T_2. Then, E_α can be calculated by the equation 3-12, which is transformed from the equation 3-11:

$$E_a = \frac{R ln\left\{\frac{\left(d_a/d_t\right)_1}{\left(d_a/d_t\right)_2}\right\}}{\left(\frac{1}{T_1} - \frac{1}{T_2}\right)} \tag{3-12}$$

where d_α/d_t is a constant during the heating process and T_1 and T_2 are the corresponding temperatures to obtain the same mass gain per area α under a heating rate of 20 and 5 °C/min, respectively.

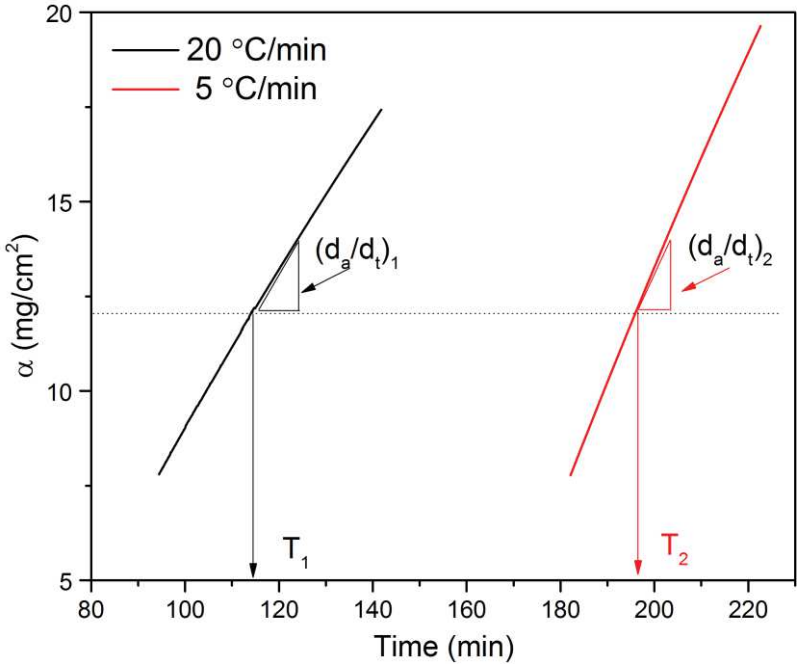

Figure 3.8. Isoconversional method for determining E_α value from the experimental function of mass gain per unit area α vs. time for Cr-based WC hardmetals under heating rates of 5 and 20 °C/min.

3.9 Wear resistance

Wear resistance is one of the most important mechanical properties for the application of hardmetals in the cutting market. Laboratory investigations of the wear resistance in this work are carried out using two different equipments with different specimen sizes: samples with 6×5×4 mm for wear tests in a Bruker-UMT-Tribolab trybometer located in University Carlos III of Madrid, and samples with 20×6.5×6 mm for the wear tests developed in a Wazau-TRM 2000-Tribometer located in Sandvik (Barcelona, Spain). These tribometers are shown in Figure 3.9. Both wear measurements on Cr-based WC hardmetals are characterised by dry sliding tests on a ball-on-plate tribometer using reciprocating lineal movement. Prior to the tribological test, samples are polished and cleaned in distilled water for 10 min followed by drying in furnace at 110 °C for 30 min.

An alumina ball of 5 mm diameter (1500-1650 HV supplied by Goodfellow) is used as a static counter material in the Bruker tribometer. The samples are moving against the alumina ball reciprocally. The tests are performed in ambient air (20 ± 2 °C, humidity 55%), under 18 N load, at a frequency of 5 Hz, and the stroke length of 5 mm for 30 min. All tests are repeated 3 times in order to have repeatability in terms of the friction coefficient (μ). The total sliding distance is fixed to 90000 mm.

A WC-6wt.% Co ball of 10 mm diameter (1950-2000 HV supplied by Fritsch) is used as a static counter material in the Wazau tribometer. These tests are performed in ambient air under 50 N load, at a frequency of 2.5 Hz, and a stroke length of 10 mm for 60 min in ambient air (20 ± 2 °C, humidity 55%). The total sliding distance is fixed to 100000 mm.

Figure 3.9. Image of sliding wear test equipments: (a) Bruker-UMT-Tribolab and (b) Wazau-TRM 2000-Tribometer.

A profilometer (Olympus DSX500, Opto-digital microscope) is used to obtain the 3D image of the wear track after sliding and to measure the value of the width and depth. The sliding test is based on a ball-on-plate configuration and the reciprocating plate adapter generates a harmonic wave, which is commonly used in the wear resistance testing [25], [26]. The volume loss values are determined by the wear track model represented in Figure 3.10. After sliding, three 2D profiles are obtained from the center of the track (b line) and 1.5 mm on each side of the center (a and c line) using the profilometer. Then, the average depth value is calculated by the following equation:

$$\overline{D} = \frac{\overline{A_w}}{\overline{W}} \tag{3-13}$$

where $\overline{D}$ is the average depth in mm, $\overline{A_w}$ is the average wear loss area of three 2D profiles for each wear track, and $\overline{W}$ is the average width of each wear track measured for three 2D profile. Thus, the wear loss volume is calculated with the following formula:

$$\Delta V = \left[\frac{1}{3} \times \pi \times \overline{D^2}(3R - \overline{D})\right] + \overline{A_w} \times l \tag{3-14}$$

where ΔV is the volume loss for wear sliding in mm^3, R is the radius of the sliding ball, and l is the sliding stroke. The wear rate is determined by the following formula:

$$W_v = \frac{\Delta v}{S} \tag{3-15}$$

where W_v is the wear rate in mm^3/mm, ΔV is the volume loss of the sample in mm^3, and S is the total sliding distance.

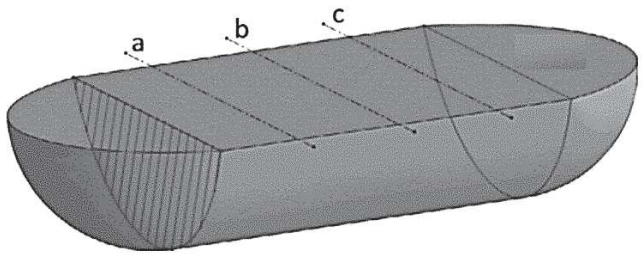

Figure 3.10. The estimated model for calculating the wear loss volume. Lines a, b, and c are indicating the three 2D profile lines [25].

3.10 References

[1] P.K. Mehrotra, *Powder processing and green shaping*, vol. 1. Elsevier Ltd, 2014.

[2] R.M. German, P. Suri, and S. Jinpark, "Review: liquid phase sintering," *J Mater Sci*, vol. 44, pp. 1–39, 2009.

[3] C.M. Fernandes and A.M.R. Senos, "Cemented carbide phase diagrams: A review," *Int. J. Refract. Met. Hard Mater.*, vol. 29, no. 4, pp. 405–418, 2011.

[4] R. M. German, "Consolidation techniques," in *Comprehensive Hard Materials*, vol. 1, Elsevier Ltd, pp. 237–263, 2014.

[5] A. Koutsospyros, W. Braida, C. Christodoulatos, D. Dermatas, and N. Strigul, "A review of tungsten: from environmental obscurity to scrutiny," *J. Hazard. Mater.*, vol. 136, no. 1, pp. 1–19, 2006.

[6] M.N. Rahaman, *Ceramic processing and sintering. 2nd edition*. Boca Raton: CRC press, 2003.

[7] P. Angerer, L.G. Yu, K.A. Khor, G. Korb, and I. Zalite, "Spark-plasma-sintering (SPS) of nanostructured titanium carbonitride powders," *J. Eur. Ceram. Soc.*, vol. 25, no. 11, pp. 1919–1927, 2005.

[8] J. Langer, D. V Quach, J. R. Groza, and O. Guillon, "A comparison between FAST and SPS apparatuses based on the sintering of oxide ceramics," *Int. J. Appl. Ceram. Technol.*, vol. 8, no. 6, pp. 1459–1467, 2011.

[9] U. Anselmi-Tamburini, S. Gennari, J. E. Garay, and Z. A. Munir, "Fundamental investigations on the spark plasma sintering/synthesis process: II. Modeling of current and temperature distributions," *Mater. Sci. Eng. A*, vol. 394, no. 1–2, pp. 139–148, 2005.

[10] G. Olivier, G.J. Jesus, D. Benjamin, K. Tobias, S. Gabi, and M. Herrmann, "Field-assisted sintering technology/spark plasma sintering: Mechanisms, materials, and technology developments," *Adv. Eng. Mater.*, vol. 16, no. 7, pp. 830–849, 2014.

[11] A. García-Junceda, L. Acebo, and J.M. Torralba, "Study and suppression of the microstructural anisotropy generated during the consolidation of a carbonyl iron powder by field-assisted hot pressing," *Metall. Mater. Trans. A*, vol. 46, no. 7, pp. 3192–3198, 2015.

[12] W.H. Bragg and W.L. Bragg, "The reflection of X-rays by crystals," *Proc. R. Soc. Lond. A*, vol. 88, no. 605, pp. 428–438, 1913.

[13] U. Holzwarth and N. Gibson, "The Scherrer equation versus the 'Debye-Scherrer equation,'" *Nat. Nanotechnol.*, vol. 6, no. 9, pp. 534–534, 2011.

[14] E. Satyanarayana, A. Flavia, C. Ramos, L.L. Shaw, and Z. Chen, "Investigation of microstructure and mechanical properties at low and high temperatures of WC-6 wt.% Co," *Int. J. Refract. Met. Hard Mater.*, vol. 58, pp. 172–181, 2016.

[15] J.I. Goldstein, D.E. Newbury, J.R. Michael, N.W.M. Ritchie, J.H.J. Scott, and D. C. Joy, *Scanning electron microscopy and X-ray microanalysis. Fourth edition*. New York: Springer, 2017.

[16] H. Engqvist and B. Uhrenius, "Determination of the average grain size of cemented carbides," *Int. J. Refract. Metals Hard Mater.*, vol. 21, pp. 31–35, 2003.

[17] "Hardmetals-Palmqvist toughness test. BS ISO 28079:2009."

[18] S. Sheikh, R.M. Saoubi, P. Flasar, M. Schwind, T. Persson, and L. Llanes, "Fracture toughness of cemented carbides: Testing method and microstructural effects," *Int. J. Refract. Met. Hard Mater.*, vol. 49, no. 1, pp. 153–160, 2015.

[19] M.L. Oyen and R.F. Cook, "A practical guide for analysis of nanoindentation data," *J. Mech. Behav. Biomed. Mater.*, vol. 2, no. 4, pp. 396–407, 2009.

[20] R.W. Armstrong, "The hardness and strength properties of WC-Co composites," *Materials (Basel).*, vol. 4, no. 7, pp. 1287–1308, 2011.

[21] W.C. Oliver and G.M. Pharr, "Measurement of hardness and elastic modulus by instrumented indentation: advances in understanding and refinements to methodology," *J. Mater. Res.*, vol. 19, no. 1, pp. 3–20, 2004.

[22] J.J. Roa, E. Jimenez-Pique, C, Verge, J.M. Tarragó, A. Mateo, J. Fair, and L. Llanes, "Intrinsic hardness of constitutive phases in WC-Co composites : Nanoindentation testing, statistical analysis, WC crystal orientation effects and flow stress for the constrained metallic binder," *J. Eur. Ceram. Soc.*, vol. 35, no. 13, pp. 3419–3425, 2015.

[23] M. Aristizabal, J.M. Sanchez, N. Rodriguez, F. Ibarreta, and R. Martinez, "Comparison of the oxidation behaviour of WC-Co and WC-Ni-Co-Cr cemented carbides," *Corros. Sci.*, vol. 53, no. 9, pp. 2754–2760, 2011.

[24] V.B. Voitovich, V.V. Sverdel, R.F. Voitovich, E.I. Golovko, and I.N. Frantsevich, "Oxidation of WC-Co, WC-Ni and WC-Co-Ni hard metals in the temperature range 500 ~ 800 °C," *Int. J. Refract. Met. Hard Mater.*, vol. 14, no. 4, pp. 289–295, 1996.

[25] Z. Doni, A.C. Alves, F. Toptan, J.R. Gomes, A. Ramalho, and M. Buciumeanu, "Dry sliding and tribocorrosion behaviour of hot pressed CoCrMo biomedical alloy as compared with the cast CoCrMo and Ti_6Al_4V alloys," *Mater. Des.*, vol. 52, pp. 47–57, 2013.

[26] K. Bonny, P. De Baets, Y. Perez, J. Vleugels, and B. Lauwers, "Friction and wear characteristics of WC-Co cemented carbides in dry reciprocating sliding contact," *Wear*, vol. 268, no. 11–12, pp. 1504–1517, 2010.

Chapter 4

Thermodynamic simulation

Contents

4.1 Thermodynamic simulation studies

Thermodynamic modelling is a powerful tool in the development of new materials. In this investigation, Thermo-Calc with database TCFE7 is applied to calculate the phases formation in Cr-based WC hardmetals, in order to optimise the compositional design. The approach to model the quaternary W-C-Cr-Fe system is firstly made to define the elements and phases to be included in the lower order W-C-Cr system, and secondly to simulate the effect of Fe/C addition on the phase diagrams of W-C-Cr-Fe system. Thus, the simulation results obtained for the Cr-based WC hardmetals are used as a help to explain the experimental observations found concerning the phases formed in the Cr-based WC hardmetals developed in this work.

4.2 Phase diagram of W-C-Cr system

The W-C-Cr system is the starting alloy system for the development of the Cr-based WC hardmetals processed in the current investigation. A complete thermodynamic analysis of the W-C-Cr system is necessary. For the realisation of this study, the accurate composition of the W-C-Cr system is fixed to: 78.1 wt.% of W, 5.1 wt.% of C, and 16.8 wt.% of Cr, which corresponds to 70 vol.% of WC in the Cr-based WC hardmetals designed in this work. The isothermal phase diagram and the vertical section for a W-C-Cr system with 16.8 wt.% of Cr are calculated by Thermo-Calc coupled with database TCFE 7. These diagrams can be seen in Figure 4.1. Thus, Figure 4.1(a) shows the isothermal phase diagram of the W-C-Cr system at 1450 °C, which is around 100 °C higher than the eutectic temperature in Cr-based WC hardmetals. This temperature is selected for the liquid phase sintering performed in this investigation. The diagram predicts the presence of two tungsten carbides: WC and W_2C, which have no chemical reaction with the Cr-based binder (α). Kurlov and Gusev [1] studied the phase-equilibrium for WC and W_2C tungsten carbides in the W-C phase diagram. They found that WC was stable from room temperature to high temperature and W_2C appeared in a temperature range from 1250 °C to 2750 °C. Mühlbauer *et al.* [2] reported that both WC (P-6m2) and W_2C (P-31m) carbides had a hexagonal structure with the same tungsten sublattice, but a different stacking sequence of W. These authors proposed that the formation of ditungsten carbide (W_2C) was due to the insufficient C content, and the transition of W_2C into WC happened during the carburisation of W_2C powders. Three types of chromium carbides Cr_3C_2, Cr_7C_3, and $Cr_{23}C_6$ occur with the increase of Cr content in the isothermal phase diagram, which agrees with the formation of the same

chromium carbides in the W-C-Cr phase diagram reported by Stecher *et al*. [3] and Rudy *et al.* [4]. Figure 4.1(b) demonstrated that there is a limited solubility of Cr in W_2C lattice as marked in the blue area, leading to the existence of W_2C below 1250 °C due to the increased stability of W_2C. Brieseck *et al.* [5] studied the diffusion and solubility of Cr in WC. Brieseck reported that $(W,Cr)_2C$ phase was formed at the interphase of Cr_3C_2-WC diffusion couple during the annealing at 1550 °C for 3 h. The red line in Figure 4.1(b) indicates the solidus phase line (above 1850 °C) in W-C-Cr system, which is much higher than 1300-1350 °C in W-C-Co system, since pure Cr alloy has an obvious higher melting point (1920 °C) than Co (1490 °C) [6].

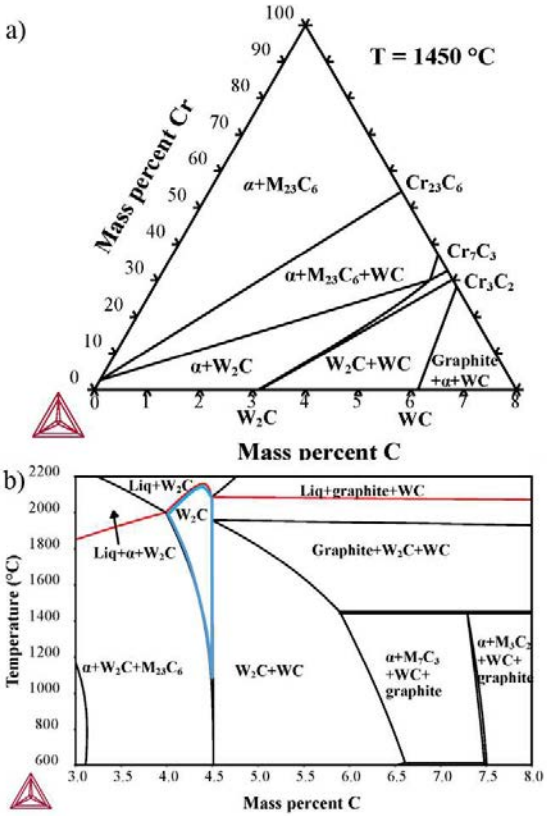

Figure 4.1. (a) Isothermal phase diagram of W-C-Cr system at 1450 °C, and (b) vertical section of W-C-Cr phase diagram with 16.8 wt.% Cr calculated by Thermo-Calc coupled with TCFE7 database. The red line represents solidus phase line.

4.3 Effect of the Fe content on the phase formation of W-C-Cr-Fe system

Based on the compositional design of the previous W-C-Cr ternary system, the binary phase diagram of the quaternary W-C-Cr-Fe system in function of C content is stablished for the following composition: 78.1 wt.% of W, 5.1 wt.% of C, 12 wt.% of Cr and 4.8 wt.% of Fe, where Fe comes from the iron content in the CrFe alloy used in this research work. The Fe content in the W-C-Cr-Fe system is modified by different extra Fe additions (1 wt.%, 3 wt.% and 5 wt.%). The addition of an extra content of Fe to the system is based

on the objectives of increasing the densification reached during LPS, and favouring the sinterability during SPS due to the large specific surface area exhibited by the carbonyl iron powders. Table 4.1 shows the weight percent of Fe, Cr, W, and C contents in the W-C-Cr-Fe system with extra Fe contents, which correspond to the designed compositions.

Table 4.1. Weight percent of Fe, Cr, W and C contents in the W-C-Cr-Fe system with different extra Fe contents (1 wt.%, 3 wt.% and 5 wt.%).

Fe (wt.%)		Total Fe (wt.%)	Cr (wt.%)	W (wt.%)	C (wt.%)
Extra Fe (addition)	Fe (CrFe powders)				
0	4.8	4.8	12.0	78.1	5.1
1	4.5	5.5	11.3	78.1	5.1
3	3.8	6.8	10.0	78.1	5.1
5	3.4	8.4	8.4	78.1	5.1

Figure 4.2 presents the corresponding equilibrium phase diagrams of W-C-Cr-Fe systems without extra Fe additions and with different extra Fe additions (1 wt.%, 3 wt.%, and 5 wt.%). The dashed vertical lines represent the equilibrium phase formation during the cooling process, in which the C content is set at 5.1 wt.%. The red line represents solidus line in W-C-Cr-Fe systems.

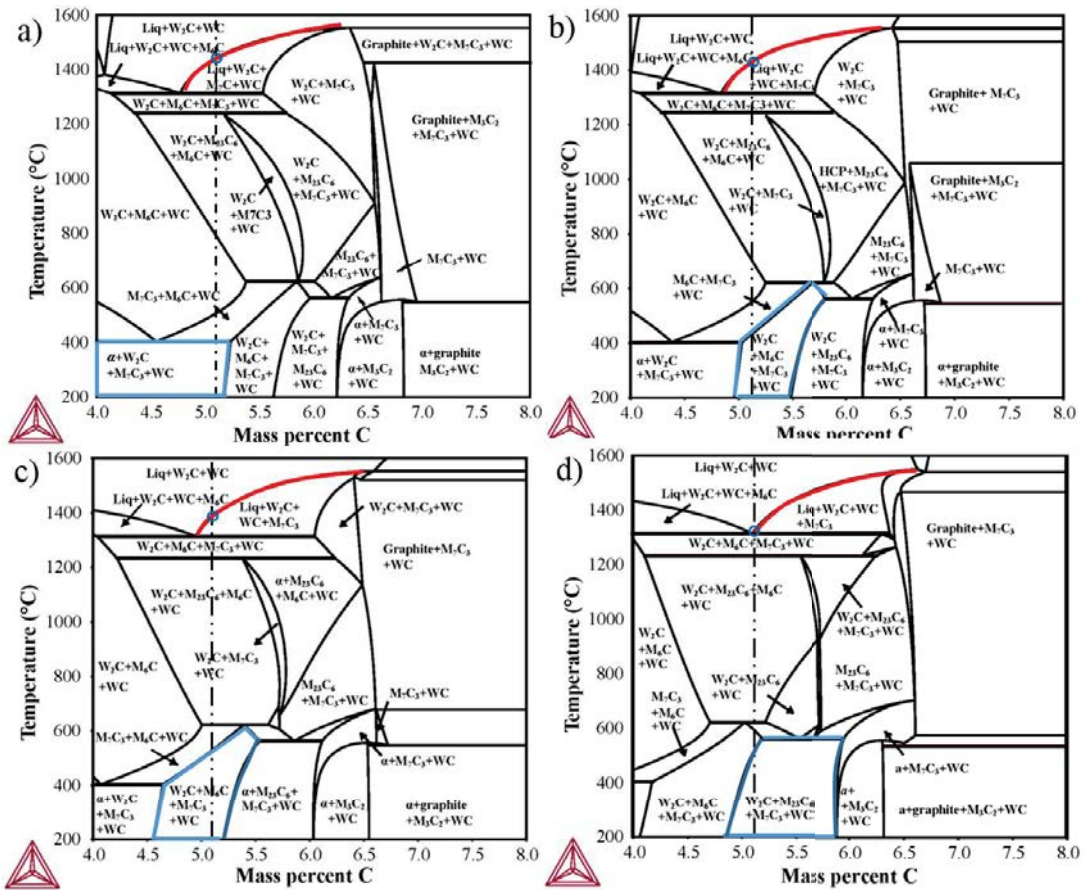

Figure 4.2. Vertical section of W-C-Cr-Fe phase diagrams with different extra Fe addition: (a) 0 wt.% Fe, (b) 1 wt.% Fe, (c) 3 wt.% Fe, and (d) 5 wt.% Fe. The dashed vertical line means the fixed C content (5.1 wt.%) and the blue circle represents the corresponding melting point. The red line represents solidus line.

Table 4.2 lists the final phases formed after cooling (marked by the blue region) in W-C-Cr-Fe systems with different Fe contents, when the phase formation becomes stable. The Cr-based matrix is designed as *a* and it is capable of dissolving some iron content. M_6C is a tungsten-iron-rich carbide corresponding to the complex FCC carbide with the composition Fe_3W_3C, which is able to dissolve some Cr. M_7C_3 and $M_{23}C_6$ are two chromium carbides, which are capable of dissolving both Fe and W.

Table 4.2. Final phase formation in W-C-Cr-Fe systems as a function of extra Fe contents from the calculated phase diagrams. "×" means the existence of the corresponding phase.

Extra Fe content (wt.%)	*a*	M_6C	WC	M_7C_3	W_2C	$M_{23}C_6$
0	×		×	×	×	
1		×	×	×	×	
3		×	×	×	×	
5			×	×	×	×

From these phase diagrams and the corresponding phase formation, it can be deduced that:

1) The temperature of the solidus line marked by the blue circle decreases slightly when the Fe content increases, as it is expected since Fe has a lower melting point than Cr. Thus, the melting point of Cr-based WC hardmetals decreases with the increase of the Fe content. This fact implies that the amount of liquid phase is higher at the same sintering temperature when increasing the Fe content, leading to a higher content of liquid phase to flow in the narrow spaces between particles and enhancing the sintering performance. Fernandes *et al*. [7] also reported that the addition of Fe in WC-CoNi hardmetals lowered the temperature of the melting point.
2) WC appears as a stable phase in all the regions of W-C-Cr-Fe systems due to its high stability and high melting point.
3) There is solubility of Cr in W_2C, and $(W,Cr)_2C$ is stable at room temperature.
4) At the selected sintering temperature of 1450 °C in LPS process, Cr-based WC hardmetals contain a limited amount of liquid and, in addition, W_2C and WC phases. Reducing the temperature below solidus line leads to the precipitation of M_7C_3 carbide. When the temperature decreases below the eutectic temperature, M_6C phase is also formed.
5) At the selected sintering temperatures from 1200 - 1350 °C in SPS process, Cr-based WC hardmetals remain in solid-state with W_2C, M_6C, M_7C_3 phases and WC,
6) With extra 1-3 wt.% Fe contents, the final formed phases *a*, WC, M_7C_3 and WC, and (marked in blue region) are transformed to M_6C, WC, M_7C_3 and W_2C, which means that the extra 1-3 wt.% Fe addition induces the formation of brittle M_6C carbide.

Goldschmidt also [8] reported that the content of M_6C carbide, in the C-Fe-W system, tended to increase when increasing Fe content. Gustafson [9] confirmed the formation of M_6C in the W-C-Cr-Fe system when increasing the Fe content. However, the formation of brittle M_6C should be inhibited or reduced since it will decrease the toughness of Cr-based WC hardmetals.

7) Figure 4.2(d) shows that extra 5 wt.% Fe content makes the original phase diagram to shift to lower C contents. Thus, when extra 5 wt.% Fe content is added, the final phases W_2C, WC, M_6C and M_7C_3 (marked in blue region) are changed to W_2C, WC, M_7C_3 and $M_{23}C_6$. Uhrenius *et al*. [10] studied the carbide/austenite equilibrium from 900 to 1100 °C in the quaternary C-Cr-Fe-W system. Their experimental results also showed that M_6C carbide was metastable in the ternary C-Fe-W system in this temperature range and that the increase of the Fe/Cr ratio destabilised the M_6C carbide in comparison with the $M_{23}C_6$ carbide.

4.4 Effect of the C content on the phase formation of W-C-Cr-Fe system

Based on the effect of Fe on the W-C-Cr-Fe system, the extra 3 wt.% Fe addition is selected due to the following reasons:

1) Although the addition of extra 5 wt.% Fe avoids the presence of M_6C carbide, it induces the formation of another more stable brittle carbide $M_{23}C_6$.
2) The addition of a higher content of Fe would decrease the total Cr content in the system. However, more Cr content in hardmetals helps to improve their wear resistance and oxidation resistance. Bonny *et al.* [11] reported the improvement of wear resistance due to the extra addition of Cr content. Marques *et al.* [12] demonstrated that the increase of Cr content in stainless steel (AISI 304) based binder is beneficial to enhance the oxidation resistance.
3) In order to develop Cr-based WC hardmetals, the binder should be a Cr-based alloy. The binder is not Cr-based alloy when extra 5wt.% Fe is added, since the weight percent of Cr and Fe reaches the same value (8.4 wt.%).

The previous studies show that the extra Fe content is beneficial for improving the sinteriablity of Cr-based WC hardmetals. On the other hand, the extra Fe content induces the formation of brittle M_6C carbide, which will decrease the mechanical properties of Cr-based WC hardmetals. Thus, different extra C contents (0.5 wt.%, 1 wt.% and 2 wt.%) are added to the W-C-Cr-Fe system with extra 3 wt.% Fe content, in order to inhibit or reduce the formation of M_6C phase. The corresponding compositions in the W-C-Cr-Fe

system with different extra C additions are shown in Table 4.3. The mass fraction of Cr-based binder is fixed at 16.8 wt.% and the C content varies from 5.10 to 6.96 wt.% due to the extra C contents.

Table 4.3. Weight percent of Fe, Cr, W and C content in the W-C-Cr-Fe system with different extra C additions (0.5 wt.%, 1 wt.% and 2 wt.%).

C (wt.%)		Fe (wt.%)	Cr (wt.%)	W (wt.%)	Total C (wt.%)
Extra C (addition)	C (WC powders)				
0	5.10	6.8	10.0	78.10	5.10
0.5	5.09	6.8	10.0	77.61	5.59
1	5.03	6.8	10.0	77.17	6.03
2	4.96	6.8	10.0	76.24	6.96

Figure 4.3 shows the vertical section of the W-C-Cr-Fe phase diagram (with extra 3 wt.% Fe content) for different extra C contents. The dashed vertical lines show the equilibrium phase formation of the W-C-Cr-Fe system with extra 0 wt.%, 0.5 wt.%, 1 wt.% and 2 wt.% content during the cooling process, in which the C contents are 5.10 wt.%, 5.59 wt.%, 6.03 wt.% and 6.96 wt.%, respectively. Table 4.4 lists the final formed phases after cooling in W-C-Cr-Fe systems with different C contents, when the phase formation becomes stable. M_3C_2 is a chromium carbide with an orthorhombic crystal structure, that is formed when extra 1 wt.% C is added [13]. Graphite with a hexagonal structure will be formed when extra 2 wt.% C is added [14].

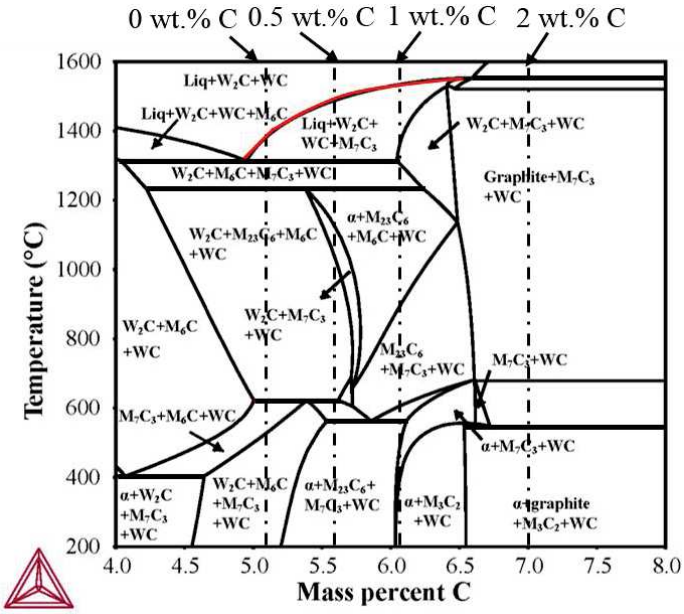

Figure 4.3. Vertical section of the optimised W-C-Cr-Fe phase diagram (extra 3 wt.% Fe content) with different extra C contents: 0 wt.%, 0.5 wt.%, 1 wt.% and 2 wt.% (indicated by the dashed lines). The red line represents solidus phase line.

Table 4.4. Final phase formation in W-C-Cr-Fe systems as a function of extra C contents from the calculated phase diagrams. "×" means the existence of the corresponding phase.

Extra C content (wt.%)	*a*	M_6C	WC	M_7C_3	W_2C	$M_{23}C_6$	M_3C_2	Graphite
0		×	×	×	×			
0.5			×	×	×	×		
1	×		×				×	
2	×		×				×	×

In order to know the properties of all these final phases, their composition, crystal structure, space group, hardness and melting point are summarised in Table 4.5.

Table 4.5. Composition, structure, space group, hardness, and melting point of the final phases formed in W-C-Cr-Fe systems.

Phase	Composition	Structure	Space group	Hardness (HV)	Melting point (°C)
WC	WC [15]	Hexagonal	P-6m2	Around 2600	2800
W_2C	W_2C [2]	Hexagonal	P-31m	2000	2200-2300
$M_{23}C_6$	$Fe_{21}W_2C_6$ [16]	Cubic	Fm-3m	1000	1250
M_6C	Fe_3W_3C [17]	Cubic	Fd-3m	1150	Around 1350
M7C3	Cr_7C_3 [18]	Orthorhombic	Pnma	1336	1665
M_3C_2	Cr_3C_2 [13]	Orthorhombic	Pnma	2280	1895
Graphite	C [14]	Hexagonal	P6mc	Very soft	Around 3900

From the phase diagram displayed in Figure 4.3, it can be concluded that:

1) The temperature of solidus phase line (marked in red line) increases when the C content increases due to the high melting point of graphite (3900 °C).
2) Extra C addition has an obvious effect on the phase formation. The incorporation of extra C contents inhibits the M_6C formation. Fernandes and Senos [7] demonstrated that the formation of M_6C carbide in the W-C-Co-Fe system can be reduced or inhibited by adding an excess C. Other experimental studies also have confirmed that adding extra C is an efficient way to reduce or prevent the formation of M_6C phase [19].
3) Moreover, the addition of carbon induces the transformation of W_2C to WC, since the WC structure is more stable than the W_2C structure at room temperature. Mühlbauer *et al*. [2] confirmed the transition of W_2C to WC by SEM and EBSD techniques during carburisation of tungsten metal powders. The transformation of W_2C to WC will improve the hardness, since WC has a higher level of hardness than W_2C [20]. Hence, the chromium carbide M_7C_3 tends to be transformed into M_3C_2 type due to the increase of the C content.
4) Extra 2 wt.% C addition induces the formation of graphite due to its high stability.

It should be highlighted that the Fe/C effect on the phase formation during SPS process will be much smaller than that in LPS process, since SPS is a solid-state sintering with

fast sintering and cooling rates, which leads to non-equilibrium states. Therefore, there is no time for the diffusion and for completing these phase transformations.

4.4 Summary

The equilibrium phase diagram of W-C-Cr-Fe system with 0 wt.% Fe addition shows that *a*, WC, M_7C_3, and W_2C phases are formed when the volume fraction of WC and Cr-based binder are fixed at 70% and 30%, respectively. Extra Fe addition (0-5 wt.%) decreases the melting point of the W-C-Cr-Fe system, which will improve the densification of Cr-based WC hardmetals sintered by LPS due to the increased amount of liquid phase at the same sintering temperature. However, extra 1 and 3 wt.% Fe additions induce the formation of brittle M_6C carbide and extra 5 wt.% Fe induces the formation of brittle $M_{23}C_6$ carbide. Both carbides are detrimental to the toughness of Cr-based WC hardmetals. In order to develop Cr-based WC hardmetals without losing oxidation resistance and wear resistance, the W-C-Cr-Fe system with extra 3 wt.% Fe content is selected as optimised system to study the possibility of enhancing their toughness by adding C content. Indeed, thermodynamic studies suggest that the addition of extra C contents inhibits the formation of M_6C carbide. Likewise, the addition of carbon induces the transformation of W_2C to WC, which is beneficial for improving the hardness of hardmetals due to the high hardness of WC, but will probably decrease the toughness. On the other hand, an extra 2 wt.% C content induces the formation of the soft graphite phase, which will decrease the hardness of hardmetals.

The calculated phase diagrams demonstrate which phases can be formed in our system and their composition at different temperatures, being very useful in the development and process design of hardmetals. Thus, they offer helpful information to guide the compositional design before experimental studies. However, the real sintering conditions could be a bit away from the modelling conditions in an equilibrium state, even during the LPS process with slow heating and cooling rates. Thus, the real effect of Fe and/or C additions on Cr-based WC hardmetals will be deeply studied in the subsequent experimental Chapters. Cr-based WC powders with the designed compositions are firstly prepared by a mechanical milling process (Chapter 5). Then, these developed Cr-based powders are sintered and consolidated by LPS (Chapter 6) and SPS (Chapter 7), respectively. The effect of Fe or Fe/C additions on microstructure, phase formation, and properties of Cr-based WC powders and hardmetals are determined by different analyses that are summarised along the following chapters containing experimental results.

4.5 References

[1] A.S. Kurlov and A.I. Gusev, "Tungsten carbides and W-C phase diagram," *Inorg. Mater.*, vol. 42, no. 2, pp. 121–127, 2006.

[2] G. Mühlbauer, G. Kremser, A. Bock, and J. Weidow, "Transition of W_2C to WC during carburization of tungsten metal powder," *Int. J. Refract. Metals Hard Mater.*, vol. 72, no. 2017, pp. 141–148, 2018.

[3] P. Stecher, F. Benesovsky, and H. Nowotny, "Untersuchungen im System Chrom–Wolfram–Kohlenstoff.," *Planseeber Pulvermetall*, vol. 12, pp. 89–95, 1964.

[4] E. Rudy and Y.A. Chang, "F. Benesovsky, Reute/Tirol," in *5th Plansee Seminar,* pp. 786–822, 1964.

[5] M. Brieseck, M. Bohn, and W. Lengauer, "Diffusion and solubility of Cr in WC," *J. Alloys Compd.*, vol. 489, no. 2, pp. 408–414, 2010.

[6] S. Haglund and J. Ågren, "W content in Co binder during sintering of WC–Co," *Acta Mater.*, vol. 46, no. 8, pp. 2801–2807, 1998.

[7] C. M. Fernandes and A.M.R. Senos, "Cemented carbide phase diagrams: A review," *Int. J. Refract. Met. Hard Mater.*, vol. 29, n. 4, pp. 405–418, 2011.

[8] H.J. Goldschmidt, "The structure of carbides in alloy steels," *J. Iron Steel Inst.*, vol. 170, no. 3, pp. 189–195, 1952.

[9] P. Gustafson, "A thermodynamic evaluation of the Fe-C-W system," *Scand. J. Metall.*, vol. 14, no. 5, pp. 259–267, 1985.

[10] B. Uhrenius, "An experimental and thermodynamic study of carbide/austenite equilibria in Fe-Cr-W-C alloys," *Met. Sci.*, vol. 14, no. 71, pp. 73–81, 1971.

[11] K. Bonny, P. De Baets, J. Vleugels, S. Huang, O. Van Der Biest, and B. Lauwers, "Impact of Cr_3C_2/VC addition on the dry sliding friction and wear response of WC-Co cemented carbides," vol. 267, pp. 1642–1652, 2009.

[12] B.J. Marques, C.M. Fernandes, and A.M.R. Senos, "Sintering, microstructure and properties of WC-AISI304 powder composites," *J. Alloys Compd.*, vol. 562, pp. 164–170, 2013.

[13] O.M. Cintho, E.A.P. Favilla, and J.D.T. Capocchi, "Mechanical–thermal synthesis of chromium carbides," *J. Alloys Compd.*, vol. 439, no. 12, pp. 189–195, 2007.

[14] H.O. Pierson, "Handbook of carbon, graphite, diamond and fullerenes. Properties, processing and applications, 1993," *NY William Andrew Publ.*

[15] A.Y. Liu, R.M. Wentzcovitch, and M.L. Cohen, "Structural and electronic properties of WC," *Phys. Rev. B*, vol. 38, no. 14, pp. 9483–9488, 1988.

[16] Y. Liu, Y. Jiang, J. Xing, R. Zhou, and J. Feng, "Mechanical properties and electronic structures of $M_{23}C_6$ (M= Fe, Cr, Mn)-type multicomponent carbides," *J. Alloys Compd.*, vol. 648, pp. 874–880, 2015.

[17] Y. Liu, Y. Jiang, R. Zhou, and J. Feng, "First-principles calculations of the mechanical and electronic properties of Fe-W-C ternary compounds," *Comput. Mater. Sci.*, vol. 82, pp. 26–32, 2014.

[18] D. Music, U. Kreissig, R. Mertens, and J. M. Schneider, "Electronic structure and mechanical properties of Cr_7C_3," *Phys. Lett. A*, vol. 326, no. 5–6, pp. 473–476, 2004.

[19] M. Tarraste, J. Kübarsepp, K. Juhani, T. Suurkivi, and J. Pirso, "Spark plasma sintering of WC hardmetals with Fe-based binder," in *European Congress and Exhibition on Powder Metallurgy. European PM Conference Proceedings*, 2016, pp. 1–6.

[20] G. Cios, P. Bała, M. Stępień, and K. Górecki, "Microstructure of cast Ni-Cr-Al-C alloy," *Arch. Metall. Mater.*, vol. 60, no. 1, pp. 145–148, 2015.

Chapter 5

Mechanical milling of Cr-based WC powders

Contents

5.1 Characterisation of the raw powders

The raw powders are fully characterised before the mechanical milling (MM) process. Figure 5.1 shows the microstructure of the WC and CrFe powders and their particle size distributions. The WC powder is fine, equiaxed and flat. The D_{50} value of WC powder is equal to 2 µm due to powders agglomeration. However, the real size of WC powder is smaller than 1 µm according to the SEM image. On the other hand, CrFe powder is individually distinguishable with an irregular shape (typical of mechanically milled powders), and D_{50} value approximates to 99 µm from the particle size distribution study.

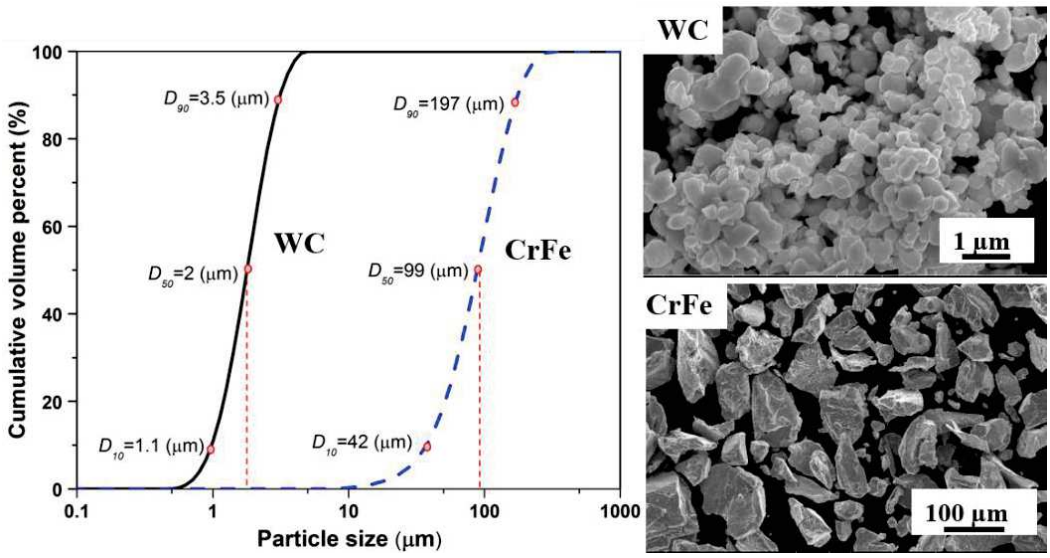

Figure 5.1. Particle size distributions of WC and CrFe powders and their corresponding morphologies obtained by SEM.

The Cr-Fe binary phase diagram is shown in Figure 5.2. The melting point of the CrFe alloy used for this investigation, and marked by the arrow, is close to 1800 °C, and there are no phase transformations of the CrFe alloy during heating up to the melting point, which explains the good stability of the binder phase during the milling process.

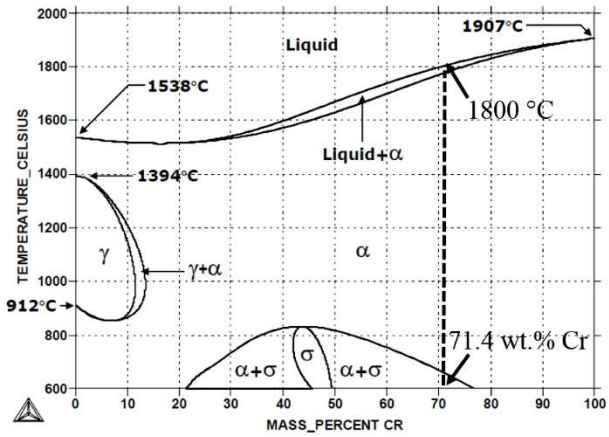

Figure 5.2. Cr-Fe phase diagram. The dotted line represents the composition of the CrFe alloy.

In order to adjust the previously designed Fe or Fe/C content in the milled Cr-based WC powders, different amounts of carbonyl iron powder (CIP) or CIP+graphite powders are added. The morphology and the particle size distribution of Fe and graphite powders are shown in Figure 5.3. The Fe powder is spherical and fine, presenting a high specific surface area. The D_{50} value of Fe powder (7.4 μm) is bigger than the size of the Fe powder (around 3 μm) measured on SEM images due to powders agglomeration. The content of C is adjusted by adding flake graphite powders (D_{50} = 15.5 μm).

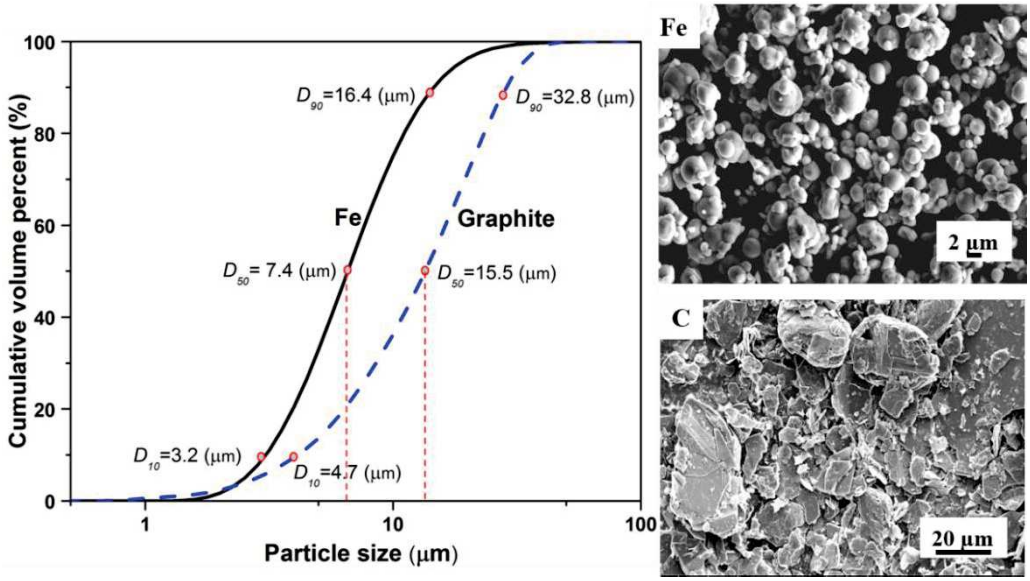

Figure 5.3. Particle size distribution of Fe (CIP) and graphite powders and their corresponding morphologies obtained by SEM.

5.2 Optimisation of mechanical milling parameters

Cr-based WC powders are prepared by mechanical milling (MM) from WC and CrFe powders. In order to achieve a suitable powder for the subsequent sintering, MM parameters are firstly optimised. The milling time plays a key role on determining the morphology, size, and crystallographic parameters of MM powders, thus influencing the final properties after sintering. Therefore, in order to analyse the evolution of the morphology and microstructure of the Cr-based hardmetal powders during milling process, powders of different milling times are fully characterised. Figure 5.4 shows the microstructural evolution of MM Cr-based powders, in which two phases are clearly distinguishable after 2 h of milling: large grey areas (Cr-based matrix) and small white areas (WC brittle particles) [1]. The size of Cr-based powders decreases with the increase of milling time since the tendency to fracture predominates over cold welding after 4 h of milling. After 4 h of milling, there are some laminar zones formed by the ductile Cr-based

matrix and the brittle WC fragments, since two phenomena occur at the same time: the welding of the deformed CrFe powders and the insertion of WC particles inside the ductile powders. After 6 h of milling, a high quantity of WC particles is embedded into the Cr-based binder. With increasing milling time, the number of WC particles embedded into Cr-based binder increases. WC particles are homogenously distributed in the Cr-based binder after 10 h of milling. After 20 h of milling, the Cr-based WC powders become much finer and with a more homogenous distribution of WC particles. This milling process follows to a brittle-ductile mechanism, and the microstructural evolution agrees with the results reported by Fogagnolo *et al.*[2]

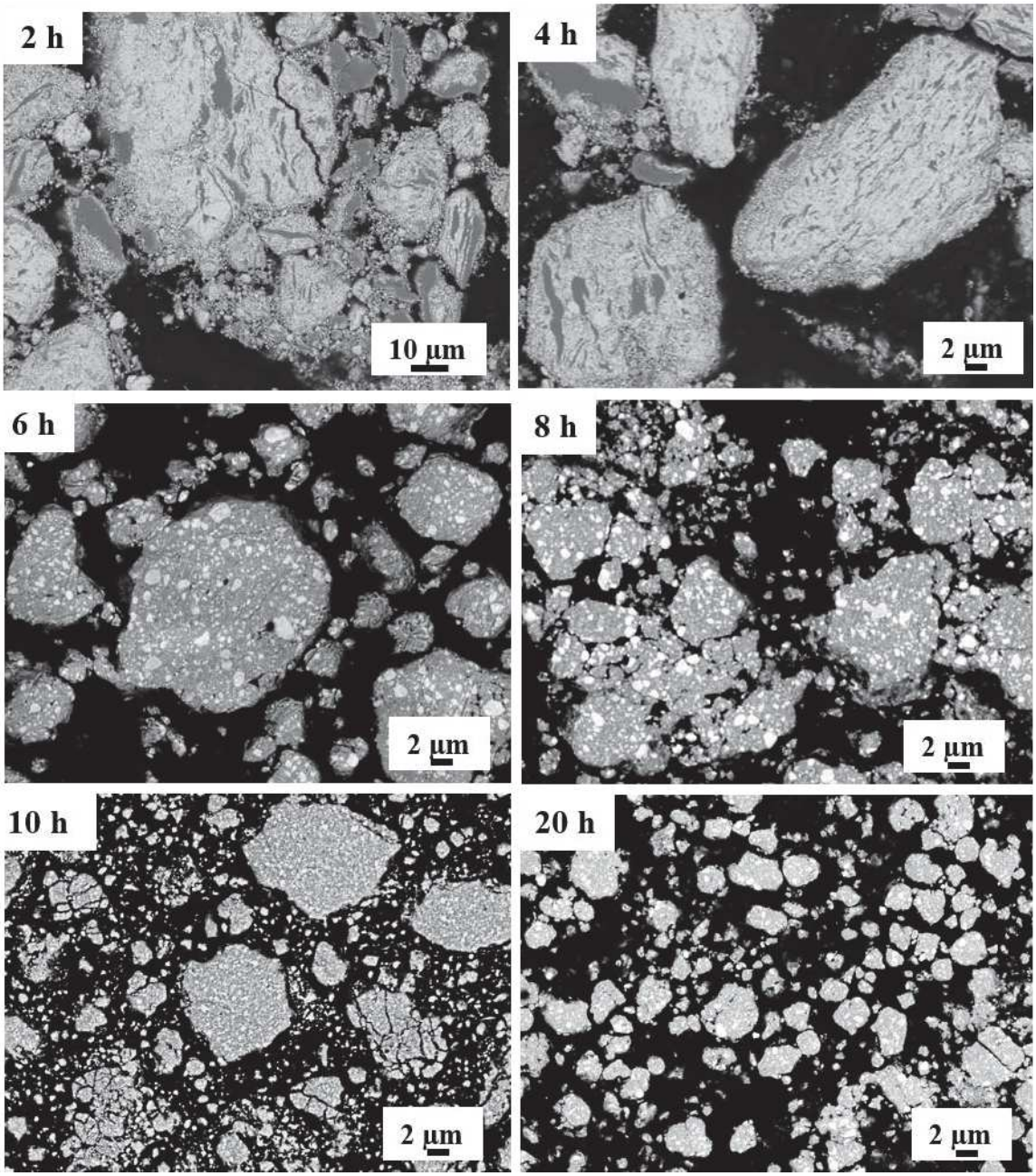

Figure 5.4. Microstructural evolution of Cr-based WC powders during mechanical milling.

Then, the particle size distribution and density of all the milled Cr-based WC powders are characterised by using the laser diffraction technique and a pycnometer, respectively. Figure 5.5 displays their particle size distribution after different milling times. The corresponding particle size values (D_{10}, D_{50}, and D_{90}) and densities are listed in Table 5.1. After 2 h of milling, a bimodal particle size distribution is observed due the distinguishable fine WC powders (the left peak) and big CrFe powders (the right peak) at the beginning of the milling. The particle size values (D_{90}) decrease with the increase of milling time, which agrees with the microstructural evolution of the Cr-based WC powders since the tendency to fracture is stronger than that for cold welding. After 20 h of milling, the curve of the particle size distribution becomes narrower and shifts to smaller particle sizes. Furthermore, after 20 h of milling time the obtained D_{10}, D_{50}, and D_{90} values are also the smallest. The MM process involves repeated cold welding, fragmentation, and dynamic recrystallisation. Longer milling time (20 h of milling) may help to obtain a homogenous dispersion of the constituents within the particles. The theoretical density of Cr-based powders is calculated to be 13.94 g/cm^3, based on the equation 3-4, when the volume percentage of WC is 70 %. The density measured after 20 h of milling is 13.80 g/cm^3, which is in good agreement with the theoretical value.

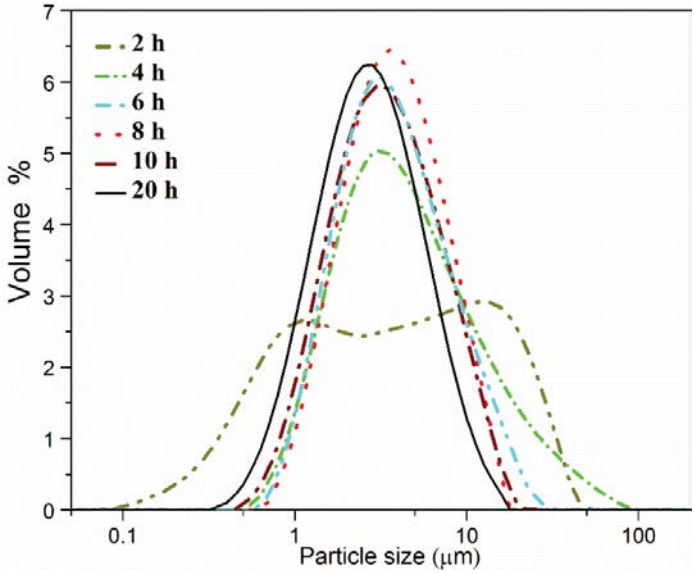

Figure 5.5. The particle size distribution of Cr-based WC powders after different milling times.

Table 5.1. D_{10}, D_{50} and D_{90} values and densities of Cr-based WC powders after different milling times.

Powders	D_{10} (μm)	D_{50} (μm)	D_{90} (μm)	Density (g/cm^3)
2h	0.60	3.88	20.70	13.60 (±0.16)
4h	1.55	4.33	17.89	13.65 (±0.14)
6h	1.66	3.91	9.36	13.71 (±0.11)
8h	1.40	3.81	9.18	13.79 (±0.10)
10h	1.57	3.27	9.06	13.81 (±0.08)
20h	1.15	2.71	6.23	13.80 (±0.08)

In addition, a crystallographic study by XRD is performed in order to further help in the selection of the optimum milling time. Figure 5.6 shows the X-ray diffraction spectra of Cr-based WC powders during the milling process. The term "Raw powders" means a mixture of WC (70 vol.%) and CrFe powders (30 vol.%) without milling. Only WC, Cr and Fe phases are detected in all the MM powders and all the spectra exhibit the same peaks with similar intensities, corresponding to these three phases. The peaks of Cr and Fe get broader with the increase of the milling time due to the reduction of the crystallite size, as explained below.

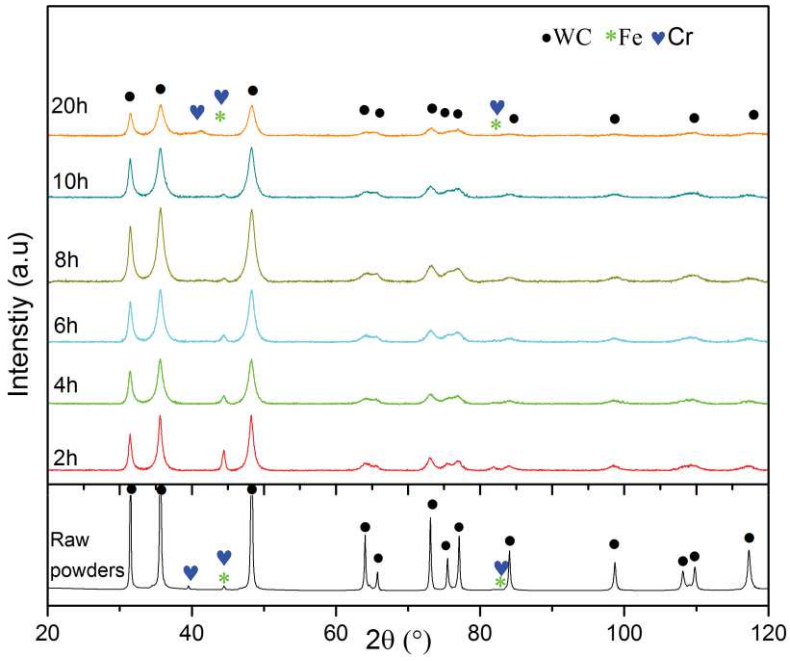

Figure 5.6. XRD spectra showing the crystallographic evolution of Cr-based hardmetal powders with milling time.

The crystallite size and the internal lattice strain are determined from these XRD patterns, considering that the milling process induces structural changes in the hexagonal WC lattice. The crystallite size (D) and the internal microstrain ($\mu\mathcal{E}$) values listed in Table 5.2 are determined from the Scherrer equation, as discussed in section 3.4.1. B is the width at half maximum of the most intense peak of WC in the diffraction pattern (value of B in radians) and θ is the Bragg angle. Figure 5.7 shows the evolution of D and $\mu\mathcal{E}$ with the increase of the milling time. The D decreases and $\mu\mathcal{E}$ increases when increasing the milling time, especially in the first 4 h of milling due to the generation of a high density of dislocations. The refinement of the crystallite size reaches a slower rate after 8 h of milling, indicating that a further refinement becomes difficult for this system. This limit in the crystallite size is dependent on the melting temperature and the activation energy for self-diffusion of the material: the higher the melting temperature and/or activation

energy the hardmetal has the lower the normalised minimum grain size [3]. Typically, the grain size of WC in Co-based WC powders can be as fine as 10-20 nm after milling for over 100 h [4]. The minimum WC grain size of Cr-based WC powders achieved after 20 h of milling approaches 7.6 nm, which is lower than that of Co-based WC hardmetals due to the higher melting point of Cr-based binder.

Table 5.2. Crystallite size (D) and internal microstrain ($\mu\mathcal{E}$) of MM Cr-based WC powders depending on milling time (the selected peak corresponding to WC phase). B (value in radian) is the width at half maximum peak and θ is the Bragg angle.

Milling time	2θ (°)	B (°)	D (nm)	$\mu\mathcal{E}$ (%)
2 h	48.283	0.785	11.093	0.764
4 h	48.285	0.969	8.986	0.942
6 h	48.315	1.005	8.665	0.977
8 h	48.304	1.056	8.246	1.026
10 h	48.300	1.068	8.156	1.056
20 h	48.302	1.154	7.610	1.113

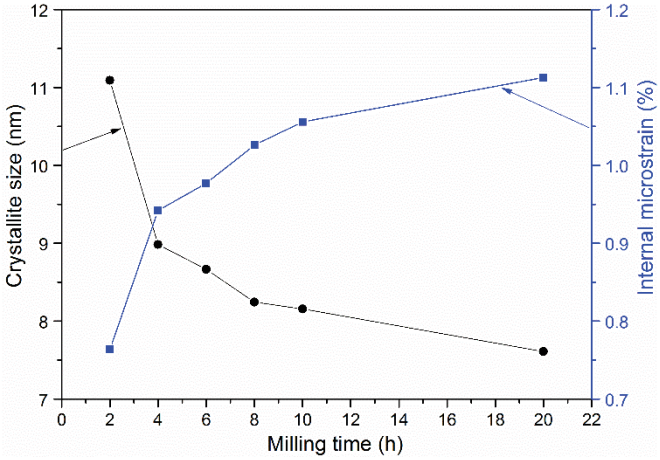

Figure 5.7. Evolution of mean crystallite size (D) and internal microstrain ($\mu\mathcal{E}$) with milling time.

On the other hand, the MM process increases the lattice distortions because of the incorporation of Cr and Fe to the hexagonal WC lattice, generating an increase of the lattice microstrain from 0.764 to 1.113 pct. The steady state, attained in the lattice strain after 20 hours of milling, is due to the balance achieved between the rate of cold welding and the rate of fracturing of the particles being milled, whereas the plastic deformation plays a negligible influence [5]. The small crystallite size and high internal microstrain achieved after 20 h of milling are beneficial parameters for obtaining a nanostructured system, since sintering is a thermally activated process, in which the crystal growth begins when the internal strain decreases under a certain value that will depend on the material [6]. In the case of the present study, the values obtained for the crystallite size and strain are in full accordance with the values reported by Mohamed and Xun [3] for different equivalent metallic systems.

Thus, the analysis of the evolution of microstructure, particle size distribution and crystallographic parameters confirm that 20 h of milling is an adequate time to obtain Cr-based WC powders with homogenous microstructure and good crystallite size and microstrain values for the subsequent sintering step.

5.3 Effect of different Fe or Fe/C additions on Cr-based WC powders

Figure 5.8 shows the particle size distribution of Cr-based WC powders with different extra Fe or Fe/C additions after 20 h of milling. The corresponding particle size values (D_{10}, D_{50}, and D_{90}) are listed in Table 5.3. All the examined Cr-based WC powders have a narrow particle size distribution with a symmetric log-normal shape, since the milling process has almost reached a steady state after 20 h of milling, even when extra Fe or Fe/C contents are added. Table 5.3 shows that the particle size values of Cr-based WC powders increase slightly with the increase of the Fe content, since these added soft and fine Fe particles tend to be welded together with hard particles and form larger particles. Nevertheless, with the increase of the C content, no remarkable differences in the particle size of Cr-based WC powders are noticed.

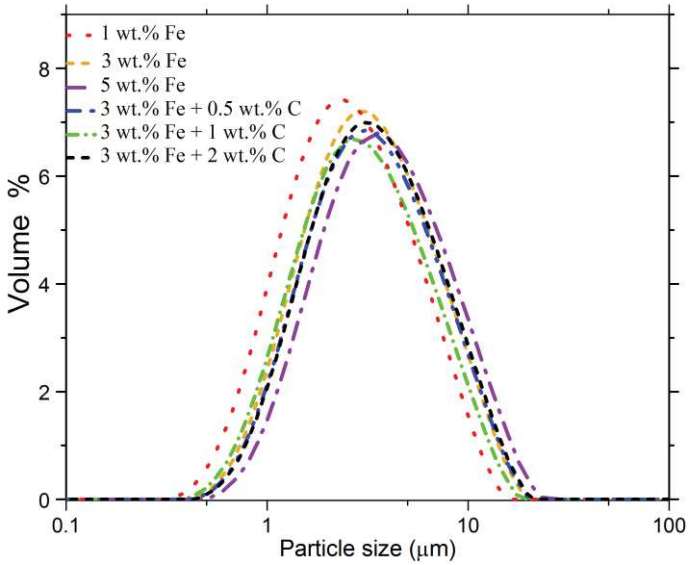

Figure 5.8. Particle size distribution of Cr-based WC powders with different extra Fe or Fe/C additions after 20 h of milling.

Table 5.3. D_{10}, D_{50} and D_{90} values and densities of Cr-based WC powders with different extra Fe or Fe/C additions after 20 h of milling.

Cr-based WC powders with extra Fe or Fe/C additions	D_{10} (μm)	D_{50} (μm)	D_{90} (μm)	Density (g/cm^3)
1 wt.% Fe	1.20	2.81	6.54	13.78 (±0.05)
3 wt.% Fe	1.30	3.34	6.89	13.74 (±0.01)
5 wt.% Fe	1.56	3.94	7.36	13.70 (±0.08)
3 wt.% Fe + 0.5 wt.% C	1.26	3.04	6.68	13.70 (±0.07)
3 wt.% Fe + 1 wt.% C	1.30	3.17	6.72	13.68 (±0.05)
3 wt.% Fe + 2 wt.% C	1.31	3.18	6.73	13.68 (±0.04)

Figure 5.9 shows the X-ray diffraction spectra of Cr-based WC powder with different extra Fe or Fe/C additions after 20 h of milling. All peaks also correspond to WC, Cr and Fe, which confirms the existence of a Cr-based phase and a WC hard phase. Two reasons contribute to explain the non-existence of other new peaks after extra additions of Fe or Fe/C: (i) there is no reaction between CrFe binder, WC, carbonyl Fe and C powders during the milling process; (ii) if small amounts of a new phase were formed, they would not be detected by XRD technique due to its accuracy of at least 1 wt.%. The peak close to 44.5° (corresponding to an Fe diffraction) increases significantly when adding 5 wt.% of extra Fe content.

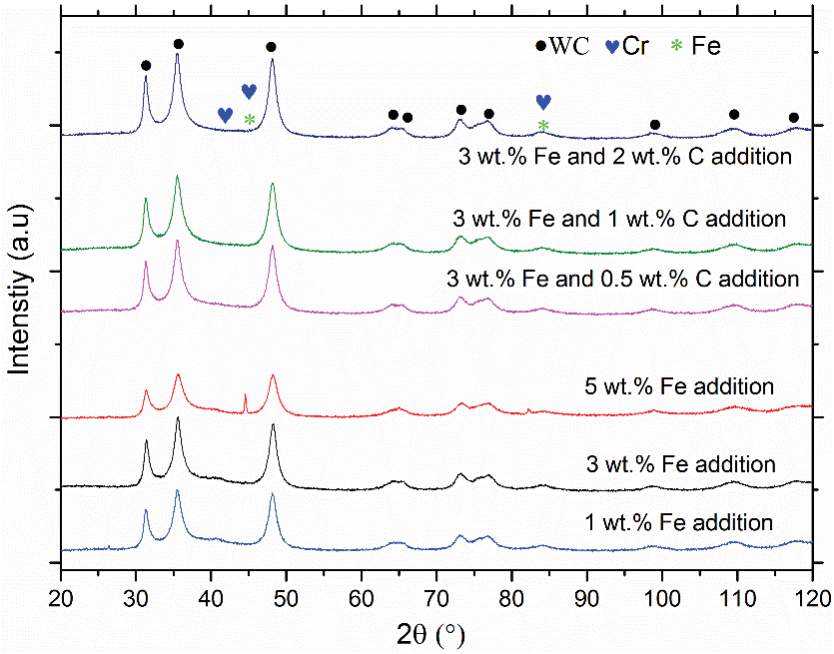

Figure 5.9. XRD spectra of Cr-based WC powders with different Fe or Fe/C additions after 20 h of milling.

Figure 5.10 shows the microstructure and morphology of Cr-based WC powders with different extra Fe additions after 20 h milling. Two main phases can be observed in all these fine and round Cr-based WC powders: a grey metallic Cr-based matrix and a white phase corresponding to WC. The BSE images taking in the cross-section of the particles clearly prove that the WC hard particles are homogenously distributed in the Cr-based binder. The particle size increases with the increase of the extra Fe content, which is consistent with the measured particle size data listed in Table 5.3. Fogagnolo *et al*. [7] reported that ductile materials improved the particle welding process in contact with hard particles. Thus, the extra soft Fe powder may improve the cold welding. Thus, this soft powder is trapped or banded with other particles under the force of colliding balls, leading to a slight increase in the particle size.

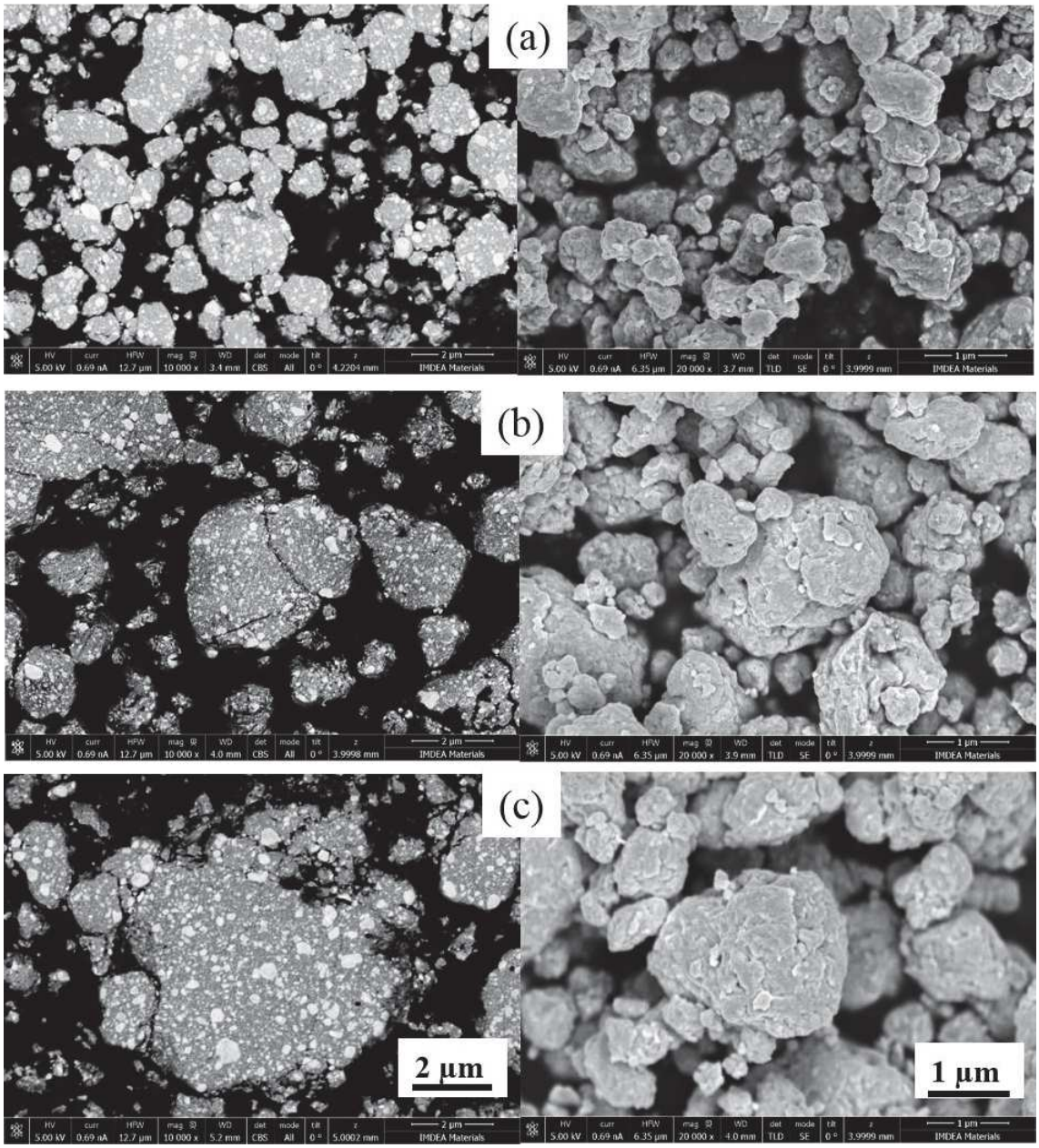

Figure 5.10. Cross-section BSE image (left) and as-milled morphology (right) of MM Cr-based WC powders with different extra Fe contents: (a) 1 wt.% Fe, (b) 3 wt.% Fe, and (c) 5 wt.% Fe.

Figure 5.11 shows the microstructure and morphology of the Cr-based WC powders with 3 wt.% Fe and different extra C contents after 20 h milling. A homogenous microstructure is also obtained in these milled Cr-based WC powders. The as-milled morphology shows that Cr-based WC powders are fine and round with sizes around 1 µm. The round WC particles are uniformly distributed in the Cr-based binder. Furthermore, the carbon content does not seem to have a significant effect on the final particle size distribution achieved, in comparison with the Cr-based WC powders with only 3wt.% of extra Fe content.

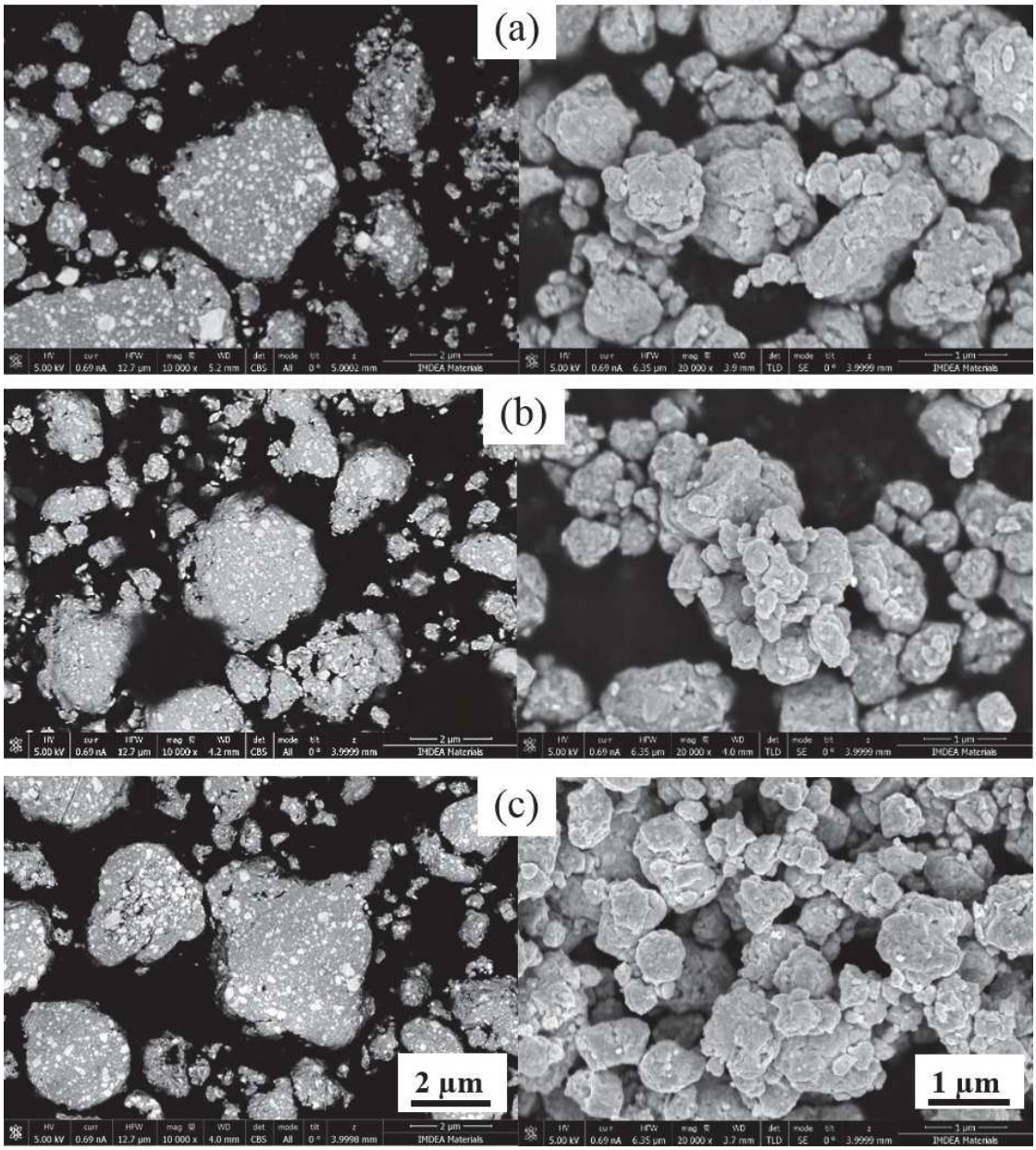

Figure 5.11. Cross-section BSE image (left) and as-milled morphology (right) of MM Cr-based WC powders with 3 wt.% Fe and different extra C additions: (a) 3 wt.% Fe and 0.5 wt.% C, (b) 3 wt.% Fe and 1 wt.% C, and (c) 3 wt.% Fe and 2 wt.% C.

The particle size distribution of the WC particles, embedded in the Cr-based binder is measured by the linear intercept method based on the cross-section BSE images of MM Cr-based WC powders with different extra Fe/C additions. Results are shown in the histograms of Figure 5.12. The average size of the WC particles are in the range of 70-100 nm after high-energy mechanical ball milling for 20 h. Many researchers have reported that high-energy milling is capable of producing nanoscale WC and WC-Co nanocomposites [8-9]. Butler *et al*. [10] produced WC particles of around 10 nm size in a Co-based binder by using the planetary ball-milling method. Production of nanoscale

WC is the first step to manufacture nanosized hardmetals materials, since hardmetals with nanocrystallite WC grain structure have the potential to significantly improve the mechanical properties of these materials [11]. In this work, the size of WC particles decreases considerably from D_{50}= 2 μm in the raw powder to 70-100 nm in the Cr-based WC powders after high-energy mechanical ball milling for 20 h at the speed of 350 rpm. The carbon content variation from 0.5 to 2 wt.% does not seem to have a significant effect on the average grain size of the WC particles within the powders. These nanosized WC particles will play a key role in the final properties of Cr-based WC hardmetals.

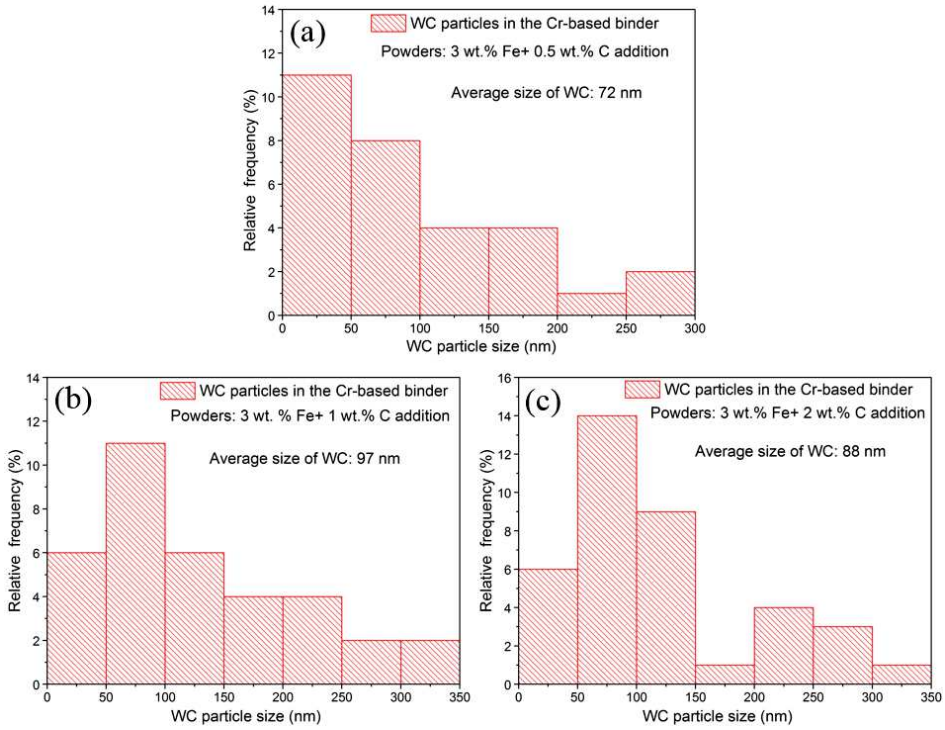

Figure 5.12. Particle size distribution of WC particles in the Cr-based binder after 20 h of milling: (a) powders with extra 3 wt.% Fe and 0.5 wt.% C addition, (b) powders with extra 3 wt.% Fe and 1 wt.% C addition, and (c) powders with extra 3 wt.% Fe and 0.5 wt.% C addition.

5.4 Summary

The average size of WC particles in the milled Cr-based WC powders after 20 h are in the range of 70-100 nm, which demonstrates that planetary ball-milling method is an efficient way to produce nanoscale WC in Cr-based WC powders. From XRD analyses, it can be concluded that the addition of extra Fe or Fe/C contents does not induce the formation of new phases. The studies showing the evolution of the particle size distribution, microstructure, crystallite size and microstrain of the MM Cr-based WC powders confirm that these powders are adequate for the subsequent sintering, since the powders are round and fine, presenting a homogenous microstructure and good crystallographic parameters.

5.5 References

[1] A. García-Junceda, I. Sáez, X.X. Deng, and J.M. Torralba, "Development of a Cr-based hard composite processed by spark plasma sintering," *Metall. Mater. Trans. A*, vol. 49, no. 4, pp. 1363–1371, 2018.

[2] J.B. Fogagnolo, F. Velasco, M.H. Robert, and J.M. Torralba, "Effect of mechanical alloying on the morphology, microstructure and properties of aluminium matrix composite powders," *Mater. Sci. Eng. A*, vol. 342, pp. 131–143, 2003.

[3] F.A. Mohamed and Y. Xun, "Correlations between the minimum grain size produced by milling and material parameters," vol. 354, no. 1–2, pp. 133–139, 2003.

[4] R. Porat, S. Berger, and A. Rosen, "Sintering behavior and mechanical properties of nanocrystallite WC/Co.," *Mater Sci Forum*, no. 225–227, pp. 629–34, 1996.

[5] D.R. Amador and J.M. Torralba, "Morphological and microstructural characterisation of low-alloying Fe powder obtained by mechanical attrition," *J. Mater. Process. Technol.*, vol. 143, pp. 776–780, 2003.

[6] L. Fuentes-Pacheco, M. Campos, and J.M. Torralba, "Thermal stability of nano structured iron powder as a function of amount and nature of reinforcement (Nb or NbC)," *Rev. Metal.*, vol. 47, no. 5, pp. 373–380, 2011.

[7] J.B. Fogagnolo, M.H. Robert, and J.M. Torralba, "Mechanically alloyed AlN particle-reinforced Al-6061 matrix composites: Powder processing, consolidation and mechanical strength and hardness of the as-extruded materials," za*Mater. Sci. Eng. A*, vol. 426, pp. 85–94, 2006.

[8] M.A. Xueming, Z. Ling, J.I. Gang, and D. Yuanda, "Preparation and structure of bulk nanostructured WC-Co alloy by high energy ball-milling," *J. Mater. Sci. Lett.*, vol. 16, no. 12, pp. 968–970, 1997.

[9] F.L. Zhang, C.Y. Wang, and M. Zhu, "Nanostructured WC/Co composite powder prepared by high energy ball milling," *Scr. Mater.*, vol. 49, no. 11, pp. 1123–1128, 2003.

[10] B.G. Butler, J. Lu, Z.Z. Fang, and R.K. Rajamani, "Production of nanometric tungsten carbide powders by planetary milling.," *Int. J. Powder Metall.*, vol. 43, no. 1, 2007.

[11] Z.Z. Fang, X. Wang, T. Ryu, K.S. Hwang, and H.Y. Sohn, "Synthesis, sintering, and mechanical properties of nanocrystallite cemented tungsten carbide-A review," *Int. J. Refract. Met. Hard Mater.*, vol. 27, no. 2, pp. 288–299, 2009.

Chapter 6

Cr-based hardmetals obtained by liquid phase sintering

Contents

6.1 Cr-based WC hardmetals obtained by liquid phase sintering

This chapter discusses the microstructural and mechanical results obtained in Cr-based WC hardmetals processed by liquid phase sintering (LPS) at 1450 °C for 30 min. This applied sintering temperature is around 100 °C above the melting point of W-C-Cr-Fe system, as shown in Chapter 4.2. The content covers the effect of extra Fe or Fe/C additions on the phase formation, microstructure, average grain size of WC, densification, hardness and fracture toughness of Cr-based WC hardmetals.

6.2 Effect of different Fe contents on sintered Cr-based WC hardmetals

6.2.1 Phase identification and microstructural analyses

Figure 6.1 shows the XRD spectra obtained with the aim of identifying the phases in the sintered Cr-based WC hardmetals with different extra Fe additions. The identification of the peak patterns confirms the existence of a Cr-based matrix, and four different carbides comprising WC, $(W,Cr)_2C$, Fe_3W_3C, and $Fe_{21}W_2C_6$, which is consistent with the expected phase formation taking into account the thermodynamic modelling, but also a Cr_2O_3 phase which is not predicted by modelling. There are studies in the literature confirming the generation of these type of carbides in similar W-C-Cr-Fe systems. Some previous research work on W-C-Cr-Fe systems suggested the formation of undesirable brittle eta-phase M_6C and another brittle carbide $M_{23}C_6$, since both Cr and Fe have a strong affinity to carbon [1-3]. Gustafson [4-5] showed the thermodynamic and experimental study of the quaternary W-C-Cr-Fe system, in which the replacement of all the Cr element in the $Cr_{23}C_6$ led to the carbide with stoichiometry $Fe_{21}W_2C_6$. Weidow *et al*. [6] found a $(W,Cr)_2C$ phase as an intermediate product in the carburisation of a $W+Cr_3C_2+C$ mixture. Brieseck *et al*. [7] reported that $(W,Cr)_2C$ phase was formed at the interphase of Cr_3C_2-WC diffusion couple during the heat treatment process, which also demonstrates the solubility of Cr in W_2C. The calculated phase diagram of W-C-Cr-Fe system in Chapter 4.2 also suggests a small solubility of Cr in W_2C in the terms of $(W,Cr)_2C$ phase.

With regard to XRD studies, some differences can be observed between the theoretically predicted and the experimentally phases detected. Although the formation of Cr_2O_3 is not predicted from the calculated phase diagram in which oxygen was not included, the XRD analyses confirm its formation, since some Cr coming from the binder may be oxidised during the sintering process due to the strong affinity of Cr with O. In addition, the calculated chromium carbide M_7C_3 is not detected in these XRD spectra due the oxidation

of Cr and loss of C. Fe_3W_3C and $Fe_{21}W_2C_6$ carbides are detected in all Cr-based WC hardmetals, which is not consistent with the modelling results that indicated that Fe_3W_3C only existed in the hardmetals with extra 1 wt.% and 3 wt.% Fe additions, and $Fe_{21}W_2C_6$ was only found in the hardmetal with extra 5 wt.% Fe addition. This is due to the non-equilibrium state taking place in the real sintering conditions, where these two carbides are formed during the heating and they remain stable after cooling.

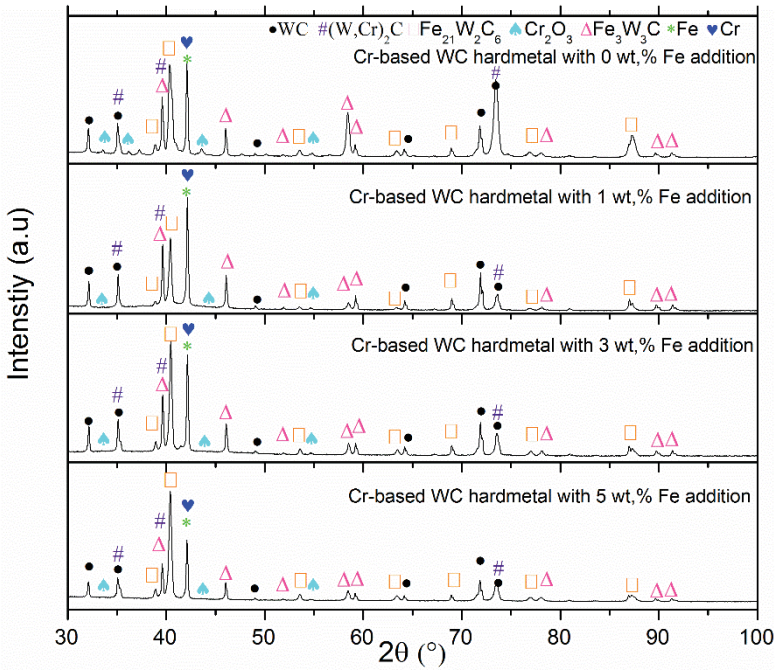

Figure 6.1. XRD spectra for Cr-based WC hardmetals sintered by LPS at 1450 °C with different extra Fe additions.

Representative micrographs of the sintered Cr-based WC hardmetals, with different extra Fe contents, are shown in Figure 6.2 in order to analyse the obtained microstructure. EDX analyses are performed on these micrographs to further investigate the composition of the formed phases, as listed in Table 6.1. Although EDX is a semi-quantitative method for measuring the content of an element in a phase, the results are still useful to quantitatively determine the formed phases and to compare these data with the previous XRD results. Figure 6.2 shows multi-phasic structures, where WC, $(W,Cr)_2C$, Fe_3W_3C, $Fe_{21}W_2C_6$ and Cr_2O_3 phases are heterogeneously distributed within the Cr-based binder, which agrees well with the previous XRD analyses. Table 6.1 with the EDX data shows that the black areas (labelled as 1) rich in Cr and O correspond to Cr_2O_3 phase, since Cr has a strong affinity to O at high temperature, although Ar atmosphere is used to limit the O content. The light grey and white areas correspond to the metallic binder (labelled as 2) and WC hard phase (labelled as 3), respectively, which are the main phases in Cr-based WC hardmetals. $(W,Cr)_2C$ is labelled as 4. Fe_3W_3C and $Fe_{21}W_2C_6$ are difficult to be

distinguished by EDX since their compositions are very similar. Thus, they are labelled as 5 in Figure 6.2. Our previous results also demonstrated the formation of a Fe_3W_3C phase mixed with a $Fe_{21}W_2C_6$ phase after studying the microstructure of a hard Cr-based composite by EBSD [8].

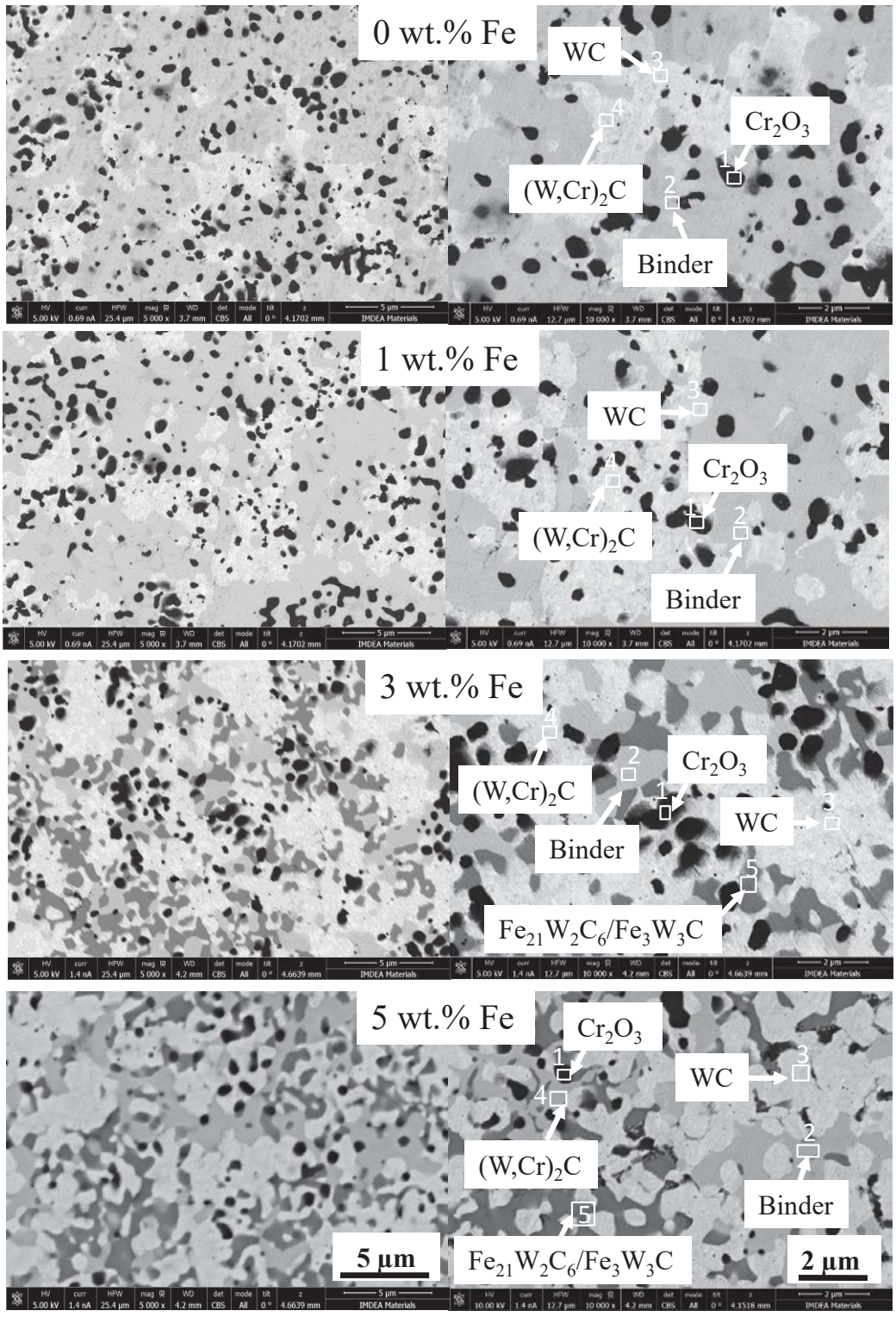

Figure 6.2. BSE micrographs with low and high magnification of Cr-based WC hardmetals with different extra Fe contents sintered by LPS (0 wt.%, 1 wt.%, 3 wt.% and 5 wt.% Fe).

Table 6.1. Chemical elemental content measured by EDX in the selected areas of Cr-based WC hardmetals with different extra Fe contents (0 wt.%, 1 wt.%, 3 wt.% and 5 wt.% Fe).

Cr-based WC hardmetals	Data	W (at.%)	C (at.%)	Cr (at.%)	Fe (at.%)	O (at.%)
0 wt.% Fe	1	2.54	15.47	26.65	5.21	50.13
	2	20.78	24.57	35.42	10.43	8.80
	3	37.83	49.85	1.66	1.98	1.67
	4	45.05	34.04	18.60	0.24	2.07
1 wt.% Fe	1	5.34	14.50	35.16	1.20	43.80
	2	19.36	17.64	48.56	11.53	2.91
	3	49.57	44.56	2.06	2.08	1.73
	4	45.80	40.21	12.21	0.54	1.24
3 wt.% Fe	1	3.14	4.25	26.47	5.32	60.82
	2	33.40	42.88	7.24	11.25	5.23
	3	47.29	45.41	3.18	3.06	1.06
	4	45.41	34.59	17.78	1.47	0.75
	5	27.82	23.71	1.68	45.32	1.47
5 wt.% Fe	1	4.47	10.13	23.76	6.45	55.19
	2	28.32	10.88	33.08	19.28	8.44
	3	37.89	45.33	6.21	3.00	7.56
	4	46.99	38.52	10.57	2.45	1.47
	5	25.77	30.47	2.61	40.21	0.94

Figure 6.3 shows the microstructural evolution of the WC grains with the addition of extra Fe contents in Cr-based WC hardmetals. The WC grains (in white colour) grow significantly with the increase of Fe content. Two reasons contribute to this phenomenon: (i) compared to fast sintering techniques, LPS process provides more energy and time for atoms to be transported and for interface motion [9]; (ii) the addition of Fe powders with high surface energy improves the sinterability, leading to the growth of WC grains [10].

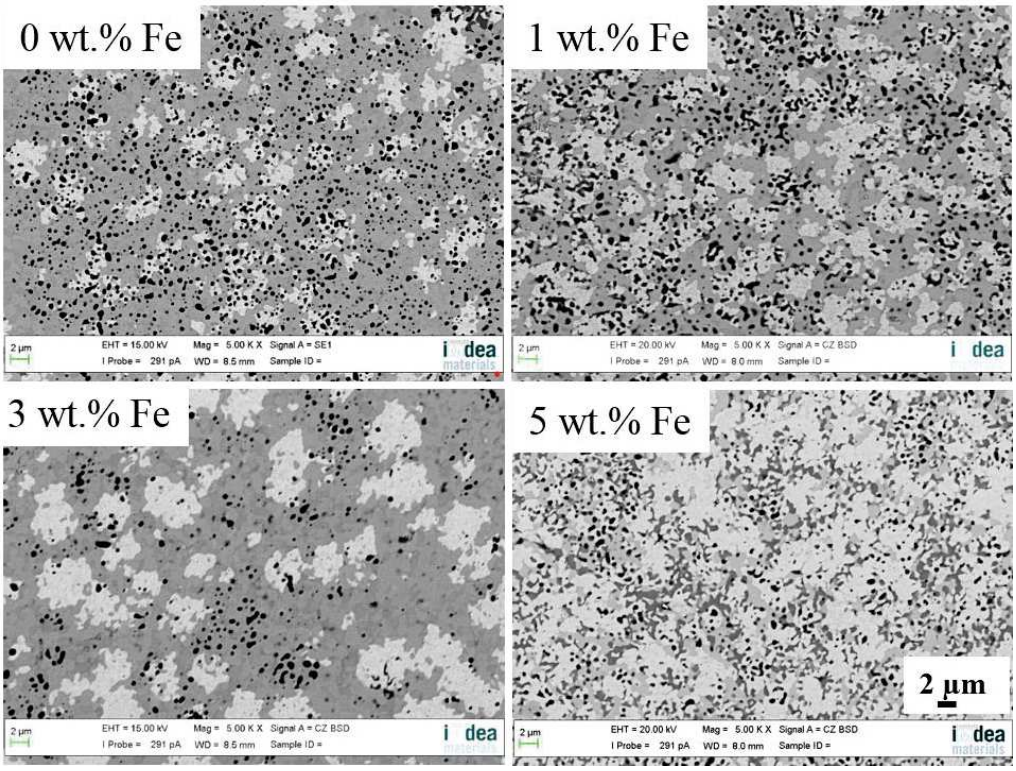

Figure 6.3. BSE micrographs showing the growth of WC grains with the increase of the extra Fe content.

6.2.2 Mechanical properties of Cr-based WC hardmetals with extra Fe contents

Generally, the mechanical properties of Cr-based WC hardmetals mainly depend on their density, composition, and WC grain size. In order to investigate the effect of adding extra Fe contents on the mechanical properties of Cr-based WC hardmetals, an analysis including the relationship between relative density, average WC grain size, Vickers hardness, and fracture toughness is needed. All these results are displayed in Figure 6.4.

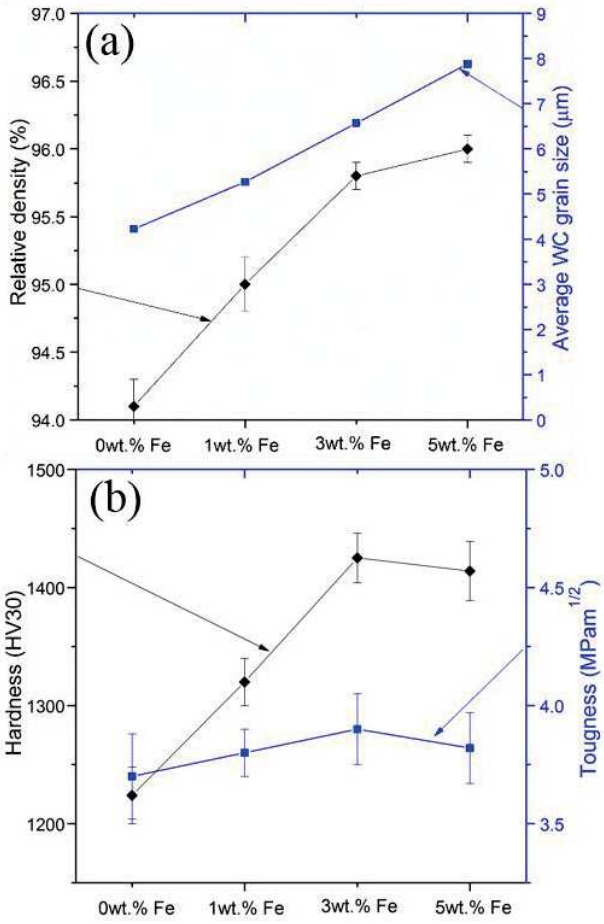

Figure 6.4 Relative density and average WC grain size (a), Vickers hardness and toughness (b) for Cr-based WC hardmetals with different extra Fe additions sintered by LPS at 1450 °C.

Figure 6.4(a) shows a relative density increase with the increase of the extra Fe content from 0 to 5 wt.%. Two main reasons contribute to this fact. Firstly, the extra Fe addition decreases the melting point of W-C-Cr-Fe system, thus improving the densification of Cr-based WC hardmetals. Secondly, the particle size of the extra Fe powder is very small (less than 1 μm) with a high amount of surface energy and this increases the sinterability of Cr-based WC hardmetals. The contact angle is also reduced by the higher surface energy due to the addition of fine Fe powders [9]. A lower contact angle induces liquid

spreading over the solid grains, providing a capillary attraction that helps to densify the system [10]. Zhu *et al*. [11] demonstrated that additions of smaller starting particles led to an improved densification. On the other hand, Figure 6.4(a) shows that the average grain size of WC increases from 4.2 μm to 7.9 μm with the increase of the Fe content from 0 to 5 wt.% due to the improvement of the sinterability, which matches with the growth of WC observed in the microstructural analysis (Figure 6.3).

Another important fact is that Cr-based WC hardmetals exhibit an enhancement of the hardness with the increase of the Fe content between 0-3 wt.%, as shown in Figure 6.4 (b), and a slight deterioration of its value when extra 5 wt.% Fe is added due to two opposite factors: (i) the improved density leads to an increase in hardness, and (ii) the hardness decreases when the growth of WC grain size takes places, according to Hall-petch relationship [12]. As shown in Figure 6.4 (a), the WC grains for hardmetals with 5 wt.% of extra Fe have a bigger average size (7.9 μm) than the size presented by the one with extra 3 wt.% Fe (6.5 μm). The fracture toughness value of Cr-based WC hardmetals firstly increases with the increase of extra Fe content from 0 wt.% to 3 wt.%, due to the enhancement of the densification, and then decreases slightly with the increase of Fe from 3 wt.% to 5 wt.%, since the amount of the brittle $Fe_{21}W_2C_6$ carbide grows, as observed in the microstructural images of Figure 6.2. Thus, the Cr-based WC hardmetal with extra 3 wt.% Fe content is selected as the precursor to study the effect of C content due to its best mechanical properties.

6.3 Effect of different C contents on sintered Cr-based WC hardmetals

6.3.1 Phase identification and microstructural analyses

Figure 6.5 shows the X-ray diffraction spectra of Cr-based WC hardmetals (all with extra 3 wt.% Fe addition) designed with different extra C additions. The XRD results show the existence of WC, Fe_3W_3C, $Fe_{21}W_2C_6$, Cr_7C_3 and binder phase. The $(W,Cr)_2C$ carbide is not detected, since the extra addition of C may prevent the formation of $(W,Cr)_2C$. Mühlbauer *et al.* [13] reported that W_2C tends to be transformed into WC phase with the increase of the C content, which may lead to the inhibition of $(W,Cr)_2C$. It is worth highlighting that Cr_2O_3 appears in the Cr-based WC hardmetals without extra C additions and now it disappears with an extra addition of C, since C could reduce most of the oxides and remove them from the sample by forming gaseous species such as CO and CO_2. Kaplan *et al.* [14] studied WC-CoCr hardmetals with an extra addition of C content,

concluding that part of the carbon eliminates the most of the oxides in the terms of CO and CO_2. Another effect of C is that it could reduce the formation of Fe_3W_3C phase. The intensity of XRD peaks corresponding to Fe_3W_3C decreases with the increase of the C content, which is also predicted by the calculated phase diagram. Generally, Fe_3W_3C is a typical brittle eta-phase found in W-C-Fe system, which decreases the toughness of hardmetals significantly even when this phase exists in small amount [5]. Some researchers have reported that the formation of eta-phases would be reduced or inhibited with the addition of C [15]. So adding extra C contents aims to avoid this undesirable brittle phase in the final microstructure. In the XRD spectra, Cr_7C_3 is detected when adding more than 1 wt.% of extra C content, not the formation of Cr_3C_2 as predicted by the modelling results since the reaction of C and O leads to a reduction of the C content and to the formation of Cr_7C_3 after cooling. The expected graphite suggested by the modelling results is not found in the XRD patterns, when extra 2 wt.% C content is added. This fact may be also explained by the preferred reaction of carbon with oxygen forming CO and CO_2.

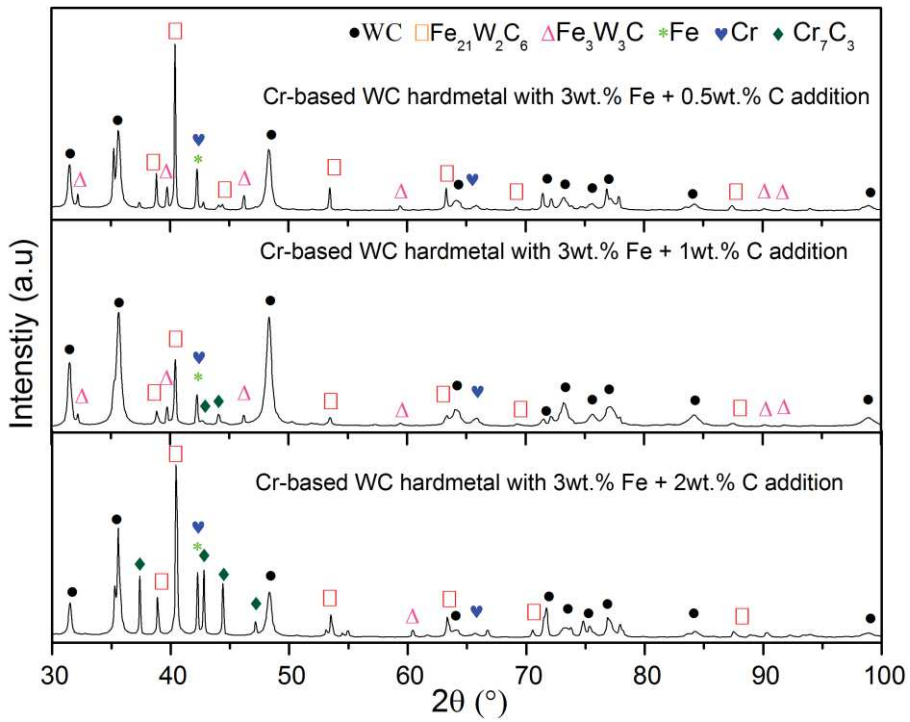

Figure 6.5. XRD spectra for Cr-based WC hardmetals (all with extra 3 wt.% Fe addition) sintered by LPS at 1450 °C with different extra C additions.

Figure 6.6 shows the representative BSE micrographs of Cr-based WC hardmetals (all with 3 wt.% extra Fe content) with different extra C additions and sintered by LPS at 1450 °C for 30 min. Very fine pores (less than 1 μm) exist in the Cr-based WC with 0.5 wt.% C addition, as shown by the small black spots present in Figure 6.6(a). The white

and grey areas represent WC hard phase and Cr-based binder, respectively. Cr_7C_3 is detected when adding more than 1 wt.% of extra C content, which agrees with the existence of Cr_7C_3 in the XRD analyses of these Cr-based hardmetals (Figure 6.5). Figure 6.6(b) shows that fine WC particles are preferentially located along the grain boundary of $Fe_{21}W_2C_6$/ Fe_3W_3C (light black) and Cr_7C_3 (dark black), since these new interfaces could become preferred sites for the precipitation of WC. As a result, the distribution of the WC hard phase becomes more uniform than that in Cr-based hardmetals without extra C additions. The growth of WC grain size is also reduced when adding extra C additions, compared to the microstructure achieved when only 3 wt.% of extra Fe is added (Figure 6.3). Kaplan also reported that the formation of M_7C_3 helped to inhibit the growth of WC by studying the effect of C on a WC-CoCr hardmetal [16].

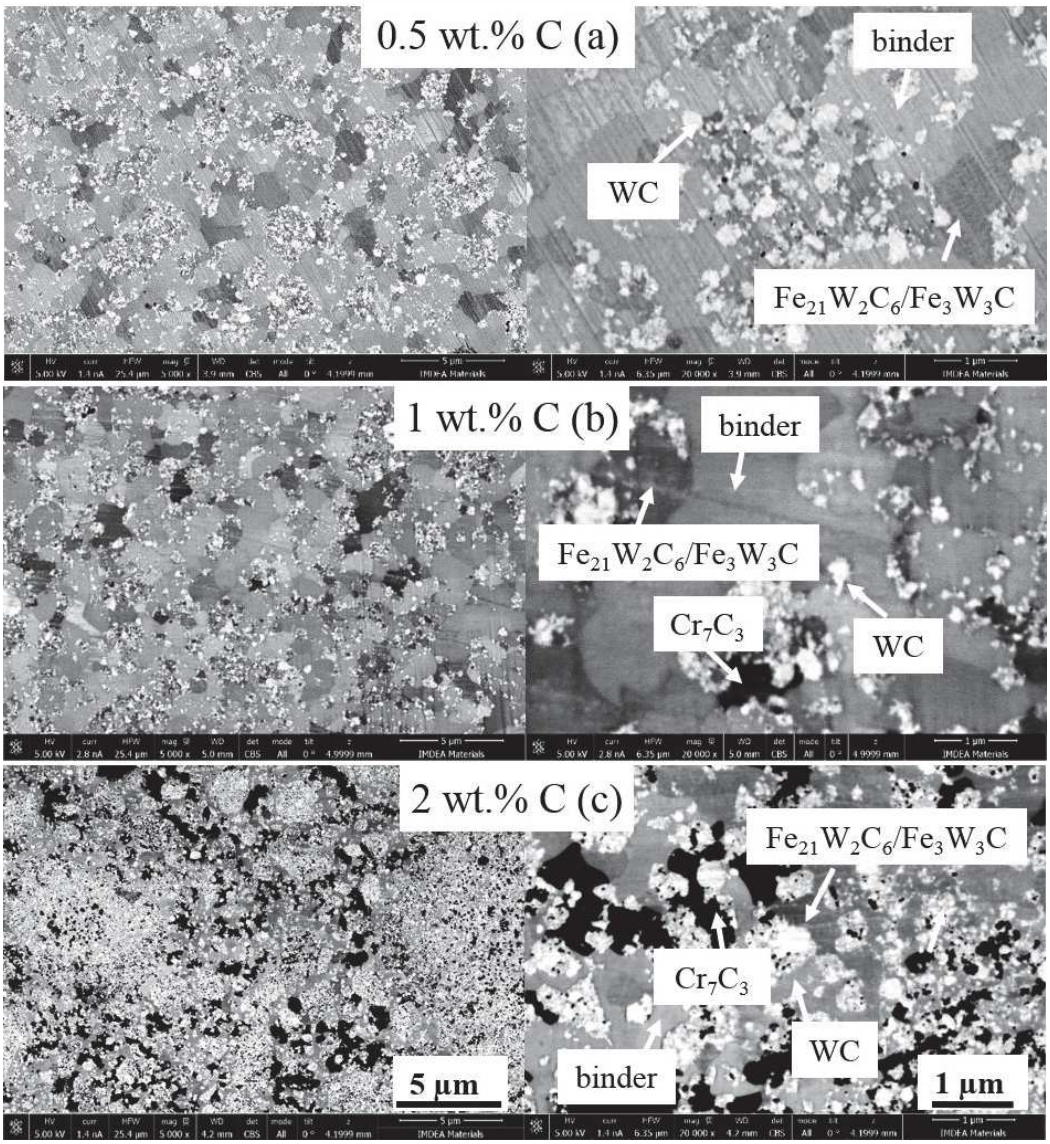

Figure 6.6. BSE micrographs with low and high magnification for Cr-based WC hardmetals (3 wt.% Fe) with different extra C additions and sintered by LPS: 0.5 wt.% C (a), 1 wt.% C (b), and 2 wt.% C (c).

6.3.2 Mechanical properties of Cr-based WC hardmetals with extra C contents

The microstructural analyses performed highlight that adding C content exerts a significate effect on the microstructure, including the reduction of the WC average grain size and the decrease in the content of Fe_3W_3C. Thus, these variations in structure definitely influence the mechanical properties. In order to study the influence of extra C contents, Figure 6.7 describes the relationship between relative density, average WC grain size, Vickers hardness and toughness for Cr-based WC hardmetals with different extra C additions.

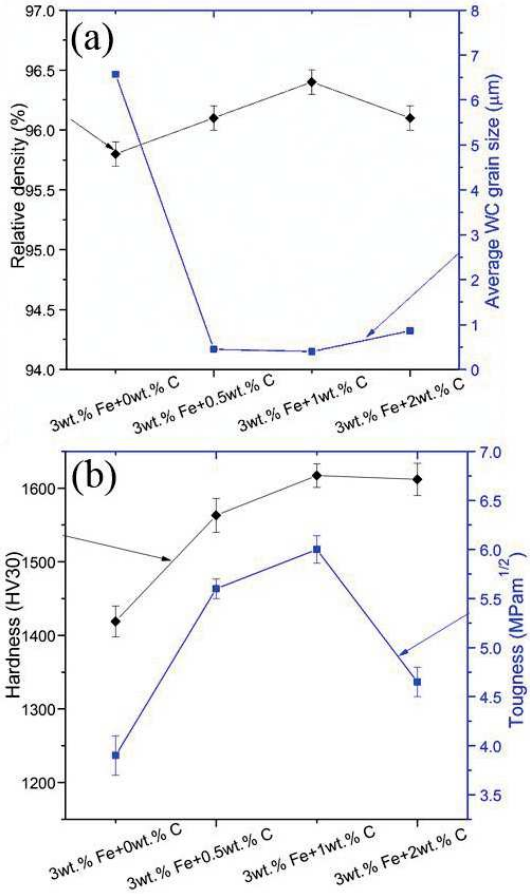

Figure 6.7. Density and average WC grain size (a), Vickers hardness and toughness (b) for Cr-based WC hardmetals (with 3 wt.% Fe) with different extra C additions sintered by LPS at 1450 °C.

Figure 6.7(a) shows that the relative density increases with the increase of extra C content between 0 wt.% and 1 wt.%, and decreases when extra 2 wt.% C is added. This fact can be due to the elimination of the oxides in the samples by adding C (0-1 wt.%), thus promoting the densification. The relative density decreases when extra 2 wt.% C is added, since more extra C content increases the melting point of W-C-Cr-Fe system due to its high melting point.

The hardness and fracture toughness of Cr-based hardmetals also exhibit an improvement with the increase of the extra C content between 0-1 wt.% and a deterioration of these values when 2 wt.% of C is added. This behaviour can be explained by three factors:

a) The mechanical properties primarily depend on the density and follow the similar trend of the density, as depicted in Figure 6.7(a).
b) The hardness increases significantly from 1419 HV30 to 1617 HV30 with the increase of the extra C content between 0-1 wt.%, since the WC average grain size decreases from 6.5 μm to 0.4 μm, as shown in Figure 6.7(a), leading to an improvement of hardness based on the Hall-petch relationship [12]. This reduction of the WC grain size is due to the effect of the carbon content on favouring the formation of Cr_7C_3 carbides, which seems to inhibit the growth of WC grains, as Kaplan suggested [16]. There is a slight decrease of the hardness with the addition of and extra C content from 1 to 2 wt.% due to the reduction of the relative density achieved and to a small growth of the WC grain size.
c) The toughness value of Cr-based WC hardmetals increases significantly with the increase of the C content (0-1 wt.% C) since the formation of brittle Fe_3W_3C is reduced. The toughness decreases when extra 2 wt.% is added, due to the decrease in the density reached and to the growth of the brittle Cr_7C_3 carbide.

Thus, the Cr-based WC hardmetal with extra 3 wt.% Fe and 1 wt.% C addition achieves the highest hardness and toughness values combination (1647 HV30 and 6.0 $MPam^{1/2}$). Usually, the fracture toughness has a tendency in complete oposition to the hardness. In PM materials, toughness is much more sensitive to the density than to other microstructural features, and this allows a simultaneous increase of hardnesss and toughness due to the improvement of the density and the achievement of an optimised microstructure when extra 1 wt.% C is added.

Althouh Cr-based WC hardmetals sintered by LPS exhibit a optimised combination of hardness and toughness values (1647 HV30 and 6.0 $MPam^{1/2}$), the fracture toughness (K_{IC}) is still low compared to that of LPSed Co-based WC hardmetals (8-20 $MPam^{1/2}$). However, Cr-based WC hardmetals are still comparable to Fe-based WC hardmetals (1496-1645 HV30 and 5.0-9.5 $MPam^{1/2}$) [17-18]. These Cr-based WC hardmetals could be used in applications such as woodcutting tools and wear-resistant tools, where a relative high hardness and low toughness are needed. Furthermore, Cr-based WC hardmetals could also be used as unimportant tools in those applications in which the low price is more important than the durability, since the complete substitution of Co binders would decrease the cost.

6.4 Summary and conclusions

In this chapter, liquid phase sintering of Cr-based WC hardmetals, with the compositions designed after the thermodynamic modelling of the phase diagrams, is performed. The effect of different extra Fe or Fe/C additions on microstructure, phase formation, densification and mechanical properties of Cr-based WC hardmetals are listed in the following conclusions:

(1) The WC grain size and the relative densification values are increased with the increase of the Fe content since fine Fe powders with high surface energy improve the sinteribililty of Cr-based WC hardmetals, and extra Fe content also decreases the melting point of the W-C-Cr-Fe system.

(2) In the case of Cr-based WC hardmetals with different Fe additions, XRD analyses confirm the formation of $(W,Cr)_2C$, Fe_3W_3C, and $Fe_{21}W_2C_6$ phases, which is consistent with the thermodynamic modelling. Furthermore, Cr_2O_3 is formed since Cr has a strong affinity to O. This oxide was obviously not expected from the thermodynamic calculation, which did not include oxygen in the phase diagrams. The microstructural analyses agree with XRD results, confirming the existence of Cr_2O_3. The study concerning mechanical properties shows that Cr-based WC hardmetal with extra 3 wt.% Fe addition achieves the best hardness and fracture toughness relationship. Thus, the Cr-based WC hardmetal with 3 wt.% Fe is selected as the precursor for further studying the effect of different extra C additions.

(3) XRD results and microstructural analyses show that Cr_2O_3 disappears with the addition of small quantities of C, since C could reduce most of the oxides and remove them from the sample by forming gaseous species such as CO and CO_2.

(4) Extra 1 wt.% C addition induces the formation of Cr_7C_3, leading to a finer WC more homogenously distributed within the Cr-based binder phase. When extra 2 wt.% C content is added, the growth of the Cr_7C_3 carbide is favoured, which is detrimental to the toughness.

(5) The Cr-based WC hardmetal with extra 3 wt.% Fe and 1 wt.% C additions achieves the best mechcanical properties due to two main reasons. One is that the relative densification is improved with the increase of the extra C content from 0 wt.% to 1 wt.%. Another reason is the formation of a microstructure with a smaller WC average grain size (< 1 μm).

Nevertheless, the fracture toughness achieved in LPSed Cr-based WC hardmetals is not too high, probably due to the existence of big brittle carbides with different compositions ($Fe_{21}W_2C_6$/Fe_3W_3C and Cr_7C_3) randomly distributed within the binder. This microstructure obtained by LPS method does not allow a significant further improvement of the toughness. For this reason, the next step of this investigation is based on the study of the viability of consolidating Cr-based WC hardmetals by a fast solid state processing technique, as is the case of Spark Plasma Sintering (SPS), in order to limit the growth of undesirable and brittel carbides, leading to the further improvement of the fracture toughness.

6.5 References

[1] P. Gustafson, "An experimental study and a thermodynamic evaluation of the Cr-Fe-W-C system," *Metall. Trans. A*, vol. 19A, pp. 2531–3546, 1988.

[2] A.V. Khvan, B. Hallstedt, and C. Broeckmann, "A thermodynamic evaluation of the Fe-Cr-C system," *Calphad Comput. Coupling Phase Diagrams Thermochem.*, vol. 46, pp. 24–33, 2014.

[3] B. Uhrenius, "An experimental and thermodynamic study of carbide/austenite equilibria in Fe-Cr-W-C alloys," *Met. Sci.*, vol. 14, no. 71, pp. 73–81, 1971.

[4] P. Gustafson, "A thermodynamic evaluation of the C-Cr-Fe-W System," *Metall. Trans. A*, vol. 19, pp. 2547–2554, 1988.

[5] P. Gustafson, "A thermodynamic evaluation of the Fe-C-W system," *Scand. J. Metall.*, vol. 14, no. 5, pp. 259–267, 1985.

[6] J. Weidow, A. Blomqvist, J. Salomonsson, and S. Norgren, "Cemented carbides based on WC pre-alloyed with Cr or Ta," *Int. J. Refract. Met. Hard Mater.*, vol. 49, pp. 36–41, 2015.

[7] M. Brieseck, M. Bohn, and W. Lengauer, "Diffusion and solubility of Cr in WC," *J. Alloys Compd.*, vol. 489, no. 2, pp. 408–414, 2010.

[8] A. García-Junceda, I. Sáez, X. X. Deng, and J. M. Torralba, "Development of a Cr-based hard composite processed by spark plasma sintering," *Metall. Mater. Trans. A*, vol. 49, no. 4, pp. 1363–1371, 2018.

[9] R. M. German, "Consolidation techniques," in *Comprehensive Hard Materials*, vol. 1, Elsevier Ltd, 2014, pp. 237–263.

[10] R.M. German, P. Suri, and S. Jinpark, "Review: liquid phase sintering," *J. Mater Sci*, vol. 44, pp. 1–39, 2009.

[11] S. Zhu, W.G. Fahrenholtz, and G.E. Hilmas, "Influence of silicon carbide particle size on the microstructure and mechanical properties of zirconium diboride–silicon carbide ceramics," *J. Eur. Ceram. Soc.*, vol. 27, no. 4, pp. 2077–2083, 2007.

[12] A.H. Chokshi, A. Rosen, J. Karch, and H. Gleiter, "On the validity of the Hall-Petch relationship in nanocrystalline materials," *Scr. Metall.*, vol. 23, no. 10, pp. 1679–1683, 1989.

[13] G. Mühlbauer, G. Kremser, A. Bock, and J. Weidow, "Transition of W_2C to WC during carburization of tungsten metal powder," *Int. J. Refract. Metals Hard Mater.*, vol. 72, no. 2017, pp. 141–148, 2018.

[14] B. Kaplan, A. Markstr, N. Susanne, and M. Selleby, "Experimental determination of the solubility of Co in the Cr-based carbides $Cr_{23}C_6$, Cr_7C_3 and Cr_3C_2," *Met. Mater. Trans. A*, vol. 11, no. 45A, pp. 4820–4828, 2014.

[15] C.M. Fernandes and A.M.R. Senos, "Cemented carbide phase diagrams: A review," *Int. J. Refract. Met. Hard Mater.*, vol. 29, no. 4, pp. 405–418, 2011.

[16] B. Kaplan, "Equilibrium aspects of Cr-alloyed cemented carbides (Doctoral dissertation, KTH Royal Institute of Technology)," 2015.

[17] M. Tarraste, J. Kübarsepp, K. Juhani, T. Suurkivi, and J. Pirso, "Spark plasma sintering of WC hardmetals with Fe-based binder," in *European Congress and Exhibition on Powder Metallurgy. European PM Conference Proceedings*, 2016, pp. 1–6.

[18] B.J. Marques, C.M. Fernandes, and A.M.R. Senos, "Sintering, microstructure and properties of WC-AISI304 powder composites," *J. Alloys Compd.*, vol. 562, pp. 164–170, 2013.

Chapter 7

Cr-based hardmetals consolidated by spark plasma sintering

Contents

7.1 Cr-based WC hardmetals obtained by spark plasma sintering

This chapter discusses the characteristics of Cr-based WC hardmetals with different extra Fe or Fe/C contents consolidated by SPS under different conditions. The Fe content and the parameters for the consolidation are optimised based on the analyses of the shrinkage, microstructure, phase formation, density, hardness and fracture toughness. Then, the effect of different extra C contents on the properties of Cr-based WC hardmetals with an optimum Fe content is investigated. Finally, these developed Cr-based hardmetals with different extra carbon contents are deeply characterised in terms of microstructure, phase formation, density, hardness, fracture toughness, nanoindentation measurements, compressive strength, oxidation resistance and wear resistance. From the properties achieved, a study of the viability of introducing these new Cr-based hardmetals in the market is addressed.

7.2 Cr-based WC hardmetals with different extra Fe contents

7.2.1 SPS conditions

A series of investigations aims to provide better knowledge in the effect of SPS parameters on the densification process of Cr-based WC hardmetals with different Fe contents. Table 7.1 lists the SPS parameters used and the corresponding Cr-based WC powders. The consolidation temperature and the applied pressure are set to 1200 °C and 50 MPa, respectively. The selected consolidation temperature is 100 °C lower than the eutectic temperature of the W-C-Cr-Fe system, when an extra 3 wt.% Fe content is added. The heating rate and holding time are in the range of 200-400 °C/min and 5-10 min, respectively.

Table 7.1. SPS parameters for Cr-based WC powders with different extra Fe contents.

Cr-based WC powders with different extra Fe contents	Consolidation temperature (°C)	Heating rate (°C/min)	Holding time (min)	Applied pressure (MPa)
0 wt.% Fe	1200	200	5	50
1 wt.% Fe	1200	200	5	50
1 wt.% Fe	1200	400	5	50
3 wt.% Fe	1200	400	5	50
3 wt.% Fe	1200	400	10	50

7.2.2 Shrinkage

The goal of this study is to analyse the effect of the heating rate and the holding time on the densification of Cr-based WC hardmetals during SPS process. The shrinkage curves of Cr-based WC hardmetals with different extra Fe contents and the evolution of the applied pressure are shown in Figure 7.1. The stroke in abscissa axis means the

displacement of the punch during the sintering, which is directly related to the densification of the Cr-based WC hardmetal. The relative density achieved for each sample is labelled near the corresponding curve. Therefore, the highest stroke corresponds to the highest density reached. Three main stages can be observed in the evolution of the stroke: (i) the stroke increases at the beginning since powders are contracted during the application of an increasing pressure from 0 to 50 MPa, (ii) then, there is a decrease in the stroke due to the thermal expansion of the powder, and (iii) the stroke in all samples significantly increases during the fast heating process, and finally remains stable during the subsequent dwell process. The highest densification of Cr-based hardmetals is achieved in the third stage, labelled as (iii), due to the simultaneous application of maximum pressure and sintering temperature. During the cooling process, the densification is finished and without relation to the stroke. Cr-based WC powders with extra Fe contents present a higher shrinkage than powders without extra Fe, since the Fe addition, in terms of a spherical and fine carbonyl iron powder with high specific surface energy, improves the rearrangement and sinterability under solid-state sintering. The curve obtained for a heating rate of 400 °C/min, when adding 1 wt.% of extra Fe content, shows a larger shrinkage than that of 200 °C/min, since a higher heating rate could supply more energy in the same time, favouring the sintering and leading to a higher densification. Another advantage of using a higher heating rate is the reduction of the processing time, which limits the grain growth of the WC grain size. On the other hand, longer holding times (10 *vs.* 5 min.) are usually beneficial for the densification of Cr-based WC hardmetals, although the grains will grow slightly, as it will be explained later.

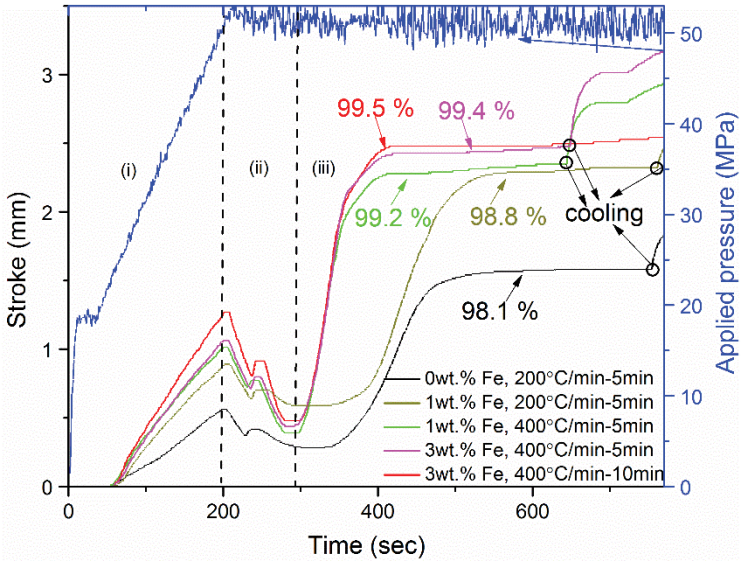

Figure 7.1 Shrinkage curves of Cr-based WC powders and evolution of the applied pressure during the consolidation by SPS. The relative density achieved is labelled in each corresponding curve.

7.2.3 Phase identification and microstructural analyses

Figure 7.2 shows the XRD spectra obtained from Cr-based WC hardmetals consolidated by SPS with different extra Fe contents. The identification of the peaks patterns confirms the existence of Cr_2O_3, $FeCr_2O_4$, WC, and Cr-based binder in the reference sample without extra iron contents. Fe_6W_6C phase appears with an extra 1 wt.% Fe content. Fe_6W_6C phase is transformed into Fe_3W_3C phase when extra 3 wt.% Fe content is added, which is consistent with the modelling results. Oliver *et al*. [1] also detected the formation Fe_6W_6C and Fe_3W_3C carbides in the densification of a W-Fe-C (O) system. In their research, the percentages of precipitated phases estimated through the areas of the XRD diffraction peaks demonstrated that Fe_6W_6C was transformed into Fe_3W_3C carbide with the increase of the Fe/W ratio. Suetin *et al*. [2] calculated the relative stability of the Fe_3W_3C and Fe_6W_6C carbides by determining their formation energies, concluding that Fe_3W_3C carbide has a higher formation energy and then this carbide is less stable.

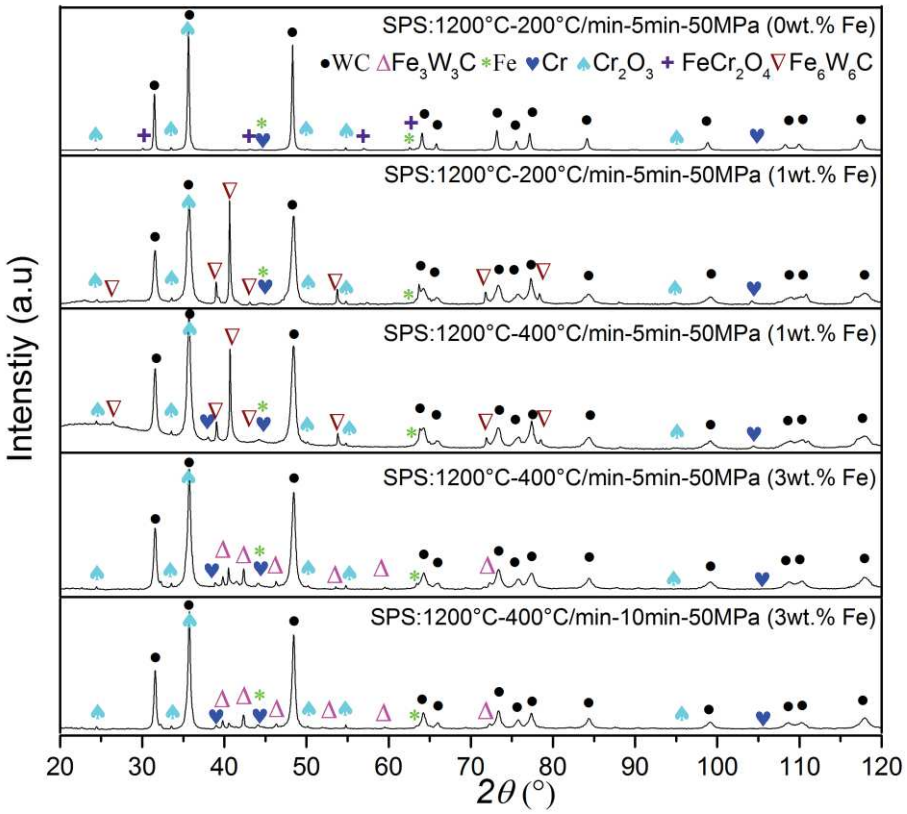

Figure 7.2. XRD spectra of Cr-based WC hardmetals sintered by SPS with different extra Fe contents.

The microstructure of the Cr-based WC hardmetals with different extra Fe contents is characterised by the presence of three phases with distinct contrast, i.e. grey (binder), white (WC), and black (Cr_2O_3), as can be seen in Figure 7.3, in which SEM images

coupled to EDX analysis are shown. A significant difference in microstructure can be observed between Cr-based hardmetals processed by SPS and LPS. The hard WC phase is fine and it is homogenously distributed in the binder phase in all SPS samples, since this solid-state sintering allows a much higher heating rate and a shorter holding time than LPS. With the increment of the iron content in SPSed hardmetals, the densification is improved and the growth of WC grain size is reduced.

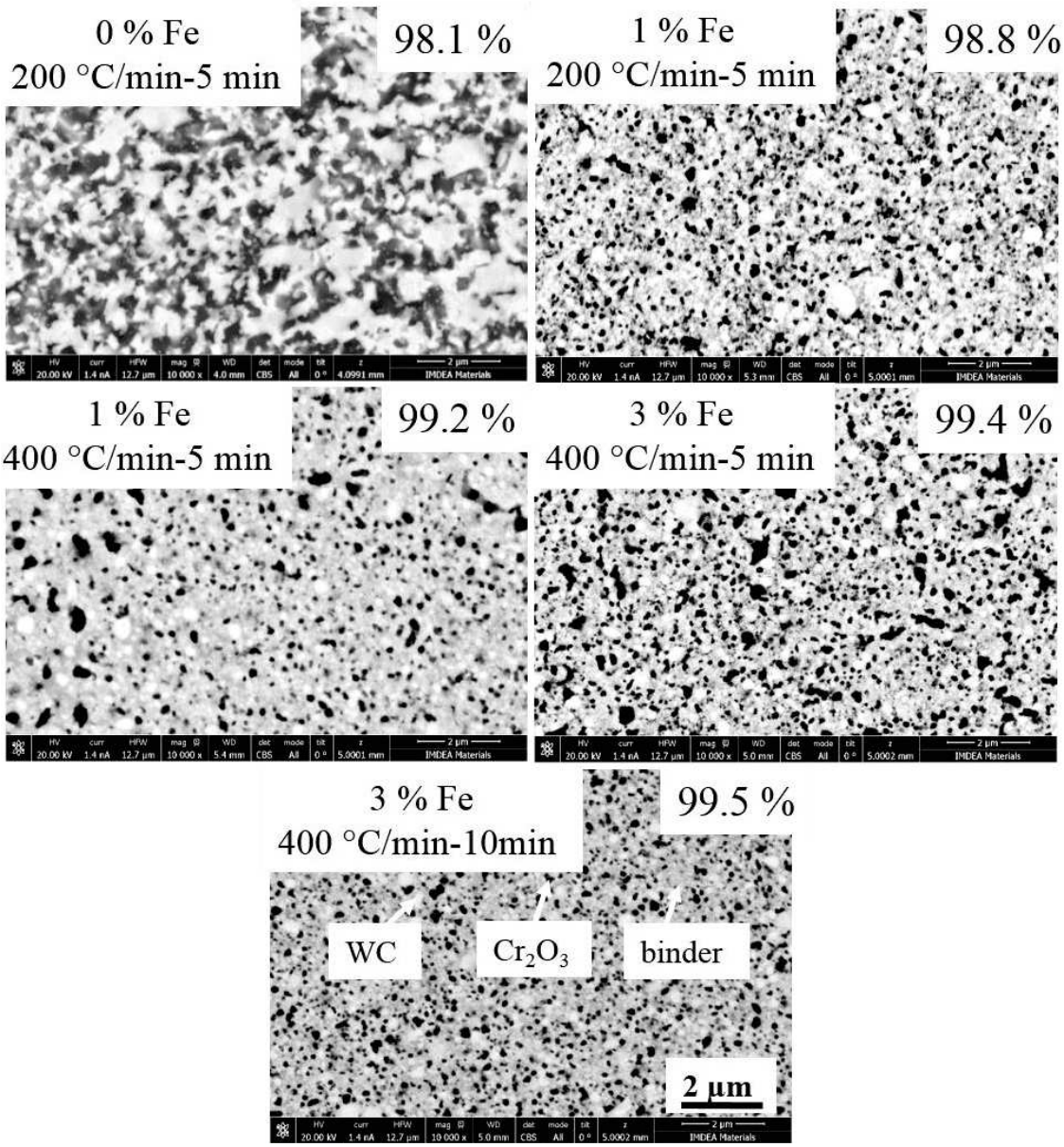

Figure 7.3. BSE micrographs of Cr-based WC hardmetals with different extra Fe additions consolidated by SPS at 1200 °C (heating rate, holding time, and relative density are labelled in each micrograph).

$FeCr_2O_4$, Fe_3W_3C and Fe_6W_6C phases detected by XRD analyses are not labelled in these micrographs due to their relative small size and content. In order to further understand the effect of the Fe content on the phase formation of different carbides (Fe_3W_3C and

Fe_6W_6C), TEM-EDX mapping analyses are carried out on the Cr-based WC hardmetals with different extra Fe contents. The EDX elemental mapping images of Cr-based WC hardmetals without Fe additions (Figure 7.4) illustrate the existence of a WC phase, which corresponds to the white region in the HAADF image. The black area comprises three phases with different compositions: (1) Cr_2O_3 phase, elemental analyses show the stoichiometric ratio of 2Cr to 3O (the formation of Cr_2O_3 is confirmed in later discussion); (2) $FeCr_2O_4$, with higher Cr content than Fe, and (3) Fe-rich binder consisting mainly of Fe and a few amount of Cr.

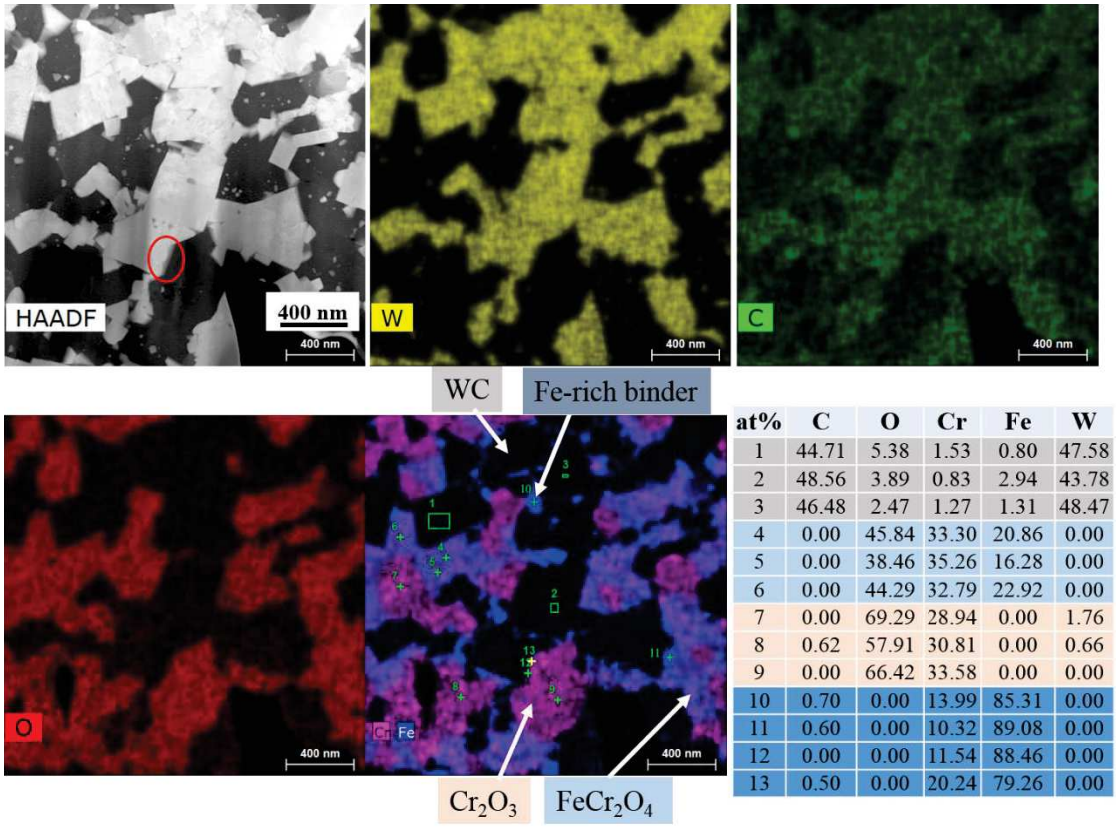

at%	C	O	Cr	Fe	W
1	44.71	5.38	1.53	0.80	47.58
2	48.56	3.89	0.83	2.94	43.78
3	46.48	2.47	1.27	1.31	48.47
4	0.00	45.84	33.30	20.86	0.00
5	0.00	38.46	35.26	16.28	0.00
6	0.00	44.29	32.79	22.92	0.00
7	0.00	69.29	28.94	0.00	1.76
8	0.62	57.91	30.81	0.00	0.66
9	0.00	66.42	33.58	0.00	0.00
10	0.70	0.00	13.99	85.31	0.00
11	0.60	0.00	10.32	89.08	0.00
12	0.00	0.00	11.54	88.46	0.00
13	0.50	0.00	20.24	79.26	0.00

Figure 7.4. HAADF-STEM image of Cr-based WC hardmetal without extra Fe contents consolidated by SPS: 1200 °C-200 °C/min-5 min-50 MPa. EDX elemental mapping images showing W (yellow), C (green), O (red), Cr (pink), and Fe (blue), and the corresponding elemental at.% values in selected areas and points of the image.

Furushima *et al.* [3] produced WC-FeAl composites by vacuum sintering technique. The author pointed that oxygen suppressed the WC grain growth, and improved the hardness and the strength due to the formation of α-Al_2O_3 on WC/WC interface. They further confirmed the existence of α-Al_2O_3 by selected area diffraction analysis, demonstrating that the composition of FeAl binder varied by the generation of α-Al_2O_3. Thus, in our particular case, the formation of Cr_2O_3 could be desirable for improving the hardness and the strength of Cr-based hardmetals.

Figure 7.5 shows a higher magnification of the interface between WC and Cr_2O_3, marked by the red circle in Figure 7.4, which reveals the existence of a thin interphase. Elemental mapping results indicate that this interphase consists of W, C, Cr and O, without any Fe content. A line scanning is performed across the interface with a thickness of around 50 nm to further analyse the elemental distribution. The elemental EDX line scanning in Figure 7.6 proves that the atomic ratio of W-Cr and C approximates to 2:1, suggesting that it could be a $(W,Cr)_2C$ carbide. Thus, elemental distribution in the interphase proves that there is some solubility of Cr in W_2C even in solid-state.

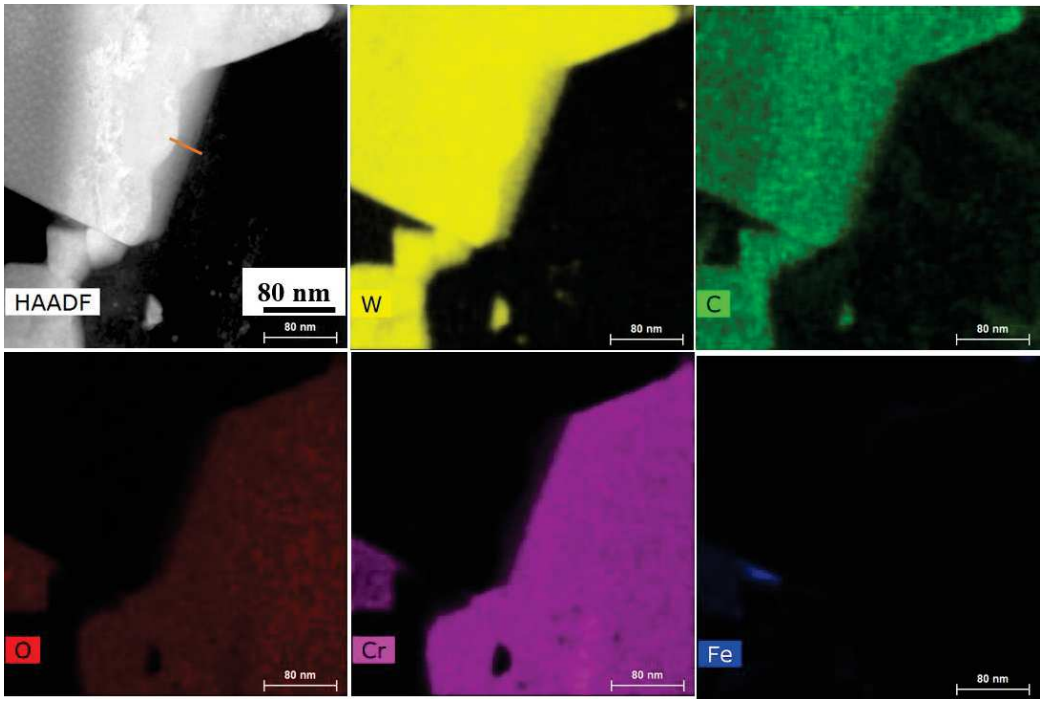

Figure 7.5. HAADF-STEM image showing an interphase formed by $(W,Cr)_2C$ along the interface between WC and Cr_2O_3, and EDX elemental mapping images showing W (yellow), C (green), O (red), Cr (pink), and Fe (blue).

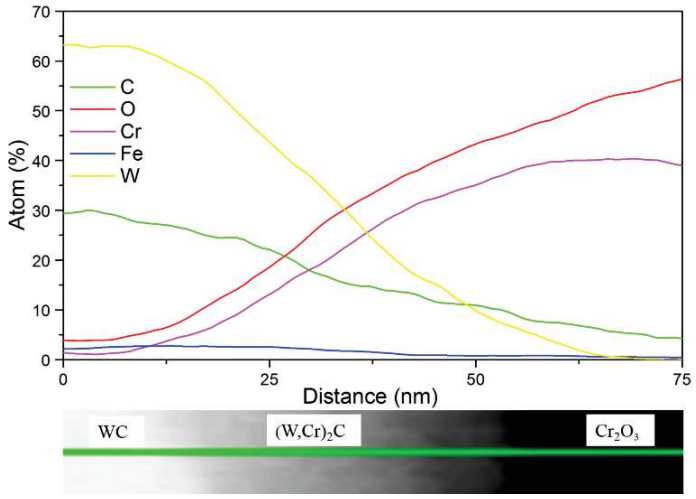

Figure 7.6. EDX line scanning profile across the interphase $(W,Cr)_2C$ generated between WC and Cr_2O_3.

In addition, a HRTEM image is obtained at the interphase (Figure 7.7). The yellow and red circles represent the W and Cr atoms, respectively, which clearly confirms the solubility of Cr in W_2C. The calculated atomic radius of W and Cr atom by measuring carefully their diameter in the HRTEM image are 217 pm and 130 pm, respectively, which fits with the real value of 210 pm for W and 128 pm for Cr [4]. This interphase does not appear at all the boundaries between WC and Cr_2O_3 phases, but it is confined to local WC particles with less C content. The nature of $(W,Cr)_2C$ is confirmed to have a hexagonal close packed structure with a lattice constant a = 4.3078 Å, obtained from the TRTEM image. W_2C is reported in the literature to present a lattice constant of 4.2410-4.2660 Å in a range of 1200-1400 °C [5]. This measured lattice parameter is larger than that of W_2C since the enlarged lattice parameter is caused by the solubility of the Cr atom in W_2C. Delanoe *et al*. [6] also reported that the partial Cr solubility in W_2C is predictable in terms of formation of $(W, Cr)_2C$ carbide in the W-C-Cr system [7]. So based on these analyses, it can be concluded that an interphase formed by $(W,Cr)_2C$ occurs between WC and Cr_2O_3 phases during SPS consolidating process, which may improve the bonding strength and the toughness of Cr-based WC hardmetals.

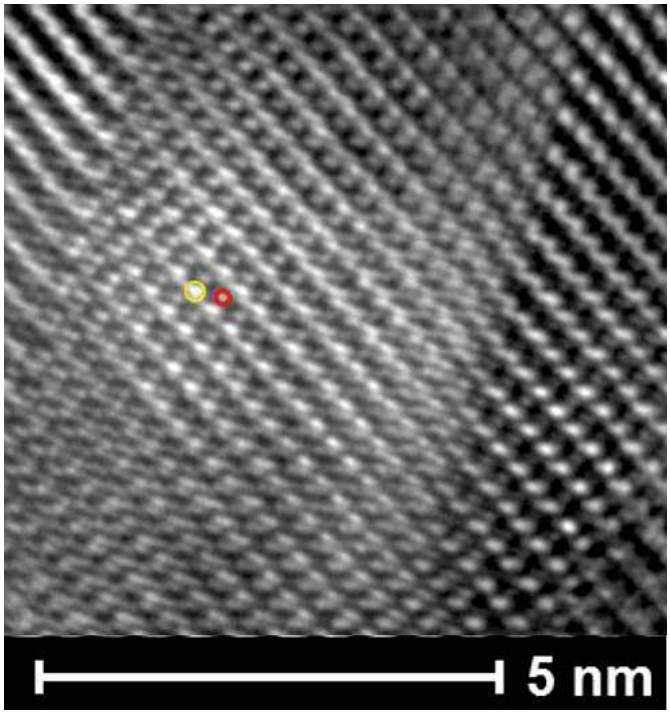

Figure 7.7. HRTEM image of the interface between WC and Cr_2O_3: W atom in yellow circle and Cr atom in red circle.

Figure 7.8 depicts a HAADF image and the EDX elemental mapping images of Cr-based WC hardmetals with an extra 1 wt.% Fe content consolidated by SPS (1200 °C-

400 °C/min-5 min-50 MPa). WC, Cr_2O_3, Fe_6W_6C and Cr-based binder phase are observed, which agrees well with the XRD results, and also a very thin layer of $(W,Cr)_2C$ carbide between Cr_2O_3 and WC. The comparison of the HAADF images of Cr-based WC with extra 0 wt.% and 1 wt.% Fe content, points out that the Fe addition has a significant effect on the microstructure and phase formation. Some regions, marked by red lines (Figure 7.8), represent the Fe_6W_6C phase. EDX point analyses indicate that the stoichiometric ratio of Fe, W, and C is closed to 6:6:1. Figure 7.8 also suggests that the growth of WC is limited when extra Fe contents are added due to the formation of Fe_6W_6C.

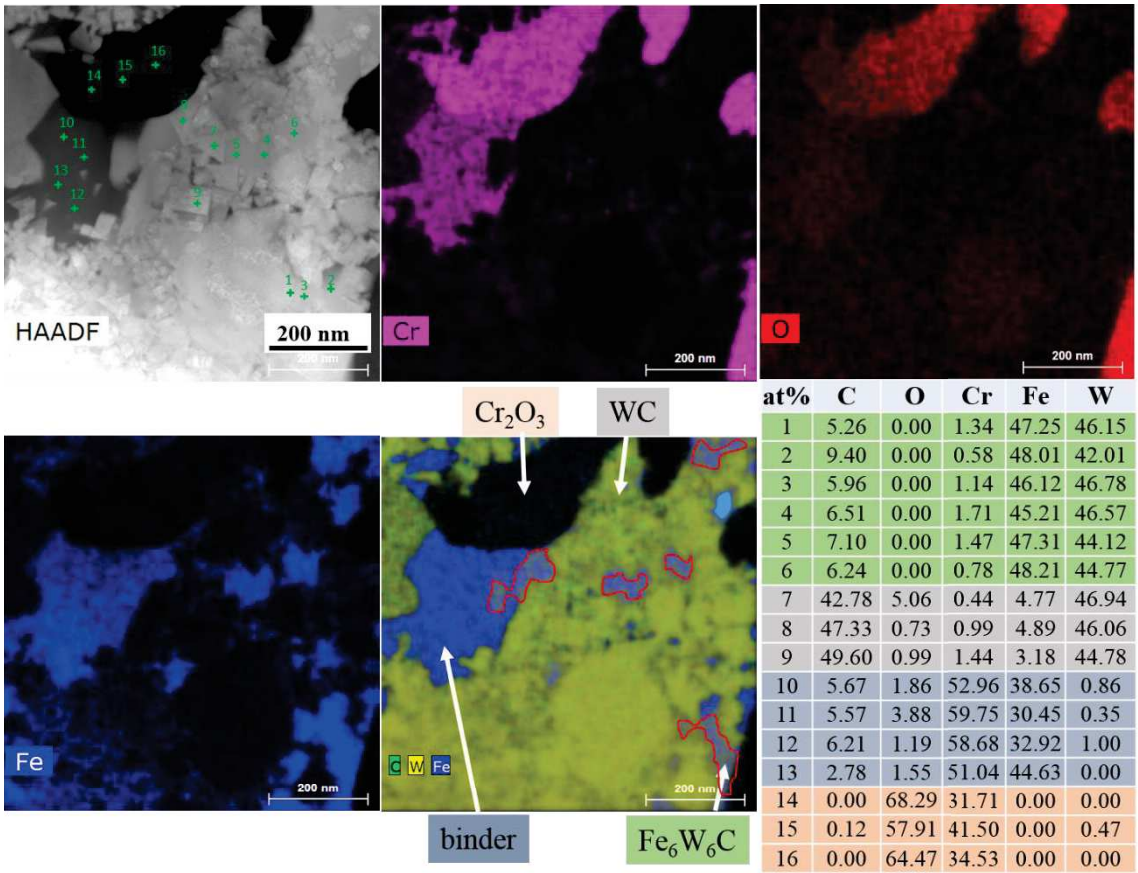

at%	C	O	Cr	Fe	W
1	5.26	0.00	1.34	47.25	46.15
2	9.40	0.00	0.58	48.01	42.01
3	5.96	0.00	1.14	46.12	46.78
4	6.51	0.00	1.71	45.21	46.57
5	7.10	0.00	1.47	47.31	44.12
6	6.24	0.00	0.78	48.21	44.77
7	42.78	5.06	0.44	4.77	46.94
8	47.33	0.73	0.99	4.89	46.06
9	49.60	0.99	1.44	3.18	44.78
10	5.67	1.86	52.96	38.65	0.86
11	5.57	3.88	59.75	30.45	0.35
12	6.21	1.19	58.68	32.92	1.00
13	2.78	1.55	51.04	44.63	0.00
14	0.00	68.29	31.71	0.00	0.00
15	0.12	57.91	41.50	0.00	0.47
16	0.00	64.47	34.53	0.00	0.00

Figure 7.8. HAADF-STEM image of the Cr-based WC hardmetal with an extra 1 wt.% Fe content consolidated by SPS: 1200 °C-400 °C/min-5 min-50 MPa. EDX elemental mapping images showing Cr (pink), O (red), Fe (blue), C (green), and W (yellow) and the corresponding elemental at.% values of selected points.

Figure 7.9 displays a HAADF image and the EDX elemental mapping images of the Cr-based WC hardmetals with an extra 3 wt.% Fe content consolidated by SPS (1200 °C-400 °C/min-10 min-50 MPa). WC, Cr_2O_3, Fe_3W_3C, binder phase and very thin $(W,Cr)_2C$ are detected. Therefore, the results suggest that the Fe_6W_6C is transformed into Fe_3W_3C phase when an extra 3 wt.% Fe content is added, which is consistent with the XRD

analyses. Both crystal structures, Fe_3W_3C and Fe_6W_6C, belong to the space group Fd-3m, where W occupies the 48f sites and Fe is placed in two non-equivalent 32e and 16d sites, whereas C is located in the 16c sites for Fe_3W_3C and in the 8a sites for Fe_6W_6C [8].

The regions 1 and 2, marked by the red lines in Figure 7.9, are rich in Cr-O, and Fe-W-C, respectively. EDX point analyses demonstrate that the stoichiometric ratio of Cr and O is 2: 3 in region 1, and of Fe, W, and C is 3:3:1 in region 2. In addition, selected area electron diffraction (SAED) patterns are obtained in the marked regions 1 and 2 to further identify the formation of Cr_2O_3 and Fe_3W_3C phases, respectively.

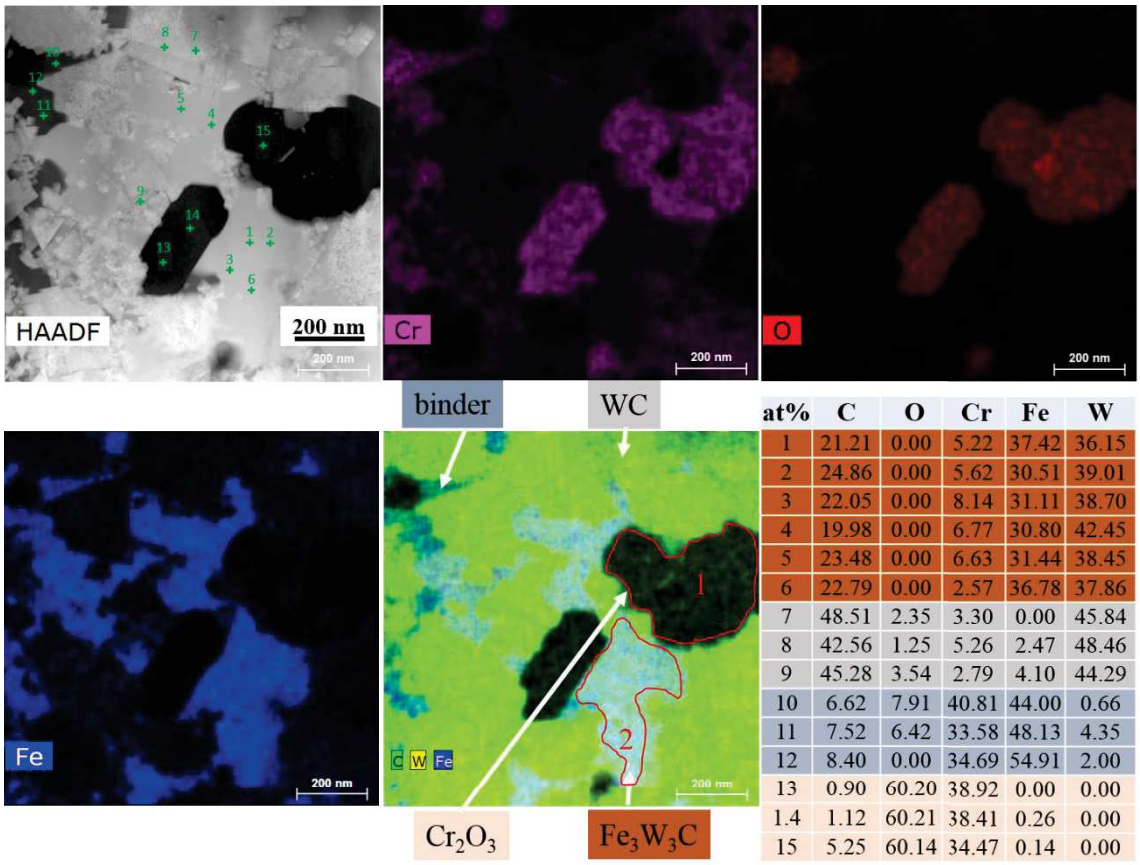

at%	C	O	Cr	Fe	W
1	21.21	0.00	5.22	37.42	36.15
2	24.86	0.00	5.62	30.51	39.01
3	22.05	0.00	8.14	31.11	38.70
4	19.98	0.00	6.77	30.80	42.45
5	23.48	0.00	6.63	31.44	38.45
6	22.79	0.00	2.57	36.78	37.86
7	48.51	2.35	3.30	0.00	45.84
8	42.56	1.25	5.26	2.47	48.46
9	45.28	3.54	2.79	4.10	44.29
10	6.62	7.91	40.81	44.00	0.66
11	7.52	6.42	33.58	48.13	4.35
12	8.40	0.00	34.69	54.91	2.00
13	0.90	60.20	38.92	0.00	0.00
1.4	1.12	60.21	38.41	0.26	0.00
15	5.25	60.14	34.47	0.14	0.00

Figure 7.9. HAADF-STEM image of the Cr-based WC hardmetal with an extra 3 wt.% Fe content consolidated by SPS: 1200 °C-400 °C/min-10 min-50 MPa. EDX elemental mapping images showing Cr (pink), O (red), Fe (blue), C (green), and W (yellow), and the corresponding elemental at.% values of selected points.

The SAED (selected area electron diffraction) patterns in regions 1 and 2 are carefully analysed and compared with the reciprocal lattices calculated from standard crystallographic parameters (Table 7.2). Figure 7.10(a) shows the standard crystalline structure of Cr_2O_3 built using the lattice parameters listed in Table 7.2. The reciprocal lattice is obtained creating a 3D crystalline structure parallel to the [110] zone axis using

the Crystalmaker software, as shown in Figure 7.10(b). Figure 7.10(c) shows the SAED pattern of the region 1. The reciprocal interplanar distances d_1, d_2, and d_3 of the crystal planes in Figure 7.10(b), and the reciprocal interplanar distances d'_1, d'_2, and d'_3 of the crystal planes in Figure 7.10(c), are measured from the center of the bright spots to the nearest spots.

Table 7.2. Crystallographic parameters of Cr_2O_3 [11] and Fe_3W_3C [12].

Phase	*a* (Å)	*b* (Å)	*c* (Å)	*Alfa* (°)	*Beta* (°)	*Gamma* (°)	Space group
Cr_2O_3	4.9570	4.9570	13.5923	90	90	120	R-3c
Fe_3C_3W	11.1075	11.1075	11.1075	90	90	90	Fd-3m

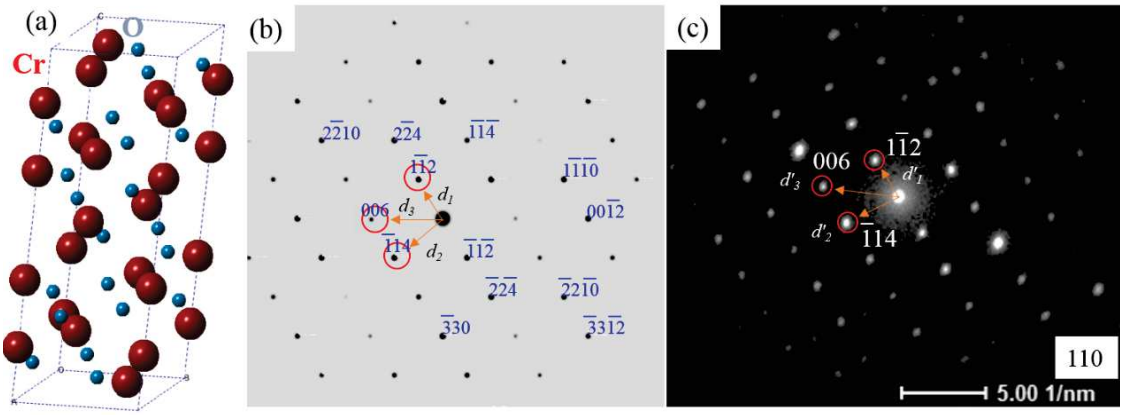

Figure 7.10. Identification of Cr_2O_3 phase: (a) crystalline structure, (b) reciprocal lattice ([110] zone axis) obtained from standard Cr_2O_3, (c) SAED pattern of region 1 in Figure 7.9.

The calculated interplanar distances ratios by means of the equations (1-2) fit well with those measured in the SAED pattern, which demonstrates that the black area must be Cr_2O_3 phase.

$$\frac{d_2}{d_1} = \frac{0.395}{0.290} = 1.362 \qquad \frac{d'_2}{d'_1} = \frac{35.751}{26.251} = 1.362 \tag{7-1}$$

$$\frac{d_3}{d'_1} = \frac{0.467}{0.290} = 1.610 \qquad \frac{d'_3}{d_1} = \frac{42.001}{26.251} = 1.600 \tag{7-2}$$

Cr_2O_3 is a hard oxide that exhibits a low friction coefficient, high wear and corrosion resistances, and high melting point (2435 °C) [9-10]. Therefore, a homogenous distribution of fine and round Cr_2O_3 phases within the microstructure may be beneficial to achieve good values of hardness, toughness, oxidation resistance and wear resistance. Figure 7.11 shows the standard crystalline structure of Fe_3W_3C built using the lattice parameters listed in Table 7.2, the reciprocal lattice of the phase creating a 3D crystalline structure parallel to the [345] zone axis using the Crystalmaker software, and the SAED pattern obtained in region 2.

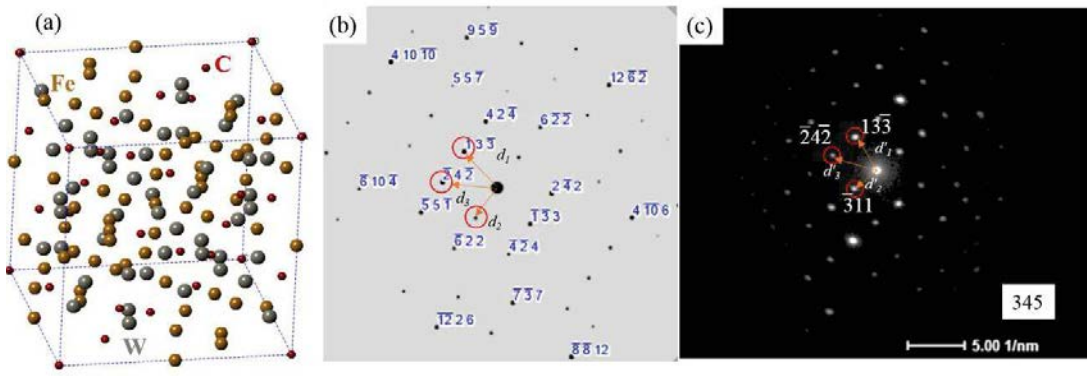

Figure 7.11. Identification of Fe_3W_3C phase: (a) crystalline structure, (b) reciprocal lattice ([345] zone axis) obtained from standard Fe_3W_3C, (c) SAED pattern of region 2 in Figure 7.9.

The interplanar distance ratios calculated with the equations (3-4) also fit well with those in the SAED pattern of Figure 7.11(c), confirming the existence of Fe_3W_3C in region 2.

$$\frac{d_2}{d_1} = \frac{0.297}{0.393} = 0.760 \qquad \frac{d\prime_2}{d\prime_1} = \frac{18.722}{24.600} = 0.761 \tag{7-3}$$

$$\frac{d_3}{d\prime_1} = \frac{0.442}{0.393} = 1.124 \qquad \frac{d\prime_3}{d_1} = \frac{27.654}{24.600} = 1.124 \tag{7-4}$$

7.2.4 Mechanical properties

The values of relative density, average WC grain size, Vickers hardness, and fracture toughness reached by SPSed Cr-based WC hardmetals with different extra iron contents, are shown in Figure 7.12.

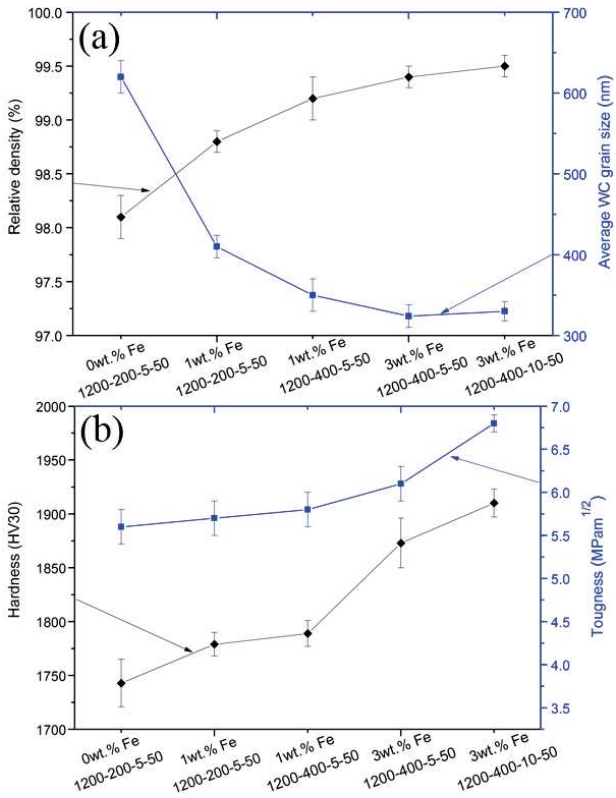

Figure 7.12. Relative density and average WC grain size (a) and Vickers hardness and fracture toughness values (b) for Cr-based WC hardmetals consolidated by SPS with different extra Fe contents.

Figure 7.12(a) highlights the increase of the relative density with the iron content. This trend is mainly due to two factors: (i) the addition of a fine and round Fe powder with a high surface energy improves the sinterability of Cr-based WC hardmetals; (ii) a higher heating rate (400 °C/min) or a longer holding time (10 min) supplies more energy for sintering, leading to a higher densification.

Figure 7.12(b) shows that the Vickers hardness slightly increases with the increase of the Fe content and it is further enhanced when a higher heating rate or a longer holding time is used, which is due to a combination of three factors: (i) extra Fe contents help to improve the density, leading to a higher hardness; (ii) the application of higher heating rates or longer holding times improves the density, which leads to further enhancement of hardness, (iii) the average grain size of WC decreases with the increase of the Fe content, since the formation of Fe_6W_6C/Fe_3W_3C prevents its growth. The WC grain size grows slightly from 324 nm to 330 nm when a longer holding time (10 min) is applied.

The fracture toughness also increases with the increase of the Fe content and it is further enhanced when higher heating rates or longer holding times are used. The main reason comes again from the improvement of the density. Moreover, the existence of a $(W,Cr)_2C$ phase between WC and Cr_2O_3 may improve the toughness.

A more homogenous microstructure than that obtained by LPS is reached during solid state sintering. In addition, SPSed samples present higher relatively densities and smaller WC grain sizes than LPS samples. The large brittle carbide like $M_{23}C_6$, detected in LPS sintering, is not found in the SPS microstructure, which improves the fracture toughness. Therefore, the differences found in the microstructure and in the phases formed in samples sintered by LPS and SPS explain the improvement of the mechanical properties, which is consistent with the assumption made in the previous chapter considering that the limitation of the growth of the brittle carbides under a solid-state sintering by a FAST technique would enhance the properties.

Although Cr-based WC hardmetal with an extra 3 wt.% Fe content exhibits a high hardness value of 1910 HV30 and a toughness value of 6.5 $MPam^{1/2}$, the toughness is still relative low. This could be due to the existence of brittle ŋ-phase, which deteriorates the toughness. Thus, the next study proposed in this investigation is based on the addition of different extra C contents into the Cr-based WC hardmetals, aiming to reduce or inhibit the formation of brittle phases.

7.3 Cr-based WC hardmetals with different extra C contents

7.3.1 SPS conditions

The Cr-based WC hardmetal with extra 3 wt.% Fe content achieves the highest hardness/toughness values, so this material is selected as the precursor for studying the effect of adding extra C contents from 0.5 wt.% to 2 wt.%. Table 7.3 lists the SPS parameters applied. The sintering temperature and the applied pressure are chosen to be increased from 1200 °C and 50 MPa to 1350 °C and 80 MPa, respectively, in order to obtain near full density, since the thermodynamic results showed that the melting point increases with the increase of the C content and a higher pressure also improves the densification. The heating rate and dwell time are fixed to 400 °C/min and 10 min, respectively. The C content is crucial for developing hardmetals, since the phase formation is largely determined by their C content. There exists C diffusion between the powders and the graphite tools during SPS process, leading to a deviation of the C content from the original design. Thus, a high purity tungsten foil (thickness of 25 μm) is used to cover the die and punches during SPS to avoid the effect of the C diffusion between the graphite tools and the powders. Two different SPS treatments (with and without using W foil) are carried out on Cr-based WC hardmetals with an extra 0.5 wt.% C content to analyse the effect of inserting a W foil on the carbon contamination of the samples. In order to determine the carbon content introduced, the real total C value in each sintered sample is measured by a chemical analysis and results are shown in Table 7.3. Indeed, when the W foil is not used, the real carbon content is a little bit higher due to carbon contamination coming from the graphite tools. Anyway, the real carbon contents measured by LECO almost match with the designed carbon compositions.

Table 7.3. SPS parameters for Cr-based WC powders with the designed total carbon contents and the real total carbon contents measured by LECO.

Cr-based WC powders with different C additions	Designed C content (wt.%)	Measured C content (wt.%)	Sintering temperature (°C)	Heating rate (°C/min)	Holding time (min)	Applied pressure (MPa)	Applied W foil
3 wt.% Fe + 0.5 wt.% C	5.59	5.27±0.09	1350	400	10	80	Yes
3 wt.% Fe + 0.5 wt.% C	5.59	5.57±0.05	1350	400	10	80	No
3 wt.% Fe + 1 wt.% C	6.03	6.17±0.09	1350	400	10	80	Yes
3 wt.% Fe+ 2 wt.% C	6.96	6.91±0.04	1350	400	10	80	Yes

7.3.2 Shrinkage

The shrinkage curves of Cr-based WC powders with different extra C contents and the evolution of the applied pressure are shown in Figure 7.13. The real total C content for

each Cr-based WC sample is given in the figure. The relative density achieved for each Cr-based WC hardmetal is also labelled near the corresponding curve. The Cr-based WC hardmetal with extra 0.5 wt.% addition presents a higher densification than those with extra 1 and 2 wt.% C contents, since the carbon content increases the melting point of the system. Three main stages could be again observed in the evolution of the stroke: (i) the stroke firstly increases due to the contraction of powders under the application of an increasing pressure from 0 to 80 MPa, (ii) then, the stroke decreases slightly due to the thermal expansion of the powders, and (iii) the stroke increases sharply during the fast heating process since the main densification is obtained under the simultaneous application of the maximum pressure and the sintering temperature, and finally remains stable during the subsequent dwell process. In order to further study the effect of C on the Cr-based WC hardmetals, their phase formation, microstructure, density and mechanical properties are investigated.

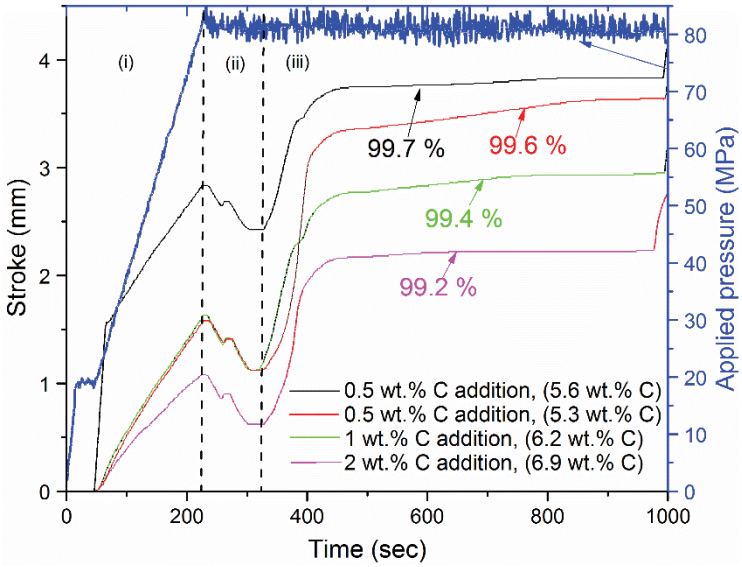

Figure 7.13. Shrinkage of Cr-based WC powders with different C contents and evolution of the applied pressure during the consolidation by SPS.

7.3.3 Phase identification and microstructural analyses

Figure 7.14 shows the XRD diffraction spectra obtained from Cr-based WC hardmetals with different C contents sintered by SPS (1350 °C+400 °C/min+10 min+80 MPa). The identification of the peaks confirms the existance of three main phases: WC, Cr_2O_3, and Cr-based binder. Small new peaks are dectected in Cr-based WC hardmetals with different C contents. The spectra with a higher magnification of the Cr-based WC hardmetals with extra 0.5 wt.% of carbon content, obtained after SPS using or not a W foil to avoid the C contamination, clearly show peaks due to the Fe_3W_3C phase formed

for the lower total carbon content (5.3 wt.% C), which disappear with a small increase in the total real carbon content (5.6 wt.% C). $(Cr,Fe)_7C_3$ and graphite are dectected in the Cr-based WC hardmetals with extra 1 wt.% and 2 wt.% additions, respectectively. Thus, the XRD results confirm that the addition of carbon could prevent the formation of the Fe_3W_3C phase. Moreover, the total carbon content in Cr-based WC hardmetal should be carefully tailored with a value around 5.6 wt.%, in order to generate a microstructure only composed of WC, Cr_2O_3, and Cr-based binder, since Fe_3W_3C is be formed if the C content is lower, whereas a higher content induces the formation of $(Cr,Fe)_7C_3$ or graphite.

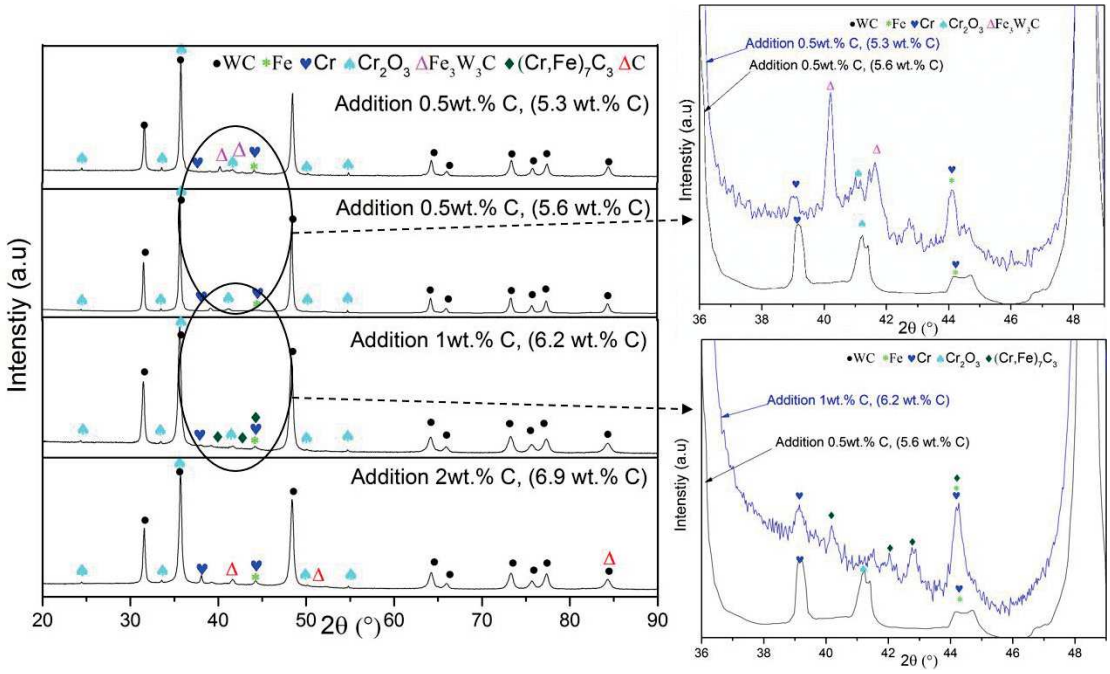

Figure 7.14. XRD spectra of the Cr-based WC hardmetals sintered by SPS with different total C contents.

Figure 7.15 presents the representative SEM micrographs of the consolidated Cr-based WC hardmetals with different extra C contents. EDX analyses are also performed to identify the different phases. Figure 7.15(a) shows that Fe_3W_3C carbide (dark grey) is indeed formed in the Cr-based WC with the lower total carbon content (5.3 wt.% C). Figure 7.15(b) proves that this η–phase disappears with a higher total carbon content (5.6 wt.% C). Figure 7.15(c) and (d) show that $(Cr,Fe)_7C_3$ (dark grey) and graphite phases (black) are found in the Cr-based WC samples with extra 1 wt.% and 2 wt.% carbon contents, respectively. The formed phases identified by microstructural analyses are completely consistent with the previous XRD results. On the other hand, the content of Cr_2O_3 decreases from 9.2 to 8.4 wt.% (the measurements are based on the calculation of its area in the BSE images) with the increase of the total C content from 5.6 to 6.9 wt.%, due to the reaction of oxygen and carbon forming a gaseous compound.

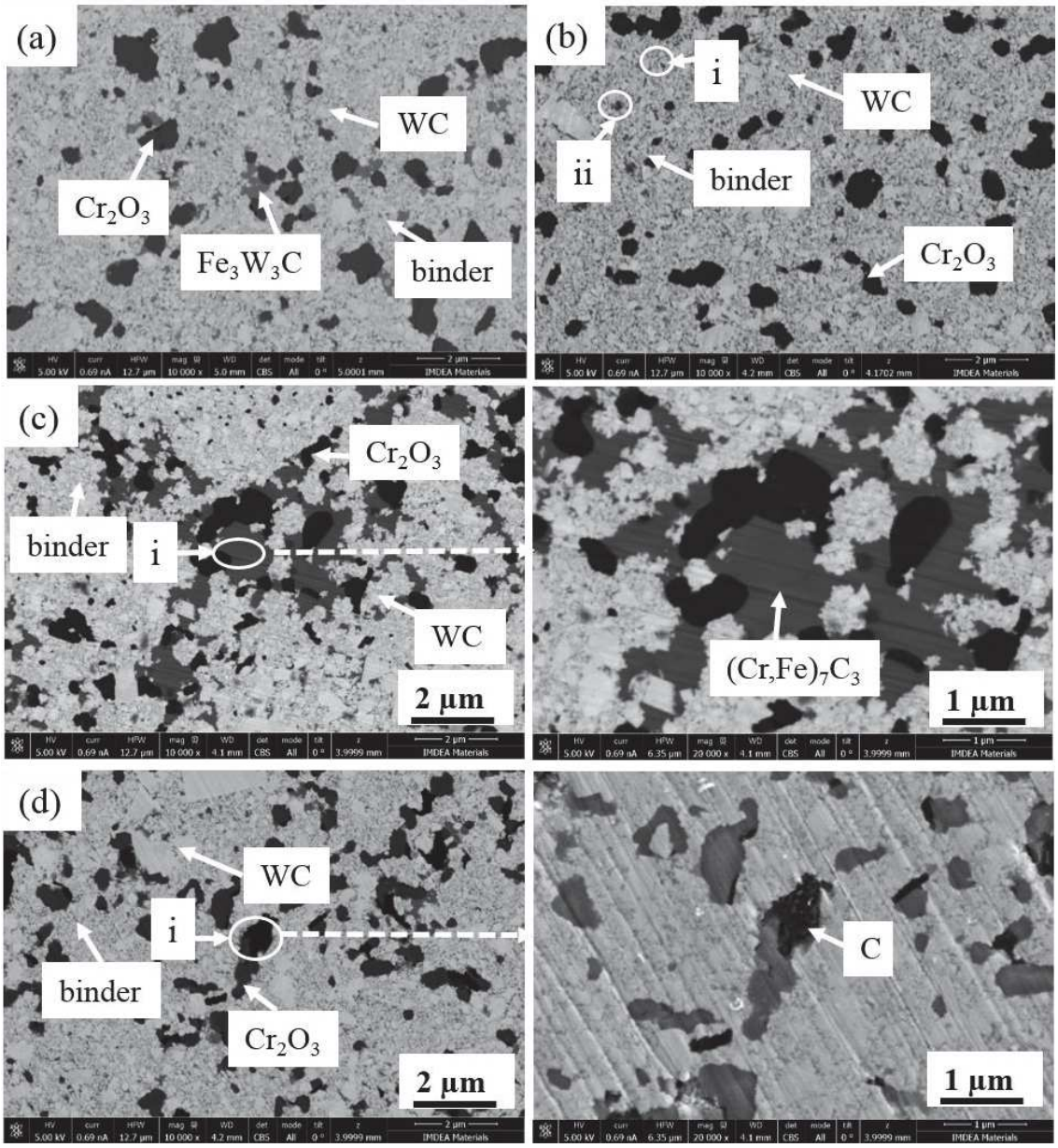

Figure 7.15. BSE micrographs of Cr-based hardmetals consolidated by SPS: (a) 0.5 wt.% C addition (total: 5.3 wt.% C), (b) 0.5 wt.% C addition (total: 5.6 wt.% C), (c) 1 wt.% C addition (total: 6.2 wt.% C), and (d) 2 wt.% C addition (total: 6.9 wt.% C). TEM lamellas are prepared in the regions (i) and (ii) of the image (b). The microstructures in the white circles of figures (c) and (d) are magnified to the right.

In order to further analyse the formed phases, TEM lamellas are prepared in the regions labelled as (i) and (ii) in the Figure 7.15(b). Then, TEM-EDX mapping analyses are carried out in the TEM lamellas to confirm the existence of $(Cr,Fe)_7C_3$ and graphite in the Cr-based WC samples. Figure 7.16 shows the HAADF-STEM images of regions (i) and (ii) in the Cr-based WC hardmetal with a total C content of 5.6 wt.%, together with the corresponding EDX elemental mapping images and the EDX analyses in selected areas. These results confirm the existence of a Cr-based binder, WC, thin $(W,Cr)_2C$ and Cr_2O_3.

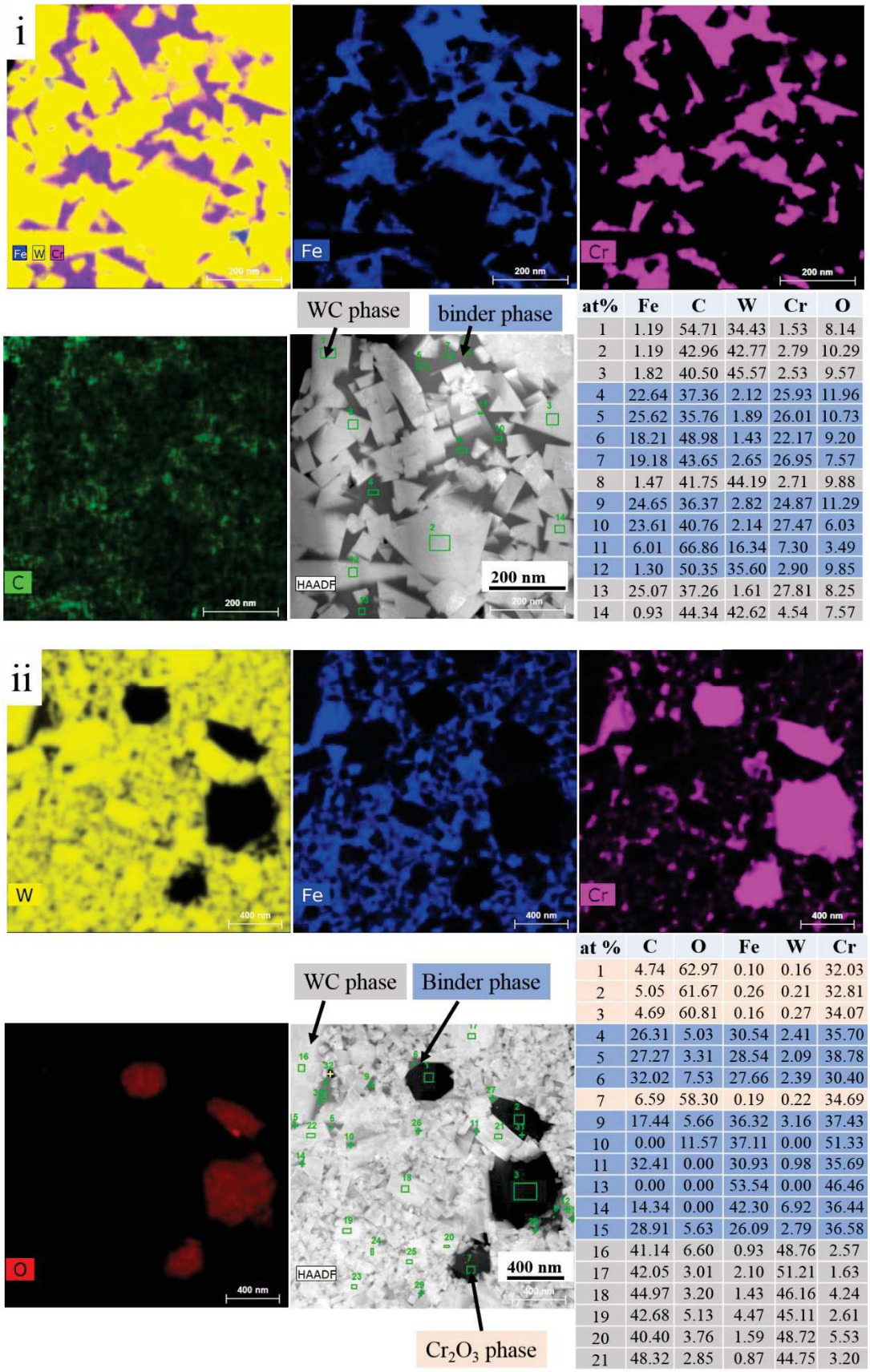

at%	Fe	C	W	Cr	O
1	1.19	54.71	34.43	1.53	8.14
2	1.19	42.96	42.77	2.79	10.29
3	1.82	40.50	45.57	2.53	9.57
4	22.64	37.36	2.12	25.93	11.96
5	25.62	35.76	1.89	26.01	10.73
6	18.21	48.98	1.43	22.17	9.20
7	19.18	43.65	2.65	26.95	7.57
8	1.47	41.75	44.19	2.71	9.88
9	24.65	36.37	2.82	24.87	11.29
10	23.61	40.76	2.14	27.47	6.03
11	6.01	66.86	16.34	7.30	3.49
12	1.30	50.35	35.60	2.90	9.85
13	25.07	37.26	1.61	27.81	8.25
14	0.93	44.34	42.62	4.54	7.57

at %	C	O	Fe	W	Cr
1	4.74	62.97	0.10	0.16	32.03
2	5.05	61.67	0.26	0.21	32.81
3	4.69	60.81	0.16	0.27	34.07
4	26.31	5.03	30.54	2.41	35.70
5	27.27	3.31	28.54	2.09	38.78
6	32.02	7.53	27.66	2.39	30.40
7	6.59	58.30	0.19	0.22	34.69
9	17.44	5.66	36.32	3.16	37.43
10	0.00	11.57	37.11	0.00	51.33
11	32.41	0.00	30.93	0.98	35.69
13	0.00	0.00	53.54	0.00	46.46
14	14.34	0.00	42.30	6.92	36.44
15	28.91	5.63	26.09	2.79	36.58
16	41.14	6.60	0.93	48.76	2.57
17	42.05	3.01	2.10	51.21	1.63
18	44.97	3.20	1.43	46.16	4.24
19	42.68	5.13	4.47	45.11	2.61
20	40.40	3.76	1.59	48.72	5.53
21	48.32	2.85	0.87	44.75	3.20

Figure 7.16. HAADF-STEM images in regions (i) and (ii) of Figure 7.15(b) in the Cr-based WC hardmetal with a total C content of 5.6 wt.%, and EDX elemental mapping images showing W (yellow), Fe (blue), Cr (pink), C(green) and O (red). Corresponding elemental at.% values in selected areas.

The WC grains are developed with prismatic shapes and with a fine average grain size of 100 nm. Considering the relationship between WC grain size and hardness of WC-Co hardmetals [13], a distribution of nanosized WC grain size may lead to an extremely high level of hardness.

Figure 7.17 shows the HAADF-STEM image of the Cr-based WC hardmetals with an extra 1 wt.% C content (total: 6.2 wt.% C), the EDX elemental mapping and the EDX area analyses performed in four different areas. The elemental mappings demonstrate that the grey area is formed by C, Fe, and Cr elements. In addition, the EDX area analyses show that the stoichiometry of C and Fe-Cr approximates to 3:7. Thus, the compound is probably $(Cr,Fe)_7C_3$, as was suggested by the XRD results. Kaplan *et al.* [14] also reported the formation of this carbide type M_7C_3 (M = Fe and Cr) in WC-CoCr hardmetals after the sintering process.

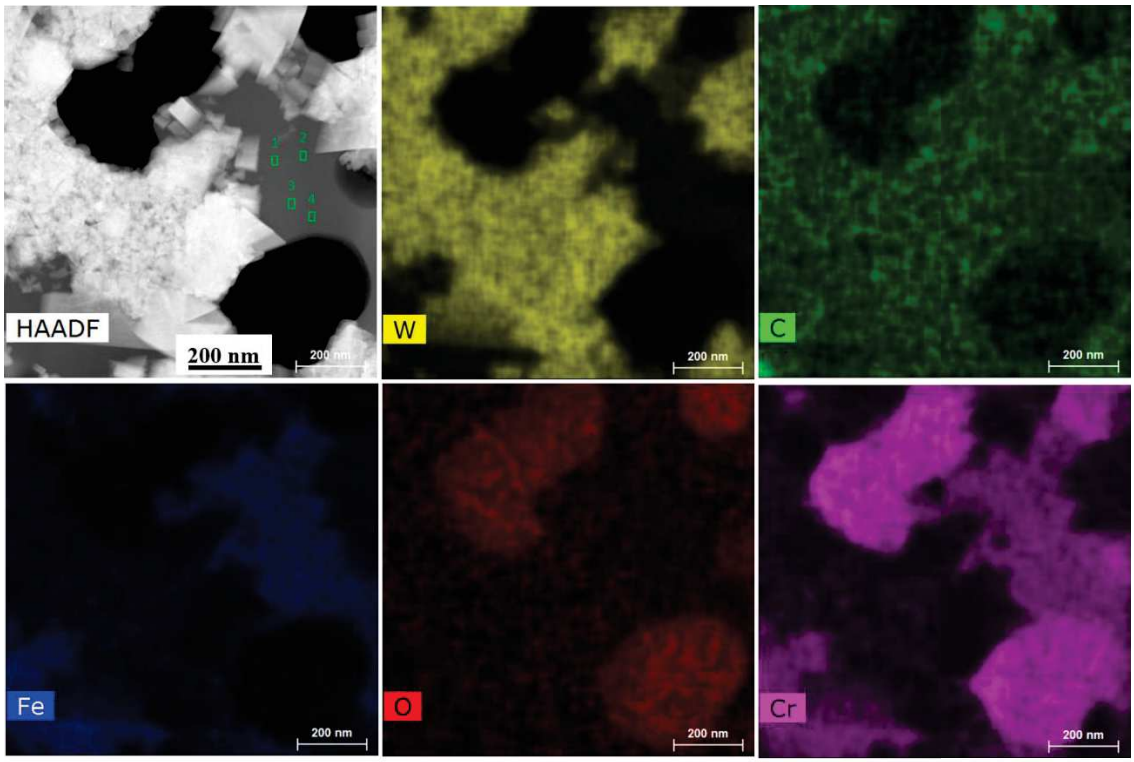

at %	C	O	Fe	W	Cr
1	30.70	0.81	22.85	4.31	41.33
2	30.49	3.10	22.07	0.90	43.44
3	31.76	2.46	18.58	2.10	45.10
4	35.80	4.00	21.92	1.42	36.86

Figure 7.17. HAADF-STEM image of the Cr-based WC hardmetal with an extra 1 wt.% C content (total: 6.2 wt.% C) consolidated by SPS. EDX elemental mapping images showing W (yellow), C (green), Fe (blue), O (red), and Cr (pink). Corresponding elemental at.% values in selected areas.

Figure 7.18 shows the HAADF-STEM image of Cr-based WC hardmetals with an extra 2 wt.% C content (total: 6.9 wt.% C), the corresponding EDX elemental mapping and the elemental at.% values in selected areas of the specimen. There is a black region with two different contrasts: a light dark and a deep black. The selected elemental mappings demonstrate that the deep black area is rich in carbon, whereas the light dark area corresponds to Cr_2O_3. Thus, some carbon exists as graphite in the Cr-based WC hardmetal with an extra 2 wt.% C content after SPS consolidation. The presence of graphite is not useful in these materials since this phase exhibits a low hardness, which is definitely harmful to the mechanical properties.

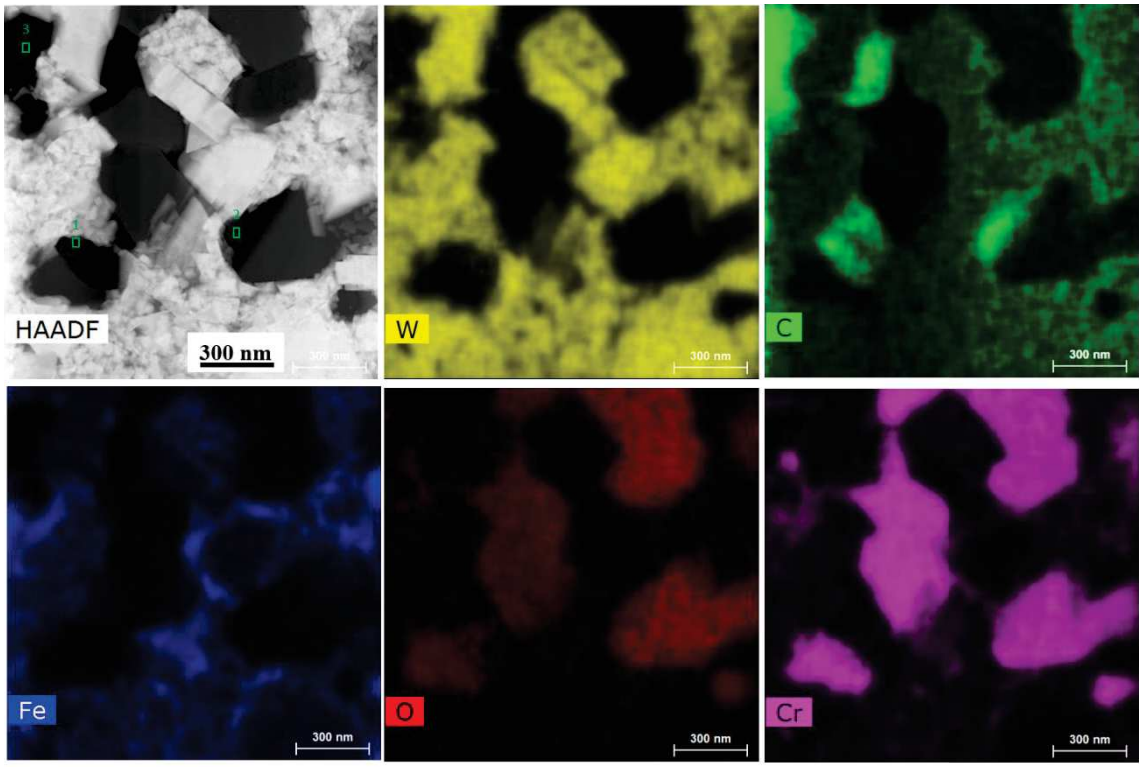

at %	C	O	Fe	W	Cr
1	96.13	0.00	0.00	3.87	0.00
2	96.06	2.30	1.14	0.10	0.40
3	99.26	0.00	0.00	0.17	0.57

Figure 7.18. HAADF-STEM image of the Cr-based WC hardmetal with an extra 2 wt.% C content (total: 6.9 wt.% C) consolidated by SPS. EDX elemental mapping images showing W (yellow), C (green), Fe (blue), O (red), and Cr (pink). Corresponding elemental at.% value in selected areas.

After the STEM analyses in these three Cr-based WC hardmetals with a total carbon contents of 5.6, 6.2 and 6.9 wt.%, it is worth mentioning that the $(W,Cr)_2C$ carbide always is found as a thin interphase between WC and Cr_2O_3. This fact is really important, since the $(W,Cr)_2C$ phase will contribute to increase the toughness of the material. This phase was not detected by XRD, probably due to its small amount within the specimen.

As main conclusion after all these microstructural analyses, it can be affirmed that the carbon content in Cr-based WC hardmetals determines the phase formation. The different phases will influence the properties. Hence, the best combination of properties would be achieved when the formation of undesirable phases, such as Fe_3W_3C, $(Cr,Fe)_7C_3$ or graphite, is avoided. Therefore, mechanical properties of Cr-based WC hardmetals with different carbon contents will be evaluated and discussed in the next sections, by means of hardness-fracture toughness measurements, nanoindentation and compressive tests.

7.3.4 Mechanical properties

7.3.4.1 Hardness and fracture toughness

Representative images of the cracks generated in Cr-based WC hardmetals with different C contents after Vickers hardness tests are shown in Figure 7.19. The values of fracture toughness (K_{IC}) are calculated from the measurement of the total crack length emanating from the four corners and the indentation lengths, using the Palmqvist indentation method with a load of 30 kg.

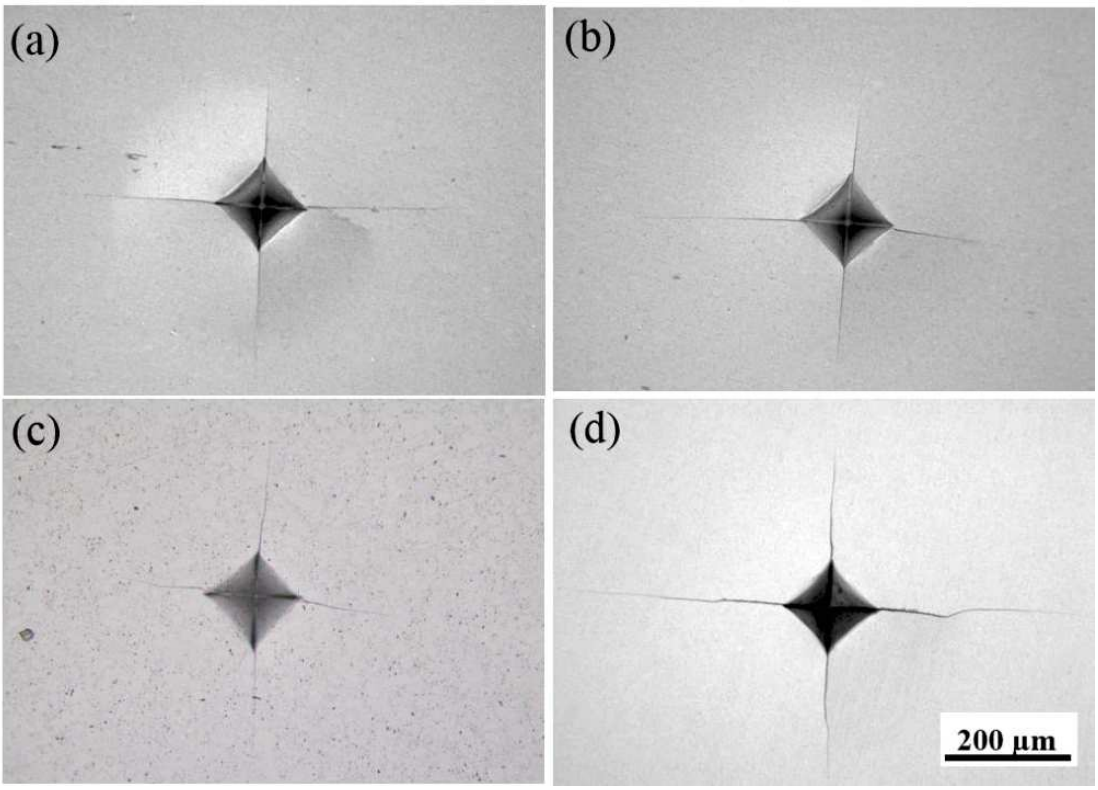

Figure 7.19. Images of the cracks generated by Palmqvist indentation performed in SPSed Cr-based WC hardmetals with different carbon contents, (a) 0.5 wt.% extra C content (total: 5.3 wt.% C), (b) 0.5 wt.% extra C content (total: 5.6 wt.% C), (c) 1 wt.% extra C content (total: 6.2 wt.% C), and (d) 2 wt.% extra C content (total: 6.9 wt.% C).

The mean values of Vickers hardness (HV30) and K_{IC} are obtained from the average value of at least four tests. Results are listed in Table 7.4.

Table 7.4. Measured total crack length and indentation length in SPSed Cr-based WC hardmetals and their corresponding average hardness and fracture toughness values.

Cr-based hardmetals with different extra C contents	Total crack length (μm)	Indentation length (μm)	HV30 (kgf/mm^2)	K_{IC} (MPam$^{1/2}$)	$\overline{\text{HV30}}$ (kgf/mm^2)	$\overline{K_{IC}}$ (MPam$^{1/2}$)
0.5 wt.% C addition (total: 5.3 wt.% C)	1.089	0.162	2086	6.6	2094±10	6.9±0.2
	1.045	0.163	2046	7.1		
	1.065	0.162	2073	6.7		
	1.054	0.162	2100	6.9		
0.5 wt.% C addition (total: 5.6 wt.% C)	0.728	0.159	2200	8.2	2219±16	8.2±0.1
	0.711	0.158	2228	8.3		
	0.767	0.158	2228	8.0		
	0.731	0.158	2220	8.2		
1 wt.% C addition (total: 6.2 wt.% C)	0.887	0.161	2146	7.3	2164±31	7.4±0.2
	0.881	0.161	2146	7.3		
	0.865	0.160	2173	7.4		
	0.860	0.162	2170	7.4		
2 wt.% C addition (total: 6.9 wt.% C)	0.850	0.170	1924	7.1	1914±13	7.0±0.1
	0.857	0.170	1924	7.0		
	0.853	0.171	1902	7.0		
	0.851	0.171	1905	7.1		

Figure 7.20 shows the relative density, average WC grain size, Vickers hardness, and fracture toughness of the Cr-based WC hardmetals with different extra carbon contents consolidated by SPS. Figure 7.20(a) shows that all these Cr-based WC hardmetals have achieved near full density, indicating that the application of a higher sintering temperature (1350 ºC instead of 1200 ºC used in samples without extra carbon contents) and a higher pressure (80 MPa instead of 50 MPa applied in samples without extra carbon contents) are beneficial sintering parameters for improving the densification. The relative density increases slightly from 99.6 to 99.7 % with the increase of the carbon content from 5.3 to 5.6 wt.%, since the small extra C addition may react with oxygen and remove some oxygen in the terms of gaseous CO/CO_2, leading to an improvement in density. Then, the relative density decreases from 99.6 to 99.2 % with the increase of the carbon content from 5.6 to 6.9 wt.%, since the addition of more C content increases the melting point of W-C-Cr-Fe system, leading to a reduction of the final densification reached.

The hardness and fracture toughness depend on the density achieved, the phases formed and the size of the grains. In particular, the toughness is very sensitive to the presence of pores, so it varies following a similar trend to that of density, as shown in Figure 7.20(b).

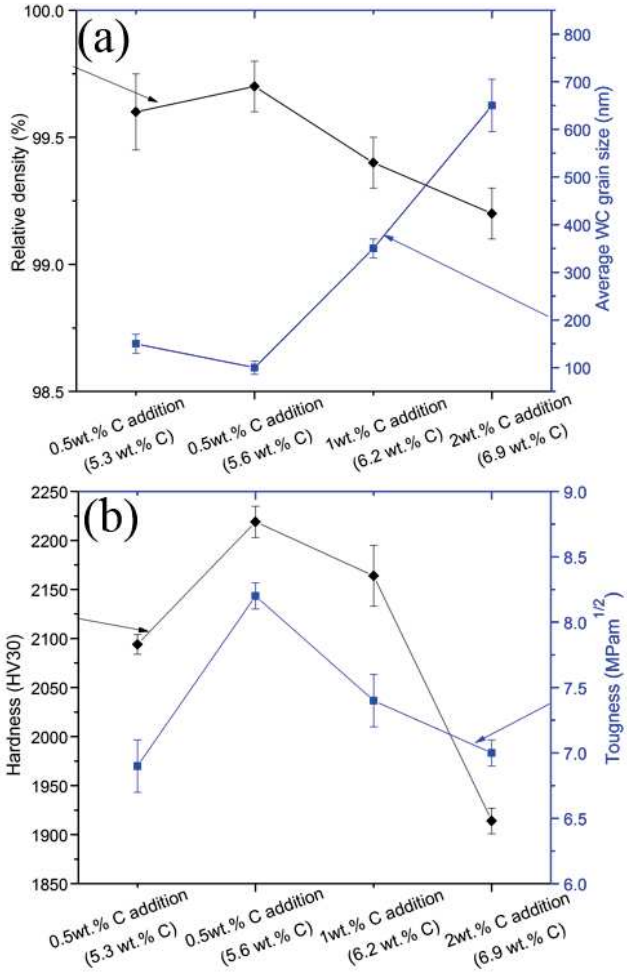

Figure 7.20 Relative density and average WC grain size (a) and Vickers hardness and fracture toughness values (b) for Cr-based WC hardmetals consolidated by SPS with different extra C contents.

Anyway, it is important to also consider that the fracture toughness increases firstly with the increase of the total carbon content from 5.3 to 5.6 wt.%, since the carbon addition reduces the formation of brittle Fe_3W_3C. Subsequently, the fracture toughness begins to decrease with the increase of the total carbon content from 5.6 to 6.9 wt.% due the formation of brittle $(Cr,Fe)_7C_3$ or graphite. Then, both factors: density and formation of different phases are responsible for the evolution followed by the fracture toughness.

On the other hand, the hardness is affected by the average WC grain size. Schubert *et al.* [13] reported that the influence of the grain size on the mechanical properties of hardmetals is commonly expressed in an equation that has the Hall-Petch form: the values of hardness increase with the reciprocal root of the grain size over the range of conventional grain sizes. When the grain size of WC reaches the nanoscale, the increase of hardness in nanostructured composites does not decrease their bulk fracture toughness [15]. The average WC grain size of Cr-based WC hardmetals with a total carbon content

of 5.6 wt.% is close to 100 nm, which is the main factor leading to an extremely high value of hardness (2219 HV30), considering that the volume fraction of WC reinforcement is only 70%, which is lower than the 80% usually added to commercial WC-Co hardmetals. With the increase of the carbon content above 5.6 wt.% the WC grain starts to grow significantly from 100 to 650 nm, decreasing notably the hardness values reached.

The Cr-based WC hardmetal with 5.6 wt.% of total carbon content has achieved the best combination of high hardness and toughness data (2219 HV30 + 8.2 $MPam^{1/2}$), which are competitive values with those exhibited by commercial WC-Co hardmetals. For this reason, this is the lower total carbon content (5.6 wt.%) selected for the subsequent analyses (nanoindentation tests, compressive tests, oxidation measurements and wear tests) since below this value the fracture toughnes and harness values are poorer.

7.3.4.2 Nanoindentation tests

The nanohardness and Young's modulus of Cr-based WC hardmetals with different extra C contents are calculated by nanoindentation tests. Twenty-five indentations are carried out on each Cr-based WC hardmetal, in order to obtain the average value of hardness and elastic modulus. Figure 7.21 shows the evolution of hardness (H) and reduced Young's modulus (E_r) as a function of the penetration depth. The measured H and E_r data, corresponding to the Cr-based WC hardmetals with extra 0.5 and 1 wt.% C contents, exhibits a more uniform distribution against the penetration depth than those of the Cr-based WC hardmetal with 2 wt.% of extra C content, probably due to the existence of a more homogeneous microstructure without presence of soft graphite. The average nanohardness and reduced modulus values of the Cr-based WC hardmetals with extra 0.5, 1 and 2 wt.% carbon contents are H=27.7±0.4 GPa and E_r =335.8±3.0 GPa, H=25.9±0.2 GPa and E_r =269.8±2.0 GPa, and H=23.4±1.7 GPa and E_r =308.6±10.1 GPa, respectively. The trend of nanohardness agrees with our previous results: the hardness decreases with the increase of the extra C content from 0.5 to 2 wt.%. The real elastic modulus (E) of Cr-based WC hardmetals with extra 0.5, 1, and 2 wt.% carbon contents are calculated with the equation 3-9 and they reach a value of E=456.0±3.1 GPa, E=337.2±2.0 GPa, and E =405.4±11.2 GPa, respectively, which are comparable data to those exhibited by commercial WC-Co hardmetals, with values are ranging from 350 to 700 GPa [16].

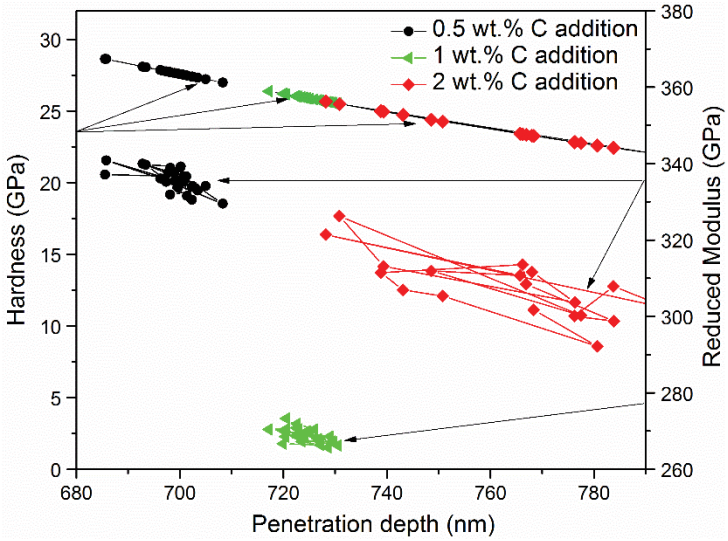

Figure 7.21. Evolution of hardness and reduced Young's modulus against penetration depth obtained by nanoindentation tests performed in Cr-based WC hardmetals with different extra C contents.

These results suggest that the presence of big areas of $(Cr,Fe)_7C$ carbide in the sample with 1 wt.% of extra carbon content (previously shown in Figure 7.15) produces a significant drop in the elastic modulus. Finally, it is worth mentioning that the nanoindentation tests demonstrate the extremely high nanohardness and good Young's modulus obtained in the Cr-based hardmetal with extra 0.5 wt.% C content.

7.3.4.3 Compressive tests

The compressive strength is another important mechanical property for hardmetals in service used as cutting tools, since it reflects the ability of the bulk material to sustain the compressive deformation. Thus, the compressive stress and strain of Cr-based WC hardmetals are investigated in this section. The compressive stress-strain curves of SPSed Cr-based WC hardmetals with different C contents at RT, 300 °C, and 600 °C are presented in Figure 7.22. All samples have a brittle fracture behaviour from RT to 600 °C, since these curves are nearly linear with limited plastic deformation until the final fracture. The Cr-based WC hardmetals with extra 0.5 wt.% of C content (total: 5.6 wt.% C) and extra 2 wt.% additions (total: 6.9 wt.% C) have the highest and the lowest maximum compressive stresses from RT to 600 °C, respectively. Lee *et al.* [17] demonstrated that the compressive strength of hardmetals was directly related to their hardness and toughness at room temperature. The Cr-based WC hardmetal with extra 0.5 wt.% C content has the best combination of hardness and toughness values at room temperature, leading to the highest compressive strength, as expected, since this hardmetal consists of only WC hard phase, $(W,Cr)_2C$, Cr_2O_3, and Cr-based binder. On the contrary, additional

$(Cr,Fe)_7C_3$ or soft graphite phase exist in the Cr-based WC hardmetals with extra 1 and 2 wt.% C contents, respectively, which will decrease their compressive strength. The fracture strain during compressive tests is controlled by the crack propagation [18]. Thus, the maximum compressive strain achieved at room or at elevated temperature is dependent on the phase formation and on the density reached by the samples. Therefore, the Cr-based WC hardmetal with extra 0.5 wt.% C content, without presenting phases such as $(Cr,Fe)_7C_3$ or graphite, having the smallest WC grain size and exhibiting the higher density, has reached the highest compressive strain which agrees with the phenomenon detected in Co-based WC hardmetals [16]. In all cases, the drop of the strength is observed with the increase of temperature since the strength of Cr-based binder becomes lower due to a softening phenomenon. This phenomenon is in good agreement with the similar tendency observed in WC-Co hardmetals, in which the reduction of their maximum compressive strength at high temperature is related to the softening of the Co phase [16]. There exist small "steps" (marked by blue circles) present in the stress-strain curve of the Cr-based WC hardmetal with an extra 0.5 wt.% carbon content (total: 5.6 wt.% C), as shown in Figure 7.22(a), due to cracks formed during the application of the pressure which may lead to delamination.

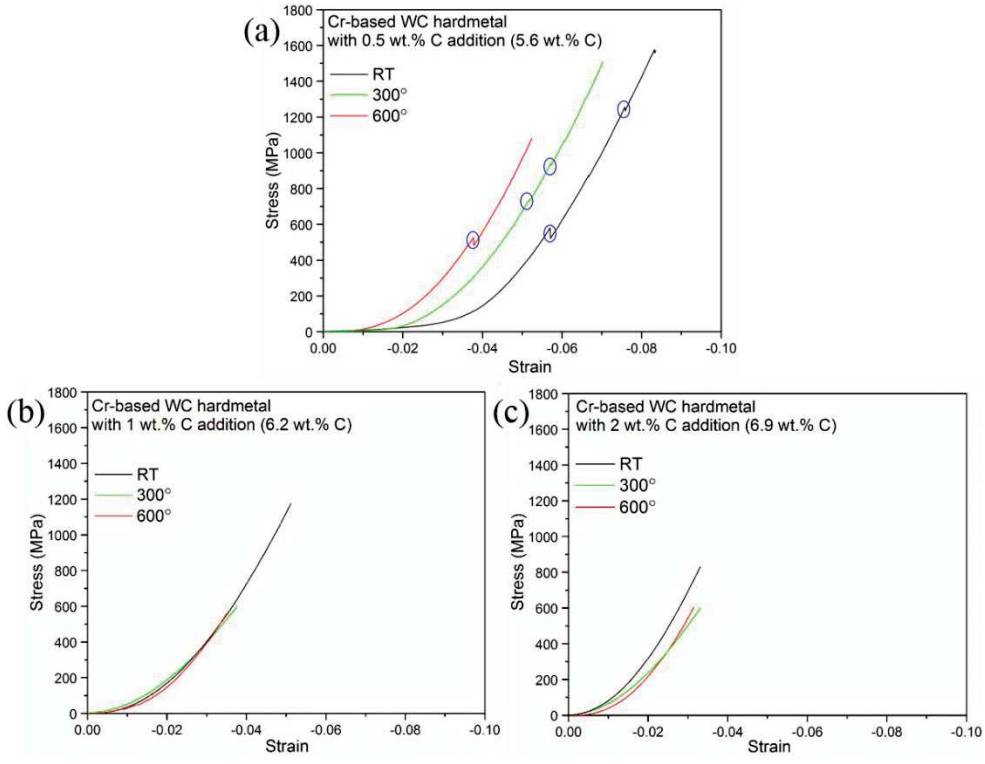

Figure 7.22. Stress-strain curves of SPSed Cr-based WC hardmetals with different extra C contents: (a) 0.5 wt.% C (total: 5.6 wt.% C), (b) 1 wt.% C (total: 6.2 wt.% C), and (c) 2 wt.% C (total: 6.9 wt.% C).

The maximum stress and strain values reached in Cr-based WC hardmetals with different extra C contents are plotted as a function of the temperature (from RT to 600 °C), as can be seen in Figure 7.23.

The analysis of the curves plotted in Figure 7.23 shows that both maximum stress and strain continually decrease with the increase of the temperature from RT to 600 °C.

The fracture stress and strain are controlled by the crack propagation and by the softening of the binder phase. In the Cr-based WC hardmetal with extra 0.5 wt.% C content, there is a smaller amount of big brittle carbides and then less crack growth.

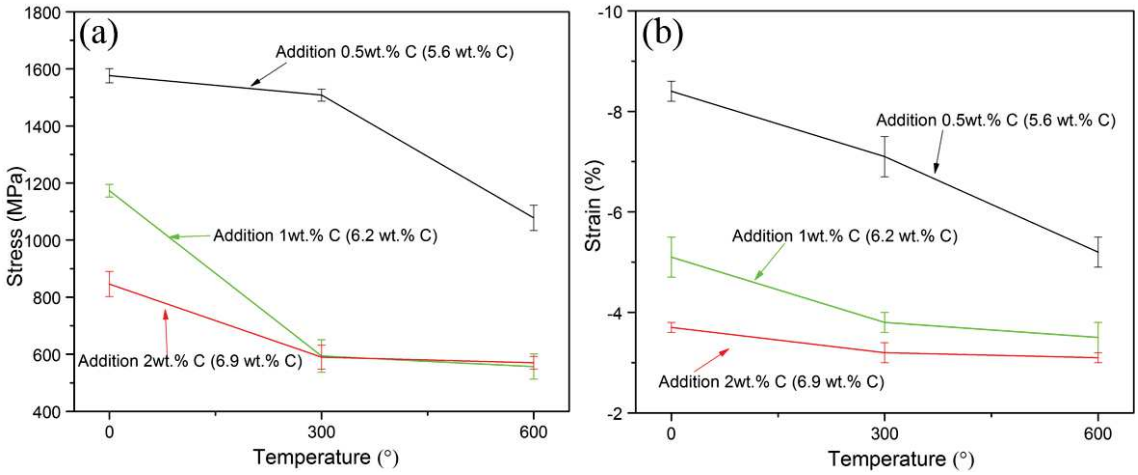

Figure 7.23. Mean value and deviation of the maximum stress (a) and strain (b) of Cr-based WC hardmetals with different C contents at RT, 300 °C, and 600 °C.

The microstructure of the Cr-based WC hardmetals with extra 0.5 wt.% C content (total: 5.6 wt.% C) after compressive test at different temperatures are presented in Figure 7.24. Figure 7.24(a), corresponding to tests performed at RT, shows a separated layer after the compressive test, which may correspond to the “steps” found in the strain-stress curve.

At elevated temperature, the softened Cr-based binder speeds up the crack propagation and further failure. Especially at 600 °C, the EDX analysis demonstrates that the surface of the tested sample is oxidised, as shown in Figure 7.24(e), which may be another reason for the reduction of the strength due to the decrease of the volume of the bulk materials under stress.

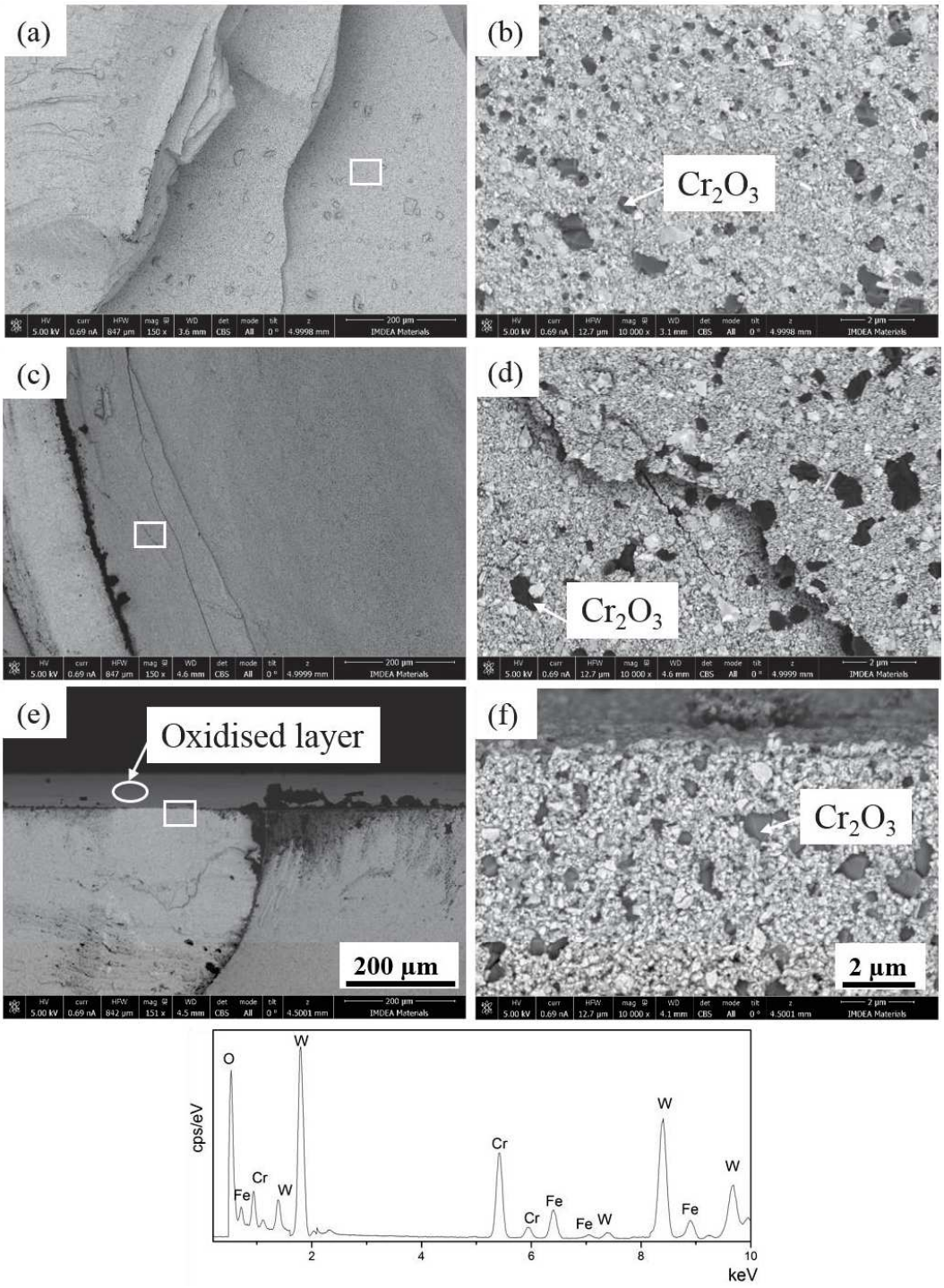

Figure 7.24. Microstructure of the Cr-based WC hardmetal with extra 0.5 wt.% C content after compressive tests under different temperatures (general view images on the left and higher magnification of the white square region on the right): (a) and (b) RT, (c) and (d) 300 °C, (e) and (f) 600 °C. EDX analysis in the oxidised layer (marked white circle region).

Figure 7.25 shows the microstructure of the Cr-based WC hardmetals with extra 1 wt.% C content after compressive test at different temperatures. The microstructural analyses show the existence of brittle $_3$ phase and the oxidised layer at 600 °C. In order to explain the fracture pathways in WC-Co hardmetals, Sigl and Exner [19] reported a fracture

model in which cracks propagate transgranularly through carbides and intergranularly between binder grains. For this nano-sized hardmetal, Sigl and Exner correlations reasonably predict an increase of both transgranular fracture through the carbide crystals, and fracture through the binder phase, since the contiguity of WC decreases with the increase of the WC grain size [20]. The compressive strength decreases with the decrease of the toughness due to a lower density and a higher WC grain size, leading to linear crack paths with less energy consumption. In addition, the thickness of the oxidised layer for the hardmetal with 1 wt.% of extra carbon content is even thicker than that of the Cr-based WC hardmetal with an extra 0.5 wt.% C contents at 600 °C, as shown in Figure 7.24(e), which is another reason for a worse compressive strength.

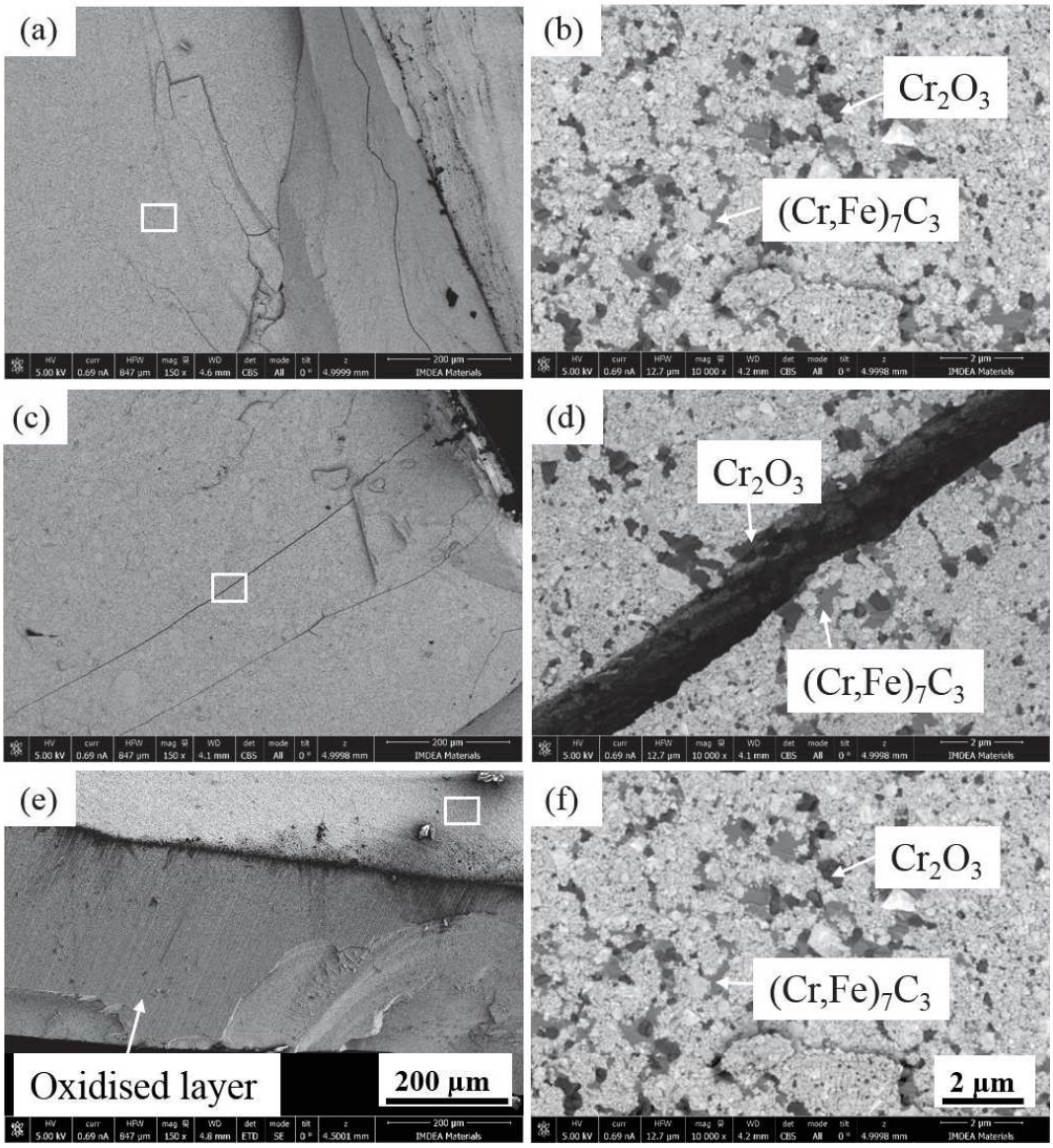

Figure 7.25. Microstructure of the Cr-based WC hardmetals with extra 1 wt.% C content after compressive tests at different temperatures (general view images on the left and higher magnification of the white square area on the right): (a) and (b) RT, (c) and (d) 300 °C, (e) and (f) 600 °C.

Figure 7.26 presents the microstructure of Cr-based WC hardmetals with extra 2 wt.% C addition after compressive test at different temperatures. More cracks and defects appear in this microstructure due the existence of soft graphite, as reported in WC-Co hardmetals [21]. Trung *et al.* [22] also found that the existence of free graphite decreases the mechanical properties of WC-stainless steel hardmetals, since graphite acts as "pores", inducing the formation and growth of cracks. Thus, the Cr-based WC hardmetal with extra 2 wt.% C content has less plastic deformation and less strength than the Cr-based WC hardmetal with extra 0.5 and 1 wt.% C additions.

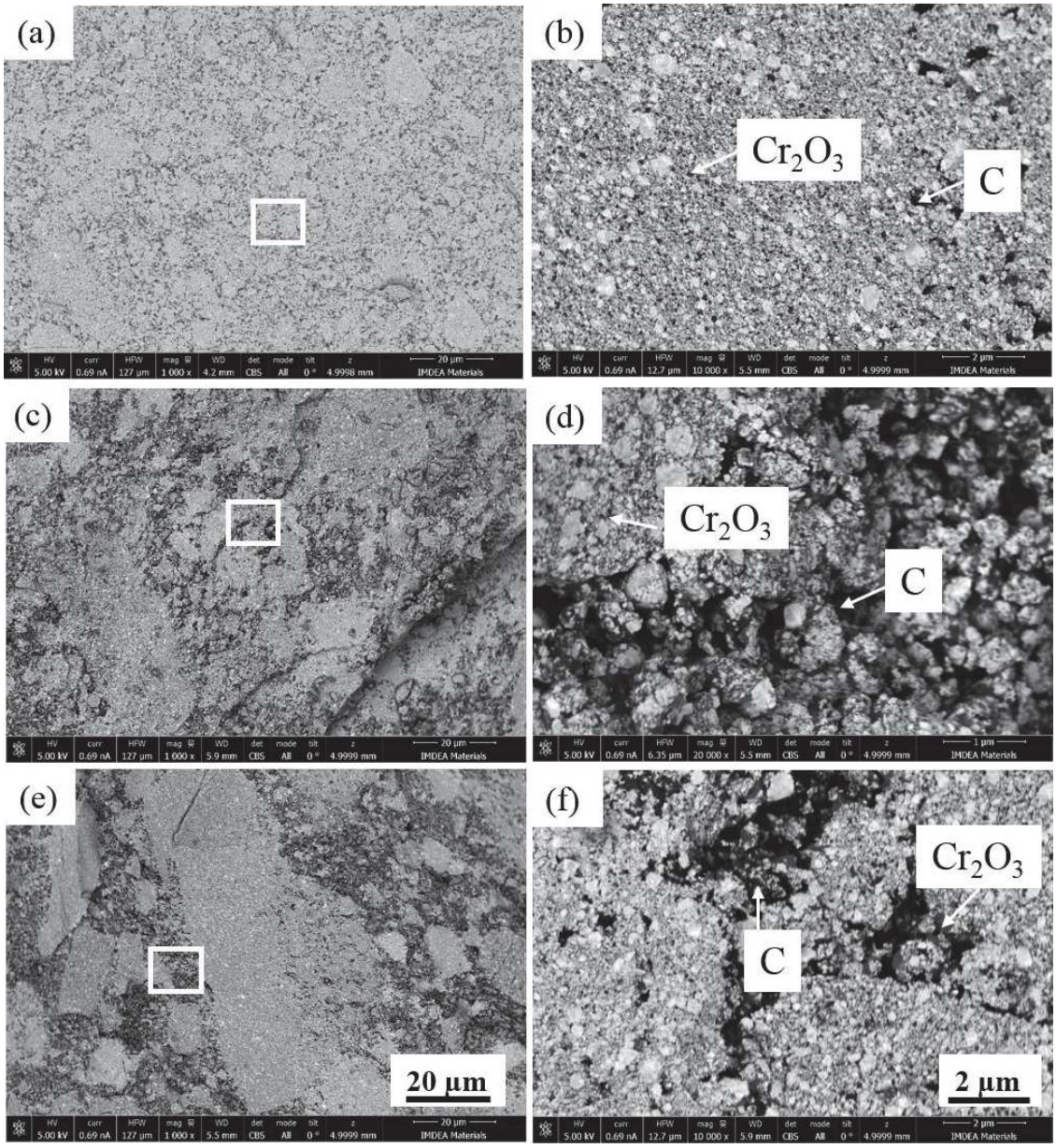

Figure 7.26. Microstructure of the Cr-based WC hardmetal with extra 2 wt.% C content after compressive tests at different temperatures (general view images on the left and higher magnification of the white square area on the right): (a) and (b) RT, (c) and (d) 300 °C, (e) and (f) 600 °C.

The above investigated mechanical properties are important approaches to assess the industrial interest of Cr-based WC hardmetals. In addition, in order to determine the viability of using them in other specific applications, such as oxidation and wear resistant parts, the oxidation and wear resistances of these Cr-based WC hardmetals also need to be deeply characterised.

7.4 Oxidation resistance

In addition to a good combination of toughness and hardness, hardmetals used as cutting tools also require a high oxidation resistance. The oxidation resistance of Cr-based WC hardmetals samples with different extra C contents are evaluated by an isothermal method using a thermogravimetric analyzer (TGA, Q50 instrument). Then, specimens are exposed at three different temperatures (750, 800, and 850 °C) at a heating rate of 20 °C/min and with a holding time of 1 h. The flow of synthetic air is of 10 ml/min. Furthermore, in order to calculate the value of the activation energy by the isoconversion method, two sintering rates (5 and 20 °C/min) are used when Cr-based WC hardmetals samples are heated at 850 °C. All these experiments are repeated for two times, in order to ensure the consistence in the results. Prior to the oxidation tests, all the samples with a cuboid shape (2×2×3 mm) are well polished and cleaned in propanol for 10 min followed by drying in furnace at 110 °C for 30 min.

Figure 7.27 shows the evolution of the mass gain per unit area (α) in Cr-based WC hardmetals with different extra C contents (0.5, 1, and 2 wt.%) after 1 h at three different temperatures: 750, 800, and 850 °C. The black line indicates the corresponding evolution of temperature during the heating process. Figure 7.27(a) shows a small reduction of the α value between 200 and 600 °C. This phenomenon may be due to the decarburisation of WC into W_2C or W in Cr-based WC hardmetals, just before these three samples begin to be oxidised. Voitovich et al. [23] also reported the formation of W_2C or metallic W as decarburisation products obtained at the initial stage of oxidation, which were responsible for the decrease of mass gain during oxidation of a WC-Co hardmetal alloy at temperatures between 50 and 600 °C. The curves demonstrate that the oxidation resistance decreases with the increase of the carbon content, since the value of α increases for the same heating treatment. The oxidation is controlled by a surface chemical reaction in which the reactant is converted to another material leaving behind the unreacted layer [24], since a typical linear increase of α with time is observed during the oxidation, taking

place during the soaking time at the maximum temperature in all Cr-based WC hardmetals. Aristizabal *et al.* [25] also demonstrated that the oxidation of WC-Co and WC-NiCoCr hardmetals between 650 and 800 °C was also controlled by a surface chemical reaction, during which empirical rate law was linear. Figure 7.27(c) shows that the heating rate (in a range from 5 to 20 ºC/min) has a small effect on the oxidation rate once the maximum temperature is reached, since the value of α increases slightly for the lowest heating rate of 5 °C/min.

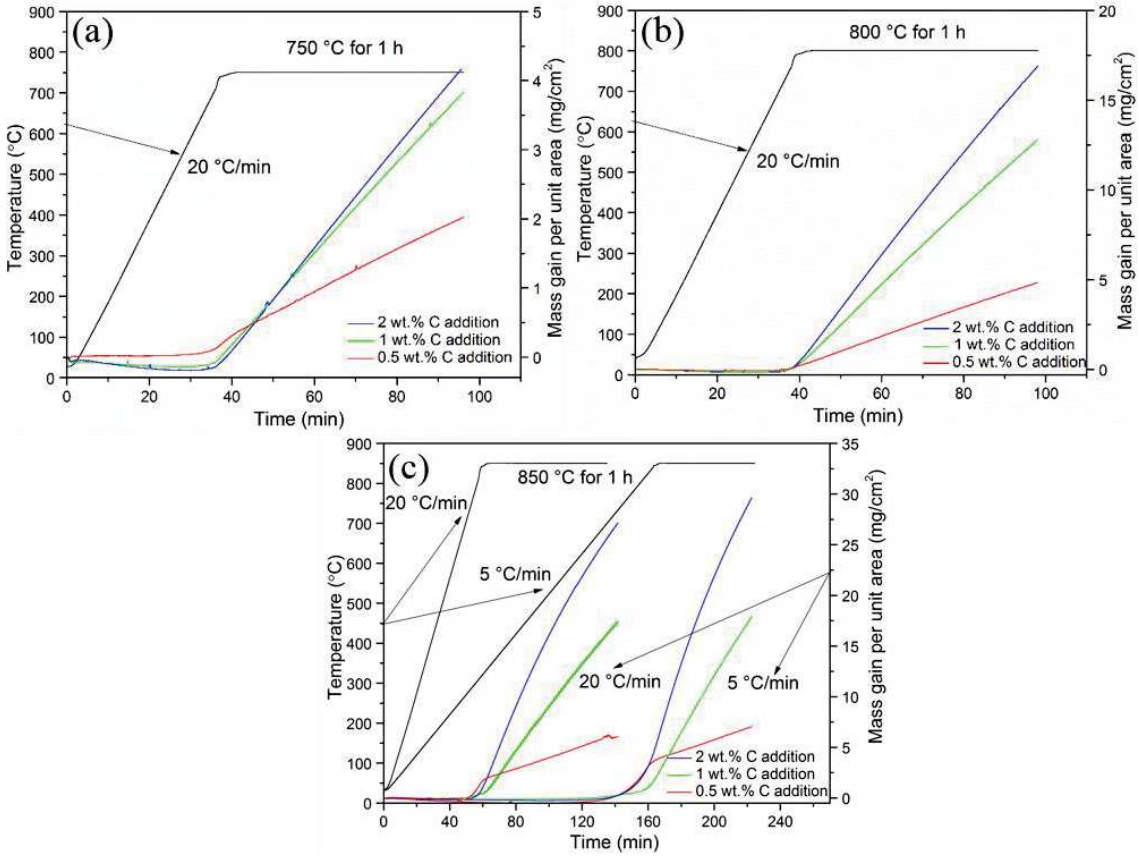

Figure 7.27. TGA analyses: mass gain per unit area (α) against time for Cr-based WC hardmetals with extra 0.5, 1 and 2 wt.% carbon contents after 1 h at different isothermal temperatures (a) 750 °C, (b) 800 °C, and (c) 850 °C.

Figure 7.28 shows mass gain per unit area (α) against temperature for Cr-based hardmetals with different extra C additions, together with Co-based and Ni-based hardmetals data detailed in the literature for the same heating conditions [25-26]. In these investigations, the increase of the binder content improved the oxidation resistance, since the metallic binder (Co, Ni and Ni-Co) decreased the oxidation rate of WC-based hardmetals compared to pure tungsten carbide [23], [25]. In this work, all the Cr-based hardmetals (WC-10Cr-6.8Fe), with only 16.8 wt.% of binder content, show a better

oxidation resistance than Co-based and Ni-based hardmetals with higher binder contents (25 wt.%). Even the Cr-based hardmetal with an extra 2 wt.% C content, which has the highest α value of the hardmetals proposed in this research, exhibits an excellent oxidation resistance compared to Co-based and Ni-based hardmetals [25]. The Cr-based WC sample with an extra 0.5 wt.% C contents exhibits the highest oxidation resistance from 750 to 850 °C, since it has the lowest α value. The oxidation rates depend on the oxidation products formed, which will be discussed in detail during the following phase identification and microstructural analyses.

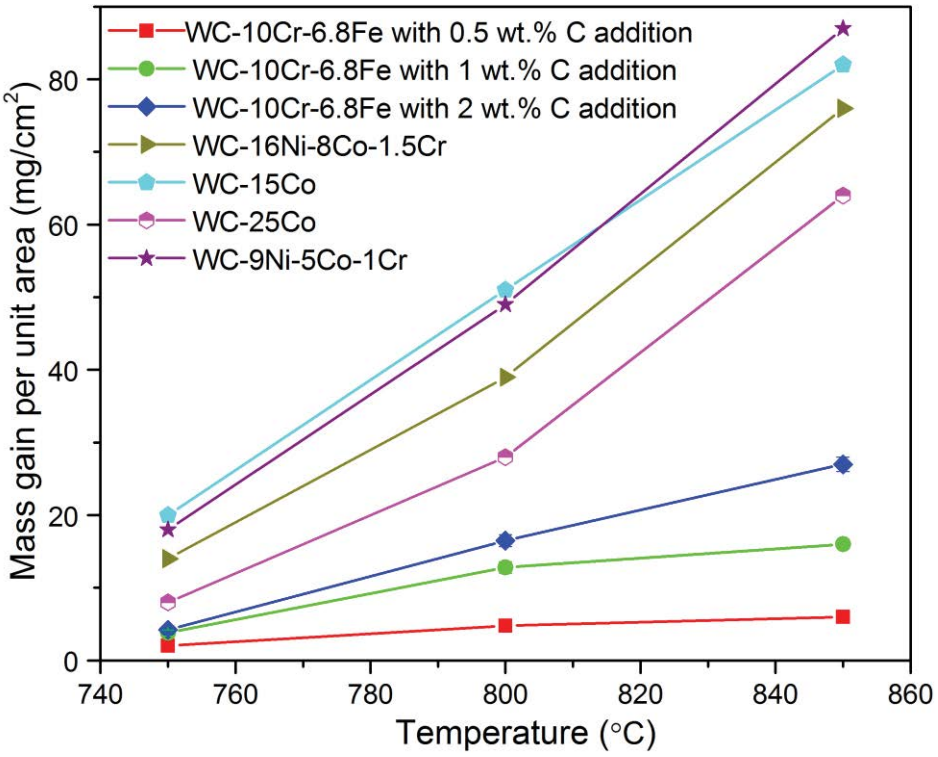

Figure 7.28. Mass gain per unit area (α) *vs.* temperature corresponding to Cr-based, Co-based and Ni-based hardmetals under the same isothermal experiments at 750, 800, and 850 °C [25-26].

Figure 7.29 presents the XRD patterns obtained from the oxide layers of Cr-based WC hardmetals with different extra C contents after the TGA tests. The XRD results show that the composition of the oxide layers formed in all the Cr-based WC hardmetals is similar, mainly consisting of tungsten trioxide, WO_3, and tungstate, M_2WO_6 (M=Cr and Fe). Iron oxide (Fe_2O_3) and chromium oxide (Cr_2O_3) are also found in the oxide layers. A peak corresponding to graphite is detected in the Cr-based WC hardmetal with extra 2 wt.% C addition, which means that graphite may also exist in the oxide layer.

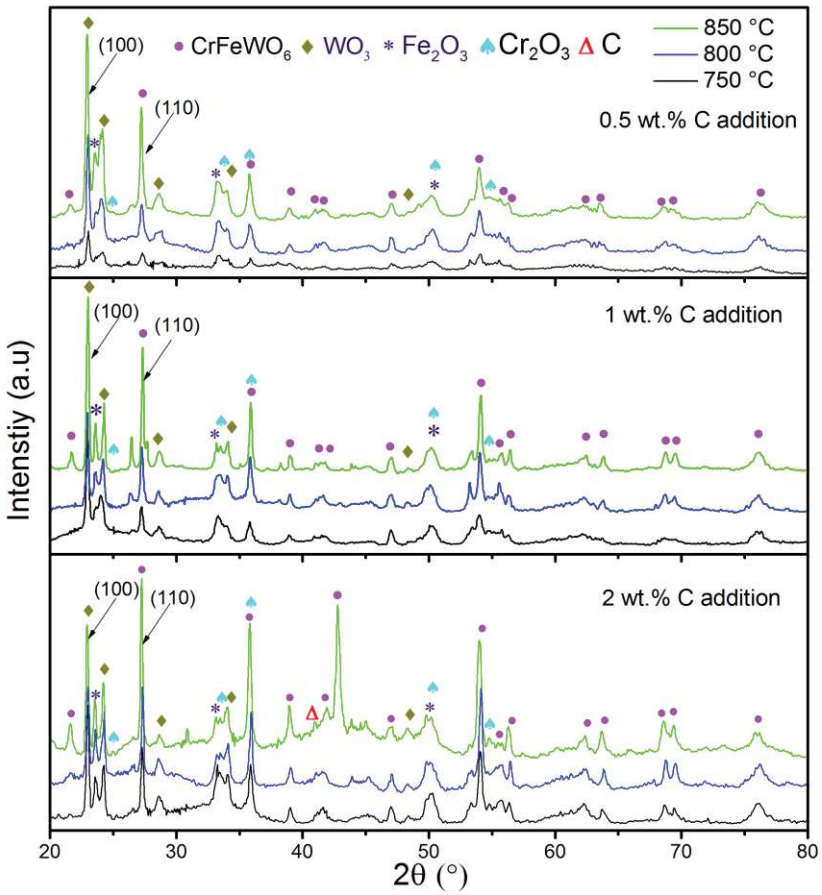

Figure 7.29. XRD diffraction patterns obtained from the oxide layers formed in Cr-based WC hardmetals with extra 0.5, 1 and 2 wt.% C contents after TGA tests at different temperatures (750, 800, and 850 °C).

Figure 7.30 displays the microstructure and phase composition (obtained by EDX area analysis) of the oxide layers present in Cr-based WC hardmetals with different carbon contents, after the isothermal TGA tests carried out at 850 °C for 1 h. The thickness of the oxide layer increases with the increase of both temperature and C content. Cr_2O_3, $CrFeWO_6$ and WO_3 phases are found in the surface of all Cr-based WC hardmetals, as expected from XRD results. Graphite is detected in the Cr-based WC hardmetal with extra 2 wt.% C addition, which is in accordance with the previous XRD results. The main oxidation products consist of two phases: $CrFeWO_6$, which appears as relatively dense agglomerates, and WO_3, having a sponge-like structure. Based on the differences found in density and morphology, it is can be inferred that $CrFeWO_6$ has a higher oxidation resistance than WO_3. Aristizabal *et al.* [25] and Bautista *et al*. [27] also demonstrated the formation of M_2WO_6 (M=Co) and WO_3 compounds in the oxide layer formed in WC-Co hardmetals. They reported that the increase of M_2WO_6 to M_2WO_6 + WO_3 ratio in the oxide layer is beneficial to improve the oxidation resistance, since the dense M_2WO_6 has a higher oxidation resistance than WO_3 with sponge-like structure.

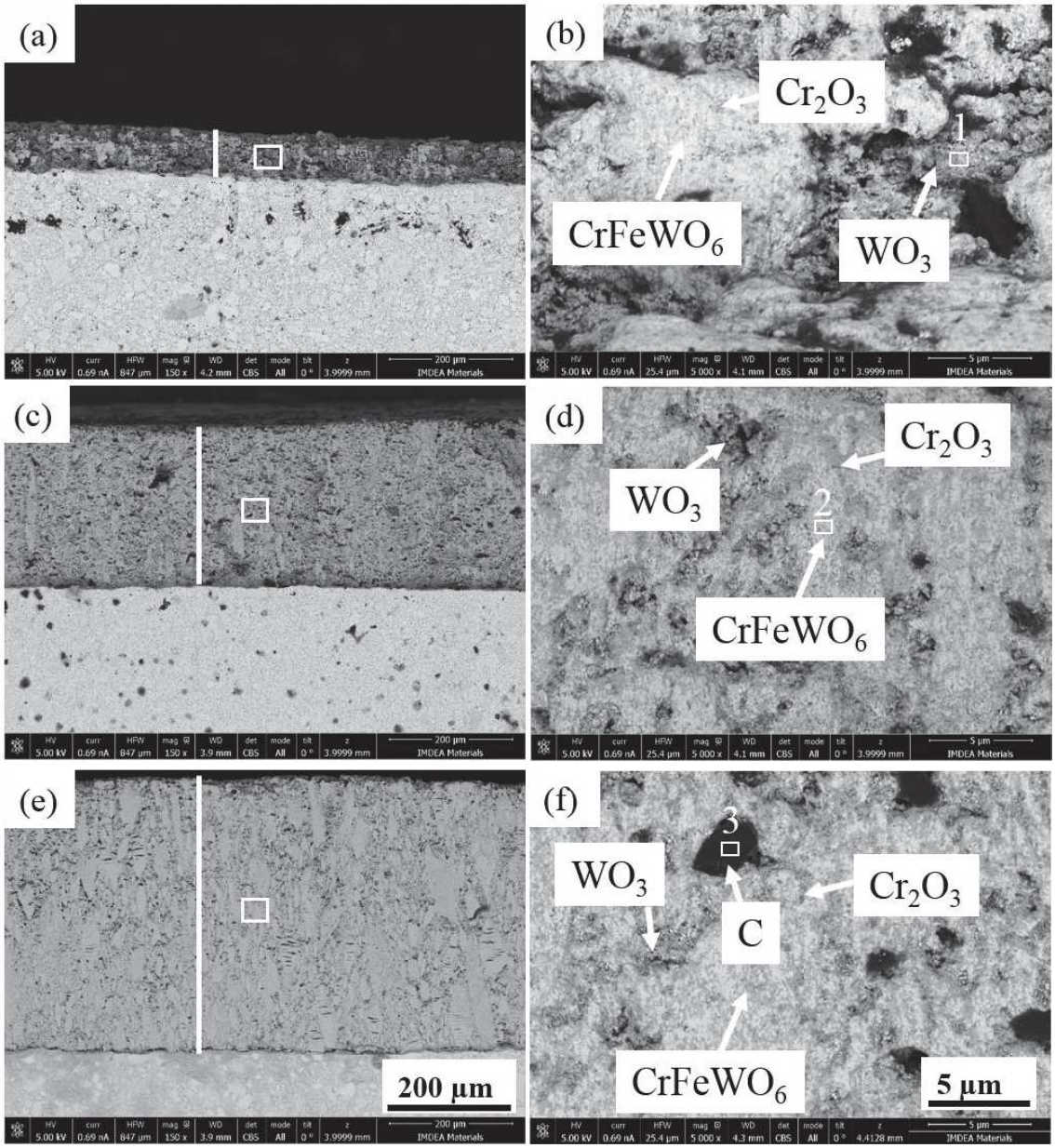

Figure 7.30. Representative BSE images of the oxide layers in Cr-based hardmetals with different extra C contents after the isothermal TGA test carried at 850 °C for 1 h with a heating rate of 20 °C/min (general view images on the left and higher magnification of the white square area on the right): (a) and (b) 0.5 wt.% C, (c) and (d) 1 wt.% C, (e) and (f) 2 wt.% C. White lines represent EDX line scanning. EDX area analyses are taken in regions labelled as 1, 2, and 3.

Selected EDX area and line scanning analyses are carried out in Cr-based WC hardmetals to further characterise the phase composition and the elemental distribution along the oxide layer, as depicted in Figure 7.31. The elemental distributions and EDX spectra shown in Figure 7.31 correspond to the line scanning across the oxide layers (white lines) and the selected areas labelled as 1, 2 and 3 in Figure 7.30, respectively. The obtained spectra confirm that $CrFeWO_6$ and WO_3 are the main oxidation products and also confirm

the existence of graphite when extra 2 wt.% C is added. Figures 7.31 (a) and (b) show the increase of the oxygen content across the oxide layer depth from the surface of the bulk material in Cr-based WC hardmetals with extra 0.5 and 1 wt.% C contents. The surface materials are converted to the oxidised products, leaving behind the unreacted matrix, and O can diffuse from the external porous oxide, leading to the accumulation of O in the surface of the unreacted materials [28]. The O content tends to be stable in the oxide layer of the Cr-based WC hardmetal with extra 2 wt.% addition, since graphite reacts with O forming CO/CO_2.

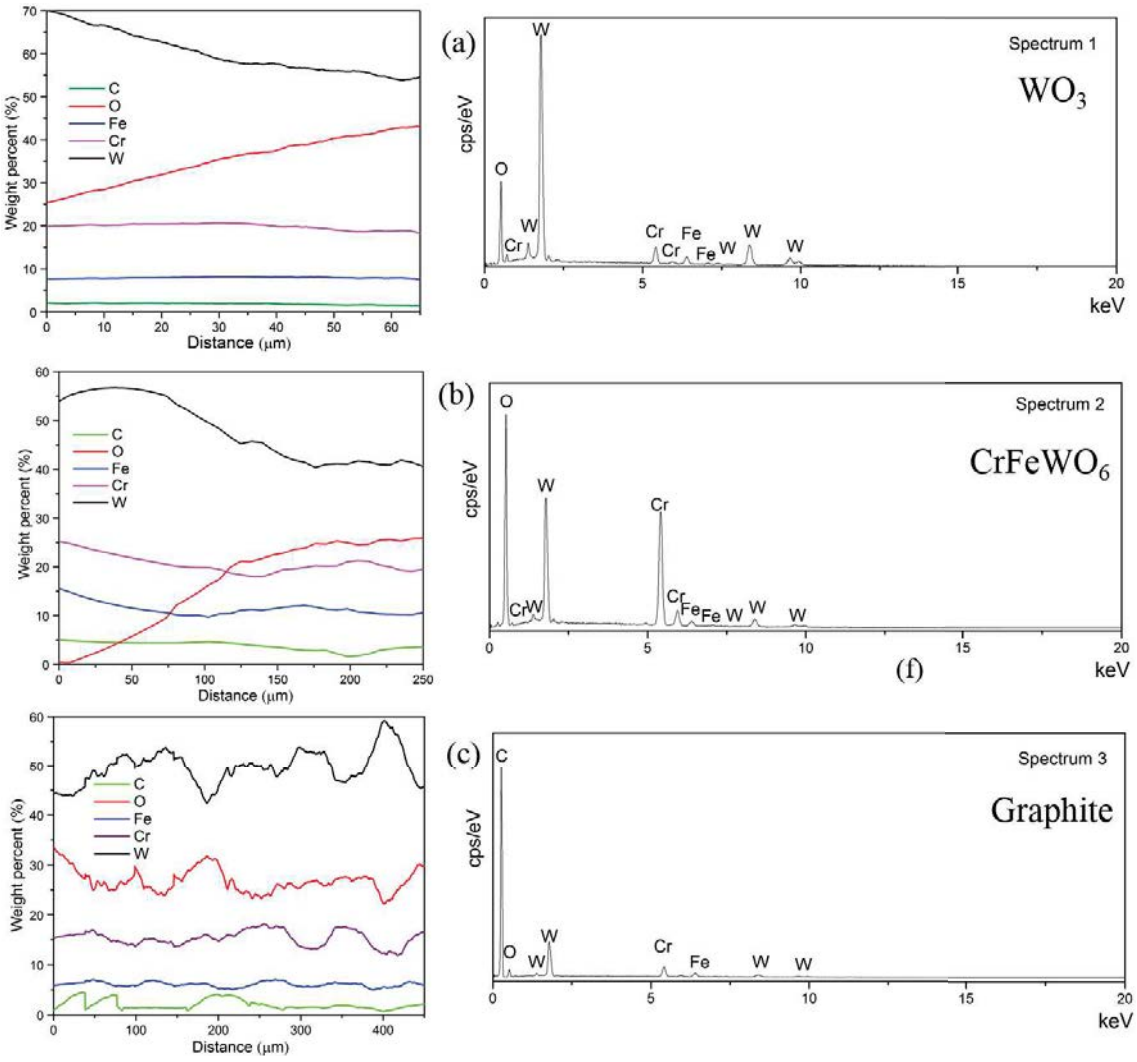

Figure 7.31. Lines canning across the oxide layers and corresponding EDX spectra in different areas of Cr-based hardmetals with different extra C contents: (a) 0.5 wt.% C, (b) 1 wt.% C, and (c) 2 wt.% C.

The original phases existing in Cr-based WC hardmetals definitely influence the oxidation rate at different temperatures. In order to know how Cr-based binder and WC phase are oxidised at different temperatures, Figure 7.32 shows the microstructural

evolution of the oxide layers between 750 and 850 °C. It is possible to observe that the interface between the oxide layer and the matrix becomes rougher when the temperature increases. Thus, more material is transformed into oxidation products. The different phases present in the original hardmetal may lead to different oxidation behaviours. For example, Cr_2O_3 has more oxidation resistance than $(Cr,Fe)_7C_3$ or graphite. The microstructural images in Figure 7.15 show that Cr-based WC hardmetal with extra 0.5 wt.% C content has the highest Cr_2O_3 phase amount, leading to the lowest oxidation rate and the thinnest oxidation layer.

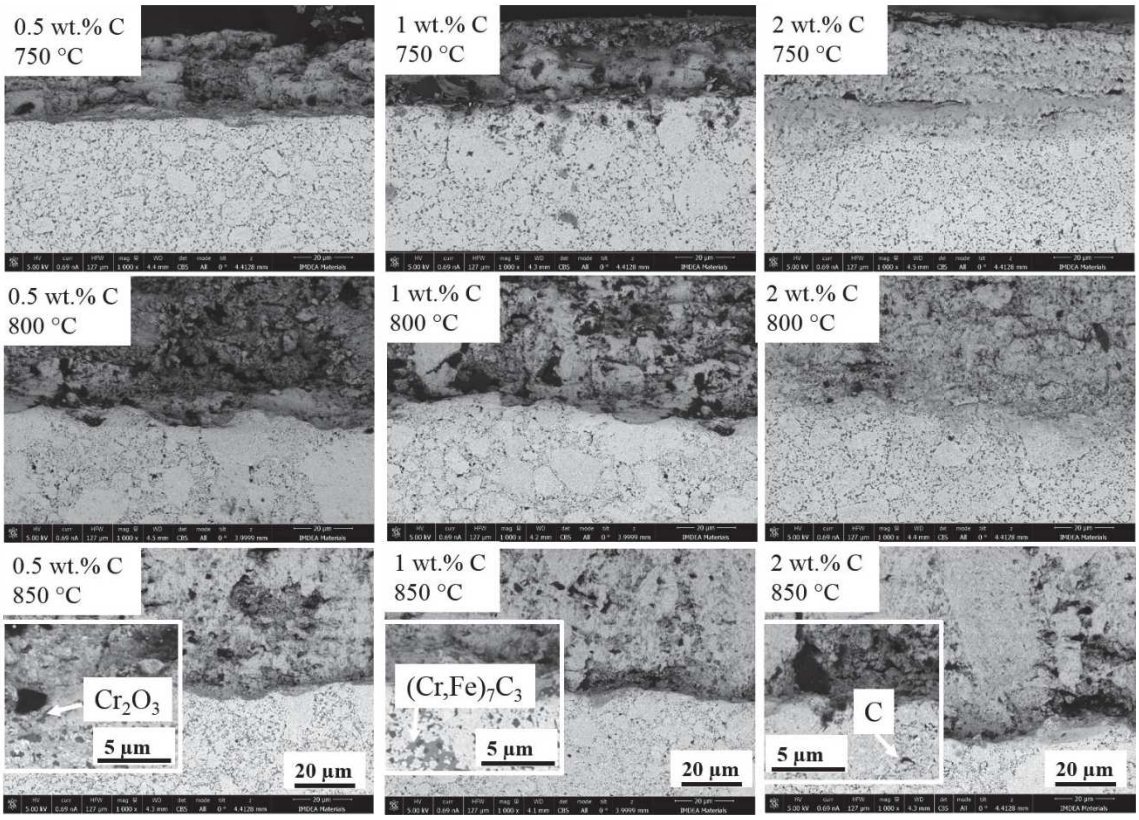

Figure 7.32. Microstructural evolution of interface between oxide layer and matrix in Cr-based WC hardmetals with the additions of 0.5, 1 and 2 wt.% C at 750, 800 and 850 °C.

In order to summarise the effect of temperature and C content on the oxidation process, mass gain per unit area (α), activation energy (E_a), M_2WO_6 (M=Cr and Fe) to $M_2WO_6 + WO_3$ ratio, and thickness of oxide layer in Cr-based WC hardmetals with different extra C contents at different temperature are listed in Table 7.5. The ratio between M_2WO_6 and M_2WO_6+WO_3 phases has been estimated by comparing the intensity of their strongest XRD diffraction peaks: (100) for WO_3 and (110) for $CrFeWO_6$ (Figure 7.29). The activation energy for oxidation is determined by the isoconversion method comparing the evolution of the mass gain per unit area (α) against time for two different heating rates (5

and 20 °C/min) [26], [29]. The value of α increases with the increase of temperature, producing more oxidised products, since a higher temperature supplies more energy for the oxidation process. The ratio between M_2WO_6 and M_2WO_6+WO_3 increases with the increase of C content, leading to an improvement of the oxidation resistance, considering that the dense M_2WO_6 phase has more oxidation resistance than porous WO_3 [30]. Suresh *et al.* [31] also reported that the oxidation products of $W_{0.5}Cr_{0.5}$ alloys from 800 to 1000 °C were mainly formed by a mixture of Cr_2O_3, Cr_2WO_6 and WO_3. On the other hand, the increase of the carbon content decreases the oxidation resistance of Cr-based WC hardmetals, due to the E_a decrease with the increase of C content. Although there are two opposite parameters acting on the corrosion resistance, the ratio M_2WO_6/M_2WO_6+WO_3 and the activation energy, the E_a seems to be the predominant factor since the hardmetal with the highest E_a and the lowest ratio is the one with the best oxidation resistance (corresponding to the lowest extra carbon content).

Table 7.5. Mass gain per unit area (α), activation energy (E_a), $CrFeWO_6$ to $CrFeWO_6$ + WO_3 ratio (estimated from the XRD intensities) and thickness of oxide layer in Cr-based WC hardmetals with different C contents at three different temperatures: 750, 800, and 850 °C.

Cr-based WC hardmetals	α (mg/cm^2)	E_a (kJ/mol)	$\frac{I\,(110)_{CrFeWO_6}}{I\,(100)_{WO_3} + I\,(110)_{CrFeWO_6}} \times 100\%$	Thickness (μm)	Temperature (°C)
Extra 0.5 wt.% C (total: 5.6 wt.% C)	2.0±0.2	269	32	17±2	750
	4.8±0.2		34	60±8	800
	6.0±0.5		41	70±10	850
Extra 1 wt.% C (total: 6.2 wt.% C)	3.8±0.4	251	33	29±5	750
	12.8±0.8		43	201±12	800
	16.0±0.4		45	260±10	850
Extra 2 wt.% C (total: 6.9 wt.% C)	4.2±0.5	221	40	160±5	750
	16.5±0.8		50	380±12	800
	27.0±1.0		54	448±15	850

After summarising the results obtained from XRD, microstructural and EDX analyses, and taking into consideration the referenced general oxidation behaviour of Ni-based WC hardmetals [23] and Co-based WC hardmetals [32], it can be concluded that Cr-based WC hardmetals exhibit a superior oxidation resistance than the other two hardmetals under the same conditions. Particularly, the Cr-based WC hardmetal with extra 0.5 wt.% C addition has the highest oxidation resistance among all Cr-based WC hardmetals.

In addition, another study of the oxidation resistance of Cr-based WC hardmetals with different extra C contents is carried out by furnace heating in air at 900 °C during 24 h, and comparing the results obtained with the data corresponding to the oxidation of WC-

AISI304 and WC-Co hardmetals under the same conditions [33], as shown in Figure 7.33. The mass gain per unit area in Cr-based WC hardmetals is much lower than that of WC-AISI304 and WC-Co hardmetals, which also demonstrates the highest oxidation resistance of Cr-based WC hardmetals. The Cr-based WC hardmetal with extra 0.5 wt.% C content again has the lowest mass gain per unit area, which agrees with the previous analyses using the TGA technique. Thus, the use of Cr-based binders in the hardmetal industry, alternatively to Co-based binder, may be advantageous in those applications in which a high oxidation resistance is needed.

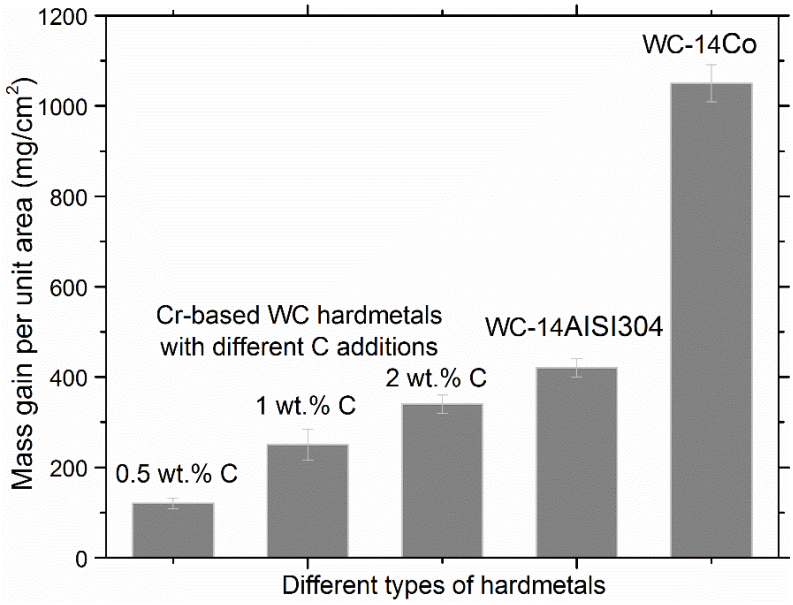

Figure 7.33. Mass gain per unit area of Cr-based WC hardmetals with different extra C contents, WC-AISI304, and WC-Co hardmetals after thermal treatment at 900 °C for 24 h in air [33].

7.5 Wear resistance

Wear resistance is one of the most important properties in hardmetals that are used as cutting tools. Many investigations have reported that the tribological characteristics of WC-Co hardmetals are directly related to their chemical composition, content of WC, microstructure, average grain size, and extra carbide additions such as using Cr_3C_2 and VC [34-35]. Generally, the wear resistance of WC-Co hardmetals increases with the increase of the volume fraction of WC and with the refinement of the WC grain size [36-38]. More particularly, wear performance improves significantly when the average WC grain is reduced towards nanometer scale [39-41]. This investigation is focused on the study of the wear resistance of Cr-based WC hardmetals with different extra C contents (0.5, 1 and 2 wt.%) by unlubricated sliding wear tests performed with two different tribometers (Bruker and Wazau-TRM 2000 equipment) under different wear conditions.

7.5.1 Dry ball-on-plate system with Bruker tribometer

7.5.1.1 Friction coefficient and wear surface analyses

Dry ball-on-plate tests are performed on a tribometer using reciprocating linear movement. In the tests, samples act as the moving body, whereas the counter materials is the static body. The imposed normal force (F_N) and the concomitant tangential friction force (F_T) of the count ball part are continuously recorded using a load and a friction sensor [42], respectively, when a load of 15 or 18 N is applied against Cr-based WC hardmetals (Figure 7.34). The static friction force (F_T) is calculated using the following equation:

$$F_T = \frac{|F_{T,max}|+|F_{T,min}|}{2} \tag{7-5}$$

The coefficient of friction (μ) is calculated from the F_T/F_N ratio. Figure 7.34 shows that the recorded normal contact force seems to correspond very well to the imposed contact load of this particular case, which is 18 N. The friction force appears either positive or negative, depending on the sliding direction.

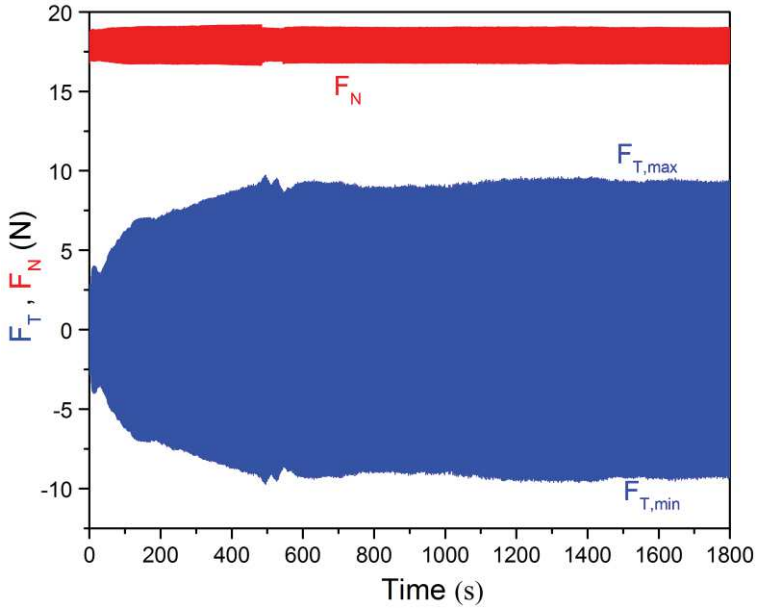

Figure 7.34. Real time normal force (F_N) and friction force (F_T) for a load of 18 N, frequency of 5 Hz, stroke length of 5 mm, as function of time for Cr-based WC hardmetals [42].

The evolution of the friction coefficient (μ) for Cr-based WC hardmetals with different extra carbon contents is displayed in Figure 7.35. Two loads (15 N and 18 N) are applied to study the effect of force on the friction coefficient, μ. Generally, the friction coefficient increases rapidly throughout the first seconds, which is attributed to the quick increase of

ball-on-disc contact area [42]. After the initial stage, the variations in μ become smaller in the "running in" stage, and it reaches an equilibrium state of stable value, since the wear track becomes smoother after ploughing away the surface asperities [43]. However, the friction coefficient observed in Cr-based WC hardmetals with an extra 2 wt.% C content appears slightly inconstant due to the existence of soft graphite phase. Thus, the surface with graphite has less resistance to overcome, which leads to an increase in surface roughness, and therefore the μ increases. Figure 7.35 highlights that a higher contact load (18 N) leads to smaller and more stable values of friction coefficient, since the increase in F_T is lower than that in F_N when the applied force increases. Thus, the highest load of 18 N is selected as the force to be applied in the next analyses. The friction coefficients measured for Cr-based WC hardmetals with extra 0.5, 1, and 2 wt.% C contents are in the range of 0.27-0.30, 0.34-0.36, and 0.43-0.51, respectively, since the different phases existing in each material have a distinctive effect on the friction coefficient [44]. $(Cr,Fe)_7C_3$ and graphite exist in the Cr-based WC hardmetals with extra 1 and 2 wt.% carbon contents, respectively, which increases the F_T due to their lower levels of hardness compared to that of WC, finally leading to the increase of the friction coefficient.

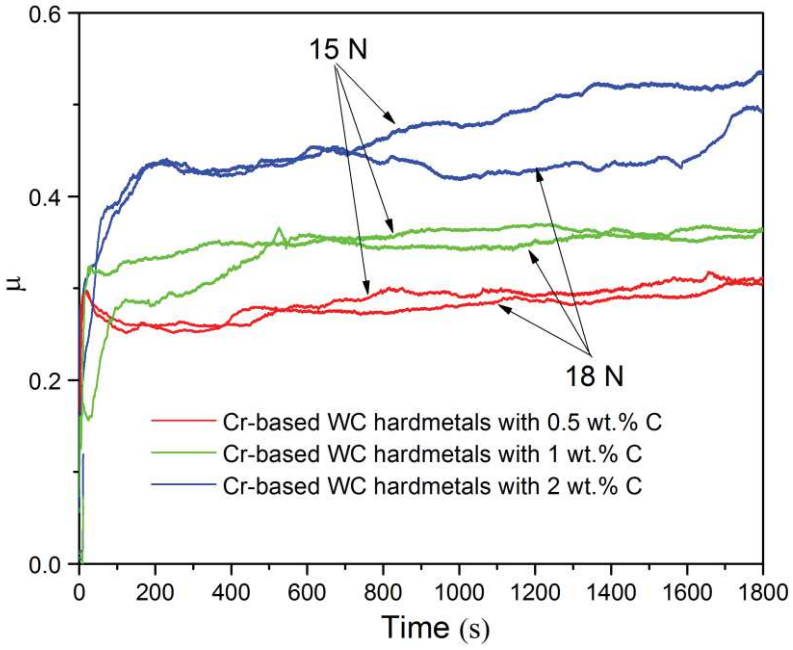

Figure 7.35. Friction coefficient as a function of time for two different contact loads (15 N and 18 N) in Cr-based WC hardmetals with different C contents tested using an alumina ball, a frequency of 5 Hz, and stroke length of 5 mm for 30 min.

Visual observations after the wear sliding tests reveal a smooth and bright appearance of the wear track in all tested samples, indicating that the surfaces of Cr-based WC hardmetals have been ploughed by the alumina ball during the wear sliding. SEM and EDX analyses are performed on the worn surfaces to obtain more information of the wear process followed. Figure 7.36 illustrates general images of the worn surfaces and a higher magnification of the central part in the wear track.

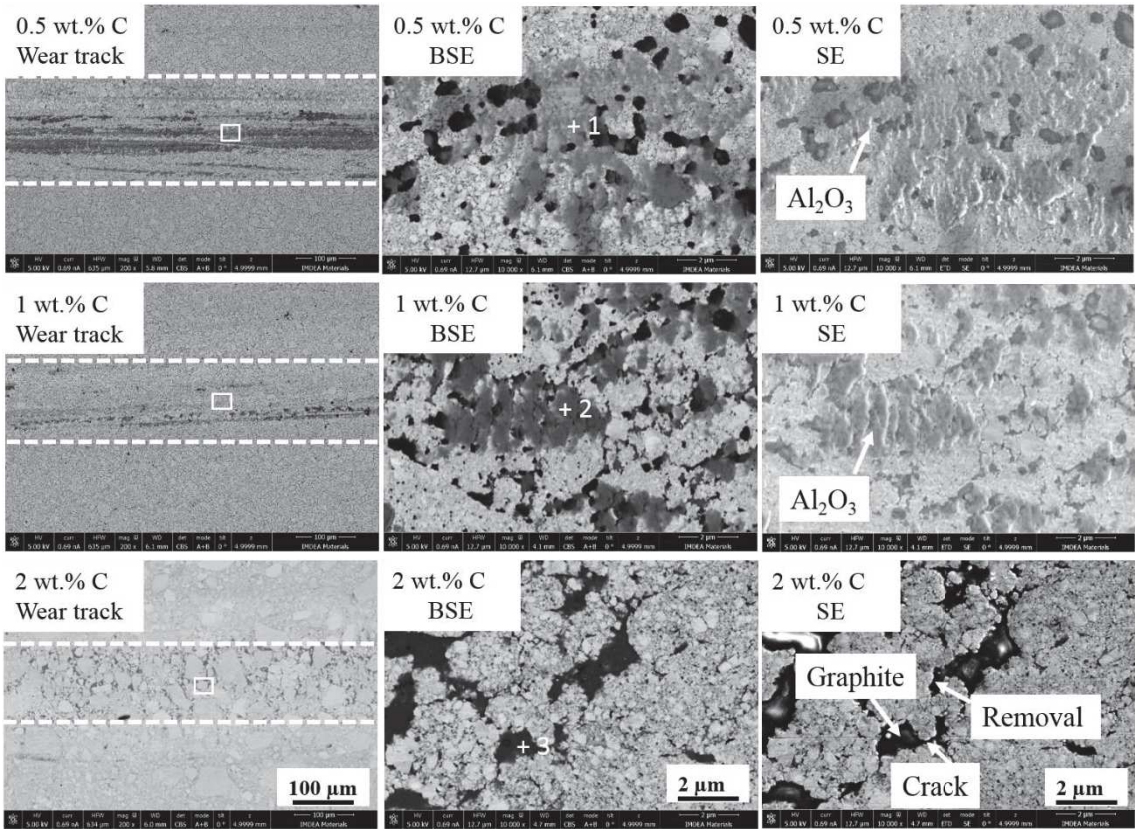

Figure 7.36. BSE and SE images of the wear track generated in Cr-based WC hardmetals with extra 0.5, 1 and 2 wt.% C contents after wear tests with a load of 18 N, frequency of 5 Hz, stroke length of 5 mm, and time of 30 min. General view images of wear track on the left and higher magnification of the central part in wear track (white square area) on the right. EDX point analyses are carried out on the positions of number 1, 2, and 3.

From the general view of the wear tracks, a slight decrease of wear track width with the increase of the carbon content (the distance between two white dashed lines in Figure 7.36) is found for Cr-based WC hardmetals. The width varies from value around 200 µm, in samples with extra 0.5 wt.% C content, to around 170 µm and 165 µm, in samples with extra 1 and 2 wt.% C contents, respectively. This phenomenon can be explained by the occurrence of different mechanisms: abrasive wear, adhesion of wear debris layers, soft phase removal, and grain cracking. The parallel grooves in all the wear tracks point out

that the abrasive wear mechanism is dominant in all Cr-based WC hardmetals. The Cr-based WC hardmetal with an extra 0.5 wt.% C content has the highest hardness, as previously reported, which leads to an increase in the wear track width due a higher volume loss coming from the alumina ball. The BSE and SE micrographs in the central part of the worn surface in the Cr-based WC hardmetals with extra 0.5 and 1 wt.% C contents show the adhesion of the wear debris layers in grey color. Actually, the existence of thin wear debris layers on the surface of hardmetals protects the Cr-based WC hardmetals, leading to an improvement of their wear resistance. BSE and SE micrographs of worn surface in Cr-based WC hardmetals with extra 2 wt.% C content, present micro cracks and surface removal of the soft graphite. The removal of the binder and/or graphite phase increases the tangential friction force, leading to a higher friction coefficient, which explains the trend followed by the friction coefficient displayed in Figure 7.35.

EDX spectrum 1, taken in the worn surface of the Cr-based WC hardmetal with an extra 0.5 wt.% content, reveals the existence of W, Al, Cr, O, Fe and C, as shown in Figure 7.37. It is indicating that the wear surface is enriched in Al and O content, coming from the alumina ball. Therefore, the worn track surface turns to be covered with a thin Al_2O_3 wear debris layer, separating the Cr-based WC hardmetal from the count sliding ball.

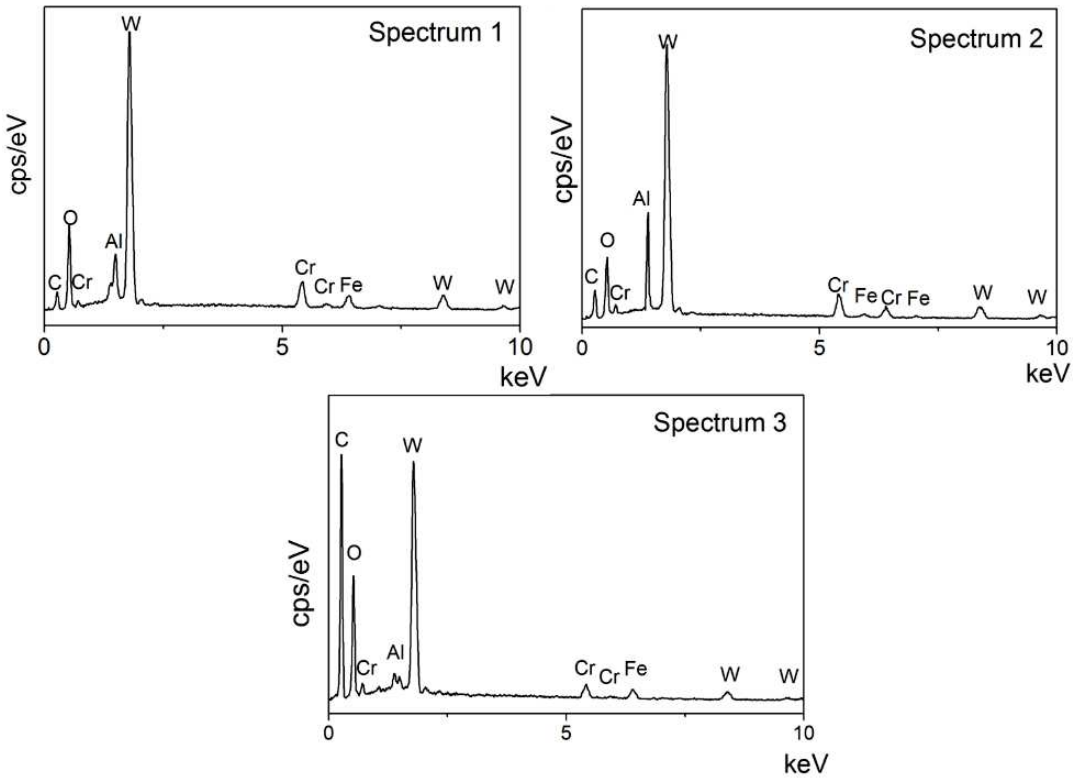

Figure 7.37. EDX analyses on wear tracks corresponding to Cr-based WC hardmetals with extra 0.5, 1, and 2 wt.% C contents, respectively.

It is worth noting that a similar EDX spectrum is obtained in the wear track of the Cr-based WC hardmetal with an extra 1 wt.% C content (spectrum 2). The spectrum 3, taken in the crack region of the hardmetal with extra 2 wt.% content, reveals more quantity of C and O, and less Al since graphite is being removing from the bulk material and probably it is covering the wear track. In fact, the micro-cracks presented in this hardmetal are induced by tangential stresses due to the reciprocal sliding contact pressure exerted by the alumina ball, which leads to the removal of the soft graphite.

7.5.1.2 Volume loss and wear rate

All samples undergo wear sliding tests for 30 min (a total sliding distance of 90000 mm) to ensure that the wear process has reached a steady-state condition and to enable post-mortem assessment of the wear volume loss values. The 3D topographies of the wear tracks are obtained by profilometry. Then at least three 2D profiles are taken from the 3D topographies to obtain the average wear loss area ($\overline{A_w}$) and the average width of each track ($\overline{W}$). The values of average depth ($\overline{D}$), average wear loss area ($\overline{A_w}$) , average volume loss ($\overline{\Delta V}$), and average wear rate ($\overline{W_v}$) are calculated according to the equations mentioned in Section 3.9.

Figure 7.38 shows the 3D topographic images of the worn surfaces for Cr-based WC hardmetals with different extra C contents after dry sliding tests. The X, Y, and Z axes represent the direction corresponding to the width, length, and depth of the wear track, respectively. The different colors in the topographic images are related to the distribution of heights: red represents the highest height, while purple indicates the lowest height. As expected, severe parallel grooves are observed in the wear tracks since abrasion wear is the main mechanism for the surface sliding against alumina ball. Figure 7.38(c) shows that the worn surface of the Cr-based WC hardmetal with extra 2 wt.% C content exhibits the narrowest and deepest wear track, whereas the Cr-based WC hardmetal with an extra 0.5 wt.% C content has the widest and shallowest one, as shown in Figure 7.38(a). Therefore, Figure 7.38 suggests that the volume loss of Cr-based hardmetals increases with the increase of the extra carbon content from 0.5 to 2 wt.%. In order to calculate the value of the volume loss, the unworn surface is set as a regular basis, where the depth is zero. At least three intersection lines are used to obtain the profile of the wear track. Then, the software installed in the profilometer equipment can automatically measure the average width and area of each profile obtained from the wear track.

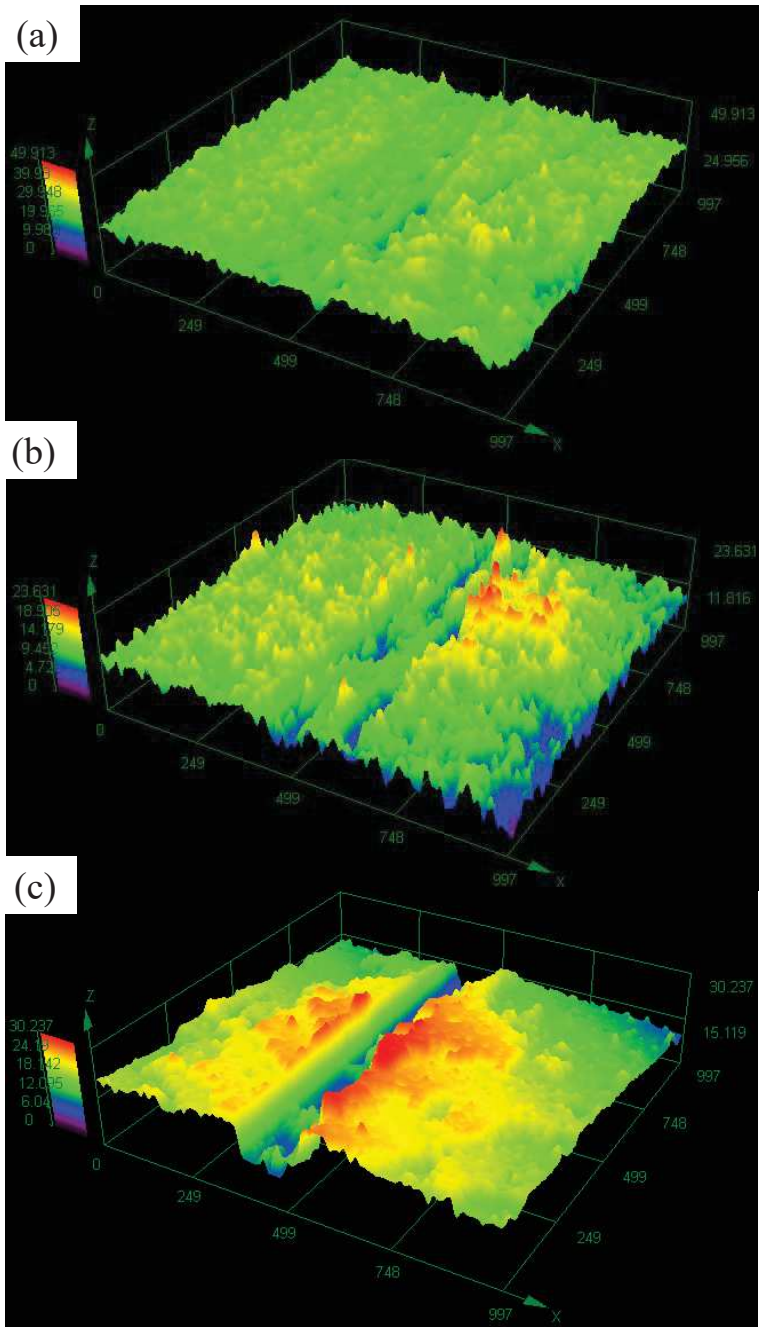

Figure 7.38. 3D topographic images showing the wear tracks of Cr-based WC hardmetals with different extra C contents after dry sliding tests with a load of 18 N, frequency of 5 Hz, stroke length of 5 mm, and time of 30 min: (a) 0.5 wt.% C, (b), 1 wt.% C, and (c) 2 wt.% C.

Figure 7.39 presents the wear track profiles taken in three different intersection lines and the corresponding optical images of the wear tracks in Cr-based WC hardmetals with different extra C contents after dry sliding tests. The average width of the track and the average wear loss area of each profile are measured by surface profilometry, and results are listed in Table 7.6. This table summarises the average width, loss area, depth, wear volume loss, and wear rate values calculated for all the Cr-based WC hardmetals tested during 30 min against an alumina ball with a load of 18 N, frequency of 5 Hz, and stroke

length of 5 mm. The lowest depth and volume loss are achieved by the Cr-based WC hardmetal with an extra 0.5 wt.% C content, whereas the highest values occur for the Cr-based WC hardmetal with an extra 2 wt.% C content, which is in full agreement with the microstructural surface analyses and 3D topographic images previously shown. The volumetric wear rates of Cr-based WC hardmetals with extra 0.5, 1 and 2 wt.% C contents vary between 5.8-6.2 $\times 10^{-11}$, 7.2-7.7$\times 10^{-11}$, and 10.6-11.7$\times 10^{-11}$ mm^3/mm, respectively. Therefore, these results remark that the Cr-based WC hardmetal with an extra 0.5 wt.% carbon content has the highest wear resistance, which is well consistent with the existence of a uniform nanosized WC grain distribution, with the smallest WC size (around 100 nm), and with the avoidance of graphite.

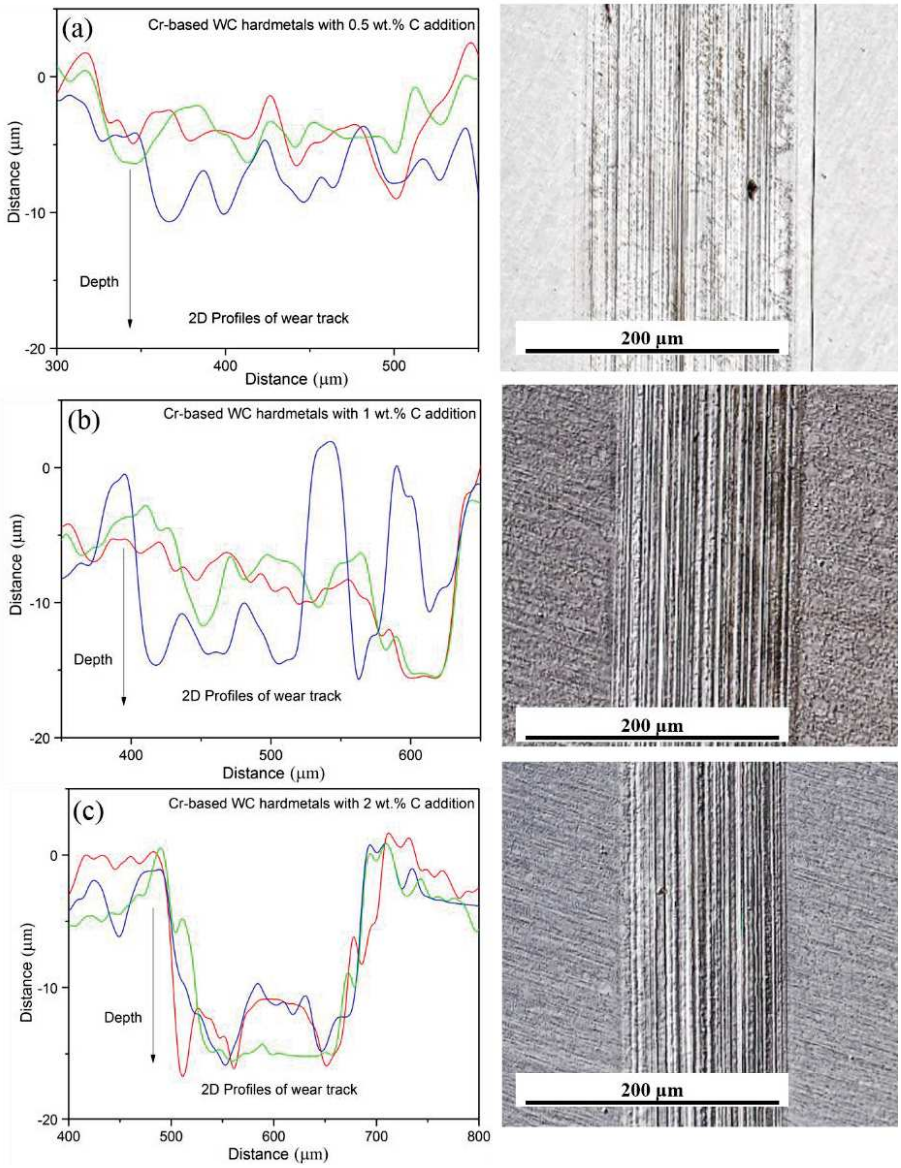

Figure 7.39. Representative wear track profiles and corresponding optical images of Cr-based WC hardmetals with different extra C contents after dry sliding tests with a load of 18 N, frequency of 5 Hz, stroke length of 5 mm, and time of 30 min: (a) 0.5 wt.% C, (b) 1 wt.% C, and (c) 2 wt.% C.

Table 7.6 Wear data obtained for Cr-based WC hardmetals with extra 0.5, 1, and 2 wt.% C contents tested with a load of 18 N, frequency of 5 Hz, and stroke length of 5 mm against alumina ball.

Cr-based WC hardmetals with different C contents	Width $\overline{W}$ (μm)	Loss area $\overline{A_w}$ (μm^2)	Depth $\overline{D}$ (μm)	Volume loss $\overline{\Delta V}$ (10^{-6} mm^3)	Wear rate $\overline{W_v}$ (10^{-11} mm^3/mm)
0.5 wt.% C	217.4±3	1047.6±226	4.7±0.2	5.2±0.2	5.8±0.1
	212.2±5	1107.7±326	5.2±0.4	5.6±0.4	6.2±0.2
	192.7+7	1007.7±287	5.1±0.2	5.1±0.2	5.8±0.1
1 wt.% C	173.6±4	1407.6±187	8.1±0.2	7.0±0.4	7.7±0.3
	178.0±5	1307.7±214	7.3±0.2	6.5±0.3	7.2±0.2
	180.6±3	1387.1±314	7.6±0.2	6.9±0.1	7.6±0.2
2 wt.% C	169.0±4	2047.6±385	12.0±0.4	9.5±1.0	10.6±0.4
	153.9±5	2243.7±585	14.5±0.2	9.6±1.2	10.7±0.4
	170.0±3	2368.5±701	13.9±0.8	10.5±0.5	11.7±0.6

Many investigations reported that the wear resistance performance depends on hardness [36], [39-40]. Figure 7.40 shows the relationship among volume loss, wear rate, and hardness for Cr-based WC hardmetals. Both volume loss and wear rate clearly decrease with the increase of the hardness. Thus, in this work the Cr-based WC hardmetal with the highest hardness (extra 0.5 wt.% C content) leads to the highest wear resistance.

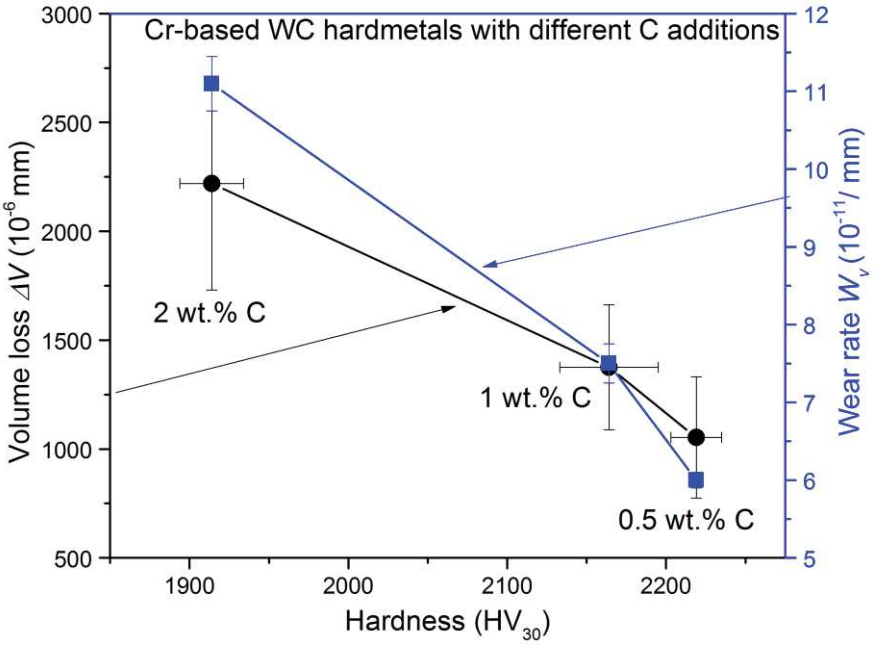

Figure 7.40. Volume loss and wear rate against hardness after dry sliding tests with a load of 18 N, frequency of 5 Hz, stroke length of 5 mm, and time of 30 min in Cr-based WC hardmetals with extra 0.5, 1, and 2 wt.% C contents.

Figure 7.41 shows the wear rate comparison between Cr-based WC hardmetals and some commercial Co-based WC hardmetals. The corresponding wear rates of Co-based WC hardmetals are transformed into the same unit (10^{-11} mm^3/mm) [43]. Cr-based WC hardmetals exhibit better wear resistance performance than Co-based WC hardmetals,

even considering that these Co-based WC hardmetals have a higher content of WC (90 wt.%) than the Cr-based WC hardmetals (83.2 wt.%). As mentioned before, the wear resistance depends on the content of WC, microstructure, WC grain size and its distribution, increasing dramatically as WC grains size is reduced. Cr-based WC hardmetals have a uniform distribution of nanosized WC grains, leading to a superior wear resistance performance. Among these Cr-based WC hardmetals, Figure 7.41 shows that the Cr-based WC hardmetals with extra 1 and 2 wt.% carbon additions exhibit a higher wear rate than hardmetal with extra 0.5 wt.% C content, due to the increase of the WC grain size and also to the existence of $(Cr,Fe)_7C_3$ or graphite.

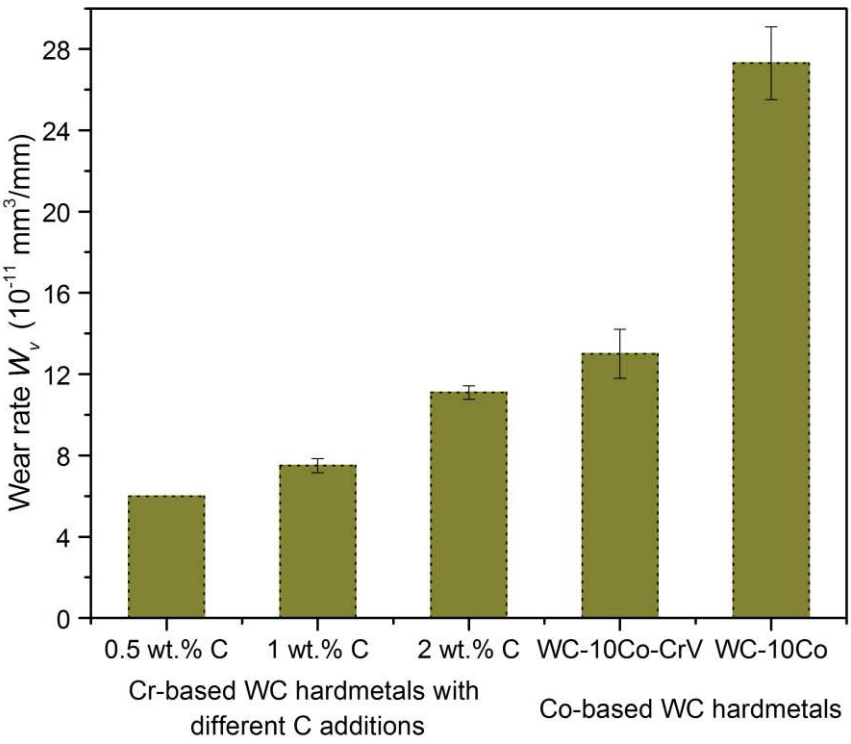

Figure 7.41. Wear rate comparison between Cr-based WC hardmetals and Co-based WC hardmetals [43].

The previous findings point out that the wear performance of Cr-based WC hardmetals is primary controlled by abrasive wear. Both wear volume loss and wear rate increase with the decrease of hardness. The existence of Al_2O_3 in the surface of the wear tracks confirms that the adhesion of wear debris layers takes place on the Cr-based WC hardmetals, which is beneficial to improve the wear resistance. Micro-cracks and some surface soft phase removals are detected in the Cr-based WC hardmetal with an extra 2 wt.% content. The uniform distribution of nanosized WC grain size in Cr-based WC hardmetals is the key-reason for achieving an excellent wear behaviour, even compared to WC-Co hardmetals with a higher content of WC hard phase.

7.5.2 Dry ball-on-plate system with Wazau tribometer

7.5.2.1 Friction coefficient and wear surface analyses

Dry ball-on-plate tests are also performed using a Wazau TRM2000 tribometer and under more aggressive experimental conditions. A WC-6wt.%Co ball (diameter of 10 mm) is rubbed in oscillating movement against Cr-based WC hardmetals (20×6.5×6 mm). These tests are performed in ambient air (20±2 °C, humidity 55%), under 50 N load, at a frequency of 2.5 Hz, and the stroke length of 10 mm for 60 min. The total sliding distance is fixed to 100000 mm. In order to study the friction condition of imposed normal contact force on Cr-based WC hardmetals, Figure 7.42 shows the evolution of the friction coefficient (μ) against time in Cr-based WC hardmetals. A similar trend in the friction coefficient is observed during the sliding process in all the samples evaluated. The friction coefficient increases quickly in the initial stage due to the increase of the ball-on-disc contact area, and then becomes stable, since the friction force achieves a constant value in the smooth wear track after polishing away the original surface roughness [42]. The friction coefficient in the Wazau tribometer is lower than that in Bruker tribometer, since the difference in hardness between WC-Co material and tested samples is smaller than that between Al_2O_3 material and tested samples. The friction coefficient of Cr-based WC hardmetals increases again slightly with the increase of the C content, as a consequence of the existence of larger WC grains and the presence of $(Cr,Fe)_7C_3$ or graphite, which is in agreement with the previous results obtained after the tests in the Bruker tribometer.

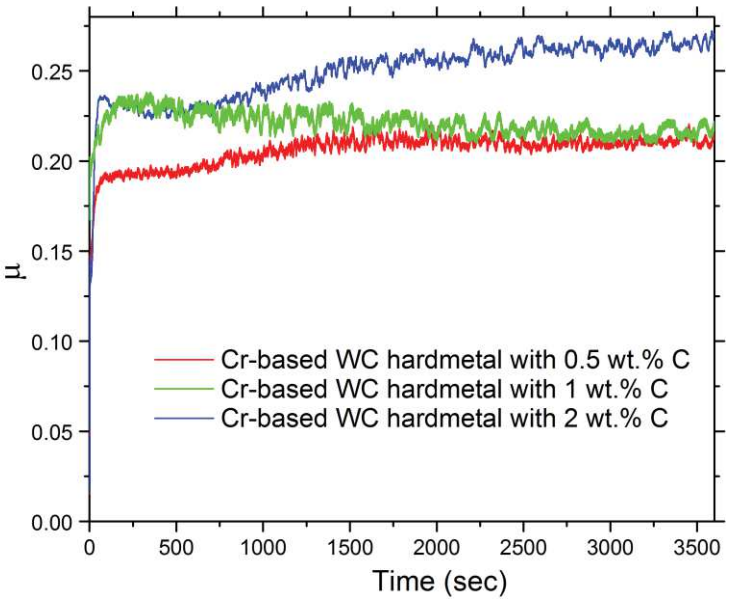

Figure 7.42. Friction coefficient (μ) against time in Cr-based WC hardmetals with different extra C contents tested using a WC-Co ball with a load of 50 N, frequency of 2.5 Hz, and stroke length of 10 mm for 60 min.

A smooth and bright wear track is found by visual observation on the surface of each Cr-based WC hardmetal after wear sliding tests. In order to further study the wear surface of Cr-based WC hardmetals, Figure 7.43 shows general images of the worn surface and images with a higher magnification of the central part in the wear track. From the general view of the wear track, it can be concluded that the width values (the distance between two white dashed lines) are around 225 μm in all Cr-based hardmetals due to the similar hardness of counter material and tested samples. The abrasive wear mechanism is also dominant in all Cr-based WC hardmetals, as indicated by the parallel grooves observed in the wear tracks. Adhesion of debris wear layers takes place in all samples, as suggested by the existence of WC-Co layers. The Cr-based WC hardmetal with an extra 1 wt.% carbon content has suffered the removal of material, whereas it was not detected during Bruker tests. This phenomenon can be attributed to more severe wear conditions, which may cause the removal of the $(Cr,Fe)_7C_3$ phase. Growth of cracks and surface phase removal are detected in the Cr-based WC hardmetal with an extra 2 wt.% carbon content due to the existence of soft graphite phase.

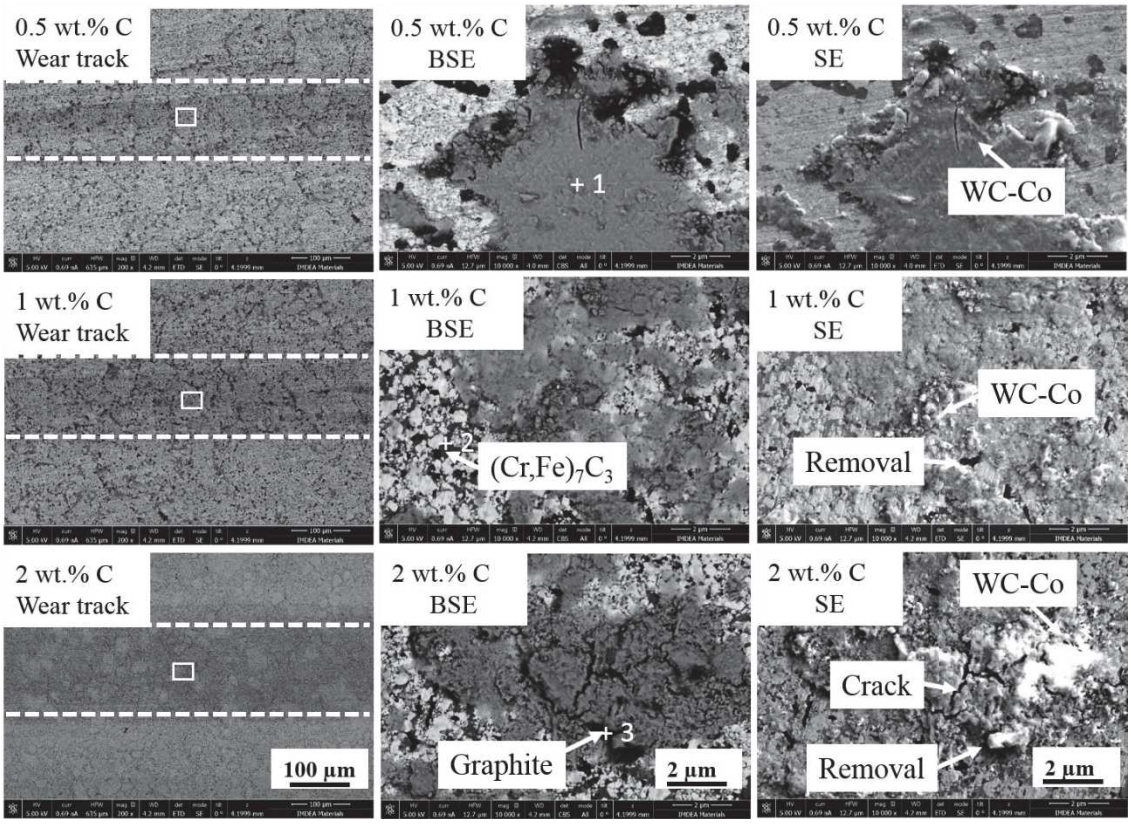

Figure 7.43. BSE and SE images of the wear track generated in Cr-based WC hardmetals with extra 0.5, 1, and 2 wt.% C contents after wear tests with a load of 50 N, frequency of 2.5 Hz, stroke length of 10 mm, and time of 60 min. General view images of wear track on the left and higher magnification of the central part in the wear track (white square area) on the right.

EDX spectra are obtained in the surface of Cr-based WC hardmetals to identify the composition of the debris layers and the composition near the cracks. Figure 7.44 shows that EDX spectrum 1, taken on the worn surface of the Cr-based WC hardmetal with an extra 0.5 wt.% C content, is enriched in Co and W, which demonstrates the existence of a WC-Co debris layer. This WC-Co layer is beneficial to improve the wear resistance. The EDX spectra 2 and 3 are taken near the cracks and they confirm the existence of $(Cr,Fe)_7C_3$ and graphite in the Cr-based WC hardmetals with extra 1 and 2 wt.% C contents, respectively, which may explain the phase removal and the crack growth.

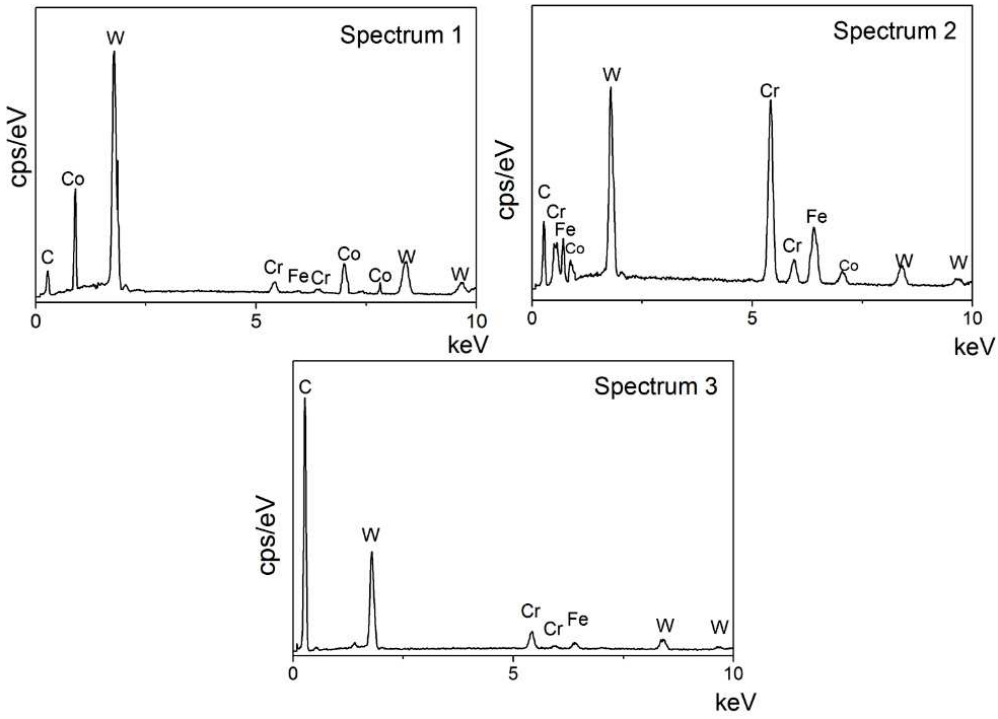

Figure 7.44. EDX analyses on wear track corresponding to Cr-based WC hardmetals with extra 0.5, 1, and 2 wt.% C contents, respectively.

7.5.2.2 Volume loss and wear rate

The method mentioned in section 3.9 is also used to calculate the volume loss and wear rate of Cr-based WC hardmetals after dry sliding wear tests using a load of 50 N, a frequency of 2.5 Hz, a stroke length of 10 mm, and a time of 60 min. Figure 7.45 presents the 3D topographic images of the worn surface for Cr-based WC hardmetals tested against a WC-Co ball. It clearly shows that the depth of the crack increases with the increase of the C content, whereas the width keeps a similar value. Hence, the volume loss of Cr-based WC hardmetals increases with the increase of the C content, which is consistent with the results obtained in the Bruker system. In order to calculate the values of volume loss and wear rate, three intersection lines are taken across the wear tracks.

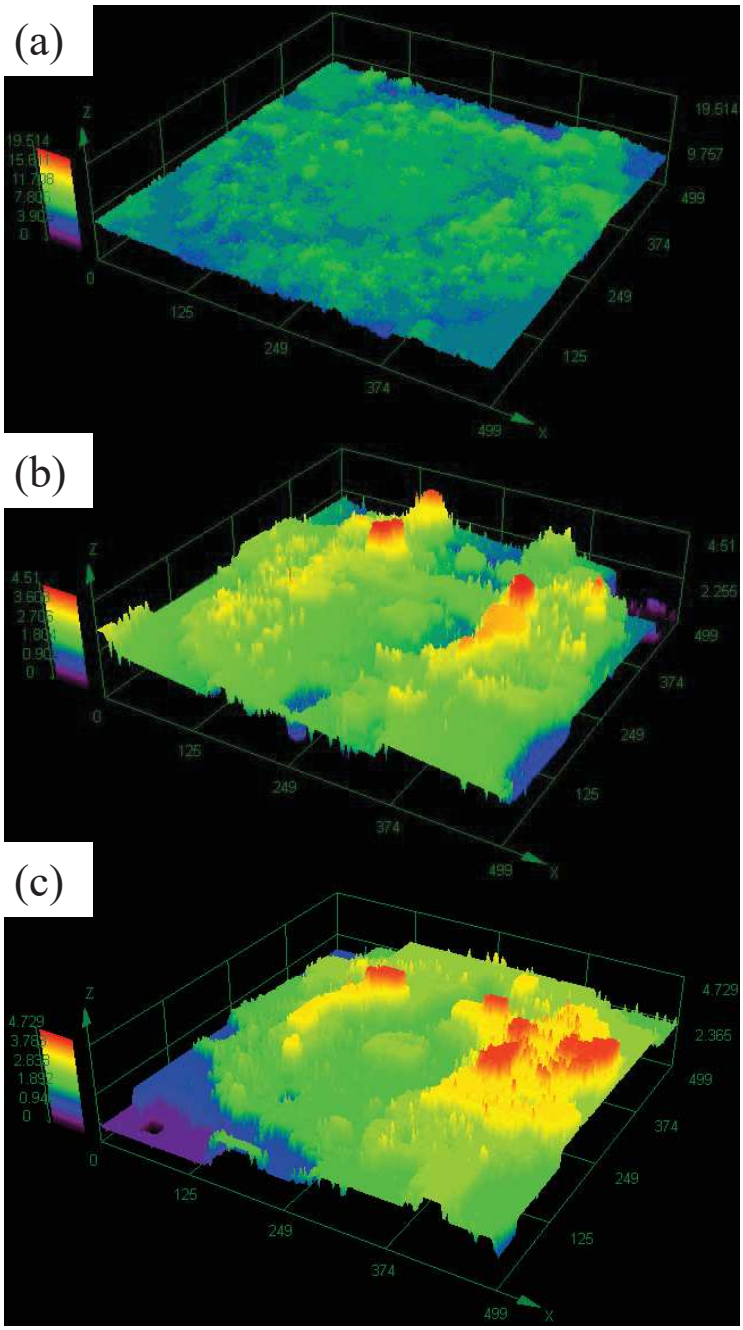

Figure 7.45. 3D topographic images showing the wear tracks of Cr-based WC hardmetals with different extra C contents after dry sliding tests with a load of 50 N, frequency of 2.5 Hz, stroke length of 10 mm, time of 60 min: (a) 0.5 wt.% C, (b), 1 wt.% C, and (c) 2 wt.% C.

Figure 7.46 shows the wear track profiles and the corresponding optical images obtained in Cr-based WC hardmetals with different extra C contents after dry sliding tests. Table 7.7 summarises all the wear data measured. The wear rates of Cr-based WC hardmetals with extra 0.5, 1, and 2 wt.% C contents are 7.0 $\pm 0.1 \times 10^{-11}$, 12.8 $\pm 0.3 \times 10^{-11}$, and 20.4 $\pm 0.4 \times 10^{-11}$ mm^3/mm, respectively.

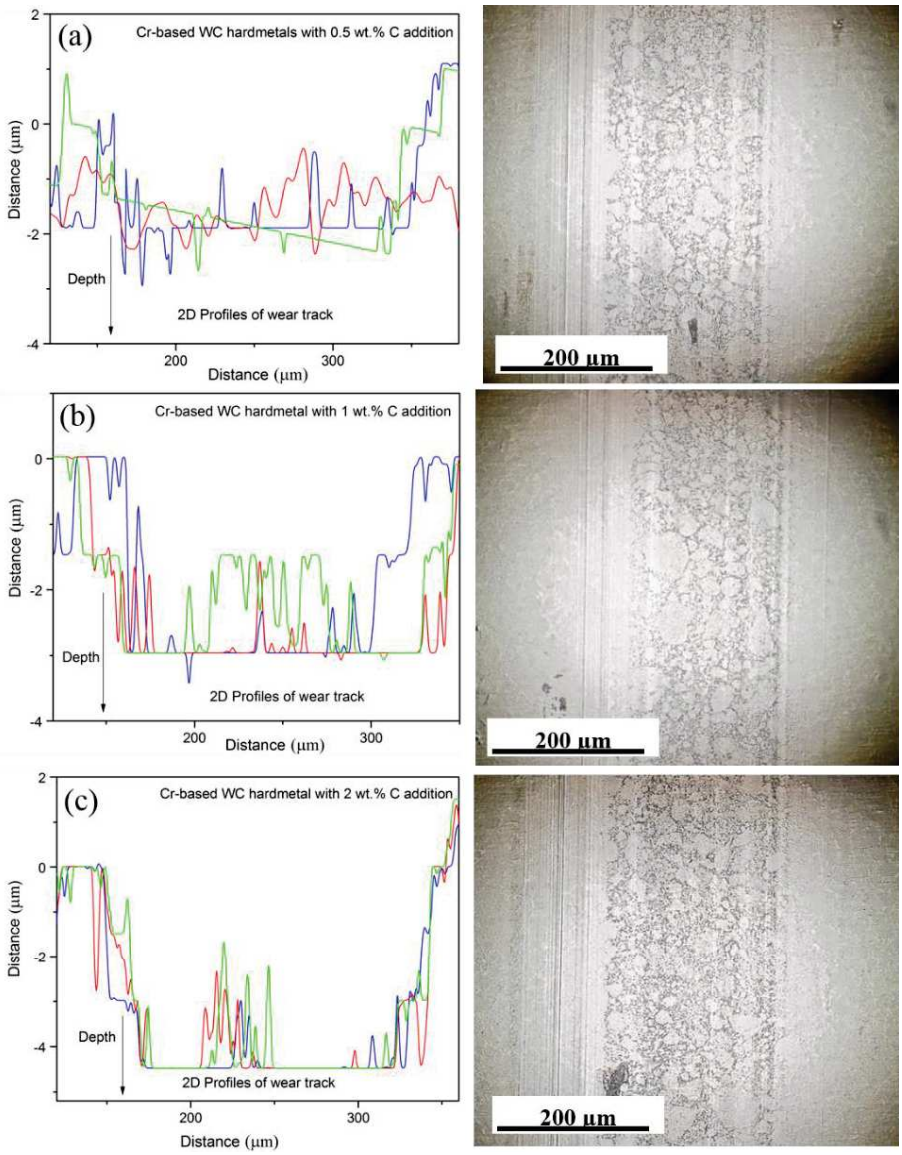

Figure 7.46. Representative wear track profiles and corresponding optical images of Cr-based WC hardmetals with different extra C contents after dry sliding tests with a load of 50 N, frequency of 2.5 Hz, stroke length of 10 mm, and time of 60 min: (a) 0.5 wt.% C, (b) 1 wt.% C, and (c) 2 wt.% C.

Table 7.7 Wear data obtained for Cr-based WC hardmetals with extra 0.5, 1, and 2 wt.% C contents tested with a load of 50 N, frequency of 2.5 Hz, and stroke length of 10 mm against a WC-6Co ball.

Cr-based WC hardmetals with different C contents	Width $\overline{W}$ (μm)	Loss area $\overline{A_w}$ (μm^2)	Depth $\overline{D}$ (μm)	Volume loss $\overline{\Delta V}$ (10^{-6} mm^3)	Wear rate $\overline{W_v}$ (10^{-11} mm^3/mm)
0.5 wt.% C	224.4±4	702.1±26	2.3±0.1	7.1±0.2	7.0±0.1
	212.2±5	687.2±32	2.4±0.3	6.9±0.4	6.9±0.2
	192.7+7	697.0±27	2.5±0.2	7.0±0.2	7.0±0.1
1 wt.% C	224.1±4	1245.7±57	3.1±0.2	12.5±0.4	12.5±0.3
	234.5±5	1307.7±42	3.2±0.2	13.1±0.3	13.1±0.2
	220.7±3	1287.4±34	3.3±0.2	12.9±0.4	12.9±0.2
2 wt.% C	222.5.±4	1929.2±85	4.3±0.4	19.3±0.5	19.3±0.3
	233.9±5	2049.3±55	4.5±0.2	20.5±0.8	20.5±0.4
	225.0±3	2074.3±71	4.4±0.3	20.7±0.7	20.7±0.3

Finally, Figure 7.47 shows a histogram including the wear rates of Cr-based WC hardmetals obtained from both Bruker and Wazau tribometer tests, and the wear rates of some Co-based WC hardmetals found in the literature [43]. Cr-based WC hardmetals show higher wear rates under the conditions applied in Wazau tribometer than those in Bruker tribometer, due to the application of more severe wear conditions, including a higher applied load (50 N), a longer time (60 min), and a harder counter material (WC-6Co). The wear rate of Cr-based WC hardmetals increases with the increase of the C content due to the reduction of the hardness. Anyway, the Cr-based hardmetal with an extra 0.5 wt.% carbon content exhibits a much lower wear rate than Co-based WC hardmetals tested under similar dry ball-on-plate wear conditions, even considering that these Co-based WC hardmetals have a higher WC content (90 wt.%) than Cr-based WC hardmetals (83.2 wt.%). The combination of a nanosized WC grain and the avoidance of $(Cr,Fe)_7C_3$ or graphite phases leads to a superior wear performance. Thus, the use of Cr-based binders in the hardmetal industry, alternatively to Co-based binders, is promising in applications in which high wear resistance is needed. Due to the combination of high wear resistance and oxidation resistance, Cr-based WC hardmetals will be useful for applications in which both high oxidation and good wear resistances are needed.

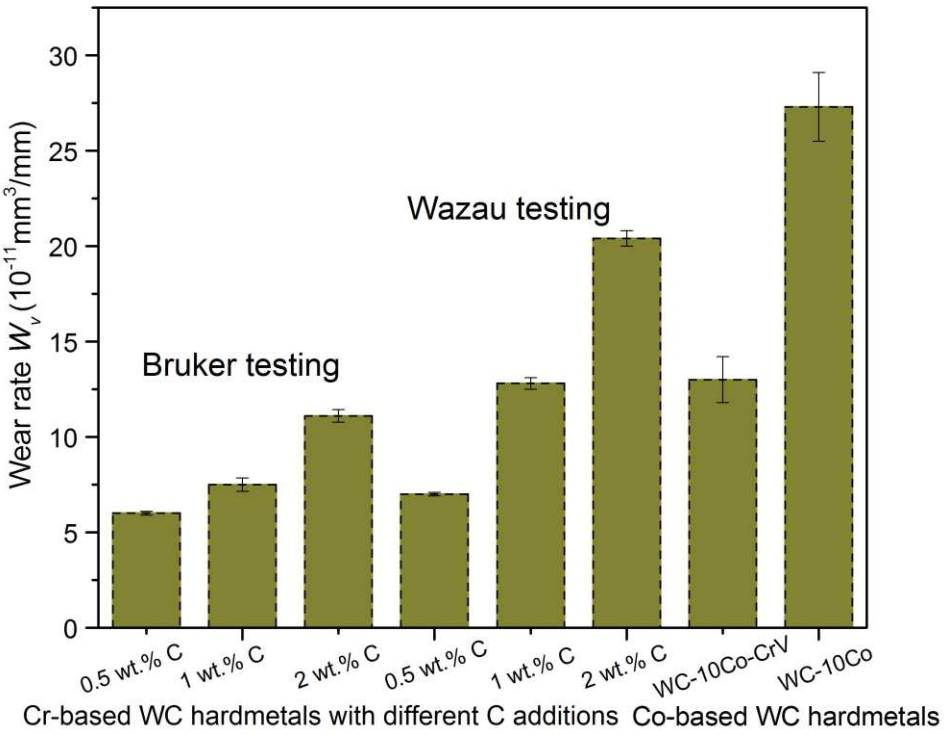

Figure 7.47. Wear rate comparison between Cr-based WC hardmetals (Bruker and Wazau tribometer test) and Co-based WC hardmetals [43].

7.6 Summary and conclusions

Cr-based WC hardmetals with the designed compositions are consolidated by spark plasma sintering under solid-state sintering. The sintering parameters are optimised based on their effects on shrinkage, phase formation, microstructure, density and mechanical properties. A high heating rate (400 °C/min), a long holding time (10 min), and a high applied pressure (80 MPa) during sintering, are beneficial parameters to improve the densification while maintaining a nanosized WC grain. The use of a W foil during SPS is useful to prevent the C diffusion from the graphite tools to the samples, leading to a good control of the final carbon content. The addition of a small content of iron as spherical carbonyl iron powder (CIP) improves the densification and limits the growth of the WC grain. Therefore, the hardness and fracture toughness values increase with the increase of the Fe content due to two facts: (i) the CIP powder helps improving the sinterability, since it has a high specific surface energy, leading to a higher hardness and fracture toughness; (ii) the growth of WC grain size is inhibited with the increase of the iron content due to the formation of Fe_3W_3C and Fe_6W_6C. The Cr-based WC hardmetal with extra 3 wt.% Fe content exhibits a high hardness value of 1910 HV30 and a fracture toughness value of 6.5 $MPam^{1/2}$. However, the extra 3 wt.% Fe content also induces the formation of brittle ŋ-phase, which limits the further improvement of the fracture toughness.

In order to further improve the toughness values, without losing oxidation and wear resistances, the effect of the addition of C to Cr-based WC hardmetals with extra 3 wt.% Fe content on the microstructure and properties is characterised by means of analysing the phase formation, microstructure, density, hardness and fracture toughness. The main conclusions achieved point out that the addition of 0.5 wt.% C reduces the formation of ŋ-phase and extra 1 and 2 wt.% C additions induce the formation of $(Cr,Fe)_7C_3$ and graphite, respectively. The real total C contents of Cr-based WC hardmetals with extra 0.5, 1, and 2 wt.% C additions are measured to be 5.6, 6.2, and 6.9 wt.% C, respectively, by using LECO technique. The Cr-based WC hardmetal with extra 3 wt.% Fe content and extra 0.5 wt.% C content reaches the best combination of hardness and fracture toughness (2219 HV30 and 8.2 $MPam^{1/2}$). The extremely high hardness reached comes from the uniform distribution of nanosized WC grain (average size of 100 nm). On the other hand, the inhibition of the formation of ŋ-phase contributes to the good fracture toughness, together with the high densification achieved. At this point, it is worth mentioning that another key point in the achievement of a good toughness in all these Cr-based WC

hardmetals is based on the formation of a thin $(W,Cr)_2C$ carbide between the WC and Cr_2O_3 phases. These properties are promising in comparison to those of Co-based WC hardmetals, considering that the volume fracture of WC reinforcement is only 70 %, which is lower than 80 % existing in the commercial Co-based WC hardmetals. Then, the Cr-based WC hardmetals with extra 0.5, 1, and 2 wt.% C contents are further characterised by nanoindentation tests, compressive tests at different temperatures (RT, 300 °C, and 600 °C), oxidation studies using a TGA equipment and three different temperatures (750, 800, and 850 °C) and also using a furnace at 900 °C, and wear tests under two different experimental conditions.

The nanoindentation tests show that the nanohardness values decrease with the increase of the C content, which also is in accordance with the Vickers hardness results. The Young's modulus of Cr-based WC hardmetals with 0.5, 1, and 2 wt.% carbon contents are calculated to be to 456.0 GPa, 337.2 GPa, and 405.4 GPa, respectively, which are comparable data to those of WC-Co hardmetals (ranging from 350 to 700 GPa).

The compressive tests demonstrate that the maximum stress and strain reached by the Cr-based WC hardmetals decrease with the increase of temperature, since the Cr-based binder becomes softer and the tested materials tend to be oxidised at elevated temperature. Another main conclusion drawn from the compressive tests, is that the maximum stress and strain decrease with the increase of the carbon content due to the decrease of the relative density, the increase of the WC grain size and the formation of $(Cr,Fe)_7C_3$ or soft graphite phases, which speeds up the crack propagation. Hence, the Cr-based WC hardmetal with an extra 0.5 wt.% carbon content has the highest compressive strength from RT (1600 MPa) to 600 °C (1100 MPa).

The oxidation tests show that all Cr-based WC hardmetals achieve a higher oxidation resistance than Co-based and Ni-based WC hardmetals under the same oxidation conditions, mainly due to their higher activation energy. The oxidation resistance decreases with the increase of the C content and temperature. Among all these Cr-based WC hardmetals, the Cr-based WC hardmetal with an extra 0.5 wt.% C content has the highest activation energy (269 kJ/mol) for oxidation, which makes this material very promising in applications where a high oxidation resistance is demanded.

The wear tests demonstrate that wear mechanism in Cr-based WC hardmetals is primarily determined by abrasive wear. Adhesion of debris wear layers, soft phase removals, and

cracks are confirmed due to the existence of a thin counter material layer, the detection of removed soft phases, and identification of cracks in the microstructure. The adhesion of debris wear layers is beneficial for improving the wear resistance due to the protection of the samples from the sliding materials. The wear rate of Cr-based WC hardmetals increases with the increase of the C content due to the reduction of the hardness as a consequence of the growth of the WC grains and to the existence of phases softer than WC, such as $(Cr,Fe)_7C_3$ or graphite. Again, the Cr-based WC hardmetal with an extra 0.5 wt.% C content exhibits the highest wear resistance and even better wear behaviour than Co-based WC hardmetals, under similar wear conditions, due to the uniform distribution of nanosized WC grains and to the avoidance of $(Cr,Fe)_7C_3$ and graphite in its microstructure.

Finally, SPSed Cr-based WC hardmetals have achieved a better combination of hardness and fracture toughness than LPSed hardmetals, which is in good accordance with the assumption that SPS technique may help limit the growth of WC and other brittle carbides. The developed novel Cr-based WC hardmetal with extra 3 wt.% Fe and 0.5 wt.% C contents has superior performance than commercial Co-based WC hardmetals, particularly in terms of oxidation resistance and wear resistance. In addition, the fracture toughness and hardness values achieved by this hardmetal are in the range of those reported for nanosized Co-hardmetals [13]. Furthermore, this Cr-based WC hardmetal will have a lower price and less toxicity than Co-based WC hardmetals. Therefore, Cr-based WC hardmetals seem to possess a bright future in the cutting tool industry, in applications in which both high oxidation resistance and wear resistance are required.

7.7 References

[1] C.J.R.G. Oliver, A. Caneiro, and J. Garcia, "Formation of nanocrystalline phases in sol-gel masses in the Fe-W-C(O) system and densification up to 1100ºC," *Procedia Mater. Sci.*, vol. 1, pp. 95–103, 2012.

[2] D.V. Suetin, I.R. Shein, and A.L. Ivanovskii, "Structural, electronic and magnetic properties of η carbides (Fe_3W_3C, Fe_6W_6C, Co_3W_3C and Co_6W_6C) from first principles calculations," *Phys. B Condens. Matter*, vol. 404, no. 20, pp. 3544–3549, 2009.

[3] R. Furushima, K. Katou, K. Shimojima, H. Hosokawa, and A. Matsumoto, "Control of WC grain sizes and mechanical properties in WC-FeAl composite fabricated from vacuum sintering technique," *Int. J. Refract. Met. Hard Mater.*, vol. 50, pp. 16–22, 2015.

[4] M. Mantina, A.C. Chamberlin, R. Valero, C.J. Cramer, and D.G. Truhlar, "Consistent van der Waals radii for the whole main group," *J. Phys. Chem. A*, vol. 113, no. 19, pp. 5806–5812, 2009.

[5] A.S. Kurlov and A.I. Gusev, *Tungsten carbides: structure, properties and application in hardmetals*, vol. 184. Springer Science & Business Media, 2013.

[6] A. Delanoë, M. Bacia, E. Pauty, S. Lay, and C.H. Allibert, "Cr-rich layer at the WC/Co interface in Cr-doped WC-Co cermets: Segregation or metastable carbide," *J. Cryst. Growth*, vol. 270, no. 1–2, pp. 219–227, 2004.

[7] M.D. Demetriou, N.M. Ghoniem, and A.S. Lavine, "Computation of metastable phases in tungsten-carbon system," *J. phase equilibria*, vol. 23, no. 4, p. 305, 2002.

[8] V. Ramnath and N. Jayaraman, "Quantitative phase analysis by X-ray diffraction in the Co-WC system," *J. Mater. Sci. Lett.*, vol. 6, no. 12, pp. 1414–1418, 1987.

[9] F.D. Lai, C.Y. Huang, C.M. Chang, L.A. Wang, and W.C. Cheng, "Ultra-thin Cr_2O_3 well-crystallized films for high transmittance APSM in ArF line," *Microelectron. Eng.*, vol. 67, pp. 17–23, 2003.

[10] E. Sourty, J.L. Sullivan, and M.D. Bijker, "Chromium oxide coatings applied to magnetic tape heads for improved wear resistance," *Tribol. Int.*, vol. 36, no. 4–6, pp. 389–396, 2003.

[11] J.A. Cline, A.A. Rigos, and T.A. Arias, "Ab initio study of magnetic structure and chemical reactivity of Cr_2O_3 and its (0001) surface," *J. Phys. Chem. B*, vol. 104, no. 26, pp. 6195–6201, 2000.

[12] D.C. Azubike, A. Chrysanthou, and U.O. Igiehon, "A Crystallographic Re-Examination of the $(Fe,W)_6C$ Phase Field in the Fe-WC System," *Powder Diffr.*, vol. 7, no. 3, pp. 162–163, 1992.

[13] W.D. Schubert, H. Neumeister, G. Kinger, and B. Lux, "Hardness to toughness relationship of fine-grained hardmetals WC-CO," *Int. J. Refract. Met. Hard Mater.*, vol. 16, pp. 133–142, 1998.

[14] B. Kaplan, S. Norgren, M. Schwind, and M. Selleby, "Thermodynamic calculations and experimental verification in the WC-Co-Cr cemented carbide system"," *Int. J. Refract. Met. Hard Mater.*, vol. 49, no. 1, pp. 400–405, 2015.

[15] Z.Z. Fang, X. Wang, T. Ryu, K.S. Hwang, and H.Y. Sohn, "Synthesis, sintering, and mechanical properties of nanocrystalline cemented tungsten carbide-A review," *Int. J. Refract. Met. Hard Mater.*, vol. 27, no. 2, pp. 288–299, 2009.

[16] E. Satyanarayana, A. Flavia, C. Ramos, L.L. Shaw, and Z. Chen, "Investigation of microstructure and mechanical properties at low and high temperatures of WC-6 wt.% Co," *Int. J. Refract. Met. Hard Mater.*, vol. 58, pp. 172–181, 2016.

[17] I.C. Lee and T. Sakuma, "High-temperature tensile fuctility in WC-Co cemented carbides," *Metall. Mater. Trans. A*, vol. 28, no. 9, pp. 1843–1847, 1997.

[18] K. Mandel, M. Radajewski, and L. Krüger, "Strain-rate dependence of the compressive strength of WC–Co hardmetals," *Mater. Sci. Eng. A*, vol. 612, pp. 115–122, 2014.

[19] L.S. Sigl and H.E. Exner, "Experimental Study of the Mechanics of Fracture in WC-Co Alloys," *Metall. Trans. A*, vol. 18, pp. 1299–1308, 1987.

[20] S. Ndlovu, "The wear properties of tungsten carbide-cobalt hardmetals from the nanoscale up to the macroscopic scale (Doctoral thesis, Friedrich-Alexander-Universität Erlangen-Nürnberg)" 2009.

[21] I. Konyashin, S. Hlawatschek, B. Ries, F. Lachmann, F. Dorn, and A. Sologubenko, "On the mechanism of WC coarsening in WC-Co hardmetals with various carbon contents," *Int. J. Refract. Met. Hard Mater.*, vol. 27, no. 2, pp. 234–243, 2009.

[22] T. Bao, H. Zuhailawati, Z. Ari, and K.N. Ishihara, "Sintering characteristics and properties of WC-10AISI304 (stainless steel) hardmetals with added graphite," *Mater. Sci. Eng. A*, vol. 605, pp. 210–214, 2014.

[23] V.B. Voitovich, V.V. Sverdel, R.F. Voitovich, E.I. Golovko, and I.N. Frantsevich, "Oxidation of WC-Co, WC-Ni and WC-Co-Ni hard metals in the temperature range 500 ~ 800 °C," *Int. J. Refract. Met. Hard Mater.*, vol. 14, no. 4, pp. 289–295, 1996.

[24] F.E. Rizzo, L.R. Bidwell, and D.F. Frank, "Thermodynamics of the tungsten-oxygen system," *Aerospace research labs wright-patterson.*, no. ARL-68-0057, 1968.

[25] M. Aristizabal, J.M. Sanchez, N. Rodriguez, F. Ibarreta, and R. Martinez, "Comparison of the oxidation behaviour of WC-Co and WC-Ni-Co-Cr cemented carbides," *Corros. Sci.*, vol. 53, no. 9, pp. 2754–2760, 2011.

[26] M. Aristizabal, N. Rodriguez, F. Ibarreta, R. Martinez, and J.M. Sanchez, "Liquid phase sintering and oxidation resistance of WC-Ni-Co-Cr cemented carbides," *Int. J. Refract. Met. Hard Mater.*, vol. 28, no. 4, pp. 516–522, 2010.

[27] A. Bautista, F. Velasco, and J. Abenojar, "Oxidation resistance of sintered stainless steels : effect of yttria additions," *Corros. Sci.*, vol. 45, no. 6, pp. 1343–1354, 2003.

[28] J. Szekely and J. W. Evans, "A structural model for gas-solid reactions with a moving boundary," *Chem. Eng. Sci.*, vol. 25, no. 6, pp. 1091–1107, 1970.

[29] S. Republic, "Isoconversional methods fundamentals, meaning and application," *J. Therm. Anal. Calorim.*, vol. 76, pp. 123–132, 2004.

[30] K.T. Jacob, "Phase relationships in the system Cr-W-O and thermodynamic properties of $CrWO_4$ and Cr_2WO_6," *J. Mater. Sci.,* vol. 15, pp. 2167–2174.

[31] S. Telu, V. Karthik, R. Mitra and S.K. Pabi, "Effect of 10 at .% Nb addition on sintering and high temperature oxidation of $W_{0.5}Cr_{0.5}$ Alloy," *Mater. Sci. Forum*., vol. 710, pp. 308–313, 2012.

[32] L. Chen, D. Yi, B. Wang, H. Liu, and C. Wu, "Mechanism of the early stages of oxidation of WC-Co cemented carbides," *Corros. Sci.*, vol. 103, pp. 75–87, 2016.

[33] B. J. Marques, C. M. Fernandes, and A. M. R. Senos, "Sintering, microstructure and properties of WC-AISI304 powder composites," *J. Alloys Compd.*, vol. 562, pp. 164–170, 2013.

[34] J. Zackrisson, B. Jansson, G. S. Uphadyaya, and H. Andrn, "WC-Co based cemented carbides with large Cr_3C_2 additions," *Int. J. Refract. Metals Hard Mater.*, vol. 16, pp. 417–422, 1998.

[35] F.J. Arenas, A. Matos, M. Cabezas, C.D. Rauso amd C. Grigorescu "Densification, mechanical properties and wear behavior of WC-VC-Co-Al hardmetals," *Int. J. Refract. Met. Hard Mater.*, vol.19, no. 4, 2001.

[36] H. Saito, A. Iwabuchi, and T. Shimizu, "Effects of Co content and WC grain size on wear of WC cemented carbide," *Wear*, vol. 261, pp. 126–132, 2006.

[37] C. Allen, M. Sheen, J. Williams, and V.A. Pugsley, "The wear of ultrafine WC-Co hard metals," *Wear*, vol. 250, pp. 604–610, 2001.

[38] R.B. Bhagat, J.C. Conway, M.F. Amateau, and R.A. Brezler, "Tribological performance evaluation of tungsten carbide-based cermets and development of a fracture mechanics wear model," *Wear*, vol. 102, no. 12, pp. 233–243, 1996.

[39] K. Jia and T.E. Fischer, "Abrasion resistance of nanostructured and conventional cemented carbides," *Wearr*, vol. 200, pp. 206–214, 1996.

[40] K. Jia and T.E. Fischer, "Sliding wear of conventional and nanostructured cemented carbides," *Wear*, vol. 204, pp. 310–318, 1997.

[41] S.I. Cha, S.H. Hong, G.H. Ha, and B.K. Kim, "Microstructure and mechanical properties of nanocrystalline WC-10Co cemented carbides," *Scr. Mater.*, vol. 44, no. 3, pp. 1535–1539, 2001.

[42] K. Bonny, P. De Baets, Y. Perez, J. Vleugels, and B. Lauwers, "Friction and wear characteristics of WC-Co cemented carbides in dry reciprocating sliding contact," *Wear*, vol. 268, no. 11–12, pp. 1504–1517, 2010.

[43] K. Bonny, P. De Baets, J. Vleugels, S. Huang, O. Van Der Biest, and B. Lauwers, "Impact of Cr_3C_2/VC addition on the dry sliding friction and wear response of WC-Co cemented carbides," *Wear*, vol. 267, pp. 1642–1652, 2009.

[44] J. Larsen-Basse, "Effect of composition, microstructure, and service conditions on the wear of cemented carbides," *JOM*, vol. 35, no. 11, pp. 35–42, 1983.

Chapter 8

Final conclusions

Contents

8. Final conclusions

This doctoral thesis has been devoted to the development of Cr-based WC hardmetals using a combination of thermodynamic modelling and experimental studies. The alloy design of Cr-based WC hardmetals is supported by Thermo-Calc. The designed Cr-based WC hardmetals are processed by a powder metallurgy (PM) route, including mechanical milling (MM) and two different sintering techniques: liquid phase sintering (LPS) and spark plasma sintering (SPS). The following main conclusion can be drawn from this investigation:

- The viability of processing new Cr-based WC hardmetals by a solid-state sintering technique, as it is the particular case of SPS, with an optimal hardness to toughness relationship and outstanding oxidation and wear resistances, is assessed in this research. Thus, the exceptional combination of oxidation resistance and wear resistance values reached may lead to a future replacement of conventional Co-based WC hardmetals in those applications in which very oxidising environments or aggressive wear conditions are applied simultaneously.

In addition, other important partial conclusions of this work are summarised as follows:

1) The use of thermo-Calc allows the study of the effect of adding extra Fe or Fe/C contents on the phase diagram of the W-C-Cr-Fe system. The formation of WC, W_2C, M_7C_3 and α phases is found in the equilibrium phase diagram of this system, when the percentage of volume fraction corresponding to WC is 70% (78.1 wt.% of W, 5.1 wt.% of C, 12 wt.% of Cr and 4.8 wt.% of Fe). Extra Fe contents in the system (0-5 wt.%) favour the sinterability of Cr-based WC hardmetals due to the high specific surface energy of the carbonyl Fe powder, and to the reduction of the melting point. However, the addition of extra 1-3 wt.% Fe contents and 5 wt.% Fe contents induces the formation of brittle M_6C carbide and $M_{23}C_6$ carbide, respectively, which are harmful phases that reduce the fracture toughness. In order to develop Cr-based WC hardmetals without decreasing significantly the Cr content, avoiding the loss of oxidation and wear resistances, the W-C-Cr-Fe system with extra 3 wt.% Fe content is selected as the optimised system to study the possibility of enhancing the toughness by adding carbon. Indeed, the addition of an extra 0.5 wt.% C content inhibits the formation of the M_6C carbide, which is beneficial for improving the toughness. On the other hand, the addition of an extra 1 wt.% C content induces the transformation

of W_2C into WC and M_7C_3 into M_3C_2, which is beneficial for enhancing the hardness. Finally, the addition of an extra 2 wt.% C content induces the formation of a soft graphite phase, which obviously decreases the hardness of these hardmetals.

2) The experimental studies demonstrate that the milling process of the Cr-based WC hardmetal powder belongs to a brittle-ductile mechanism, in which the brittle WC particles are homogenously distributed in the soft Cr-based matrix. The particle size and the crystalline size decrease, while the internal microstrain increases, with the milling time. The Cr-based WC powder after 20 h of milling at 350 rpm is adequate for the subsequent sintering step, since this powder is round and fine, with a homogenous microstructure and good crystalline size and microstrain parameters.

3) Cr-based WC hardmetals designed by thermodynamic modelling are processed by liquid phase sintering at 1450 °C for 30 min. Extra Fe additions improve the densification and induce the growth of the WC grain size due to the high surface energy introduced by the fine and round carbonly iron powder and to the reduction of the melting point of the system. XRD analyses confirm the formation of $(W,Cr)_2C$, Fe_3W_3C and $Fe_{21}W_2C_6$ phases, which are also predicted by the thermodynamic modelling. The formation of Cr_2O_3 is obviously not expected from the simulation results due to the modelling of a quaternary W-C-Cr-Fe system without oxygen. XRD and microstructural analyses confirm its formation due to the strong affinity of Cr to O at high temperature, since some limited O content inevitably exists in the real sintering environment. The Cr-based WC hardmetal with an extra 3 wt.% Fe content achieves the best hardness and fracture toughness values. Therefore, the Cr-based WC hardmetal with an extra 3 wt.% Fe content is selected as the precursor for further studying the effect of adding different carbon contents.

4) Indeed, the extra C addition prevents the formation of the undesirable η-phase (Fe_3W_3C) in the LPSed hardmetals and induces the transformation of W_2C into WC, which improve the mechanical properties. XRD and microstructural analyses confirm that Cr_2O_3 also disappears with an extra C addition, since C could remove most oxides by forming gaseous CO/CO_2. More importantly, an extra 1 wt.% C content induces the formation of $Fe_{21}W_2C_6$ and Cr_7C_3 phases, limiting the growth of WC grains and leading to a fine WC homogenously distributed within Cr-based binder. On the other hand, an extra 2 wt.% C content induces the growth of these two carbides, leading to a heterogeneous microstructure and, consequently, a reduction

of toughness is found. Therefore, the LPSed Cr-based WC hardmetal with extra 3 wt.% Fe and 1 wt.% C contents achieves the best mechanical properties (1647 HV30 and 6.0 $MPam^{1/2}$) due to the improved densification and to its homogenous microstructure with small WC grain size (<1 μm). However, the toughness achieved is still not enough high, mainly due to the existence of big brittle carbides such as $Fe_{21}W_2C_6$ and Cr_7C_3. Thus, the viablity of consolidating Cr-based WC hardmetals by a fast solid-state-processing is subsequently evaluated, in order to prevent or limit the formation of undesirable brittle carbides and to further improve the fracture toughness by reducing the growth of the microstructure.

5) Cr-based WC hardmetals with the designed compositions are also processed by spark plasma sintering under solid-state conditions. The study of different sintering parameters reveals that a higher heating rate (400 °C/min), a longer holding time (10 min), and a higher applied pressure (80 MPa) are beneficial conditions to enhance the densification of the final sample. Again, the addition of a round and fine carbonyl iron powder improves the densification by favoring the sintering and limits the growth of the WC grain due to the formation of Fe_6W_6C and Fe_3W_3C carbides. Hence, the hardness and fracture toughness values increase with the increase of the Fe content. The Cr-based WC hardmetal with an extra 3 wt.% Fe content exhibits a high hardness value of 1910 HV30 and a fracture toughness value of 6.5 $MPam^{1/2}$. However, the extra 3 wt.% Fe content also induces the formation of brittle Fe_3W_3C phase, which limits the further improvement of the fracture toughness.

6) In order to further improve the toughness without losing hardness, different extra carbon contents are added into Cr-based WC hardmetals with extra 3 wt.% Fe content. The addition of 0.5 wt.% C reduces the formation of the η-phase (Fe_3W_3C), whereas extra 1 wt.% and 2 wt.% C contents also avoid the η-phase formation but, as a negative effect, these carbon contents induce the formation of $(Cr,Fe)_7C_3$ and graphite, respectively. The real total carbon contents in Cr-based WC hardmetals with an extra 0.5 wt.%, 1 wt.% or 2 wt.% C content are measured to be 5.6 wt.%, 6.2 wt.%, and 6.9 wt.% C, respectively. The Cr-based WC hardmetal with extra 3 wt.% Fe and 0.5 wt.% C contents has achieved the best hardness and fracture toughness relationship (2219 HV30 and 8.2 $MPam^{1/2}$). This extremely high hardness comes from the uniform distribution of nanosized WC grain (average grain size of 100 nm), whereas the inhibition of the Fe_3W_3C formation, together with the formation of a thin $(W,Cr)_2C$ phase along the interfaces between WC and Cr_2O_3, contribute to the good fracture toughness achieved.

7) Then, other mechanical properties of SPSed Cr-based WC hardmetals, such as nanoindentation tests and compressive tests, are evaluated. Furthermore, their oxidation resistance and wear performance are assessed in order to study the viability of using these innovative hardmetals in cutting tools.
8) The nanoindentation tests prove that the nanohardness decreases with the increase of the carbon content. The Young's modulus of Cr-based WC hardmetals with 0.5 wt.%, 1 wt.%, and 2 wt.% C contents are calculated as 456.0 GPa, 337.2 GPa, and 405.4 GPa, which are comparable values to those presented by commercial WC-Co hardmetals (ranging values from 350 to 700 GPa).
9) The compressive tests demonstrate that the maximum stress and strain reached by Cr-based WC hardmetals decrease when the temperature increases and also with the increase of the carbon content due to different factors: the density decreases together with an increase of the WC grain size and $(Cr,Fe)_7C_3$ (1 wt.% extra carbon) or graphite (2 wt.% extra carbon) are formed. The Cr-based WC hardmetal with an extra 0.5 wt.% carbon content has the highest compressive strength (around 1600 MPa at RT).
10) The oxidation tests show that all Cr-based WC hardmetals achieve significant higher oxidation resistances than Co-based and Ni-based WC hardmetals under the same conditions, mainly due to their high activation energy for oxidation. Among these Cr-based WC hardmetals, the hardmetal with the lowest extra carbon content (0.5 wt.%) has the highest activation energy (269 kJ/mol) for oxidation, which leads to the lowest mass gain and makes this sample very useful in applications where a high oxidising environment is present.
11) The dry ball-on-plate wear tests demonstrate that the wear mechanism in Cr-based WC hardmetals is determined by abrasive wear, producing adhesion of debris layers, soft phase removals and cracks growth. The adhesion of wear debris layers is beneficial for improving the subsequent wear due to the protection of the tested samples from the sliding materials. The wear rate of Cr-based WC hardmetals increases with the increase of the carbon content, as a result of the reduction of the average hardness within the bulk. Again, the Cr-based WC hardmetal with an extra 0.5 wt.% carbon content exhibits the highest wear resistance and it is remarkable that its value is much higher than those reported for commercial Co-based WC hardmetals under similar wear conditions, which also makes this material very interesting for applications under aggressive wear conditions.

As a summary of the conclusions, it should be noted that the Cr-based WC hardmetal with extra 3 wt.% Fe and 0.5 wt.% C contents achieves the best comprehensive performance including mechanical properties, oxidation resistance and wear resistance. These good properties are mainly due to the existence of a homogenous microstructure comprising nanosized WC, binder Cr-based alloy, thin $(W,Cr)_2C$ carbide and Cr_2O_3 oxide. Therefore, this novel Cr-based WC hardmetal has demonstrated to possess a great potential to be introduced in the cutting tool market in applications in which a combination of high oxidation resistance and extreme wear resistance is needed.